Evaluating the Impacts of Dispersed Metals' Local Environments on Catalytically Relevant Outcomes for Chromium- or Platinum-Containing Zeolite Catalysts

By

NOAH WILLIAM FELVEY

DISSERTATION

Submitted in partial satisfaction of the requirements for the degree of

DOCTOR OF PHILOSOPHY

in

Chemical Engineering

in the

OFFICE OF GRADUATE STUDIES

of the

UNIVERSITY OF CALIFORNIA

DAVIS

Approved:

Coleman X. Kronawitter, Co-Chair

Ron C. Runnebaum, Co-Chair

Bruce C. Gates

Committee in Charge

2022

# Table of Contents

## Abstract

When supported metal catalysts contain metal components existing at or near atomic dispersion, the support surface largely controls the properties of the highly dispersed metal species by determining the local chemical bonding environments of the metals. The framework structures of zeolites afford unique bonding environments for supported metals which can result in catalysts having unusual properties. The research described in this dissertation was aimed at identifying potential advantages of using zeolites as supports for catalysts containing chromium or platinum – two industrially applied catalyst metals whose intra-zeolite chemistries are not fully resolved in the literature.

Chromium was dispersed on HZSM-5. Samples were characterized using X-ray absorption near edge structure (XANES) and infrared (IR) spectroscopies and evaluated for ethane dehydrogenation. At low chromium loadings, chromium was located at zeolite aluminum sites and Cr/HZSM-5 samples displayed stable ethane dehydrogenation activity with time on stream. Higher chromium loadings resulted in catalysts with higher dehydrogenation activity per chromium atom but that deactivated quickly, and this was correlated to higher fractions of electron-rich or multinuclear chromium present in these samples. The results represent an attempt to assess the potential for catalytic application of Cr/ZSM-5, taking into account the speciation of chromium among various anchoring sites on the zeolite surface.

Platinum was dispersed onto HZSM-5 and characterized using X-ray absorption and IR spectroscopies. During exposure of Pt/ZSM-5 to high-temperature, oxidizing conditions, $Pt^{2+}$ ions were stabilized at six-membered rings in the zeolite that contained paired-aluminum sites. This interpretation was informed by a theory-guided analysis of X-ray absorption fine structure spectroscopy (EXAFS) data. These $Pt^{2+}$ ions formed highly uniform platinum gem-dicarbonyls, and the steps leading toward formation of platinum clusters were monitored through the evolution of IR spectra during exposure of platinum carbonyls to reducing conditions. Platinum clusters in HZSM-5 were redispersed into $Pt^{2+}$ cations under high-temperature, oxidizing conditions, with the $Pt^{2+}$ cations returning to paired-aluminum, six-membered ring sites. Similar platinum *gem*-dicarbonyl complexes formed in several commercially used zeolites (ZSM-

5, Beta, mordenite, and Y), demonstrating the generality of the chemistry across zeolite frameworks. The findings connect catalyst structural properties to critical performance outcomes for an industrially-relevant catalyst material system.

Chromium was dispersed onto a series of MFI zeolites with various support compositions. The catalysts were characterized by IR or X-ray absorption spectroscopies and evaluated for ethane dehydrogenation with or without $CO_2$. The copresence of $Cr^{2+}$ and $Cr^{3+}$ in siliceous or borosilicate MFI zeolites was correlated with significant enhancements in the rates ethane dehydrogenation when $CO_2$ was added to the reaction mixture. The aluminosilicate MFI zeolite, in contrast, stabilized chromium in the +2 oxidation state during reaction, resulting in a catalyst that exhibited low rates of $CO_2$ reduction to CO by $H_2$ and no enhancement of ethane dehydrogenation by $CO_2$. The mechanistic role of $CO_2$ is discussed in the context of ethane dehydrogenation with Cr/MFI catalysts.

Additional experiments characterizing Cr/zeolite or Pt/zeolite samples provided insights into the local environments of the supported metals. Platinum carbonyl complexes in HZSM-5 and Y zeolite were characterized by XAS in order to complement the results of IR spectroscopy. Similar chromium or platinum species existed in zeolites of identical framework structure but different heteroatom identity. Supported chromium or platinum species similar to those found in HZSM-5 were found to exist in zeolites other than HZSM-5.

## Acknowledgements

I am grateful to my parents for their unending love and for providing every opportunity imaginable,

to my friends for making Davis a home,

and to my advisors, Ron and Coleman, for somehow always having faith in me.

I’m very lucky.

# **Chapter 1.** Introduction

## 1.1 Introduction

A current goal in the field of catalysis science consists in controlling the properties of small metal ensembles (dimensions < 2 nm) in supported-metal catalysts.[1] Smaller metal nanoparticles contain higher fractions of their atoms exposed to incoming molecules, reducing the amount of expensive or scarce metal located on the interior of nanoparticles that does not directly participate in catalysis. Smaller metal nanoparticles also display different properties from larger nanoparticles or bulk metals, providing opportunities for catalyst design.[1] At the lower limit of metal ensemble size are mononuclear, or atomically dispersed, metal species that can display radically different properties due to the absence of metal–metal bonding.[1,2] Atomically dispersed metals bond only with atoms of the support, making the support a critical parameter controlling of the chemistry of the supported metal.[3] Two classes of catalysts that highlight this concept are represented by materials consisting of (1) platinum or (2) chromium dispersed on the surfaces of oxide supports.[4,5]

Platinum-containing catalysts, in which platinum is typically present as supported metallic nanoparticles, have been used widely in industry for decades, especially for their efficiency in catalyzing hydrogenations.[6] More recently, efficient catalytic conversion have been reported for catalysts containing atomically dispersed platinum species, and the properties of these catalysts are found to depend strongly on characteristics of the supports.[7] Mononuclear platinum species have also been shown to be involved in the structural evolution of nanoparticles subjected to harsh redox conditions associated with industrial applications.[8,9]

Chromium-containing catalysts have long been recognized to contain active sites composed of supported, mononuclear metal species.[10–12] More than one third of polyethylene is produced using the Phillips catalyst, $Cr/SiO_2$, which contains mononuclear chromium cations bonded to oxygen atoms of $SiO_2$.[12] Only a small fraction of chromium present in $Cr/SiO_2$ catalysts is believed to be active for polymerization, highlighting the degree to which the local bonding environment imposed by the support controls the chemistry of the supported metal.[12] Chromium-based catalysts are used also for alkane

dehydrogenation, enabling the efficient utilization of abundant natural gas supplies.[13] Although the dehydrogenation mechanism is roughly understood, developing structure–function relationships to aid the design of improved catalysts remains a challenge.

Zeolites are a class of microporous, crystalline, aluminosilicate oxide materials that are widely used for separations as molecular sieves or for catalysis as acid catalysts.[14,15] The use of zeolites as supports for metal catalysts is associated with many benefits. Encapsulation of metals within zeolites provides opportunities to closely integrate metal catalytic functionality with zeolite surface acid sites to enable bifunctional catalytic conversions with selectivities modulated by transport limitations in the molecular-scale pores of the zeolite.[16,17] Zeolite-supported metal nanoparticles have been observed to be stable against Ostwald ripening, allowing to maintain the particle size distribution for longer catalyst lifetimes.[18] The structure and stability of dispersed metal or metal oxide clusters on zeolites are impacted profoundly by tetrahedral aluminum sites in the zeolite framework, allowing for the stabilization of catalytic sites in the microporous zeolite voids that would not form on other supports.[19] The surfaces of crystalline zeolites present well-defined bonding sites for supported metals, resulting in structurally precise populations of supported metal species that are amenable to characterization.[20,21] The work described in Chapters 2–5 focuses on utilizing these properties of zeolites as catalyst supports to assist the design of improved chromium- or platinum-containing catalysts.

In Chapter 2, catalysts composed of chromium dispersed on zeolite ZSM-5 were investigated in the context of catalytic ethane dehydrogenation. Probe molecule FTIR and XANES were used to characterize the nature of chromium sites across a range of chromium loadings and in the presence of various extra-framework cations on ZSM-5. These characteristics were related to catalytic performance in ethane dehydrogenation toward the goal of developing design principles for Cr/zeolite catalysts for improved alkane conversions.

Chapter 3 describes an experimental and theoretical investigation of the structure, bonding, and local environment of cationic platinum species in zeolite ZSM-5, which are key intermediates in the cycling of platinum during operation and regeneration as hydrocarbon conversion catalysts. Upon exposure of

platinum clusters to $O_2$ at 700 °C, oxidative fragmentation of platinum clusters was observed, forming $Pt^{2+}$ ions that were stabilized at six-membered rings in the zeolite that contained paired aluminum sites. When exposed to CO under mild conditions, these $Pt^{2+}$ ions formed highly uniform platinum *gem*-dicarbonyls, which informed on the speciation of platinum on the zeolite surface and the processes leading to the formation of platinum clusters.

Chapter 4 describes results of experiments involving a series of Cr/MFI zeolite catalysts with various support compositions. Samples were synthesized, characterized by IR or X-ray absorption spectroscopies, and evaluated for ethane dehydrogenation with or without $CO_2$ in order to identify supported chromium structures whose respective catalytic activities are impacted by the presence of $CO_2$. The mechanistic role of $CO_2$ is discussed in the context of ethane dehydrogenation with Cr/MFI catalysts.

Appendices A and B report the results of experiments that were performed along with those described in Chapters 2–4 but did not fall within the scope of any of the Chapters. The results include characterization by IR and X-ray absorption spectroscopies of chromium-zeolite (Appendix A) and platinum-zeolite (Appendix B) samples. The results provide comparisons between metal species supported on zeolites having different framework structure or composition. This may inform future work that extends from the results of Chapters 2–4.

## 1.2 References


(1) Liu, L.; Corma, A. Metal Catalysts for Heterogeneous Catalysis: From Single Atoms to Nanoclusters and Nanoparticles. *Chem. Rev.* **2018**, *118*, 4981–5079.

(2) Gates, B. C.; Flytzani-Stephanopoulos, M.; DIxon, D. A.; Katz, A. Atomically Dispersed Supported Metal Catalysts: Perspectives and Suggestions for Future Research. *Catal. Sci. Technol.* **2017**, *7*, 4259–4275.

(3) DeRita, L.; Resasco, J.; Dai, S.; Boubnov, A.; Thang, H. V.; Hoffman, A. S.; Ro, I.; Graham, G. W.; Bare, S. R.; Pacchioni, G.; Pan, X.; Christopher, P. Structural Evolution of Atomically Dispersed Pt Catalysts Dictates Reactivity. *Nat. Mater.* **2019**, *18*, 746–751.

(4) Chen, Y.; Sun, H.; Gates, B. C. Prototype Atomically Dispersed Supported Metal Catalysts: Iridium and Platinum. *Small* **2020**, *17*, 2004665.

(5) Brown, C.; Krzystek, J.; Achey, R.; Lita, A.; Fu, R.; Meulenberg, R. W.; Polinski, M.; Peek, N.; Wang, Y.; Van De Burgt, L. J.; Profeta, S.; Stiegman, A. E.; Scott, S. L. Mechanism of Initiation in the Phillips Ethylene Polymerization Catalyst: Redox Processes Leading to the Active Site. *ACS*

*Catal.* **2015**, *5*, 5574–5583.

(6) Ertl, G.; Knozinger, H.; Schuth, F.; Weitkamp, J. *Handbook of Heterogeneous Catalysis*; Wiley-VCH Verlag, 2008.

(7) Resasco, J.; Christopher, P. Atomically Dispersed Pt-Group Catalysts: Reactivity, Uniformity, Structural Evolution, and Paths to Increased Functionality. *J. Phys. Chem. Lett.* **2020**, *11*, 10114–10123.

(8) Goodman, E. D.; Johnston-Peck, A. C.; Dietze, E. M.; Wrasman, C. J.; Hoffman, A. S.; Abild-Pedersen, F.; Bare, S. R.; Plessow, P. N.; Cargnello, M. Catalyst Deactivation via Decomposition into Single Atoms and the Role of Metal Loading. *Nat. Catal.* **2019**, *2*, 748–755.

(9) Moliner, M.; Gabay, J. E.; Kliewer, C. E.; Carr, R. T.; Guzman, J.; Casty, G. L.; Serna, P.; Corma, A. Reversible Transformation of Pt Nanoparticles into Single Atoms inside High-Silica Chabazite Zeolite. *J. Am. Chem. Soc.* **2016**, *138*, 15743–15750.

(10) Zecchina, A.; Groppo, E. Surface Chromium Single Sites: Open Problems and Recent Advances. *Proc. R. Soc. A Math. Phys. Eng. Sci.* **2012**, *468*, 2087–2098.

(11) Groppo, E.; Lamberti, C.; Bordiga, S.; Spoto, G.; Zecchina, A. The Structure of Active Centers and the Ethylene Polymerization Mechanism on the $Cr/SiO_2$ Catalyst: A Frontier for the Characterization Methods. *Chem. Rev.* **2005**, *105*, 115–183.

(12) McDaniel, M. P. *A Review of the Phillips Supported Chromium Catalyst and Its Commercial Use for Ethylene Polymerization*, 1st ed.; Elsevier Inc., 2010; Vol. 53.

(13) Sattler, J. J. H. B.; Ruiz-Martinez, J.; Santillan-Jimenez, E.; Weckhuysen, B. M. Catalytic Dehydrogenation of Light Alkanes on Metals and Metal Oxides. *Chem. Rev.* **2014**, *114*, 10613–10653.

(14) Corma, A.; Martinez, A. Zeolites and Zeotypes as Catalysts. *Adv. Mater.* **1995**, *7*, 137–144.

(15) Corma, A. From Microporous to Mesoporous Molecular Sieve Materials and Their Use in Catalysis. *Chem. Rev.* **1997**, *97*, 2373–2419.

(16) Goel, S.; Wu, Z.; Zones, S. I.; Iglesia, E. Synthesis and Catalytic Properties of Metal Clusters Encapsulated within Small-Pore (SOD, GIS, ANA) Zeolites. *J. Am. Chem. Soc.* **2012**, *134*, 17688–17695.

(17) Wang, C.; Guan, E.; Wang, L.; Chu, X.; Wu, Z.; Zhang, J.; Yang, Z.; Jiang, Y.; Zhang, L.; Meng, X.; Gates, B. C.; Xiao, F. S. Product Selectivity Controlled by Nanoporous Environments in Zeolite Crystals Enveloping Rhodium Nanoparticle Catalysts for $CO_2$ Hydrogenation. *J. Am. Chem. Soc.* **2019**, *141*, 8482–8488.

(18) Moliner, M.; Gabay, J.; Kliewer, C.; Serna, P.; Corma, A. Trapping of Metal Atoms and Metal Clusters by Chabazite under Severe Redox Stress. *ACS Catal.* **2018**, *8*, 9520–9528.

(19) Dinh, K. T.; Sullivan, M. M.; Narsimhan, K.; Serna, P.; Meyer, R. J.; Dincă, M.; Román-Leshkov, Y. Continuous Partial Oxidation of Methane to Methanol Catalyzed by Diffusion-Paired Copper Dimers in Copper-Exchanged Zeolites. *J. Am. Chem. Soc.* **2019**, *141*, 11641–11650.

(20) Uzun, A.; Bhirud, V. A.; Kletnieks, P. W.; Haw, J. F.; Gates, B. C. A Site-Isolated Iridium Diethylene Complex Supported on Highly Dealuminated Y Zeolite: Synthesis and Characterization. *J. Phys. Chem. C* **2007**, *111*, 15064–15073.

(21) Liang, A. J.; Bhirud, V. A.; Ehresmann, J. O.; Kletnieks, P. W.; Haw, J. F.; Gates, B. C. A Site-Isolated Rhodium-Diethylene Complex Supported on Highly Dealuminated Y Zeolite: Synthesis and Characterization. *J. Phys. Chem. B* **2005**, *109*, 24236–24243.

# **Chapter 2.** Ethane dehydrogenation over Cr/ZSM-5: Characterization of active sites through probe molecule adsorption FTIR

Adapted from publication in *Catalysis Science and Technology*

N. W. Felvey, M. J. Meloni, C. X. Kronawitter, R. C. Runnebaum, *Catal. Sci. Technol.*, **2020**, 10, 5069-5081.

DOI: 10.1039/d0cy01022g

## 2.1 Abstract

Dispersed Cr species supported on zeolite ZSM-5 were investigated in the context of catalytic ethane dehydrogenation. Probe molecule FTIR and XANES were used to characterize the nature of Cr sites across a range of Cr loadings and in the presence of various extra-framework cations on ZSM-5. These characteristics were related to catalytic performance in ethane dehydrogenation toward the goal of developing design principles for Cr/zeolite catalysts for improved alkane conversions. Diffuse reflectance infrared Fourier transform spectroscopy (FTIR-DRIFTS) with nitric oxide (NO) and carbon monoxide (CO) probe molecules was determined to be an effective tool for distinguishing various types of Cr species present after exposure to reducing conditions typical of alkane dehydrogenation catalysis. It was found that 0.5 wt% Cr/H-ZSM-5 is a stable, ethylene-selective catalyst whose Cr sites are reduced at reaction temperature (650 °C) in the presence of either ethane or $N_2$. Zeolite framework Al sites were determined to be critical for the stabilization of active Cr sites during ethane dehydrogenation – in the absence of available Al sites, Cr sites quickly deactivated. It was also found that greater Cr/Al molar ratios yielded a greater abundance of electron-rich $Cr^{2+}$ species after reduction. This trend correlated with increased ethane dehydrogenation activity and decreased stability in time-on-stream studies. Both high activity and enhanced stability were observed for Cr/Ca-ZSM-5. Taken together, these results indicate that ethane dehydrogenation over Cr/ZSM-5 is optimized when Cr preferentially situates adjacent to isolated framework Al sites.

## 2.2 Introduction

Zeolite-supported metal catalysts with well-defined structure present a unique opportunity to develop highly active and selective catalysts while simultaneously establishing a more fundamental understanding of reaction sites. The zeolite surface provides precise binding sites for supported metals, resulting in active sites that are amenable to more targeted characterization. Under reaction conditions, zeolite micropores can stabilize small metal and metal oxide clusters that would not normally be stable on conventional (bulk) metal oxide supports.[1,2] The structure and stability of dispersed metals on zeolites are impacted profoundly

by the proximity to one another of tetrahedral aluminum (Al) sites in the zeolite framework as well as the distribution of these Al sites among possible crystallographic locations.[3–5] The relationship between Al siting and supported metal properties was made clear for cobalt-exchanged zeolites developed for selective catalytic reduction of $NO_x$ (SCR),[5] and it is a central theme in the more recent literature on copper-exchanged zeolites for SCR[2] and selective partial methane oxidation.[6,7] Leveraging control of Al siting in a wide variety of zeolite frameworks is a promising strategy for development of unique and productive active-site structures using Earth-abundant metals. While zeolite-supported metals such as Co,[5] Cu,[2,6,7] Ni,[8] Zn,[9–11] and Ga[12,13] are often studied, a deeper understanding of Cr in zeolite-based catalysts has yet to develop.

Supported-Cr catalysts are applied industrially for catalytic dehydrogenation of light alkanes[14] (typically with $Cr/Al_2O_3$), a technology crucial to the efficient utilization of natural gas feedstocks. Active sites are known to be mononuclear or oligonuclear Cr species, which are highly sensitive to their coordination to the support.[15–17] Process limitations associated with their industrial utilization include non-selective side reactions, coke formation, and in the case of ethane dehydrogenation, low catalyst activity.[14]

In this context, the hydrothermal stability and controllable acidity of zeotype supports create opportunities to design new Cr-based catalysts. In fact, Cr/zeolite catalysts have been shown to be active for a number of reactions,[18–22] but determination of the binding sites of Cr within zeolite structures remains unresolved. One notable exception is the insertion of Cr into tetrahedral vacancy defects, or silanol nests, in all-silica zeotypes.[22–24] Cr located at these sites resemble the mononuclear Cr species formed on amorphous $SiO_2$ but show enhanced stability under certain reaction conditions. In contrast to silanol nests, Al sites in zeolites display a variety of configurations, providing the potential for a diversity of supported Cr structures, including multinuclear metal oxide clusters. A critical evaluation of the Cr structures present in zeolites is lacking; it remains unclear whether Al binding sites can be exploited to stabilize active and selective Cr structures.

Probe molecule spectroscopy is a powerful tool used to provide information about the electronic state and coordinative availability of dispersed metal sites. Earlier studies of Cr supported on zeolite ZSM-

5 (Si/Al = 27) successfully observed multiple types of Cr by FTIR using nitric oxide (NO) as a probe molecule.[25,26] It was also shown that carbon monoxide (CO) was an ineffective probe at room temperature, as it was not able to coordinate these Cr cations. The two most abundant Cr species displayed differing reduction behaviors and responses to NO adsorption after reduction, implying that these Cr cations resided at distinct binding sites on the ZSM-5 surface. More recently, comparison of experimental Raman bands with results from density functional theory (DFT) calculations of calcined Cr/ZSM-5 allowed identification of two types of Cr differing in the number of Al sites with which they interact.[21] These two types of Cr displayed distinct reduction behavior, consistent with previous reports. At low Cr loading (0.8 wt%) these catalysts were active for methane conversion, but additional amounts of Cr did not increase activity. In this case, the state of Cr after reduction was not determined, as the distinct Raman signals associated with Cr-oxo species were not present after reduction.

In the present study, we combine FTIR probe molecule spectroscopy with relevant catalytic reactor measurements in order to relate the state of reduced Cr species in Cr/ZSM-5 to the catalytic activity and stability for ethane dehydrogenation. In contrast to trends observed for methane conversion, we find that ethane dehydrogenation activity per Cr site increases substantially with Cr loading. At the highest loadings examined, high activity per Cr is accompanied by decreased stability, which provides additional insight into the nature of Cr present. Our results enable a first-pass evaluation of the potential to design effective Cr-based dehydrogenation catalysts through use of zeolite supports.

## 2.3 Experimental Methods

### Catalyst Preparation

**Support preparation and ion exchange.** $NH_4$-ZSM-5 (Si/Al =15, Zeolyst CBV-3024E) as received was converted to the protonic form by calcination under 50 mL $min^{-1}$ flow of synthetic air in a 19 mm OD quartz tube fitted with valves to exclude ambient air, which was placed into a horizontal tubular furnace. Temperature was ramped at a rate of 2 °C $min^{-1}$ to 500 °C, with 1 h isothermal holds at 120 °C, 200 °C,

and 300 °C, and held at 500 °C for 3 h. Obtained H-ZSM-5 was transferred without exposure to ambient air into an argon-filled glovebox where it was stored.

Na-ZSM-5 was prepared by ion exchange of H-ZSM-5 with sodium nitrate ($NaNO_3$). H-ZSM-5 was stirred at room temperature for 3 days in an aqueous solution of 1 M $NaNO_3$ (80 mL $g^{-1}$ zeolite), which was periodically adjusted to pH 7 with 1 M sodium hydroxide (NaOH). The solids were subsequently separated by centrifugation and washed four times with 50 mL ultra-pure water per g zeolite. After drying for at least 3 h in an oven at 120 °C, the sample was crushed to a powder form and calcined under the identical conditions as used to prepare H-ZSM-5. The calcined sample was stored in the glovebox prior to use.

Ca-ZSM-5 was prepared by ion exchange with calcium nitrate ($Ca(NO_3)_2$). H-ZSM-5 was stirred for 2 h in an aqueous solution of 1 M $Ca(NO_3)_2$ in a closed glass vessel placed in an oil bath at 80 °C. After 2 h, the vessel was cooled in an ice bath and centrifuged. Recovered solids were resuspended in a fresh 1 M $Ca(NO_3)_2$ solution and exchange was repeated at 80 °C for 2 h. This process was repeated once more for a total of three exchanges. The cooled solution was then separated by centrifugation and washed four times with 50 mL ultra-pure water per g zeolite. The sample was dried and calcined using the same procedure as that for Na-ZSM-5.

Deposition of $Cr(acac)_3$. Preparation of Cr/H-ZSM-5, Cr/Na-ZSM-5, and Cr/Ca-ZSM-5 followed the same procedure. All steps of the preparation were performed without exposing the samples to ambient air. In the glovebox, zeolite (up to 0.5 g) was added with an appropriate amount of chromium(III) acetylacetonate ($Cr(acac)_3$) to a 2 mL glass ampoule. The ampoule was transferred to a Schlenk line, where it was evacuated and flame-sealed at approximately 80 mtorr pressure. The sealed ampoule, containing the light purple mixture, was heated in the calcination furnace at 5 °C $min^{-1}$ to 200 °C and held for 2 h. Then temperature was ramped at 5 °C $min^{-1}$ to 300 °C and held for 2 h. Sample color changed to either green or brown/gray during vacuum heat treatment. After vacuum heat treatment, the sample was transferred to the glovebox, where it was removed from the ampoule and placed into the quartz tube calcination reactor. The sample in the calcination tube was transferred to the furnace, where it was heated under 50 mL $min^{-1}$ flow

of air at 5 °C $min^{-1}$ to 300 °C and 2 °C $min^{-1}$ from 300 °C to 500 °C, at which temperature the furnace was held for 3 h. After cooling, the calcination tube was transferred back to the glovebox, where samples were stored prior to use. X-ray diffractograms verify crystallinity of the MFI structure before and after Cr deposition (Fig. S2.1).

**Diffuse Reflectance Fourier-Transform Infrared Spectroscopy (DRIFTS)**

Powder samples were prepared for DRIFTS by loading pure sample (7–9 mg) into a ceramic sample cup and pressing gently to achieve a flat surface. The loaded sample cup was placed into a Pike Technologies DiffusIR Heated Chamber inside the glovebox, allowing air-free transfer to the spectrometer. DRIFTS measurements were performed using a Bruker Tensor II FTIR Spectrometer equipped with a Pike Technologies DiffusIR MidIR Accessory. Spectra were collected using 256 scans and 2 $cm^{-1}$ resolution. For spectra of samples under nitrogen atmosphere, a background spectrum of dried potassium bromide powder (KBr) under $N_2$ was used, and data are reported as Kubelka–Munk spectra. For spectra of samples with adsorbed probe molecules, a background spectrum of the sample was collected just prior to introduction of the probe gas, and data are reported as log of inverse reflectance. More detail is given in the Supporting Information.

Sample reductions were performed in the DRIFTS heated chamber. The chamber was ramped at 10 °C $min^{-1}$ to the desired temperature under 30 mL $min^{-1}$ $N_2$ flow. At the desired temperature, composition of the gas flow was changed and held for 30 min, keeping total flow rate at 30 mL $min^{-1}$. After 30 min treatment, the heated chamber was purged with 30 mL $min^{-1}$ $N_2$ for another 30 min before cooling the chamber under $N_2$ flow. Probe molecules were dosed at 30 °C. Details regarding probe molecule dosing are included in the Supporting Information.

**Catalytic Activity**

Ethane dehydrogenation was carried out in a quartz down- flow, packed-bed reactor with 4 mm ID. Sample powders were sieved between mesh sizes 60–40 before use. Reactor effluent was measured online by an

Agilent 7890a gas chromatography (GC) unit equipped with FID and TCD detectors. Details about the reactor and GC are included in the Supporting Information.

In a typical reaction experiment, the reactor was heated in a tubular furnace at 5 °C $min^{-1}$ to 650 °C under 48 mL $min^{-1}$ $N_2$ flow. Holding at 650 °C, flow was switched to bypass the reactor in order to initialize gas flow rates and composition for ethane dehydrogenation. Unless otherwise specified, the flow rates used were 44 mL $min^{-1}$ $N_2$ and 4 mL $min^{-1}$ $C_2H_6$. Space velocity was adjusted by changing the mass of catalyst in the bed. After initial flow rates stabilized, flow was reintroduced to the reactor and the reaction began. The reactor spent about 20 min under static $N_2$ at 650 °C before flow of $C_2H_6$ began. Catalyst bed pressure was 3 psig.

**X-ray Absorption Near Edge Structure (XANES) Spectroscopy**

XANES fluorescence spectra were collected at Beamline 4-3 at the Stanford Synchrotron Radiation Lightsource at SLAC National Laboratory. Samples were loaded into a stainless-steel flow cell equipped with cartridge heaters and Kapton windows. Reported XANES spectra were energy-calibrated and normalized.

**Thermogravimetric Analysis-Mass Spectrometry (TGA-MS) TGA-MS**

TGA-MS experiments were performed using a Netzsch STA 449 F3 Jupiter thermogravimetric analysis unit with QMS 403 D Aeolos mass spectrometer. Samples (20–30 mg) were loaded into alumina crucibles and placed into the TGA under ambient air. For measurement of carbon deposition, in order to remove adsorbed moisture, samples were held for one hour at 120 °C under flow of synthetic air. Then temperature was ramped 5 °C $min^{-1}$ to 700 °C. Between 150 °C and 500 °C, $CO_2$ was detected by MS, and the corresponding mass loss was calculated. To estimate the Brønsted acid site density of H-ZSM-5, temperature-programmed desorption (TPD) of 2-propanamine was performed. 2-Propanamine was injected into a stream of $N_2$ flowing over the sample at 30 °C. Temperature was ramped at 5 °C $min^{-1}$ to 150 °C, where it was held for 30 min to allow desorption of physisorbed 2-propanamine and moisture. Next,

temperature was ramped at 5 °C $min^{-1}$ to 527 °C and held for 30 min. Results from TPD of 2-propanamine are included in the Supporting Information (Fig. S2.2).

**Physisorption**

Nitrogen physisorption measurements were performed using a Micromeritics 3Flex physisorption/chemisorption Instrument. Nitrogen adsorption isotherms were measured at −196 °C. Surface areas were determined by the BET method, and micropore volume was determined by the t-plot method. Results of physisorption measurements are included in the Supporting Information (Fig. S2.3 and Table S2.1).

## 2.4 Results and Discussion

**Al Sites in ZSM-5 Enable Stable Dehydrogenation Activity**

The premise of this investigation is that the activity of zeolite-supported Cr depends strongly on the coordination of Cr to the support. We first distinguish between two categories of binding sites for Cr: (1) charge-balancing bridging hydroxyls (Al–OH–Si), referred to here as "Al sites", where Al is located in a tetrahedral position of the zeolite framework and (2) silanols (Si–OH) that exist at defects in the zeolite lattice and external surfaces of zeolite crystallites. To begin to assess the impact of binding site on the activity of Cr, we prepared two 0.5 wt% Cr/ZSM-5 samples, one using the H-form of ZSM-5 and the other using the Na-exchanged form of the same ZSM-5.

Fig. 2.1 contrasts 0.5 wt% Cr/H-ZSM-5 and Cr/Na-ZSM-5 samples. The initial activity, expressed as turnover frequency (TOF), of Cr/H-ZSM-5 for ethane dehydrogenation at 650 °C was nearly twice that of Cr/Na-ZSM-5 (Fig. 2.1a). Cr/H-ZSM-5 also displayed stable activity while Cr/Na-ZSM-5 lost more than 70% of its initial activity during three hours under reaction conditions (Fig. 2.1b). Initial ethane conversion was below 3% in both experiments. The DRIFTS spectrum of Na-ZSM-5 (Fig. S2.4) indicates the disappearance of the peak at 3608 $cm^{-1}$, caused by the replacement by $Na^+$ of protons at Al sites. It was expected that the presence of $Na^+$ cations would block Cr from binding at associated Al sites, forcing Cr to bind at silanol sites in Cr/Na-ZSM-5. For Cr/H-ZSM-5, where hydroxyls at Al sites were available to anchor

Cr, a stable and more active dehydrogenation catalyst resulted. Results from a control experiment using bare H-ZSM-5 were used to estimate that the contribution of Brønsted acidity to the measured ethane conversion accounts for only one sixth of the total activity of 0.5 wt% Cr/H-ZSM-5, indicating that the measured activity is representative of the activity of supported Cr species.

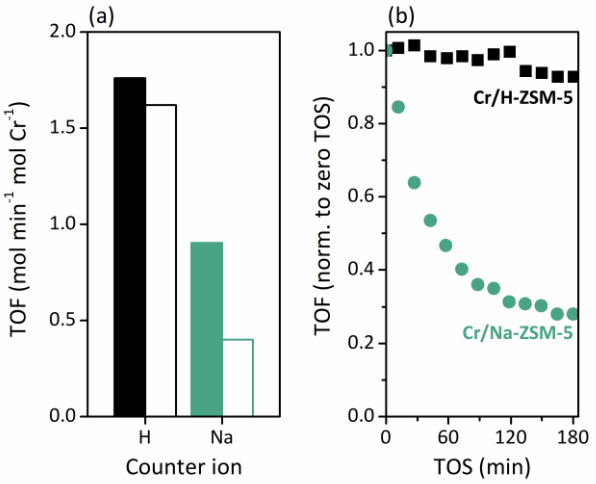


**Figure 2.1.** (a) Rate of ethane conversion at 650 °C at zero time on stream (filled bars) and after one hour on stream (empty bars) for 0.5 wt% Cr/ H-ZSM-5 and 0.5 wt% Cr/Na-ZSM-5 catalysts. (b) Normalized rate of ethane conversion versus time-on-stream for same samples and reaction conditions as Fig. 2.1a.

At comparable ethane conversion (Table S2.2), the initial ethylene selectivity of Cr/Na-ZSM-5 was higher (99.6%) than that of Cr/H-ZSM-5 (93.8%), consistent with the expectation that side reactions (e.g. oligomerization, cracking) occur at Brønsted acid sites in Cr/H-ZSM-5. The small amount of deposited carbon (less than 1 wt%) on Cr/H-ZSM-5 after 3 h on stream measured by TGA-MS (Fig. S2.9) did not cause extensive deactivation. An even smaller amount of coke was observed for Cr/Na-ZSM-5 (Fig. S2.8), but extensive deactivation was evident in the time-on-stream data. This result implies that Cr aggregation likely plays a major role in the deactivation of Cr/Na-ZSM-5.

To gain insight into the state of Cr in these samples, XANES and NO adsorption DRIFTS measurements were recorded after reduction in CO at 300 °C. Reduction with CO at 300–350 °C is a common treatment for activation of supported Cr catalysts, and the use of these reduction conditions enables direct comparison of the present results to literature, which documents the formation of mainly $Cr^{2+}$ in

$Cr/SiO_2$ catalysts[27] and a mixture of $Cr^{2+}$ and $Cr^{3+}$ in $Cr/Al_2O_3$ catalysts.[17] No consensus regarding the oxidation states of Cr in reduced Cr/H-ZSM-5 has been established.

XANES spectra of fresh Cr/H-ZSM-5 and Cr/Na-ZSM-5 display intense pre-edge peaks at 5993 eV, indicating that Cr was present as dispersed, tetrahedral $Cr^{6+}$ species after calcination (Fig. S2.5).[27,28] After reduction in CO at 300 °C, XANES spectra display edge energies at ca. 6002 and pre-edge features at 5988, 5990, and 5995 eV, characteristic of supported $Cr^{2+}$ (Fig. 2.2a).[27,28] These results indicate the average oxidation state of Cr was close to 2+ in both samples after reduction.

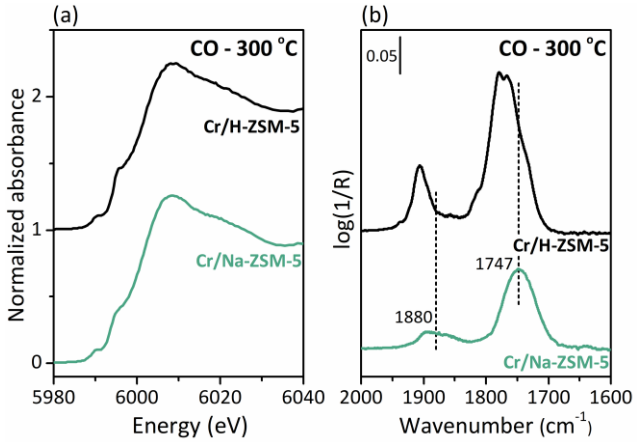


**Figure 2.2.** (a) XANES spectra of 0.5 wt% Cr/H-ZSM-5 and 0.5 wt% Cr/Na- ZSM-5 after 30 min reduction in CO at 300 °C. Samples remained under CO flow at 300 °C while spectra were collected. (b) FTIR-DRIFTS spectra of NO adsorbed at 30 °C on 0.5 wt% Cr/H-ZSM-5 and 0.5 wt% Cr/Na-ZSM-5 samples after reduction in CO at 300 °C.

DRIFTS spectra of NO adsorption onto CO-reduced Cr/H-ZSM-5 and Cr/Na-ZSM-5 reveal clear differences (Fig. 2.2b). NO adsorption onto Cr/Na-ZSM-5 reduced in CO at 300 °C yielded broad peaks centered at 1747 $cm^{-1}$ and ca. 1880 $cm^{-1}$, similar to those often observed for $Cr^{2+}/SiO_2$ treated under the same conditions. In $Cr^{2+}/SiO_2$ samples,[23,27,29–31] peaks often observed at 1743–1755 $cm^{-1}$ and 1856–1880 $cm^{-1}$ have been shown to arise from antisymmetric and symmetric N–O stretching vibrations of $Cr^{2+}$ dinitrosyl species, respectively. The similarity of the NO spectrum of Cr/Na-ZSM-5 to that of $Cr/SiO_2$ leads us to conclude that Cr in Cr/Na-ZSM-5 was located mainly at silanol sites after CO reduction at 300 °C.

It is possible for Cr to bind at either external silanols or internal silanols at framework vacancies (silanol nests). DRIFTS spectra of Na-ZSM-5 and Cr/Na-ZSM-5 (Fig. S2.4) show that the intensity of the

O–H stretching band due to external silanols (3744 $cm^{-1}$) decreased considerably after Cr loading, whereas the broad band due to internal silanols (3530 $cm^{-1}$) displayed no obvious change.[24] In a previous study, when Cr was located mainly at silanol nests in dealuminated zeolite beta, a Cr-mononitrosyl characterized by a sharp N–O stretching peak at 1794 $cm^{-1}$ was observed.[24] This peak was not observed for Cr/Na-ZSM-5 in the present study. These results are consistent with the location of Cr at external silanol sites, but the coexistence of Cr at silanol nests cannot be conclusively ruled out.

NO adsorption onto Cr/H-ZSM-5 after CO reduction at 300 °C (Fig. 2.2b) resulted in a clearly different spectrum from adsorption onto Cr/Na-ZSM-5. Peak intensities are higher, and the dominant peaks are blue-shifted more than 30 $cm^{-1}$ with respect to Cr/Na-ZSM-5. It is also apparent from the line shape that the spectrum associated with Cr/H-ZSM-5 is comprised of several overlapping, sharper peaks, suggesting that multiple Cr species with distinct structures were present in Cr/H-ZSM-5. In contrast, the broad peaks in the Cr/Na-ZSM-5 spectrum imply a higher degree of heterogeneity of Cr structures due to aggregation of Cr or a distribution of surface binding environments occupied by dispersed Cr species.

DRIFTS spectra of NO adsorption after reduction in $H_2$ at 650 °C, conditions more similar to those present in the reactor during ethane dehydrogenation, indicate an even greater contrast between Cr/H-ZSM-5 and Cr/Na-ZSM-5 (Fig. 2.3). In Cr/H-ZSM-5, several sharp peaks appeared that were not present after reduction at 300 °C. The availability of Al binding sites for Cr in Cr/H-ZSM-5 resulted in the formation of multiple, distinct Cr species that were not present in Cr/Na-ZSM-5. These observations are consistent with the expectations and motivations of this study – that Al sites in zeolites provide a mechanism to control Cr speciation. Peak assignments are discussed in more detail in the next section.

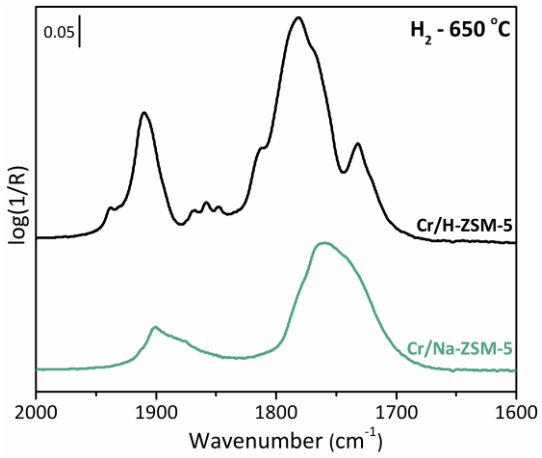


**Figure 2.3.** FTIR-DRIFTS spectra of NO adsorbed at 30 °C on 0.5 wt% Cr/ H-ZSM-5 (black) and 0.5 wt% Cr/Na-ZSM-5 (green) after reduction at 650 °C in $H_2$.

These experiments, and the ability to control Cr siting, were uniquely enabled through anhydrous Cr deposition. Although aqueous techniques can be employed to produce highly dispersed supported-metal species, aqueous methods for Cr dispersion onto zeolites have complications. The extent of ion exchange of high charge (typically 3+), hydrated Cr cations for one or more singly-charged zeolite charge-balancing protons is not easily controlled. Speciation of hydrated Cr cations to structures with higher nuclearity depends on pH, which varies with solution concentration and surface potential of the support.[32] For this study, we controlled both Cr loading and the zeolite surface potential (e.g. by exchanging zeolite $H^+$ for $Na^+$), while attempting to maintain high Cr dispersity. In aqueous conditions, Cr may exchange with $Na^+$ at Al sites. In contrast, the anhydrous approach facilitated anchoring of Cr selectively at silanol sites in Cr/Na-ZSM-5. The sample preparation method used here, discussed in detail in the Supporting Information, was adapted from techniques which were previously shown to be effective for grafting the molecular Cr precursor $Cr(acac)_3$ onto amorphous silica.[33–35]

Furthermore, it was necessary to use complementary techniques for the above characterization. The oxidation state of Cr in Cr/H-ZSM-5 is difficult to determine on the basis of NO adsorption with DRIFTS alone, especially considering the limited number of reference spectra available in the existing literature. The location of Cr on the zeolite surface, however, is not readily apparent in the XANES spectra. The variety of Cr speciation and relative uniformity of supported Cr are distinguished more clearly using

DRIFTS with NO. The results discussed so far demonstrate the potential to control the speciation of Cr using Al sites in ZSM-5 and highlight the complexity of the Cr/H-ZSM-5 material system.

**Further Evaluation of Cr Sites in Cr/H-ZSM-5 by DRIFTS**

**Reduction of Cr/H-ZSM-5.** Additional insights were expected to be gained by evaluating the state of Cr after reduction in conditions close to those used for ethane dehydrogenation. To further explore the state of Cr after reduction at higher temperatures, we carried out NO adsorption experiments after reduction at 650 °C in different environments. Notably, Cr was reduced even under inert gas flow ($N_2$) and yielded similar NO adsorption results (Fig. 2.4) to the sample treated at the same temperature in $H_2$ (Fig. 2.3). Furthermore, exposure at 650 °C to a 10% ethane ($C_2H_6$) gas flow for 30 minutes yielded similar results (Fig. 2.4).

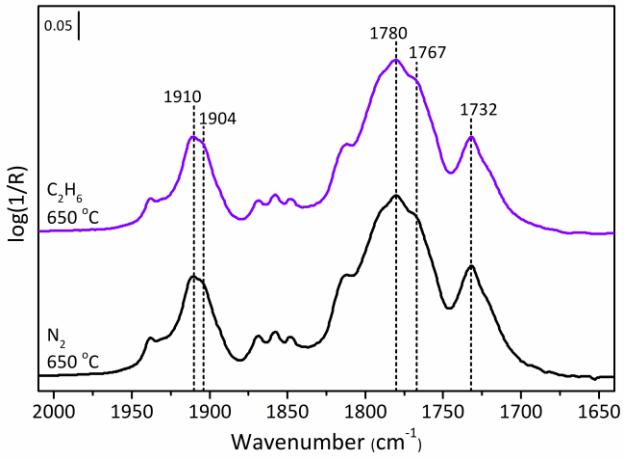


**Figure 2.4.** FTIR-DRIFTS spectra of NO adsorbed at 30 °C on 0.5 wt% Cr/H-ZSM-5 after treatment at 650 °C in $N_2$ (black) or 10% $C_2H_6$ in $N_2$ (purple).

Auto-reduction of Cr under inert gas has been previously observed at 500 °C by in-situ Raman spectroscopy of Cr/H-ZSM-5 samples prepared by aqueous impregnation.[21] In that study, Wachs and coworkers identified two types of Cr-oxo species assigned to Cr at Al sites in H-ZSM-5. The Raman band for one of these species disappeared under Ar flow at 500 °C, implying reduction of this type of Cr, while the other band was eliminated only upon exposure of the sample to methane. Similarly, the Cr/H-ZSM-5 samples in this study likely contained multiple types of Cr, but exposure to a hydrocarbon feed did not induce further reduction of Cr. Thus, it seems Cr in these samples was fully reduced under inert flow at 650

°C. Either the Cr species previously observed to be reduced only in the presence of methane above 500 °C was not present in the sample evaluated here, or it was present and reduced under inert flow at temperatures between 500 °C and 650 °C.

**Possible forms of Cr in ZSM-5.** In silicon-rich zeolites, three types of binding sites exist for bare, divalent, extra-framework cations.[5,36–39] In ZSM-5, the α, β, and γ sites are composed of Al–O–Si–O–Si–O–Al sequences present in six-membered rings, where the two negatively charged Al sites balance the 2+ charge of the extra-framework cation. In $Co^{2+}$-exchanged ZSM-5, it was determined that α sites are located in the walls of the straight channels, β sites are located in the intersections of the straight and sinusoidal channels, and γ sites are located in the sinusoidal channels.[37] Local environments and reactivities of extra-framework cations have been shown to depend on the sites at which cations are located.[5,36,40] For the zeolite used in this study (Zeolyst 3024E, Si/Al = 15), the fraction of Al present in these paired Al sites was estimated by Bell and coworkers[41] to be 0.39. A 3:1 ratio of β sites to α sites was found, along with a negligible amount of γ sites.

After calcination, dispersed Cr on amorphous $SiO_2$ is mostly present in the 6+ oxidation state as $[Cr(=O)_2]^{2+}$ chromate species bound to support surface oxygens.[27] Reduction in CO above 300 °C converts these species mostly to bare, divalent $Cr^{2+}$ cations. Either of these forms of Cr may exist at paired Al sites in ZSM-5. $Cr^{3+}$ may also be charge-balanced by a paired Al site if it bears a single negatively-charged extra-framework ligand, such as hydroxyl in $[Cr–OH]^{2+}$. In addition, it is possible for extra-framework Cr to bind at single Al sites. Oxidized forms of these may include $Cr^{5+}$ as $[Cr(=O)_2]^{+}$ and $Cr^{6+}$ as $[Cr(=O)_2(OH)]^{+}$. During reduction, these could hypothetically convert to $Cr^{3+}$ as $[Cr=O]^{+}$ and $Cr^{2+}$ as $[Cr–OH]^{+}$, respectively. Multinuclear Cr species are possible as well, which may take the form of $Cr_xO_y$ balanced by one or more Al sites. Other Cr species are also possible, but the structures listed here are thought to be most likely to exist and provide a framework for discussing the speciation of extra-framework Cr in ZSM-5.

The Raman bands reported in ref. 21 were compared with results from density functional theory (DFT) calculations, allowing the authors to propose structures of the two types of Cr species observed, which differ by the oxidation state of Cr and the number of Al sites that each Cr cation occupies. The

structure that was reduced under inert flow was proposed to be $[Cr(=O)_2]^{2+}$ on two Al sites or $[Cr(=O)_2(OH)]^{+}$ on one Al site, and the other structure was proposed to be $[Cr(=O)]^{+}$ on one Al site. We use these assignments as a basis for interpreting our DRIFTS data.

Based on the number of peaks in the NO adsorption spectra in Fig. 2.3 and 2.4, it seems there were multiple Cr species present after reduction in $N_2$, $H_2$, or $C_2H_6$. The population of Cr was most likely split between isolated Al sites and paired Al (α and β) sites. Additional adsorption experiments were performed in order to gain information about Cr present in reduced catalysts. Although these experiments alone were not intended to definitively identify the structures and binding sites of Cr, the study was designed as a preliminary assessment of the properties of reduced Cr species in ZSM-5 and their respective relevance to catalysis.

**Cr nitrosyls on Cr/H-ZSM-5.** Using DRIFTS with NO adsorption, two types of Cr-dinitrosyl species in Cr-exchanged H-ZSM-5 were distinguished by Hadjiivanov and coworkers in ref. 25. The first type, which were predominant after reduction below 500 °C, formed dinitrosyls with antisymmetric/symmetric N–O stretching bands at 1782 $cm^{-1}$/1910 $cm^{-1}$. These were assigned as $Cr^{3+}$-dinitrosyl species. The second type, which became more abundant with reduction temperatures above 500 °C, formed dinitrosyls observed at 1768 $cm^{-1}$/1902 $cm^{-1}$. These were assigned as $Cr^{2+}$-dinitrosyls. During evacuation, the second type of dinitrosyl decomposed, forming mononitrosyl species with an N–O stretching band at 1783 $cm^{-1}$. No Cr-nitrosyls were formed before reduction.

These Cr-nitrosyl species were present in the Cr/H-ZSM-5 prepared in this study as well. After reduction in $N_2$ flow at 650 °C, dinitrosyl antisymmetric/symmetric modes at 1780 $cm^{-1}$/1911 $cm^{-1}$ and 1767 $cm^{-1}$/1904 $cm^{-1}$ and a mononitrosyl N–O stretching mode at 1789 $cm^{-1}$ were observed under static NO pressure at 30 °C (Fig. 2.5a, gray curve). As the DRIFTS cell was purged with $N_2$, weakly bound NO desorbed (Fig. 2.5a, red curves). As described in ref. 25, peaks at 1767 $cm^{-1}$/1904 $cm^{-1}$ decreased simultaneously with an increase of intensity at 1789 $cm^{-1}$, consistent with conversion to a mononitrosyl. A slight gain of intensity at 1780 $cm^{-1}$/1911 $cm^{-1}$ suggests a small fraction of these dinitrosyls formed by desorption of NO from Cr species with more than two nitrosyl ligands. In addition to the peaks observed in

ref. 25, minor peaks at 1732 $cm^{-1}$, 1814 $cm^{-1}$, 1848 $cm^{-1}$, 1858 $cm^{-1}$, 1869 $cm^{-1}$, 1930 $cm^{-1}$, and 1938 $cm^{-1}$ decreased in intensity during brief $N_2$ flow. Previously, addition of more than two NO ligands into the coordination sphere of Cr in $Cr/SiO_2$ resulted in shifting of dinitrosyl bands and the appearance of additional IR bands.[23] It was proposed that a small fraction of tetranitrosyl species formed at Cr sites with excess electron density, giving rise to peaks blue-shifted from the dinitrosyl symmetric stretching frequency (above 1875 $cm^{-1}$) and red-shifted from the dinitrosyl antisymmetric stretching frequency (below 1740 $cm^{-1}$). In the Cr/H-ZSM-5 investigated here, peaks at high and low frequency ends of the spectrum may be due to Cr species with more than two NO ligands. Another possibility is that peaks blue-shifted from the dominant dinitrosyl peaks result from a small amount of Cr present in higher oxidation states. Peaks at 1814 $cm^{-1}$, 1930 $cm^{-1}$, and 1938 $cm^{-1}$ could be due to a small amount of $Cr^{3+}$ remaining after reduction, in line with peaks observed previously for $Cr/Al_2O_3$.[42] Alternatively, $Cr^{3+}/Cr^{4+}$ could result from oxidation of $Cr^{2+}$ by NO or $N_2O$. In fact, a small peak at 2249 $cm^{-1}$ due to $N_2O$ was observed during NO adsorption (Fig. S2.11).

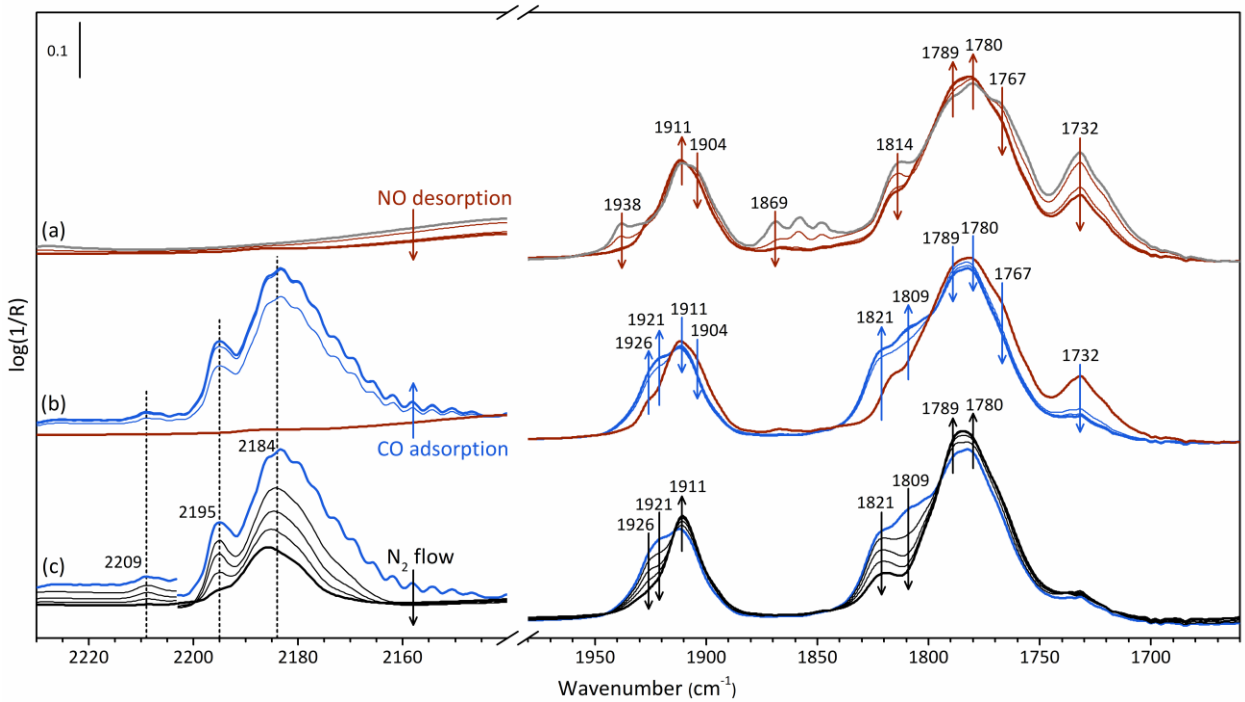


**Figure 2.5.** (a) FTIR-DRIFTS spectra of NO adsorbed at 30 °C on 0.5 wt% Cr/H-ZSM-5 after treatment at 650 °C in $N_2$ (gray) and subsequent spectra taken during $N_2$ flow (red). (b) FTIR-DRIFTS spectra taken after 10 minutes of NO desorption under $N_2$ flow (red) and during subsequent CO adsorption (blue). (c)

FTIR-DRIFTS spectra taken after 10 minutes of CO adsorption (blue) and during CO desorption under $N_2$ flow (black). Data above 2203 $cm^{-1}$ offset in (c) for clarity.

**Co-adsorption of NO and CO.** To obtain additional information on the oxidation state of Cr, the sample was exposed to CO, which is a sensitive probe of electronic state of transition metals. Although it was previously reported that CO did not form stable carbonyl complexes with Cr cations in reduced Cr-H-ZSM-5 at room temperature,[26] we report here that Cr-carbonyl species formed on Cr cations already containing one or more NO ligands.

Following NO adsorption (Fig. 2.5a, gray curve), weakly bound NO desorbed under $N_2$ flow until the spectra were fairly stable over time (Fig. 2.5a and b, red curves). Next, CO was introduced to the cell (see Supporting Information for methodology). Peaks at 1732 $cm^{-1}$, 1767 $cm^{-1}$/1904 $cm^{-1}$, 1780 $cm^{-1}$/1911 $cm^{-1}$, and 1789 $cm^{-1}$ lost intensity, while new peaks developed at higher frequencies (Fig. 2.5b and c, blue curves). This was due to addition of CO to Cr-dinitrosyl species, as observed in Cr/$SiO_2$ and Cr/silicalite samples.[23,31] Blue-shifting of dinitrosyl peaks is explained by decreased electron density at Cr after addition of CO. Simultaneously, carbonyl peaks appeared in the region 2170 $cm^{-1}$ to 2210 $cm^{-1}$, typical of supported-Cr catalysts.[27]

As gas-phase CO was purged from the DRIFTS cell by $N_2$ flow, Cr-carbonyl peaks became more visible (Fig. 2.5c). The major peak at 2184 $cm^{-1}$ and shoulder at 2179 $cm^{-1}$ can be assigned to the symmetric and antisymmetric stretching vibrations of $Cr^{2+}$ dicarbonyls.[27] Interestingly, carbonyl peaks at 2184 $cm^{-1}$ and 2179 $cm^{-1}$, which are considered a fingerprint of $Cr^{2+}$ dicarbonyls in Cr/$SiO_2$ Phillips catalysts, were not observed for Cr/Na-ZSM-5 under similar conditions (Fig. S2.13). Cr/Na-ZSM-5 displayed only one broad carbonyl band centered at 2174 $cm^{-1}$. A small shoulder at 2171 $cm^{-1}$ was also present for Cr/H-ZSM-5. Peaks around 2170 $cm^{-1}$ were assigned in previous reports to carbonyls co-adsorbed with NO to $Cr^{2+}$ sites in Cr/$SiO_2$.[27,43] Presumably, electron donation from NO to Cr causes red-shifting of carbonyl bands from those formed in the absence of NO.

Finally, two carbonyl peaks with unusually small FWHM (<10 $cm^{-1}$) were observed at 2195 $cm^{-1}$ and 2209 $cm^{-1}$. The sharpness of these peaks suggests they are due to Cr carbonyl species with uniform

structures, likely located at specific Al sites in the zeolite.[44] Cr carbonyls around 2195 $cm^{-1}$ can result from $Cr^{2+}$ or $Cr^{3+}$ cations,[17] but definitive assignment is difficult due the confounding impacts of the zeolite support and co-adsorbed nitrosyls in the ligand sphere of Cr. The 2209 $cm^{-1}$ peak is likely due to the presence of a small amount of $Cr^{3+}$ or $Cr^{4+}$. A carbonyl band at 2204–2206 $cm^{-1}$ was previously assigned to adsorption of CO on $Cr^{4+}$(=O) sites in $Cr/SiO_2$ formed by oxidation of $Cr^{2+}$ by $N_2O$.[43,45]

Upon desorption of CO (Fig. 2.5c, black curves), the intensity of nitrosyl bands associated with Cr species having both NO and CO ligands decreased, while bands of Cr nitrosyl species at 1780 $cm^{-1}$/1911 $cm^{-1}$ and 1789 $cm^{-1}$ were restored. The overlap of peaks in Fig. 2.5c makes distinguishing individual peaks difficult, but close examination of difference spectra facilitates assignment of groups of peaks to individual Cr species. Fig. 2.6 displays difference spectra obtained by subtraction of spectra collected at increasing times during CO desorption. Sharp loss peaks at 1809 $cm^{-1}$ and 1921 $cm^{-1}$ dominate during the first minute of $N_2$ flow, suggesting that a mixed NO/CO Cr complex lost at least one weakly bound carbonyl ligand. Absorbance of gas-phase CO obscured the carbonyl region in this spectrum but was no longer a problem at later times. Between one and four minutes of CO desorption, the nitrosyl region was still dominated by loss peaks at 1809 $cm^{-1}$ and 1921 $cm^{-1}$, and in the carbonyl region by a loss peak at 2182 $cm^{-1}$. From four to nine minutes, loss peaks at 1821 $cm^{-1}$, 1926 $cm^{-1}$, and 2195 $cm^{-1}$ grew more prominent. This allows tentative assignment of two Cr NO/CO species: $Cr^{2+/3+}(NO)_2(CO)$ with $\nu_{NO,as}/\nu_{NO,s}/\nu_{CO}$ at 1821/1926/2195 $cm^{-1}$, and $Cr^{2+}(NO)_2(CO)$ with $\nu_{NO,as}/\nu_{NO,s}/\nu_{CO}$ at 1809/1921/2182 $cm^{-1}$. The carbonyl loss peak at 2182 $cm^{-1}$ is indicative of a $Cr^{2+}$ monocarbonyl, whereas peaks at 2184/2179 $cm^{-1}$ in Fig. 2.5c are characteristic of $Cr^{2+}$ dicarbonyls.[27] Thus it is possible that dicarbonyl species $Cr^{2+}(NO)_2(CO)_2$ or $Cr^{2+}(NO)(CO)_2$ were formed as well. These results show that several highly coordinatively unsaturated Cr species existed after reduction in $N_2$ at 650 °C.

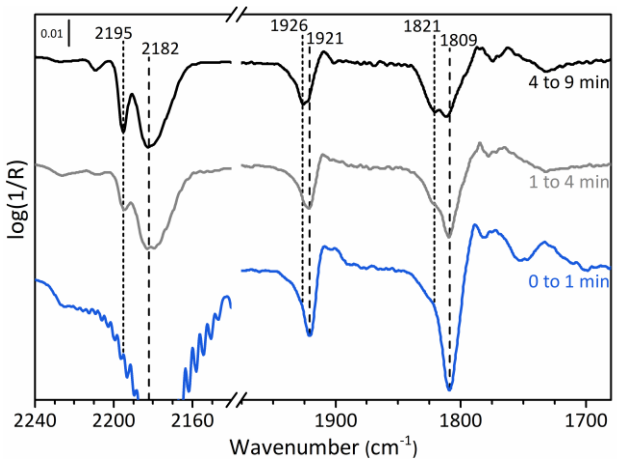


**Figure 2.6.** FTIR-DRIFTS difference spectra of NO and CO adsorbed at 30 °C on 0.5 wt% Cr/H-ZSM-5 after treatment at 650 °C in $N_2$. Spectra were taken during increasing time of $N_2$ flow and were processed by subtracting the earlier time spectrum from the later time spectrum, as labelled on the figure.

It is evident that further characterization is necessary to definitively claim the surface binding configuration of Cr in reduced Cr/H-ZSM-5. Rather than attempt to extract more information from the single sample, we prepared a set of Cr/H-ZSM-5 catalysts with increasing Cr loading in order to observe changes in the capacity of ZSM-5 to stabilize dispersed Cr active sites. It was expected that at higher loadings, Cr would anchor at additional locations on the zeolite surface and would be more likely to form multinuclear Cr species. Meaningful trends in ethane dehydrogenation performance would indicate broadly which forms of Cr are most relevant for dehydrogenation, and how a zeolite support may be utilized to design improved dehydrogenation catalysts.

**Capacity of ZSM-5 as a Support for Cr**

On the basis of interpretation of Raman spectra of Cr/H-ZSM-5 (Si/Al = 15, Zeolyst CBV 3024E), it was observed in ref. 21 that at Cr loading above 0.5 wt% (0.10 Cr/Al), Cr tended to bind at silanol sites after calcination. Particularly when there were fewer Al binding sites for each Cr (high Cr/Al), reaction conditions were thought to force Cr from Al to silanol sites where they were less active for methane conversion. Similarly, activity and stability of ethane conversion reported herein were higher for Cr located at Al sites compared with Cr at silanols (Fig. 2.1). Motivated by these observations, we prepared Cr/H-ZSM-5 samples using the same zeolite product (Zeolyst CBV 3024E) varying Cr loading from 0.27 to 1.6

wt%, corresponding to 0.05 to 0.30 Cr/Al (molar ratio). It has been reported[41] that the fraction of Al present in pairs in this zeolite was 0.39 – therefore, a maximum of ca. 0.20 Cr/Al could be stabilized at Al sites if a pair of Al sites is required to stabilize each Cr cation. The range of Cr/Al in this set of samples was chosen in order to observe differences among compositions below and above this 0.20 Cr/Al threshold.

**Ethane DH performance as a function of Cr loading.** Catalysis results for ethane dehydrogenation at 650 °C by Cr/ H-ZSM-5 samples with varying Cr loading are shown in Fig. 2.7. All reactions were performed at ethane conversion below 8% (see Supporting Information for details). Initial rates of ethane conversion, normalized per mole of Cr, were essentially constant at low Cr loadings (Fig. 2.7a). The slight downward trend at low Cr/Al is thought to be caused by added ethane conversion from Brønsted acid sites in the zeolite, which becomes more relevant with decreasing Cr loading (increasing Brønsted acid/Cr). Based on the ethane conversion measured for bare H-ZSM-5, it is estimated that for 0.10 Cr/Al, 18% of the measured ethane conversion may be attributed to activity of the zeolite support. This number decreases with increasing Cr loading. For 0.30 Cr/Al, only 2% of total activity is estimated to be due to activity of the zeolite support. If a simple correction is made, subtracting the conversion measured for an equivalent mass of bare H-ZSM-5, the trend at Cr/Al $\leq$ 0.12 becomes relatively flat (Fig. S2.15). Above Cr/Al = 0.12, rates of ethane conversion per mole Cr increase monotonically, contrary to what was found for methane conversion.[21] Doubling Cr/Al from 0.15 to 0.30 results in more than doubling of the initial rate of ethane conversion from 2.3 to 4.8 mol $min^{-1}$ mol $Cr^{-1}$. Apparent activation energies for 0.10 Cr/Al and 0.17 Cr/Al samples are fairly similar (Fig. 2.7c), indicating that similar active sites may have been responsible for most of the activity in these samples.

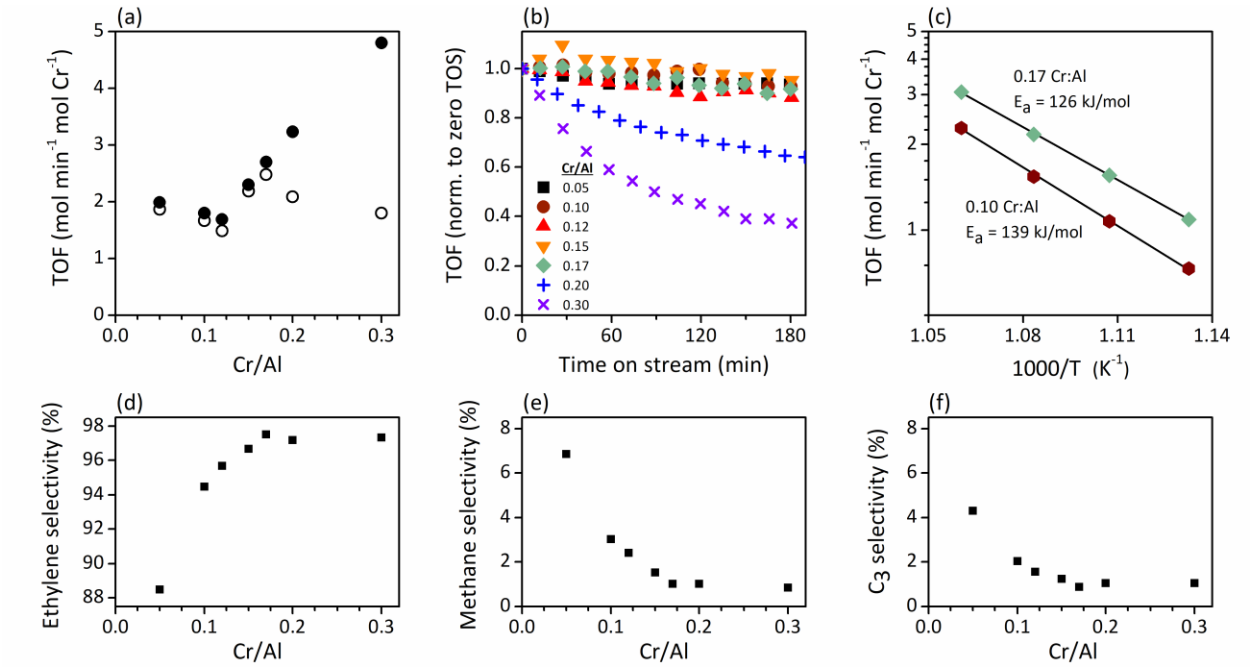


**Figure 2.7.** Ethane dehydrogenation performance of Cr/H-ZSM-5 catalysts with increasing Cr loading (0.10 Cr/Al corresponds to 0.54 wt% Cr). Reaction conditions: T = 650 °C; P = 3 psig; flow rates: 4 sccm ethane, 44 sccm $N_2$; catalyst amount: 8–45 mg. (a) Initial turnover frequency (TOF) of ethane conversion (filled circles) and TOF after 3 h (empty circles) as a function of Cr/Al molar ratio. (b) TOF of ethane conversion, normalized to the initial value, as a function of time on stream. (c) TOF of ethane conversion versus inverse temperature. Apparent activation energies labelled on the plot were calculated by fitting data to the Arrhenius equation. Ethane conversion was measured at 670, 650, 630, and 610 °C. (d)–(f) Initial selectivity to (d) ethylene, (e) methane, and (f) propane and propylene combined versus Cr/Al.

Ethylene selectivity also increased with Cr/Al, while selectivities to side products methane, propane, and propylene decreased (Fig. 2.7d–f). Most likely, methane and $C_3$ side products formed largely by oligomerization and cracking on Brønsted acid sites. When ethane dehydrogenation was performed over H-ZSM-5, 21.4% selectivity to methane and 10.8% selectivity to $C_3$ products were measured at 0.72% ethane conversion (Table S2.2). With increasing Cr loading, the activity of ethylene-selective Cr sites was increasingly dominant with respect to catalysis at Brønsted acid sites, resulting in higher ethylene selectivity. Because Cr can bind at Al sites, increasing Cr/Al likely also decreased the concentration of Brønsted acid sites, further suppressing side reactions.

Differences in stability of ethane dehydrogenation activity on stream were observed as well (Fig. 2.7b). For Cr/Al $\leq$ 0.17, more than 85% of initial activity was retained after three hours on stream. Increasing Cr/Al above 0.17, faster deactivation was observed, with the 0.30 Cr/Al sample losing over 60%

of its initial activity over 3 h. With increasing Cr/Al, the rate of ethane conversion per mole Cr after 3 h on stream passed through a maximum at 0.17 Cr/Al. Carbon deposition (coking) and aggregation of Cr are thought to be the main contributors to deactivation observed in these experiments. $N_2$ physisorption measurements of the 0.10 Cr/Al sample showed no loss of micropore volume after reaction (Fig. S2.3 and Table S2.1). After 3 h operating at 4% ethane conversion, the 0.17 Cr/Al sample contained about 1.2% mass of carbon, as measured by TGA-MS (Fig. S2.10). This amount of carbon deposition did not, however, result in substantial deactivation. Furthermore, catalytic tests of the 0.30 Cr/Al sample performed at different initial ethane conversions (7.5% and 2.8%) resulted in nearly identical amounts of deactivation (Fig. S2.16), suggesting that increasing partial pressure of products (i.e. ethylene) did not influence the rate of deactivation. Together, these results suggest that, although coke can form at Cr sites or Brønsted acid sites, coking was not the primary cause of deactivation. Instead, when substantial deactivation occurred, aggregation of Cr was likely the cause.

Paired Al sites are expected to be the most stable binding sites for Cr, as Cr generally requires at least two negatively charged support oxygens.[32,46] With increasing Cr/Al, if paired Al sites become populated, additional Cr is more likely to either: i) populate isolated Al sites, ii) form multinuclear Cr species, or iii) populate silanol sites. To assess whether any of these possibilities were responsible for the observed trends in dehydrogenation activity with increasing Cr/Al, samples with various Cr loadings were characterized by DRIFTS.

**DRIFTS of Cr/H-ZSM-5 with varying Cr loading.** DRIFTS spectra in the hydroxyl region of H-ZSM-5 and Cr/H-ZSM-5 samples with 0.10 Cr/Al, 0.17 Cr/Al, and 0.30 Cr/Al after 1 h under $N_2$ flow at 650 °C are shown in Fig. 2.8. The two main peaks are due to bridging hydroxyls located at zeolite framework Al sites (3608 $cm^{-1}$) and external silanols (3744 $cm^{-1}$).[21,25] The two minor peaks at 3658 $cm^{-1}$ and 3777 $cm^{-1}$ are due to hydroxyls of extra-framework Al.[21,24] With increasing Cr loading, the intensity of the Al bridging hydroxyl peak decreased substantially, suggesting that Cr binds at Al sites. The silanol band decreased as well, showing that a small fraction of Cr resides at silanol sites at all loadings. However, since the bridging hydroxyl peak loses considerably more intensity with increased Cr loading, we conclude that

even up to loading of 0.30 Cr/Al, most of the Cr is located at Al sites after the heat treatment in inert. Very little, if any, change in the extra-framework Al hydroxyl peaks was observed, implying that these sites do not play a significant role in Cr speciation.

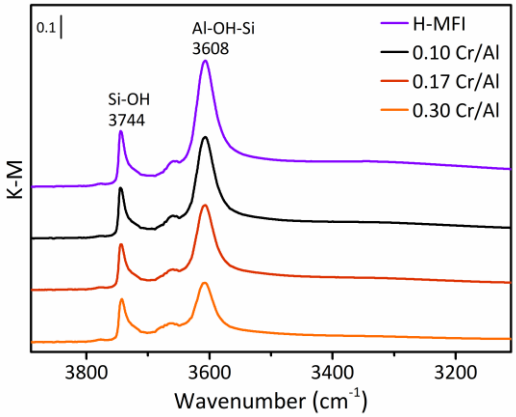


**Figure 2.8.** DRIFTS spectra in the hydroxyl region of H-ZSM-5 and Cr/H- ZSM-5 samples with Cr loading 0.10, 0.17, and 0.30 Cr/Al. Measurements were taken at 100 °C under $N_2$ after treatment under $N_2$ at 650 °C for 1 h. Spectra were normalized by the intensity of the zeolite Si–O–Si overtone peak at 1987 $cm^{-1}$.

NO adsorption on 0.10, 0.17, and 0.30 Cr/Al samples after treatment in $N_2$ at 650 °C allowed comparison of the distribution of Cr species present among samples with low, intermediate, and high dehydrogenation activity, respectively (Fig. 2.9). Intensity of all nitrosyl peaks increased with Cr loading, but trends in relative peak area were observed. First, the dinitrosyl characterized by 1767 $cm^{-1}$/1904 $cm^{-1}$ bands grew with respect to the dinitrosyl bands at 1780 $cm^{-1}$/1911 $cm^{-1}$. Most strikingly, absorbance at low frequencies grew substantially with increasing Cr/Al. A peak at 1732 $cm^{-1}$ with a shoulder at 1720 $cm^{-1}$ grew with Cr/Al, and at 0.30 Cr/Al, a shoulder around 1695 $cm^{-1}$ became clearly visible. Additionally, at 0.30 Cr/Al, increases in intensity around 1750 $cm^{-1}$ and 1890 $cm^{-1}$ suggest that a higher fraction of Cr resides at silanol sites. However, it is unlikely that peaks at 1732 $cm^{-1}$ and 1720 $cm^{-1}$ are due to Cr at silanol sites since resolved peaks in this range were not observed in Cr/Na-ZSM-5, and they were not reported previously for Cr/$SiO_2$ or Cr/silicalite.[23,27,31]

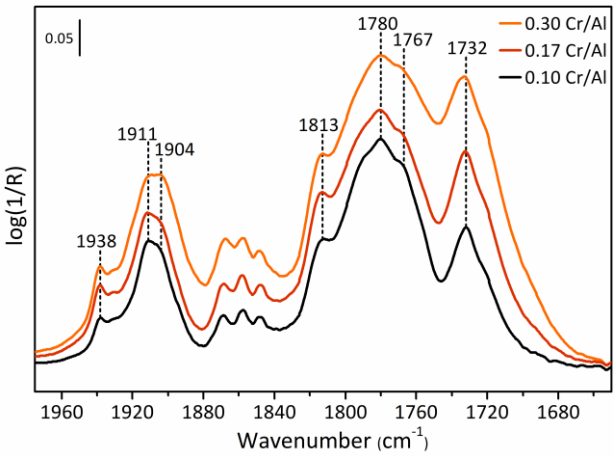


**Figure 2.9.** FTIR-DRIFTS spectra of NO adsorbed at 30 °C on Cr/H-ZSM-5 samples with Cr loading 0.10, 0.17, and 0.30 Cr/Al after treatment under $N_2$ at 650 °C for 1 h.

The presence of Cr at silanol sites at high Cr/Al is consistent with the quick deactivation observed in these samples, but as Cr/Na-ZSM-5 had the lowest activity among all samples tested, it is unlikely that Cr at silanol sites is responsible for the high activity observed at high Cr/Al. Instead, Cr species giving rise to nitrosyl peaks at 1732 $cm^{-1}$ and 1720 $cm^{-1}$ may be responsible for higher dehydrogenation activity with increasing Cr/Al. Previously reported $Cr^{2+}$ dinitrosyls[23,27,31] do not display antisymmetric N–O stretching frequencies below 1742 $cm^{-1}$. In a prior study, pyridine co-adsorbed with NO on $Cr/SiO_2$ caused red-shifting of nitrosyl frequencies by 20–60 $cm^{-1}$. Electron donation from pyridine to Cr allowed stronger interaction between Cr 3d and NO $\pi^*$ orbitals, weakening the NO bond.[31] Similarly, the low frequency of the nitrosyl peaks that dominate at high Cr/Al in our samples suggests that these Cr species are more electron-rich than Cr species that are most abundant at low Cr/Al. We expect these to be $Cr^{2+}$ species, as $Cr^{+}$ is not generally observed in supported Cr catalysts. In one study, red-shifting of dinitrosyl stretching bands to 1736 $cm^{-1}$ and 1868 $cm^{-1}$ led earlier researchers to propose that a dichromate-like species in $Cr/SiO_2$–$TiO_2$ may display higher electron density than a monochromate.[47] The similarity of these reported frequencies to peaks observed in the present samples at 1732 $cm^{-1}$ and 1868 $cm^{-1}$ lead us to the tentative assignment of these peaks to stretching bands of $Cr^{2+}$ dinitrosyls exhibiting higher electron density, possibly in the form of multinuclear Cr species ($Cr_xO_y$) which become more abundant as Cr loading increases.

It was previously concluded that multinuclear Cr in $Cr/Al_2O_3$ are more active for propane dehydrogenation than mononuclear Cr.[15] However, when multinuclear Cr aggregates become too large, dehydrogenation activity drops. This is consistent with the present result that highly active samples with high Cr/Al also deactivate more quickly. The higher surface density of Cr may encourage formation of multinuclear active sites, but excessive aggregation can result in lowered activity and blocking of micropore volume. Insufficient quantity of stable binding sites for Cr may also result in migration of Cr to external silanols, another potential source of deactivation.[21] While a detailed understanding of deactivation mechanisms was not the focus of this study, it must be kept in mind that the NO adsorption experiments were performed after treatment at 650 °C for 1 h. If catalysts deactivate over this short time scale at that temperature, the NO adsorption spectrum may not fully reflect the active state of the sample. Future work will be aimed at identifying unique active structures of Cr stabilized on the zeolite surface.

**Impact of Paired Al Sites as Binding Sites for Cr**

In an attempt to gain insight into the binding of Cr at Al sites, a sample was prepared using ZSM-5 that was exchanged with $Ca^{2+}$ prior to Cr deposition. The divalent $Ca^{2+}$ cation was expected to exchange preferentially at paired Al sites,[3] selectively blocking Cr from occupying these sites. The resulting catalyst, 0.5 wt% Cr/Ca-ZSM-5 (0.10 Cr/Al), displayed more than triple the initial activity of Cr/H-ZSM-5 of equal Cr loading. It was more active per mole of Cr than 0.30 Cr/Al Cr/H-ZSM-5 and showed less deactivation (Fig. S2.17). While the 0.30 Cr/Al Cr/H-ZSM-5 sample lost over 60% of its initial activity over 3 h, 0.10 Cr/Al Cr/Ca-ZSM-5 lost less than 35% of initial activity over the same amount of time. Thus, a highly active catalyst with enhanced stability resulted when the quantity of paired Al sites was reduced and the Cr loading kept reasonably low.

The DRIFTS spectrum of the hydroxyl region of Cr/Ca-ZSM-5 provides information about the location of Cr in this sample (Fig. 2.10a). While the silanol bands at 3744 $cm^{-1}$ changed very little in 0.10 Cr/Al Cr/H-ZSM-5 and Cr/Ca-ZSM-5 compared with H-ZSM-5, clear changes were observed in the intensities of the bridging hydroxyl peaks at 3608 $cm^{-1}$.

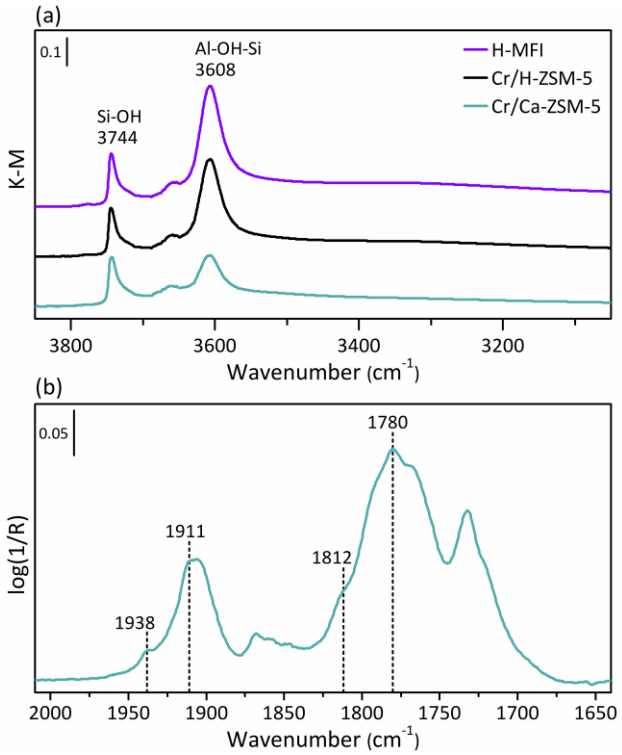


**Figure 2.10.** (a) FTIR-DRIFTS spectra of the hydroxyl region of H-ZSM-5, Cr/H-ZSM-5 (0.10 Cr/Al), and Cr/Ca-ZSM-5 (0.10 Cr/Al) under $N_2$ at 100 °C after treatment at 650 °C for 30 min. H-ZSM-5 and Cr/H-ZSM- 5 were treated under $N_2$ and Cr/Ca-ZSM-5 was treated under $H_2$. Spectra were normalized by the intensity of the zeolite Si–O–Si overtone peak at 1987 $cm^{-1}$. (b) FTIR-DRIFTS spectrum of NO adsorbed at 30 °C on Cr/Ca-ZSM-5 (0.10 Cr/Al) after treatment in $H_2$ at 650 °C for 30 min.

Comparison of peak intensities provides a rough estimate of concentration of Al bridging hydroxyls in the samples. The bridging hydroxyl peak height for 0.10 Cr/Al Cr/H-ZSM-5 was 81% of the peak height of H-ZSM-5, which yields a ratio of two Al sites occupied per Cr. If $Ca^{2+}$ exchange removed hydroxyls at all paired Al sites, this would account for a loss of 39% of the bridging hydroxyls compared with H-ZSM-5. Assuming also a ratio of two Al sites consumed per Cr cation for 0.10 Cr/Al Cr/Ca-ZSM-5, it would be expected that 41% of Al sites would remain after addition of Cr. In fact, the bridging hydroxyl peak height of the Cr/Ca-ZSM-5 sample was found to be 43% of the peak height in H-ZSM-5. This suggests that a considerable amount of Al sites were titrated by $Ca^{2+}$ exchange, forcing a greater fraction of Cr to bind at isolated Al sites.

The NO adsorption DRIFTS spectrum (Fig. 2.10b) of Cr/Ca-ZSM-5 reduced in $H_2$ at 650 °C showed a drop in relative intensity of the pairs of peaks at 1780 $cm^{-1}$/1911 $cm^{-1}$ and 1812 $cm^{-1}$/1938 $cm^{-1}$

compared with 0.10 Cr/Al Cr/H-ZSM-5 (Fig. 2.3). Peaks at 1767 $cm^{-1}$/1904 $cm^{-1}$, 1732 $cm^{-1}$, and 1720 $cm^{-1}$ became more prominent, similar to the trend observed with increasing Cr/Al for Cr/H-ZSM-5 (Fig. 2.9). The broad absorbance between 1732 $cm^{-1}$ and 1767 $cm^{-1}$ which was observed at high Cr/Al was also observed for Cr/Ca-ZSM-5. However, based on the spectrum of the hydroxyl region of Cr/Ca-ZSM-5, the broad absorbance in the NO adsorption spectrum seems not to result from Cr at silanol sites. Instead, this absorbance may be due to nitrosyls of multinuclear Cr species at Al sites. Furthermore, the sharp carbonyl peaks at 2195 $cm^{-1}$ and 2208 $cm^{-1}$ were less pronounced for Cr/Ca-ZSM-5 (Fig. S2.14), suggesting that these are carbonyls of Cr located at paired Al sites. It is also possible that the pairs of peaks at 1780 $cm^{-1}$/1911 $cm^{-1}$ and 1812 $cm^{-1}$/1938 $cm^{-1}$, which were lower in intensity when there were fewer available paired Al sites, are due to dinitrosyls of Cr located at α and β paired Al sites.

In Cr/Ca-ZSM-5, Cr was directed away from paired Al sites, binding instead at isolated Al sites and possibly forming multinuclear species. This catalyst, as a result, displayed much higher activity than when Cr was allowed to bind at paired Al sites. 0.10 Cr/Al Cr/Ca-ZSM-5 also displayed more stable activity on stream than 0.30 Cr/Al Cr/H-ZSM-5, which had similar initial activity. The lower surface density of Cr in Cr/Ca-ZSM-5 may be the reason for higher stability, as excessive aggregation was reduced with respect to 0.30 Cr/Al Cr/H-ZSM-5.

## 2.5 Conclusions

Speciation of Cr at Al sites in zeolite ZSM-5 meaningfully impacts ethane dehydrogenation activity and stability. Reduced Cr was found to anchor mainly at zeolite Al sites in all Cr/H- ZSM-5 samples, and clear trends in catalysis were observed with increasing Cr loading up to 1.6 wt% (0.30 Cr/Al). Specifically, at low Cr/Al, catalysts were associated with stable dehydrogenation activity, while at increased Cr/Al, catalysts were more active but less stable on stream. A variety of Cr structures present in Cr/H-ZSM-5 samples were differentiated by NO and CO probe molecule adsorption and co-adsorption DRIFTS measurements. Several Cr species that possessed high degrees of coordinative unsaturation (unsaturated to the extent that they could coordinate at least three adsorbate molecules at 30 °C) were observed. NO

adsorption DRIFTS indicated that the most active samples contained greater amounts of more electron-rich, possibly multinuclear, $Cr^{2+}$ species. The presence of $Ca^{2+}$ on ZSM-5 before Cr introduction modified the distribution of reduced Cr species and resulted in a threefold increase in dehydrogenation activity.

This evidence suggests that highly active and stable Cr dehydrogenation catalysts may be designed by controlling the distribution of Al binding sites on zeolite supports, and that probe molecule spectroscopy is an effective tool for differentiating reduced Cr sites in zeolites. Although the present study does not definitively identify the structures and binding sites of Cr in ZSM-5, the results educate future investigation and indicate the value of understanding this catalyst system in greater detail. Additional research combining experiment and theory towards identification and further evaluation of the variety of dispersed Cr species stabilized by zeolites will be useful for development of catalysts containing uniform Cr active sites.

## 2.6 Conflicts of Interest

The authors have no conflicts to declare.

## 2.7 Acknowledgements

The authors acknowledge Dr. Simon Bare and Dr. Adam Hoffman for their help in collecting XAS data. Use of the Stanford Synchrotron Radiation Lightsource, SLAC National Accelerator Laboratory, is supported by the U.S. Department of Energy, Office of Science, Office of Basic Energy Sciences under Contract No. DE-AC02-76SF00515. Co-ACCESS funded by the Chemical Sciences Program. Chemical Sciences, Geosciences, and Biosciences Division, Basic Energy Sciences of the U.S. DOE Office of Science is acknowledged for the X-ray absorption spectroscopy.

## 2.8 References

(1) L. Liu, M. Lopez-Haro, C. W. Lopes, C. Li, P. Concepcion, L. Simonelli, J.J.Calvino and A.Corma, *Nat. Mater.*, **2019**, 18, 866.

(2) C. Paolucci, I. Khurana, A. A. Parekh, S. Li, A. J. Shih, H. Li, J. R. Di Iorio, J. D. Albarracin-Caballero, A. Yezerets, J. T. Miller, W. N. Delgass, F. H. Ribeiro, W. F. Schneider and R. Gounder, *Science*, **2017**, 357, 898.

(3) O. Bortnovsky, Z. Sobalik and B. Wichterlova, *Microporous Mesoporous Mater.*, **2001**, 46, 265.

(4) P. Sazama, E. Tabor, P. Klein, B. Wichterlova, S. Sklenak, L. Mokrzycki, V. Pashkkova, M. Ogura and J. Dedecek, *J. Catal.*, **2016**, 333, 102.

(5) D. Kaucky, A. Vondrova, J. Dedecek and B. Wichterlova, *J. Catal.*, **2000**, 194, 318.

(6) A. R. Kulkarni, Z. J. Zhao, S. Siahrostami, J. K. Norskov and F. Studt, *Catal. Sci. Technol.*, **2018**, 8, 114.

(7) M. A. Newton, A. J. Knorpp, V. L. Sushkevich, D. Palagin and J. A. Van Bokhoven, *Chem. Soc. Rev.*, **2020**, 49, 1449.

(8) S. Moussa, P. Concepcion, M. A. Arribas and A. Martinez, *ACS Catal.*, **2018**, 8, 3903.

(9) Y. Zhang, S. Wu, X. Xu and H. Jiang, *Catal. Sci. Technol.*, **2020**, 10, 835.

(10) S. S. Arzumanov, A. A. Gabrienko, A. V. Toktarev, Z. N. Lashchinskaya, D. Freude, J. Haase and A. G. Stepanov, *J. Phys. Chem. C*, **2019**, 123, 30473.

(11) A. Mehdad, N. S. Gould, B. Xu and R. F. Lobo, *Catal. Sci. Technol.*, **2018**, 8, 358.

(12) N. M. Phadke, J. Van Der Mynsbrugge, E. Mansoor, A. B. Getsoian, M. Head-Gordon and A. T. Bell, *ACS Catal.*, **2018**, 8, 6106.

(13) X. Niu, X. Nie, C. Yang and J. G. Chen, *Catal. Sci. Technol.*, **2020**, 10, 1881.

(14) C. A. Gartner, A. C. van Veen and J. A. Lercher, *ChemCatChem*, **2013**, 5, 3196.

(15) R. L. Puurunen and B. M. Weckhuysen, *J. Catal.*, **2002**, 210, 418.

(16) B. M. Weckhuysen, R. A. Schoonheydt, J. M. Jehng, I. E. Wachs, S. J. Cho, R. Ryoo, S. Kijlstra and E. Poels, *J. Chem. Soc., Faraday Trans.*, **1995**, 91, 3245.

(17) G. A. Martino, C. Barzan, A. Piovano, A. Budnyk and E. Groppo, *J. Catal.*, **2018**, 357, 206.

(18) B. M. Weckhuysen, H. J. Spooren, R. A. Schoonheydt and K. U. Leuven, *Zeolites*, **1994**, 14, 450.

(19) B. M. Weckhuysen, D. Wang, M. P. Rosynek and J. H. Lunsford, *J. Catal.*, **1998**, 346, 338.

(20) P. Michorczyk, K. Zenczak-Tomera, B. Michorczyk, A. Wegrzyniak, M. Basta, Y. Millot, L. Valentin and S. Dzwigaj, *J. $CO_2$ Util.*, **2020**, 36, 54.

(21) J. Gao, Y. Zheng, Y. Tang, J. M. Jehng, R. Grybos, J. Handzlik, I. E. Wachs and S. G. Podkolzin, *ACS Catal.*, **2015**, 5, 3078.

(22) J. Janas, J. Gurgul, R. P. Socha, J. Kowalska, K. Nowinska, T. Shishido, M. Che and S. Dzwigaj, *J. Phys. Chem. C*, **2009**, 113, 13273.

(23) A. Zecchina, G. Spoto, G. Ghiotti and E. Garrone, *J. Mol. Catal.*, **1994,** 86, 423.

(24) K. Hadjiivanov, A. Penkova, R. Kefirov, S. Dzwigaj and M. Che, *Microporous Mesoporous Mater.*, **2009**, 124, 59.

(25) M. Mihaylov, A. Penkova, K. Hadjiivanov and M. Daturi, *J. Mol. Catal. A: Chem.*, **2006**, 249, 40.

(26) A. Penkova and K. Hadjiivanov, *Catal. Commun.*, **2003**, 4, 485.

(27) E. Groppo, C. Lamberti, S. Bordiga, G. Spoto and A. Zecchina, *Chem. Rev.*, **2005**, 105, 115.

(28) M. Botavina, C. Barzan, A. Piovano, L. Braglia, G. Agostini, G. Martra and E. Groppo, *Catal. Sci. Technol.*, **2017**, 7, 1690.

(29) A. Zecchina, E. Garrone, C. Morterra and S. Coluccia, *J. Phys. Chem.*, **1975**, 79, 978.

(30) G. Ghiotti, E. Garrone, G. Della Gatta, B. Fubini and E. Giamello, *J. Catal.*, **1983**, 80, 249.

(31) E. Garrone, G. Ghiotti, C. Morterra and A. Zecchina, *Z. Naturforsch., B: J. Chem. Sci.*, **1987**, 42, 728.

(32) B. M. Weckhuysen, I. E. Wachs and R. A. Schoonheydt, *Chem. Rev.*, **1996**, 96, 3327.

(33) I. V. Babich, Y. V. Plyuto, P. Van Der Voort and E. F. Vansant, *J. Colloid Interface Sci.*, **1997**, 189, 144.

(34) B. M. Weckhuysen, R. Ramachandra Rao, J. Pelgrims, R. A. Schoonheydt, P. Bodart, G. Debras, O. Collart, P. Van Der Voort and E. F. Vansant, *Chem. – Eur. J.*, **2000**, 6, 2960.

(35) A. Hakuli and A. Kytokivi, *Phys. Chem. Chem. Phys.*, **1999**, 1, 1607.

(36) Z. Sobalik, J. Dedecek, D. Kaucky, B. Wichterlova, L. Drozdova and R. Prins, *J. Catal.*, **2000**, 194, 330.

(37) J. Dedecek, D. Kaucky and B. Wichterlova, *Microporous Mesoporous Mater.*, **2000**, 35–36, 483.

(38) J. Dedecek, Z. Sobalik and B. Wichterlova, *Catal. Rev.: Sci. Eng.*, **2012**, 54, 135.

(39) J. J. Dedecek, S. Sklenak, C. Li, B. Wichterlova, V. Gabova, J. Brus, M. Sierka and J. Sauer, *J. Phys. Chem. C*, **2009**, 113, 1447.

(40) S. Sklenak, P. C. Andrikopoulos, S. R. Whittleton, H. Jirglova, P. Sazama, L. Benco, T. Bucko, J. Hafner and Z. Sobalik, *J. Phys. Chem. C*, **2013**, 117, 3958.

(41) A. Janda and A. T. Bell, *J. Am. Chem. Soc.*, **2013**, 135, 19193.

(42) J. B. Peri, *J. Phys. Chem.*, **1974**, 78, 588.

(43) A. Zecchina, C. Otero Arean and E. Groppo, *ChemCatChem*, **2010**, 2, 259.

(44) A. S. Hoffman, C. Y. Fang and B. C. Gates, *J. Phys. Chem. Lett.*, **2016**, 7, 3854.

(45) E. Groppo, A. Damin, C. Otero Arean and A. Zecchina, *Chem. – Eur. J.*, **2011**, 17, 11110.

(46) M. P. McDaniel, Adv. Catal., 1985, 33, 47. 47 S. J. Conway, J. W. Falconer and C. H. Rochester, J. Chem. Soc., Faraday Trans., 1989, 85, 79.

## 2.9 Supporting Information

### Supporting Information Table of Contents

**Experimental Details**

**Chemicals.** All chemicals were used as received. $NH_4$-ZSM-5 (CBV 3024E, Zeolyst), 2-propanamine ($C_3H_9N$, 99+%, Alfa Aesar) chromium (III) acetylacetonate ($Cr(acac)_3$, 99.99%, Sigma-Aldrich), sodium hydroxide (NaOH, ≥97.0%, Sigma-Aldrich), sodium nitrate ($NaNO_3$, 99.0%, Alfa Aesar), calcium nitrate tetrahydrate ($Ca(NO_3)_2{\cdot}4H2O$, 99+%, Acros Organics), chromium (III) oxide ($Cr_2O_3$, US Research Nanomaterials), sodium chromate anhydrous ($Na_2CrO_4$, Fisher Chemical), potassium bromide (KBr, Pike Technologies), aluminum oxide ($\alpha$-$Al_2O_3$, 180 micron, >99.7%, Alfa Aesar), nitrogen[a] ($N_2$, 99.9997%, Airgas), nitrogen[b] ($N_2$, 99.999%, Praxair), ethane ($C_2H_6$, 99.999%, Matheson), carbon monoxide (CO, 99.999%, Matheson), hydrogen ($H_2$, 99.999%, Praxair), nitric oxide (NO, 1%/bal. $N_2$, Matheson).

[a]Used for DRIFTS experiments

[b]Used for packed-bed reactor

**Vapor deposition of $Cr(acac)_3$.** In previous studies, vapor-phase $Cr(acac)_3$ reacted with $SiO_2$ surface hydroxyls (silanols) between 200-240 °C, anchoring Cr to the support.[1–3] During calcination, the remaining organic ligands decomposed, leaving $Cr^{6+}$ surface species typical of a $Cr/SiO_2$ sample with highly dispersed Cr. Similarly, we expected zeolite external surface hydroxyls (external silanols) and bridging hydroxyls (at Al sites) to react with $Cr(acac)_3$, anchoring Cr to the zeolite surface. $Cr(acac)_3$/ZSM-5 mixtures inside vacuum-sealed ampoules were treated at 200 °C and subsequently 300 °C in to ensure quantitative grafting of $Cr(acac)_3$ onto the zeolite. After vapor deposition of $Cr(acac)_3$ under vacuum, samples were calcined in air at 500 °C. TGA-MS analysis of calcination of a 0.5 wt% Cr/H-ZSM-5 sample (Fig. S2.4) demonstrates that the measured mass loss closely matched the mass loss expected when all Cr is incorporated into the calcined sample. Furthermore, XANES spectra show that after calcination, Cr is mainly present as $Cr^{6+}$ (Fig. S2.2). Due to the known surface mobility of Cr under oxidizing conditions at temperatures above 300 °C,[4–6] we expected the location of Cr after calcination to reflect the relative preference of Cr for various binding sites on the zeolite surface, rather than the location where $Cr(acac)_3$ initially grafts during vacuum treatment. In a previous study, Cr was observed by UV-vis spectroscopy to

migrate from $SiO_2$ to alumina ($Al_2O_3$) and zeolite surfaces.[5] This suggests that Cr may preferentially locate at Al sites in zeolites, rather than defect silanols.

**Diffuse Reflectance Infrared Fourier Transform Spectroscopy (DRIFTS).** All probe molecule experiments were performed isothermally at 30 °C. Initially, the DRIFTS cell contained pure $N_2$ at 0 psig. Subsequently, 1% NO gas (balance $N_2$) was flowed into the cell at 30 mL/min with the cell outlet valve closed, thus introducing NO pressure to the cell. After 30 s of flow, the cell inlet valve was closed, sealing the cell containing a known quantity of NO ($4.5 \times 10^{-6}$ mol; this equates to between 3 and 5 moles NO in headspace per mole Cr in sample). Estimating the volume of the cell to be 20 mL, the partial pressure of NO in the cell was 0.55 kPa, before NO adsorption onto the sample. Total pressure is estimated to be 76 kPa-g. Samples were allowed to equilibrate for 10 min after NO dosing, during which time spectra stabilized. To supply a second dose of NO, first the cell pressure was vented quickly through the outlet valve. Next, NO was flowed into the cell at 30 mL/min for 30 s (with outlet valve closed) before sealing the cell again. The second dose of NO resulted in small increases in all NO peaks, without significant changes to relative peak intensities. A third dose resulted in very little, if any, changes to the DRIFTS spectrum. NO adsorption spectra reported in this study were taken after the second dose of NO. The typical NO adsorption procedure did not include a third dose of NO.

After NO adsorption, the cell pressure was vented through the outlet valve and the cell was purged with pure $N_2$ flow. After 10 min of 30 mL/min $N_2$ flow, spectra were fairly stable. The cell outlet valve was closed and 3 mL/min CO diluted in 27 mL/min $N_2$ was flowed into the cell for 30 s before closing the inlet valve to seal the cell. Again, 10 min equilibration time was allowed for spectra to stabilize before venting the cell and purging with 30 mL/min $N_2$ flow. Spectra were taken every minute during CO desorption. The small volume of the cell allowed gas phase CO to be removed within one minute, so that adsorbed CO DRIFTS peaks were not obscured by absorbance from gas phase CO.

All DRIFTS measurements taken in the absence of probe molecules were reported as K-M spectra. A reference reflectance spectrum ($R_{KBr}$) of dried potassium bromide (KBr) under nitrogen flow was

collected by backgrounding the spectrometer. Relative reflectance (R') spectra were calculated by the formula:

$$R' = \frac{R_s}{R_{KBr}}$$

where $R_s$ is the sample reflectance. For small values of R', the Kubelka-Munk function was used to convert relative reflectance to a pseudo-absorbance by the formula:

$$KM = \frac{(1 - R')^2}{2R'}$$

where KM is the Kubelka-Munk function, which is proportional to absorbance for small values of R'. When zeolite samples were measured using KBr as the background, R' is small and the spectra were reported as KM.

To measure spectra of adsorption of probe molecules, a background spectrum ($R_{bg}$) of the sample was collected just prior to introduction of the probe gas. Sample spectra were taken after exposure of the sample to probe molecules, and relative reflectance (R') was calculated as:

$$R' = \frac{R_s}{R_{bg}}$$

In this case, the values of R' tended to be close to 1, since the zeolite absorbs strongly compared with the small quantity of adsorbed probe molecules. When R' > 0.6, it was shown previously that the Kubelka-Munk function is not linearly proportional to absorbance.[7] Instead, log inverse reflectance, log(1/R'), is a better approximation of absorbance. Probe molecule spectra were reported in this study as log(1/R').

**Catalytic Packed-Bed Reactor Measurements.** The packed-bed reactor consisted of a 6.35 mm OD quartz tube, fitted at either end with ultra-torr compression fittings (Swagelok), flexible stainless-steel tubing (6.35 mm OD) and quick-connect valves. The valves allowed for sample transfer from the glovebox without exposure to ambient air. In the glovebox, samples were sieved to mesh size 60-40 and loaded into the quartz tube between two lengths of α-alumina powder (2 g each). The purpose of the alumina was to

reduce the dead volume of the reactor and situate the catalyst sample at the center of the heated zone of the furnace. The bed, comprised of alumina and catalyst sample, was supported by a small plug of quartz wool.

Stainless steel tubing (1/8" OD) carried all gas flows. Gases were mixed upstream of the reactor, and gas flow rates were controlled by mass flow controllers (Brooks). Three-way valves upstream and downstream of the reactor allowed gas flow to bypass the reactor. Downstream of the reactor, gas lines were heated to 120 °C using heating tape all the way to the GC inlet system, which was heated to 110 °C.

Reactor effluent gas was analyzed by an Agilent 7890a Gas Chromatography unit. Permanent gases detected by TCD were separated using molecular sieve, Porapak Q, and Porapak N columns. A separate channel with $N_2$ carrier gas and a molecular sieve column was used to detect $H_2$ by TCD. A third channel measured hydrocarbons by FID. Hydrocarbons were separated using a HP-PLOT $Al_2O_3$ S column (19095P-S25, Agilent).

The GC was calibrated using a custom gas mix supplied by Matheson (relative accuracy within 2%). Calibration curves were used to convert peak areas to mole fractions. In all experiments, $N_2$ served as an inert internal standard. All reaction experiments were carried out under the same conditions. A blank reactor experiment was run, measuring 0.059 % ethane conversion for a packed bed of 4 g α-alumina with no catalyst. This value was subtracted from measured ethane conversion before calculating rate of reaction. Ethane conversion was maintained below 10% to achieve a differential reactor yielding accurate reaction rates. In most cases, conversion was kept below 4%. Space velocity was controlled by varying the mass of catalyst in the reactor, keeping flow conditions constant. For time-on-stream data, initial time values (zero TOS) were determined by linear extrapolation from the first two data points measured. Reaction parameters were calculated as follows.

$$ethane\ conversion = \frac{molar\ flow\ rate\ of\ carbon\ (C)\ in\ products}{molar\ flow\ rate\ of\ total\ C\ in\ effluent\ (ethane + products)}$$

$$selectivity,\ product\ i = \frac{molar\ flow\ rate\ of\ C\ in\ product\ i}{molar\ flow\ rate\ C\ in\ all\ products}$$

$$space\ velocity = \frac{molar\ flow\ rate,\ ethane\ in\ feed}{moles\ Cr\ in\ packed\ bed}$$

$$rate\ of\ ethane\ conversion = (space\ velocity) \times (ethane\ conversion)$$

**Supporting Figures**

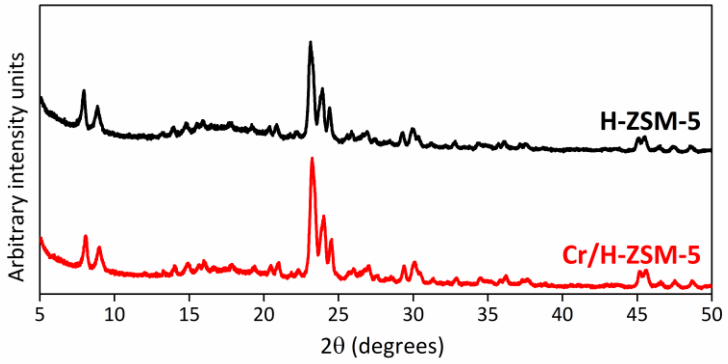


**Figure S2.1.** X-ray diffraction patterns for H-ZSM-5 and Cr/H-ZSM-5 (0.10 Cr/Al) after calcination in air at 500 °C. The results verify the crystallinity and presence of the MFI framework structure in both samples. Measurements were performed using a PANalytical X'Pert Pro diffractometer with Cu Kα radiation.

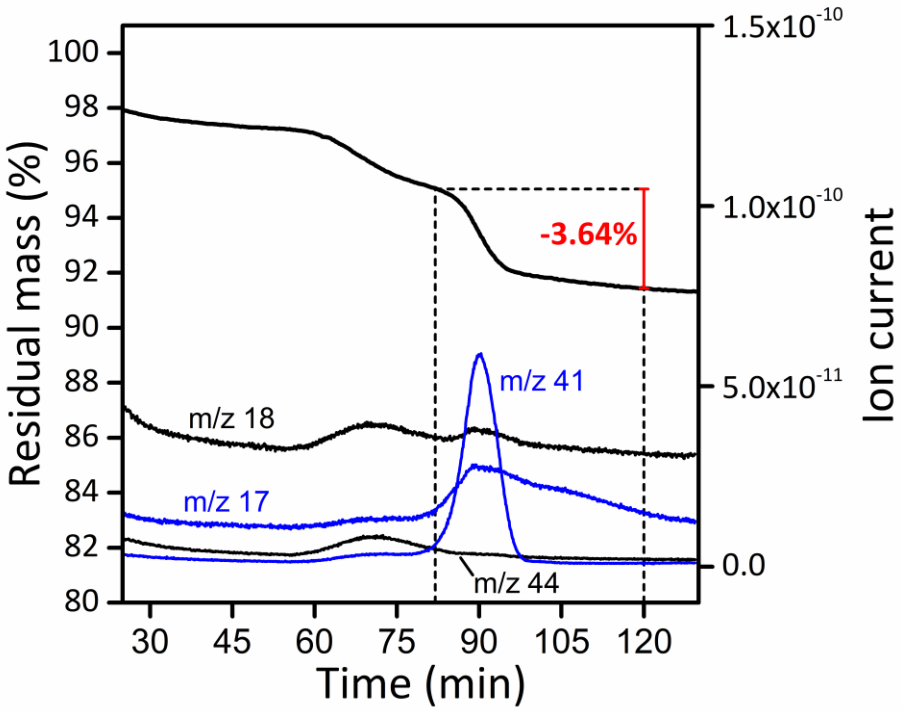


**Figure S2.2.** Temperature-programmed desorption of 2-propanamine. Mass spectrum signals at m/z 41 and m/z 17 correspond to propene and ammonia, respectively, which form and desorb following decomposition of 2-propanamine on Brønsted acid sites at around 300-350 °C.[8] The molar amount of 2-propanamine that decomposes corresponds to an equivalent molar amount of Brønsted acid sites in the zeolite. From this experiment, the Brønsted acid site density was calculated to be 616 μmol/g, consistent with previously determined values.[9,10]

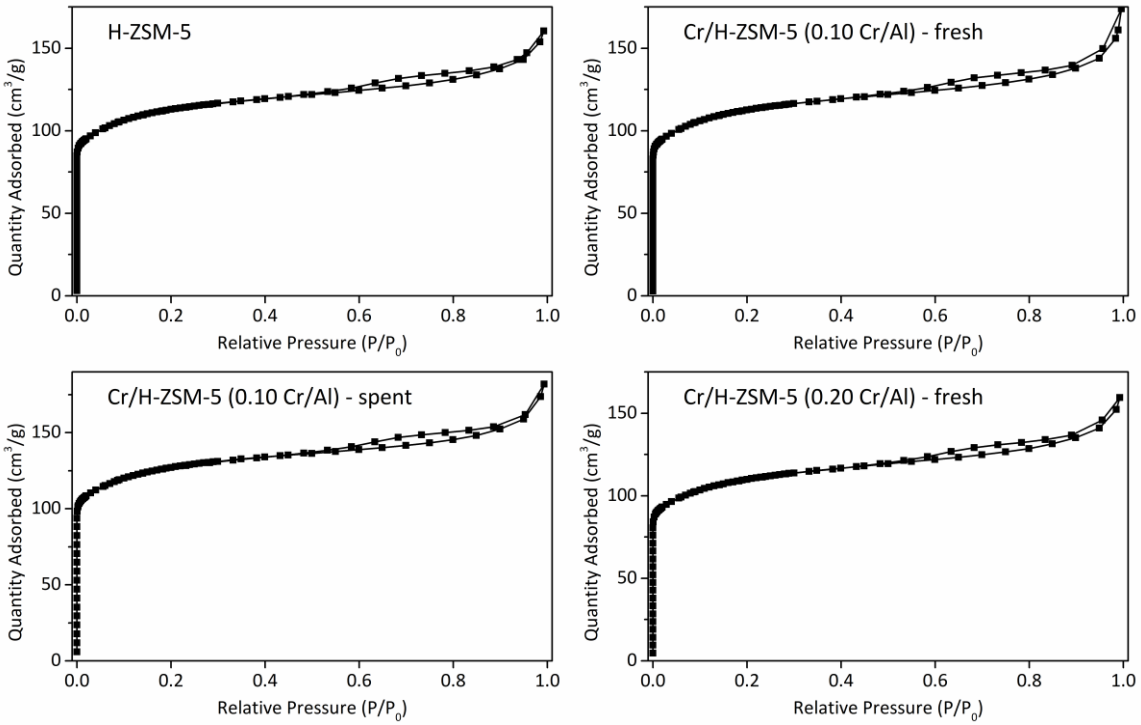


**Figure S2.3.** $N_2$ adsorption isotherms collected at -196 °C. Calculated surface areas and pore volumes are shown in Table S2.1. Isotherms for H-ZSM-5 and fresh Cr/H-ZSM-5 samples were collected after calcination. Isotherm for spent Cr/H-ZSM-5 (0.10 Cr/Al) was collected after sample was used for ethane dehydrogenation at 650 °C for 3 hours, operating at ca. 4% ethane conversion. All samples were degassed under vacuum at 300 °C for 3 hours before $N_2$ adsorption.

(a)

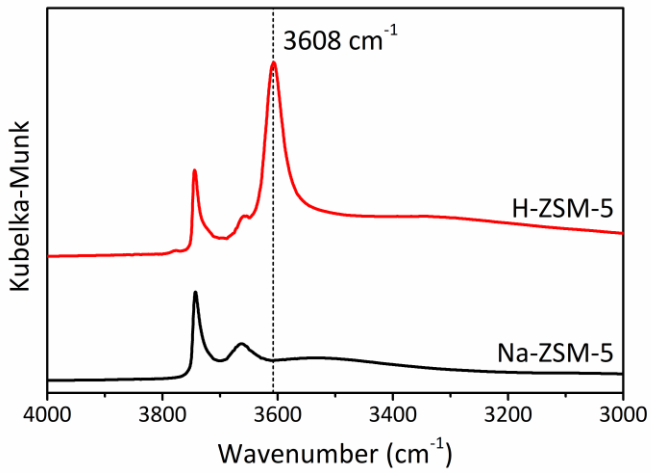


(b)

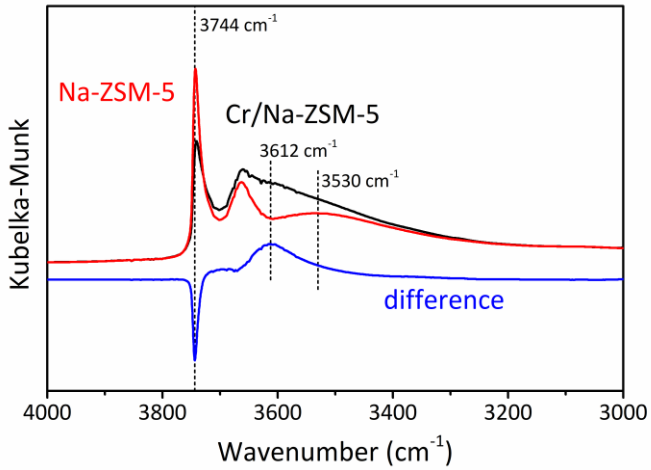


**Figure S2.4.** (a) DRIFTS spectra in the OH region of calcined supports H-ZSM-5 and Na-ZSM-5 before Cr deposition. Spectra were taken at 100 °C under $N_2$ flow after samples were treated at 650 °C for 1 hour under flowing $N_2$. These spectra demonstrate that Na-exchange of H-ZSM-5 caused disappearance of the peak at 3608 $cm^{-1}$ due to zeolite bridging hydroxyls (Al-OH-Si).[11] No significant change to external silanol (3744 $cm^{-1}$) and extra-framework Al hydroxyl (3658 $cm^{-1}$ and 3777 $cm^{-1}$) peaks[11, 12] was observed. (b) DRIFTS spectra in the OH region of Na-ZSM-5 (red) after 30-minute treatment in $N_2$ at 300 °C, Cr/Na-ZSM-5 (black) after reduction in CO at 300 °C, and the difference spectrum (blue). Spectra were taken at 100 °C under $N_2$ flow and normalized by the intensity of the zeolite Si-O-Si overtone peak at 1987 $cm^{-1}$. Significant decrease in intensity of the 3744 $cm^{-1}$ band due to external silanols (SiOH) after Cr loading suggests that Cr resides largely at external silanol sites. The band at 3530 $cm^{-1}$ due to internal silanols ("silanol nests")[12] does not change significantly with Cr loading, as is seen in the difference spectrum. This demonstrates that silanol nests are not the dominant binding site for Cr in Cr/Na-ZSM-5, although it does not rule out the possibility that a fraction of Cr present does replace Si in framework defect silanol nests. The increase in intensity at 3612 $cm^{-1}$ is difficult to assign. The broadness of the difference peak suggests that this could be due to perturbation of silanols by Cr or a small amount of moisture. It could also be explained by the formation of a small amount of bridging hydroxyls (Al-OH-Si). It has also been shown

that bridging hydroxyls (Cr-OH-Si) can form when Cr replaces vacant framework T sites,[13] but a definitive assignment of the resulting O—H stretching band in FTIR has not been made.

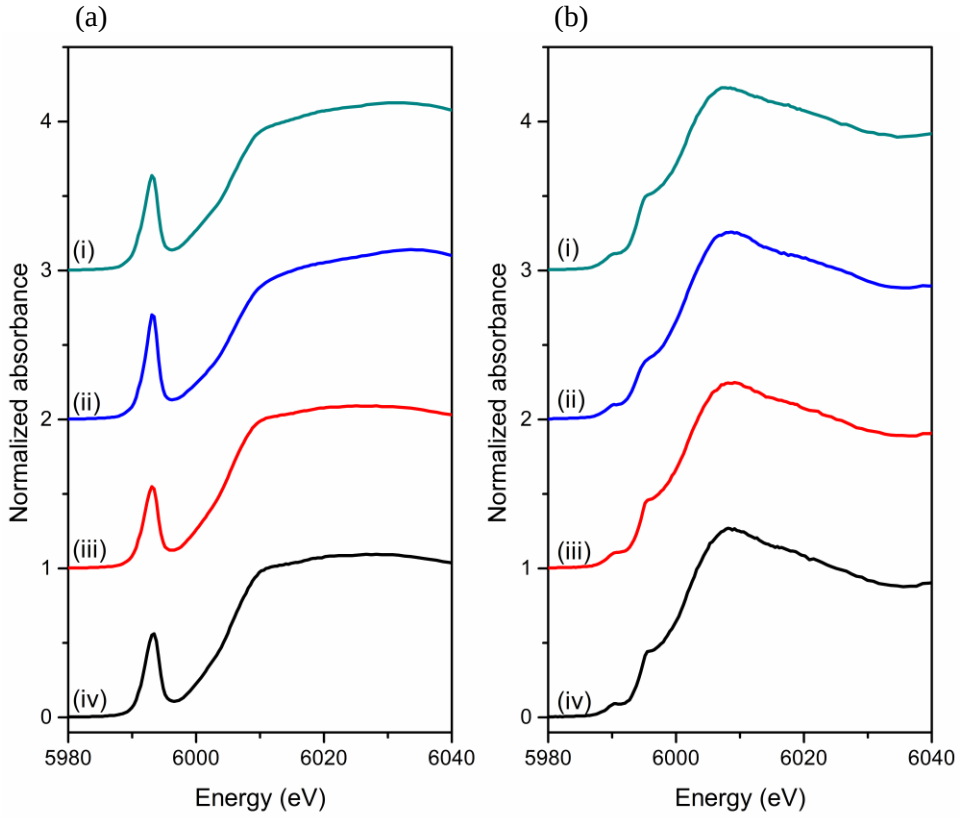


**Figure S2.5.** Samples legend below. (a) XANES spectra of fresh samples after calcination. Spectra were taken at room temperature under helium flow. In all samples, an intense pre-edge peak at 5993 eV indicates that Cr is present predominantly as tetrahedral $Cr^{6+}$ species.[14, 15] This peak is also present in the spectrum of $Na_2CrO_4$ in Fig. S2.3. (b) XANES spectra of samples from Fig. S2.2(a) after reduction at 300 °C in 10% CO (bal. $N_2$) for 30 min. Spectra were taken at 300 °C under 10% CO flow. Shifting of the edge to ca. 6002 eV and appearance of pre-edge features at 5988, 5990, and 5995 eV suggest the presence of mainly $Cr^{2+}$ in all samples after reduction.[14, 15] However, the presence of a minority of Cr in higher oxidation states cannot be ruled out.

Samples:

(i) 0.10 Cr/Al Cr/Ca-ZSM-5

(ii) 0.10 Cr/Al Cr/Na-ZSM-5

(iii) 0.10 Cr/Al Cr/H-ZSM-5

(iv) 0.17 Cr/Al Cr/H-ZSM-5

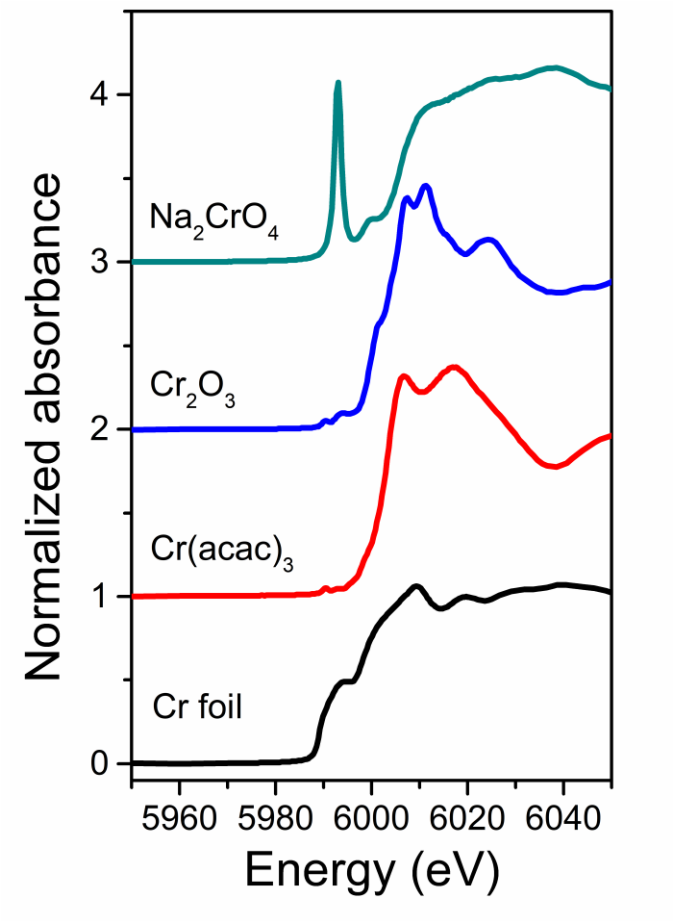


**Figure S2.6.** XANES spectra of reference compounds taken under ambient air at room temperature.

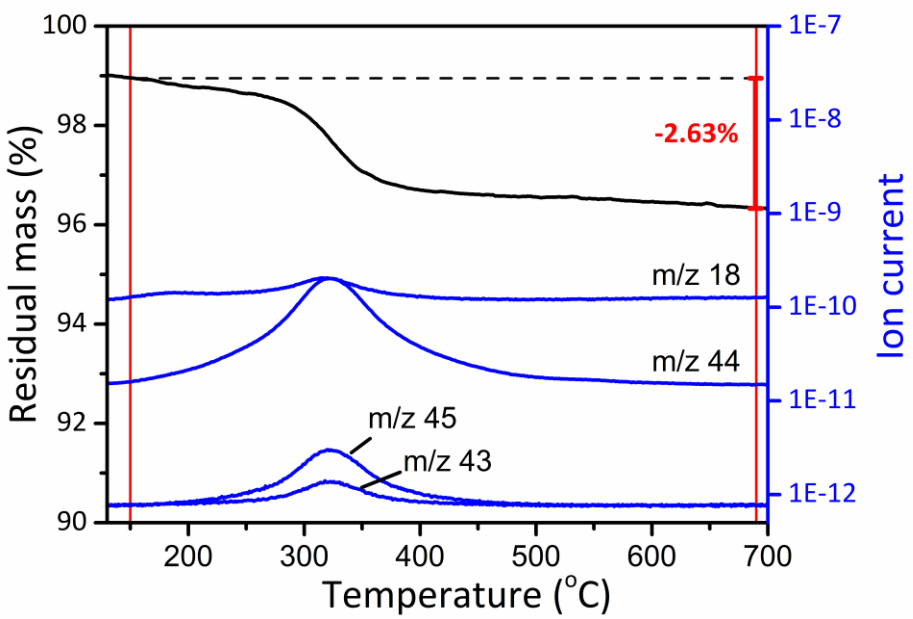


**Figure S2.7.** TGA-MS calcination of $Cr(acac)_3$/H-ZSM-5 mixture used for preparation of 0.10 Cr/Al Cr/H-ZSM-5. Isothermal soak at 120 °C for one hour removed adsorbed water that accumulated on the sample during transfer to the TGA. Mass loss during desorption of carbon-containing products is labelled. Mass spectrometer signals for water (m/z 18) and $CO_2$ (m/z 44) were the major signals observed. Signals for m/z 45 and m/z 43 were also observed, as previously reported.[2] Acetylacetone, acetic acid, and acetone display major fragments at m/z 43. Acetic acid displays a major fragment at m/z 45. No deviation from baseline was observed at mass m/z 151, a major fragment of $Cr(acac)_3$.

This sample was prepared by vacuum heat treatment of a mixture of 18.15 mg $Cr(acac)_3$ and 500.5 mg H-ZSM-5. Assuming all Cr remains on the zeolite surface during calcination and is converted from $Cr(acac)_3$ to $Cr^{6+}(=O)_2$, the expected mass loss during calcination is calculated as:

$$mol\ Cr\ in\ sample = \frac{(18.15\ mg)}{(MW_{Cr}\ g/mol) \times (1000\frac{mg}{g})} = 5.20 \times 10^{-5}\ mol\ Cr$$

$$expected\ mass\ loss\ (mg) = (mol\ Cr) \times \left(MW_{Cr(acac)3}\frac{g}{mol} - MW_{CrO2}\frac{g}{mol}\right) \times \left(1000\frac{mg}{g}\right) = 13.79\ mg$$

$$expected\ \%\ mass\ loss = \frac{(expected\ mass\ loss, mg)}{18.15\ mg + 500.5\ mg} = 2.66\%$$

Where $MW_i$ denotes molar weight of component i.

The close correspondence of the measured mass loss to the expected mass loss demonstrates that all Cr is incorporated into the sample during vacuum treatment and calcination.

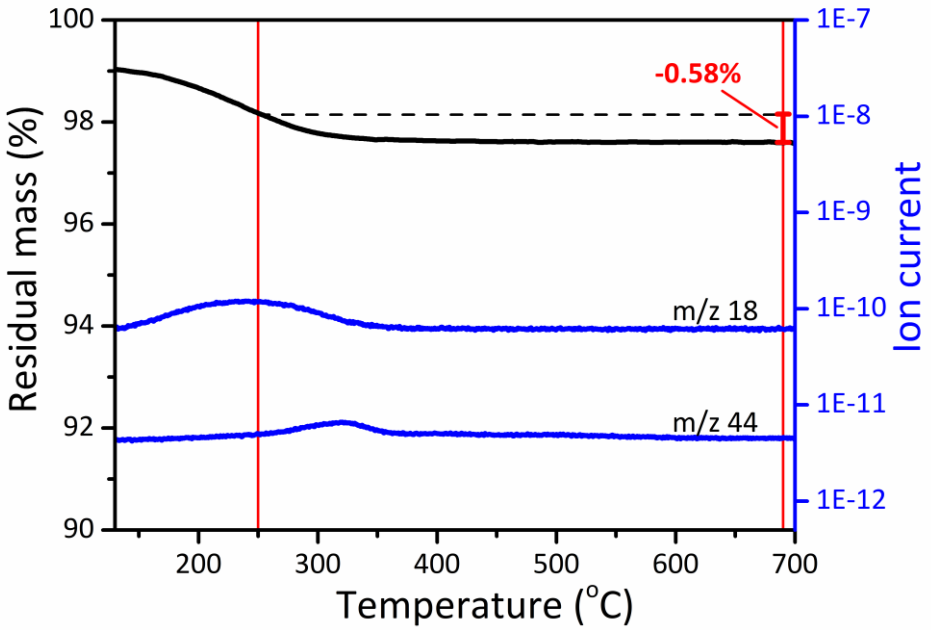


**Figure S2.8.** TGA-MS decoking of spent 0.10 Cr/Al Cr/Na-ZSM-5. Prior to decoking, catalyst was used for ethane dehydrogenation at 650 °C for three hours operating at 3% initial ethane conversion. Sample was cooled under $N_2$ flow and loaded to the TGA. After one-hour isothermal at 120 °C to remove moisture adsorbed to the sample after exposure to ambient lab air, TGA furnace was ramped at 5 °C/min with synthetic air flow to combust deposited carbon from the sample. The mass spectrometry signal for $CO_2$ (m/z 44) was used to identify carbon combustion. The mass loss due to coke is labelled on the figure.

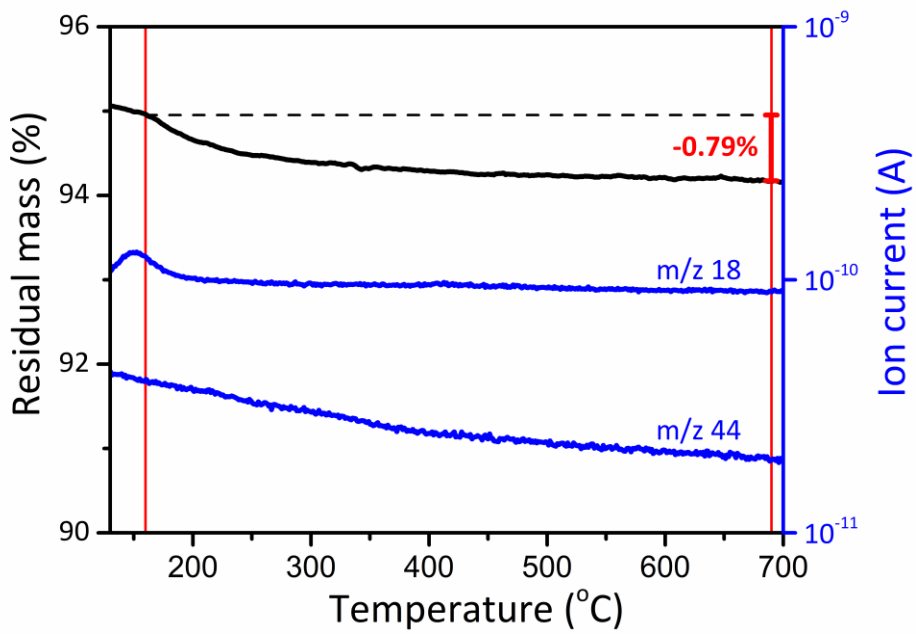


**Figure S2.9.** TGA-MS decoking of spent 0.10 Cr/Al Cr/H-ZSM-5. Prior to decoking, catalyst was used for ethane dehydrogenation at 650 °C, operating at 4% ethane conversion for three hours. Sample was cooled under $N_2$ flow and loaded to the TGA. After one-hour isothermal at 120 °C to remove moisture adsorbed to the sample after exposure to ambient lab air, TGA furnace was ramped at 5 °C/min with synthetic air flow to combust deposited carbon from the sample. The mass spectrometry signal for $CO_2$ (m/z 44) was used to identify carbon combustion. Baseline m/z 44 signal was slightly high during this experiment due to the use of pure $CO_2$ flow in a previous experiment run on the instrument. The temperature range used to determine mass loss was taken to be the same as that used in Fig. S2.7. The mass loss due to coke is labelled on the figure.

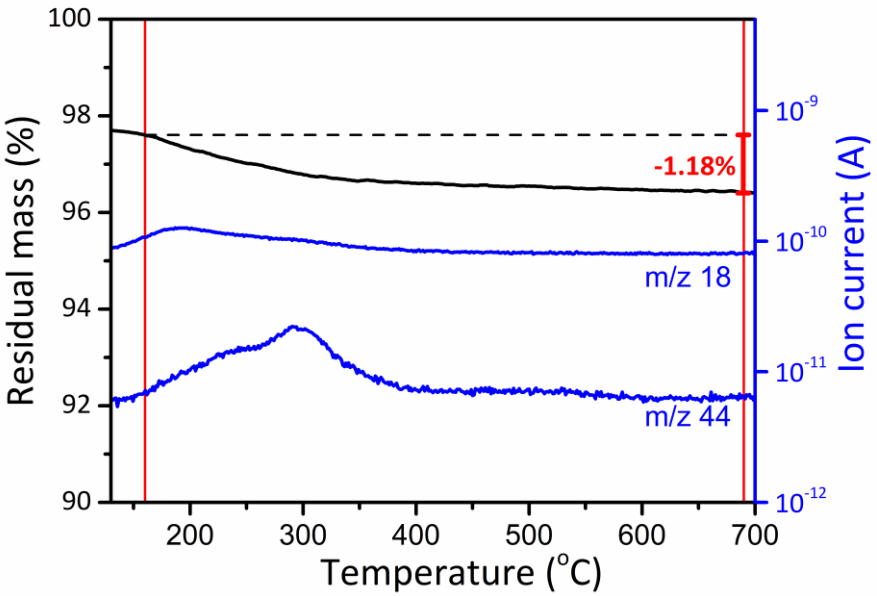


**Figure S2.10.** TGA-MS decoking of spent 0.17 Cr/Al Cr/H-ZSM-5. Prior to decoking, catalyst was used for ethane dehydrogenation at 650 °C, operating at 4% ethane conversion for 3 hours. Sample was cooled under $N_2$ flow and loaded to the TGA. After one-hour isothermal at 120 °C to remove moisture adsorbed to the sample after exposure to ambient lab air, TGA furnace was ramped at 5 °C/min with synthetic air flow to combust deposited carbon from the sample. The mass spectrometry signal for $CO_2$ (m/z 44) was used to identify carbon combustion. The mass loss due to coke is labelled on the figure.

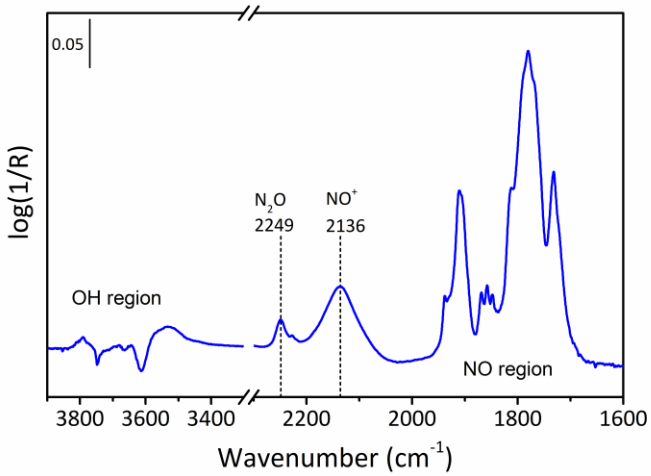


**Figure S2.11.** DRIFTS spectra of NO adsorption at 30 °C on 0.10 Cr/Al Cr/H-MFI after treatment for one hour at 650 °C under $N_2$ flow. Peaks due to $N_2O$ (2249 $cm^{-1}$) and $NO^+$ (2136 $cm^{-1}$) were observed during NO adsorption.[12]

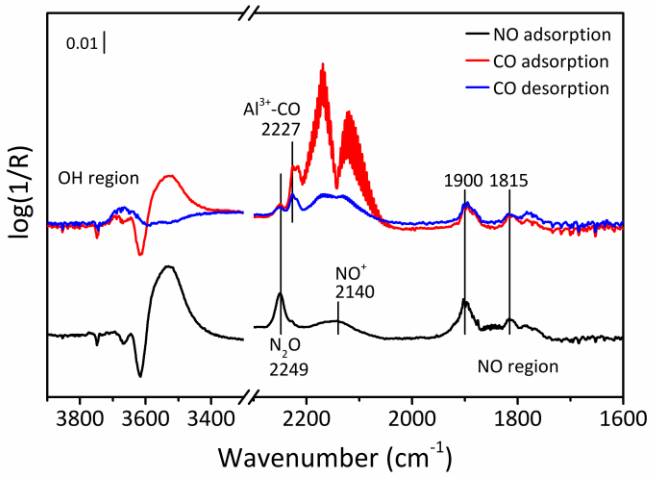


**Figure S2.12.** DRIFTS spectra of NO and CO adsorption at 30 °C on H-MFI after treatment for one hour at 650 °C under $N_2$ flow. Black curve: spectrum taken under static NO pressure. Red curve: spectrum taken after NO purge and introduction of static CO pressure. Blue curve: spectrum taken after one minute of purging CO from cell with 30 mL/min $N_2$.

Only very small peaks appeared in the nitrosyl region (see scale bar to compare with other samples). In the carbonyl region, only peaks at ca. 2227 $cm^{-1}$, characteristic of extra-framework $Al^{3+}$ carbonyls, were observed.[12]

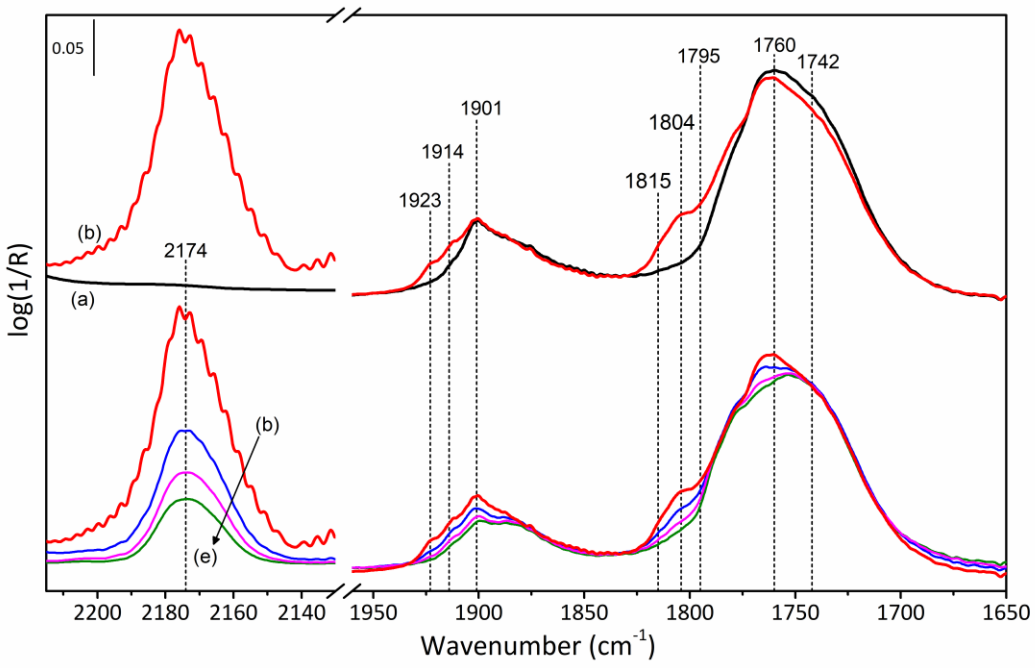


**Figure S2.13.** DRIFTS spectra of NO and CO adsorption at 30 °C on 0.10 Cr/Al Cr/Na-ZSM-5 after treatment for one hour at 650 °C under 10% $H_2$ flow (bal. $N_2$). (a) Spectrum taken under static NO pressure. (b) Spectrum taken after venting NO and introducing static CO pressure. (c)-(e) Spectra taken while cell was purged with $N_2$ flow. $N_2$ purge was not performed prior to CO dosing.

In contrast to Cr/H-ZSM-5 and Cr/Ca-ZSM-5 samples, no isosbestic point in the NO region was observed during CO desorption. This indicates that Cr dinitrosyl species in Cr/Na-ZSM-5 were unstable, as they were destroyed upon brief $N_2$ purge.

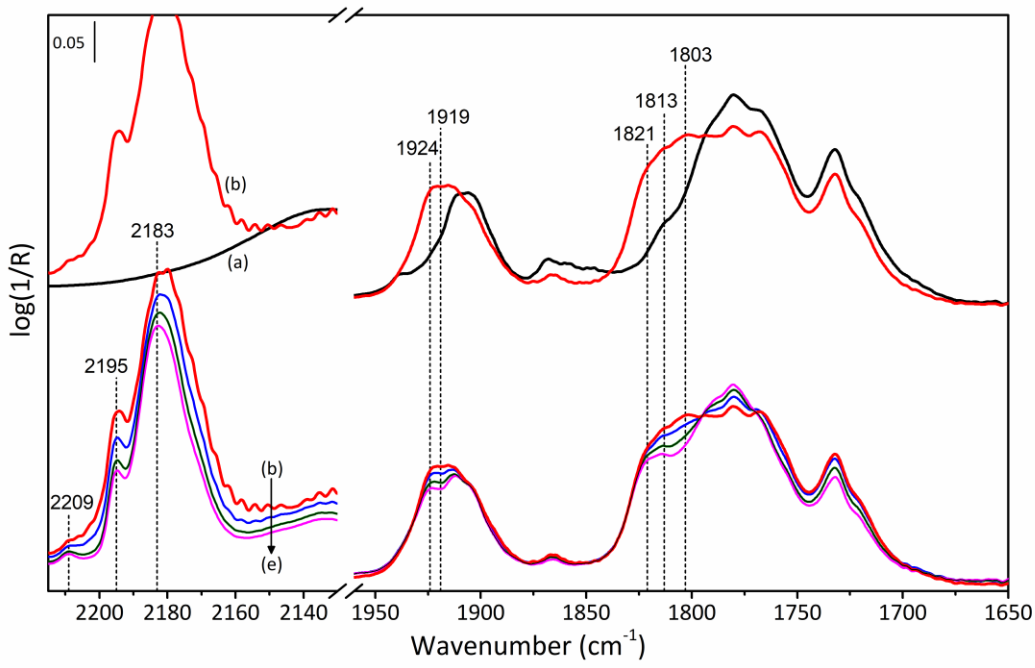


**Figure S2.14.** DRIFTS spectra of NO and CO adsorption at 30 °C on 0.10 Cr/Al Cr/Ca-ZSM-5 after treatment for one hour at 650 °C under 10% $H_2$ flow (bal. $N_2$). (a) Spectrum taken under static NO pressure. (b) Spectrum taken after venting NO and introducing static CO pressure. (c)-(e) spectra taken while cell was purged with $N_2$ flow. $N_2$ purge was not performed prior to CO dosing.

Isosbestic point at ca. 1795 $cm^{-1}$ in spectra (b)-(e) indicates desorption of CO restores Cr-dinitrosyl species.

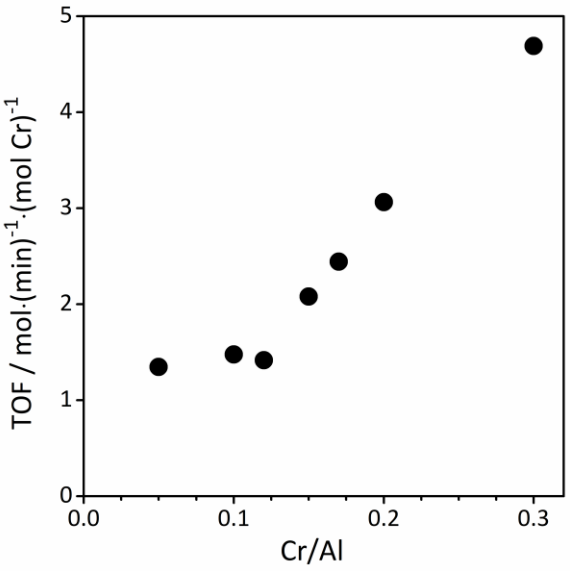


**Figure S2.15.** Turnover frequency (TOF) of ethane conversion, adjusted for contribution of acid catalysis by zeolite Brønsted acid sites. Measured ethane conversion values were adjusted by subtracting the conversion measured for an equivalent mass of blank H-ZSM-5 (0.013% conversion per mg). This adjusted conversion value was used to calculate adjusted TOF.

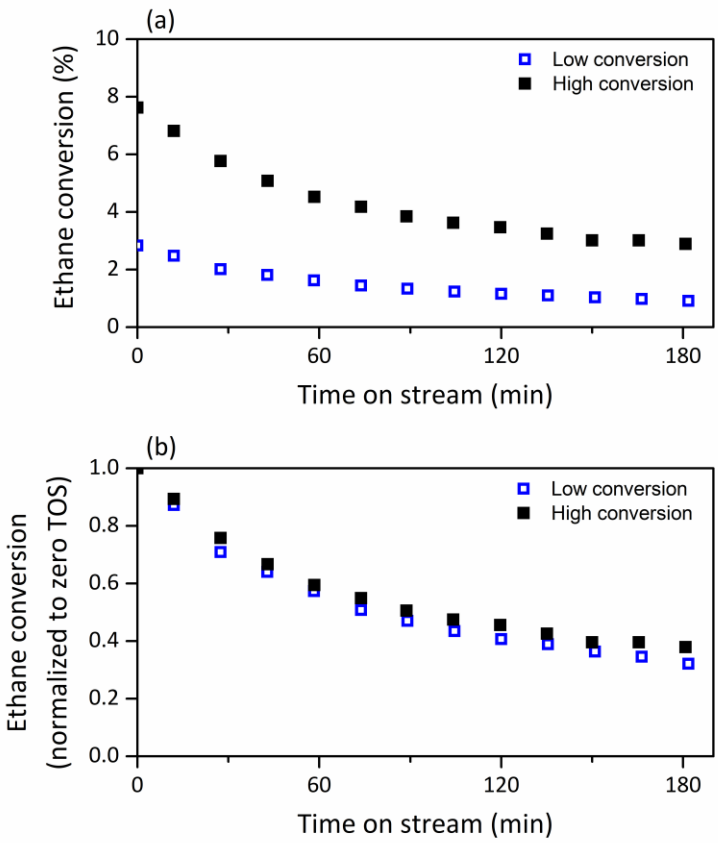


**Figure S2.16.** (a) Time on stream ethane conversion (650 °C) for 0.30 Cr/Al Cr/H-MFI. Two separate experiments were performed at different conversion, which was controlled by the mass of catalyst in the bed. (b) Time on stream ethane conversion, normalized by initial value, for the same experiments as in panel (a).

The rate of deactivation was not influenced by ethane conversion, suggesting that increasing partial pressure of products (i.e. ethylene) was not the primary cause for deactivation.

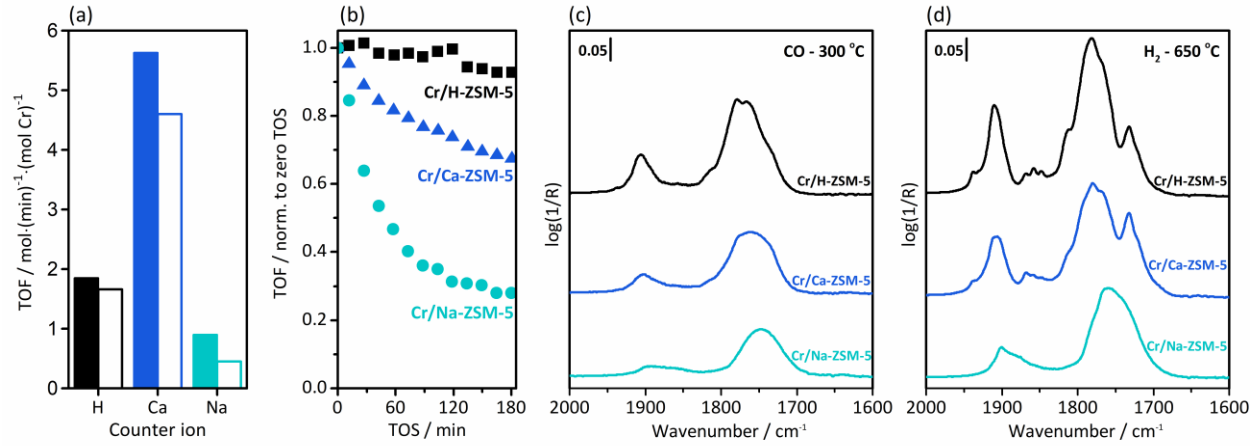


**Figure S2.17.** Comparison of 0.5 wt% Cr/H-ZSM-5, 0.5 wt% Cr/Ca-ZSM-5, and 0.5 wt% Cr/Na-ZSM-5 catalysts. (a) Rate of ethane conversion at zero time on stream (full bars) and after one hour on stream (open bars). (b) Normalized rate of ethane conversion as a function of time-on-stream. (c) FTIR spectra of NO adsorbed at 30 °C after reduction in CO at 300 °C. (d) FTIR spectra of NO adsorbed at 30 °C after reduction in $H_2$ at 650 °C.

## Supporting Tables

**Table S2.1.** Summary of surface area measurements.

| | H-ZSM-5 | 0.10 Cr/Al Cr/H-ZSM-5 - fresh | 0.10 Cr/Al Cr/H-ZSM-5 - spent | 0.20 Cr/Al Cr/H-ZSM-5 - fresh |
|---|---|---|---|---|
| BET surface area ($m^2/g$) | 420.1 | 409.6 | 474.5 | 408.8 |
| Micropore surface area ($m^2/g$) | 313.0 | 302.8 | 336.0 | 281.2 |
| External surface area ($m^2/g$) | 107.1 | 106.8 | 138.5 | 127.7 |
| Micropore volume ($cm^3/g$) | 0.128 | 0.127 | 0.136 | 0.114 |

**Table S2.2.** Summary of ethane dehydrogenation catalysis data.

| | Cat. Mass | Zero time on stream* | | | | One hour on stream* | | | |
|---|---|---|---|---|---|---|---|---|---|
| | (mg) | $X_{C2H6}$ | $S_{C2H4}$ | $S_{CH4}$ | $S_{C3}$ | $X_{C2H6}$ | $S_{C2H4}$ | $S_{CH4}$ | $S_{C3}$ |
| H-ZSM-5 | 32.0 | 0.72 | 66.8 | 21.4 | 10.8 | 0.65 | 68.3 | 8.86 | 6.39 |
| 0.10 Cr/Al Cr/Na-ZSM-5 | 22.1 | 1.16 | 99.6 | 0.44 | - | 0.57 | 99.3 | 0.75 | - |
| 0.10 Cr/Al Cr/Ca-ZSM-5 | 26.4 | 8.68 | 95.5 | 1.82 | 1.90 | 7.09 | 96.3 | 1.44 | 1.56 |
| 0.10 Cr/Al Cr/H-ZSM-5 | 26.5 | 2.81 | 94.5 | 3.04 | 2.05 | 2.59 | 94.8 | 2.94 | 1.94 |
| 0.05 Cr/Al Cr/H-ZSM-5 | 44.4 | 2.66 | 88.5 | 6.85 | 4.31 | 2.50 | 89.3 | 6.40 | 3.97 |
| 0.12 Cr/Al Cr/H-ZSM-5 | 21.4 | 2.59 | 95.7 | 2.42 | 1.55 | 2.44 | 95.8 | 2.31 | 1.48 |
| 0.15 Cr/Al Cr/H-ZSM-5 | 21.9 | 4.41 | 96.7 | 1.53 | 1.24 | 4.56 | 96.7 | 1.53 | 1.22 |
| 0.17 Cr/Al Cr/H-ZSM-5 | 14.6 | 3.57 | 97.5 | 1.03 | 0.87 | 3.54 | 97.5 | 1.02 | 0.87 |
| 0.20 Cr/Al Cr/H-ZSM-5 | 16.1 | 6.05 | 97.2 | 1.03 | 1.05 | 5.18 | 97.4 | 0.97 | 0.96 |
| 0.30 Cr/Al Cr/H-ZSM-5 | 8.8 | 7.48 | 97.3 | 0.86 | 1.05 | 4.53 | 98.6 | 0.50 | 0.40 |
| 0.30 Cr/Al Cr/H-ZSM-5 | 2.4 | 2.84 | 98.3 | 0.57 | 0.50 | 1.63 | 98.8 | 0.54 | 0.25 |

*$X_{C2H6}$ = % conversion ethane; $S_i$ = % selectivity to product(s) i
Reactor conditions: T = 650 °C; P = 3 psig; flow rates: 4 sccm ethane, 44 sccm $N_2$

**Table S2.3.** Previously reported Cr-nitrosyl band assignments.

| | Previously reported bands ($cm^{-1}$)[11, 12, 16–19] | | | | | |
|---|---|---|---|---|---|---|
| | $Cr/SiO_2$ | $Cr/Al_2O_3$ | $Cr/SiO_2$-$TiO_2$ | Cr-H-ZSM-5 | Cr/silicalite-1 | Cr/Si-Beta |
| | Ref [16] | Ref [17] | Ref [18] | Ref [11] | Ref [19] | Ref [12] |
| $\nu_s/\nu_{as}$, $Cr^{2+}(NO)_2$ | 1865/1747, 1880/1755 | 1880/1755 | 1856/1742, 1868/1736 | 1902/1768 | 1860-1875/1745 | 1883**/1755** |
| $\nu_s/\nu_{as}$, $Cr^{3+}(NO)_2$ | | 1905/1775 | 1875/1755 | 1910/1782 | | |
| $\nu_{N-O}$, $Cr^{2+/3+}$-NO | 1810-1815 | 1940, 1875, 1820 | 1807 | 1890, 1815, 1782 | 1800 | 1794 |

**Cr oxidation state unknown

**Table S2.4.** Previously reported nitrosyl and mixed-ligand band assignments for $Cr/SiO_2$.

| | Previously reported bands ($cm^{-1}$)[16, 19] | |
|---|---|---|
| | **$Cr/SiO_2$** Ref [19] | **$Cr/SiO_2$** Ref [16] |
| $Cr^{2+}(NO)_2$ | 1856/1743 | 1865/1747, 1880/1755 |
| $Cr^{2+}(NO)_3$ | 1862*/1845*/1745* | |
| $NO^{\delta+}$ in $Cr^{2+}(NO)_4$ | 1908*/1885*/1875* | |
| $NO^{\delta-}$ in $Cr^{2+}(NO)_4$ | 1725*, 1700* | |
| $Cr^{2+}(NO)_2(CO)$ | 2180†*, 2170†*, 1880*/1760* | 2179†, 1886/1760 |
| $Cr^{2+}(NO)_2$(pyridine) | | 1850/1702 |
| $Cr^{2+}(NO)$(pyridine) | | 1710, 1725 |

*adsorption at liquid nitrogen temperature
†carbonyl band

**Table S2.5.** Cr nitrosyl and carbonyl bands observed in this study.

| | Observed bands ($cm^{-1}$) | | |
|---|---|---|---|
| | **Cr/H-ZSM-5** | **Cr/Na-ZSM-5** | **Cr/Ca-ZSM-5** |
| $Cr^{2+}(NO)_2$ | 1904/1767, 1869/1732 | 1860-1880/1747 | 1904/1767, 1869/1732 |
| $Cr^{n+}(NO)_2$ | 1911/1780 | 1900/1760 | 1911/1780 |
| $Cr^{n+}$ - NO | 1789 | | 1789 |
| $Cr^{2+}(NO)_2(CO)$ | 2182†/1921/1809 | 2174†, 1912, 1804 | 2183†/1919/1813 |
| $Cr^{n+}(NO)_2(CO)$ | 2195†/1926/1821 | 1921, 1814 | 2195†/1924/1821 |
| Unassigned nitrosyl bands | 1938, 1930, 1858, 1848, 1814, 1720 | | 1803 |

†carbonyl band

## References


(1) I. V. Babich, Y. V. Plyuto, P. Van Der Voort and E. F. Vansant, J. *Colloid Interface Sci.*, **1997**, 189, 144.

(2) A. Hakuli and A. Kytökivi, *Phys. Chem. Chem. Phys.*, **1999**, 1, 1607.

(3) B. M. Weckhuysen, R. Ramachandra Rao, J. Pelgrims, R. A. Schoonheydt, P. Bodart, G. Debras, O. Collart, P. Van Der Voort and E. F. Vansant, *Chem. - Eur. J.*, **2000**, 6, 2960.

(4) B. M. Weckhuysen, I. E. Wachs and R. A. Schoonheydt, *Chem. Rev.*, **1996**, 96, 3327.

(5) B. M. Weckhuysen, B. Schoofs and R. A. Schoonheydt, *J. Chem. Soc., Faraday Trans.*, **1997**, 93, 2117.

(6) M. P. McDaniel, K. S. Collins and E. A. Benham, *J. Catal.*, **2007**, 252, 281.

(7) J. Sirita, S. Phanichphant and F. C. Meunier, *Anal. Chem.*, **2007**, 79, 3912.

(8) G. Kofke, R. J. Gorte and W. E. Farneth, *J. Catal.*, **1988**, 114, 34.

(9) A. J. Jones, R. T. Carr, S. I. Zones and E. Iglesia, *J. Catal.*, **2014**, 312, 58.

(10) O. A. Abdelrahman, K. P. Vinter, L. Ren, D. Xu, R. J. Gorte, M. Tsapatsis and P. J. Dauenhauer, *Catal. Sci. Technol.*, **2017**, 7, 3831.

(11) M. Mihaylov, A. Penkova, K. Hadjiivanov and M. Daturi, *J. Mol. Catal. A: Chem.*, **2006**, 249, 40.

(12) K. Hadjiivanov, A. Penkova, R. Kefirov, S. Dzwigaj and M. Che, *Microporous Mesoporous Mater.*, **2009**, 124, 59.

(13) J. Janas, J. Gurgul, R. P. Socha, J. Kowalska, K. Nowinska, T. Shishido, M. Che and S. Dzwigaj, *J. Phys. Chem. C*, **2009**, 113, 13273.

(14) E. Groppo, C. Lamberti, S. Bordiga, G. Spoto and A. Zecchina, *Chem. Rev.*, **2005**, 105, 115.

(15) M. Botavina, C. Barzan, A. Piovano, L. Braglia, G. Agostini, G. Martra and E. Groppo, *Catal. Sci. Technol.*, **2017**, 7, 1690.

(16) E. Garrone, G. Ghiotti, C. Morterra and A. Zecchina, *Z. Naturforsch., B: J. Chem. Sci.*, **1987**, 42, 728.

(17) J. B. Peri, *J. Phys. Chem.*, **1974**, 78, 588.

(18) S. J. Conway, J. W. Falconer and C. H. Rochester, *J. Chem. Soc., Faraday Trans.*, **1989**, 85, 79.

(19) A. Zecchina, G. Spoto, G. Ghiotti and E. Garrone, *J. Mol. Catal.*, **1994**, 86, 423.

# **Chapter 3.** Interconversion of Atomically Dispersed Platinum Cations and Platinum Clusters in Zeolite ZSM-5 and Formation of Platinum *gem*-Dicarbonyls

Adapted from publication in *Journal of the American Chemical Society*

N. Felvey, J. Guo, R. Rana, L. Xu, S. R. Bare, B. C. Gates, A. Katz, A. R. Kulkarni, R. C. Runnebaum, C. X. Kronawitter, *J. Am. Chem. Soc.*, **2022**,

DOI: 10.1021/jacs.2c05386

## 3.1 Abstract

Catalysts composed of platinum dispersed on zeolite supports are widely applied in industry, and coking and sintering of platinum during operation under reactive conditions require their oxidative regeneration, with the platinum cycling between clusters and cations. The intermediate platinum species have remained only incompletely understood. Here, we report an experimental and theoretical investigation of the structure, bonding, and local environment of cationic platinum species in zeolite ZSM-5, which are key intermediates in this cycling. Upon exposure of platinum clusters to $O_2$ at 700 °C, oxidative fragmentation occurs, and $Pt^{2+}$ ions are stabilized at six-membered rings in the zeolite that contain paired aluminum sites. When exposed to CO under mild conditions, these $Pt^{2+}$ ions form highly uniform platinum *gem*-dicarbonyls, which can be converted in $H_2$ to $Pt^{\delta+}$ monocarbonyls. This conversion, which weakens the platinum–zeolite bonding, is a first step towards platinum migration and aggregation into clusters. X-ray absorption and infrared spectra provide evidence of the reductive and oxidative transformations in various gas environments. The chemistry is general, as shown by the observation of platinum *gem*-dicarbonyls in several commercially used zeolites (ZSM-5, Beta, mordenite, and Y).

## 3.2 Introduction

Noble metals nanoparticles dispersed on oxide and zeolite supports constitute a class of robust, widely used industrial catalysts for which it is desired to stabilize small metal clusters under reactive conditions to maximize the utilization of the expensive metals.[1] Encapsulation of metals within zeolites provides opportunities to closely integrate metal functionality with zeolite surface acid sites to enable bifunctional catalytic conversions with selectivities modulated by transport limitations in the molecular-scale pores of the zeolite.[2–5] Platinum-containing zeolite catalysts are applied industrially for hydrocarbon conversions, such as naphtha upgrading,[6] and are promising candidates for conversions of biomass-derived feedstocks.[7–9] Controlling the location of highly dispersed platinum clusters within the zeolite and maintaining the desired form of platinum under reaction conditions are a continuing challenge.[10]

In hydrocarbon conversion, catalyst deactivation is typically caused by coking and loss of platinum surface area by sintering.[11] The harsh oxidative conditions required to remove coke often exacerbate the sintering, resulting in the formation of platinum nanoparticles that are too large to fit within the zeolite micropores.[12] The deactivation thus results in the loss of both activity and selectivity. The purpose of oxidative regeneration is to redisperse the platinum via cationic platinum intermediates stabilized by strong bonding to the support.[10,12,13]

Recently, X-ray absorption spectroscopy (XAS) was used to monitor the interconversion of chabazite (CHA)-supported platinum clusters and cations.[12,13] The reversibility of this transformation resulted in catalysts that maintained high platinum dispersions during the redox cycling. The stabilization of the atomically dispersed platinum under high-temperature oxidizing conditions was attributed to the strong bonding of platinum at cation exchange sites located near framework aluminum atoms, but the nature of the cationic platinum sites and their locations within the zeolite have not been identified.

The importance of framework aluminum sites in zeolites for stabilization and charge compensation of extra-framework platinum ions or partially charged clusters has been recognized,[12–15] but their influence on the state of platinum is not well understood. Much more is known regarding the bonding of cations of other metals or metal-oxo clusters at aluminum sites in zeolites; the wealth of knowledge gained through theoretical and spectroscopic characterizations of copper,[16–20] iron,[21–24] and palladium[25–27] located at zeolite aluminum sites has enabled researchers to envisage new adsorptive and catalytic processes associated with interactions between adsorbed molecules and metal ions or clusters having precisely controlled structures. Local framework structures consisting of multiple aluminum sites in close proximity to each other have been implicated in the stabilization of divalent cations or multinuclear metal-oxo clusters having unique structures.[16,20,23,28] These paired aluminum sites have thus emerged as a critical design parameter.[29,30]

Understanding of the adsorptive properties of atomically dispersed noble metals and their mobility within zeolites is essential for understanding the synthesis or oxidative redispersion of the catalysts.[14,31,32] Infrared (IR) spectra have shown how the structures of rhodium and of iridium in zeolites reversibly alternate between single-atom cationic complexes and few-atom clusters when the conditions are mild.[33–35]

The essentially molecular supported species in these catalysts have distinctive spectroscopic signatures, and, when probed with CO, the atomically dispersed species form metal *gem*-dicarbonyls, which are essential to understanding of the chemistry.[36–38] The comparable chemistry of platinum in zeolites is less well understood—even though platinum dominates as an industrial catalyst and has been the subject of extensive research to elucidate its intrazeolite chemistry.[39–44] Thus, surprisingly, characterization of well-defined structures of platinum in zeolites, such as platinum *gem*-dicarbonyls, is not well represented in the literature.

Here we report elucidation of the chemistry of platinum in widely used zeolite catalyst supports, including HZSM-5. IR and X-ray absorption spectra, bolstered by results from calculations using density functional theory (DFT), show how the chemistry of oxidative cluster fragmentation/reductive cluster formation depends on the zeolite sites for platinum bonding and how carbonyl-containing complexes of atomically dispersed platinum transform under reactive conditions.

## 3.3 Results

**Platinum-Containing HZSM-5 Samples Synthesized with Various Binding Sites in the Zeolite**

Ammonium-form ZSM-5 was supplied by Zeolyst and converted to its protonic form before use. Platinum was incorporated into HZSM-5 by conventional aqueous ion-exchange with $Pt(NH_3)_4(NO_3)_2$ (details in the Supporting Information). The zeolite composition was determined by inductively coupled plasma mass spectrometry (ICP-MS); the sample contained 0.37 wt% platinum and had an Si/Al ratio of 31 (atomic); 23% of the framework aluminum was present in pairs, as determined by the $Co^{2+}$ exchange capacity (Table 3.1).[45] The platinum loading was chosen to be relatively low to give samples with the platinum in limited numbers of sites (Pt/Al ratio = 0.04, atomic, Table 3.1) and to maximize sample uniformity and simplify the chemistry,[46] while remaining in an industrially relevant range.[47]

For comparison, a ZSM-5 sample was synthesized using published procedures to contain a low concentration of paired aluminum sites while having an Si/Al ratio (Si/Al = 25, atomic) similar to that of the commercial sample.[45] The fraction of aluminum present in pairs was estimated to be 5% by the $Co^{2+}$

exchange capacity (Table 3.1). Platinum was incorporated into this HZSM-5 sample by the same method used for the commercial HZSM-5 (details in the Supporting Information). This sample, referred to as low-pair Pt/ZSM-5, contained 0.14 wt% platinum. $N_2$ physisorption, X-ray diffraction, and ICP-MS results characterizing the platinum-containing ZSM-5 samples are shown in the Supporting Information (Figures S3.1-S3.3; Tables S3.1 and S3.2). Elemental compositions and contents of Al pairs of each of the platinum-containing zeolites investigated are shown in Table 3.1.

**Table 3.1. Elemental Analyses of Pt-containing Zeolites**

| Sample | Si/Al | wt% Pt | Pt/Al | Paired Al (%)[a] |
|---|---|---|---|---|
| Pt/ZSM-5 | 31 | 0.37 | 0.036 | 23 |
| Low-pair Pt/ZSM-5 | 25 | 0.14 | 0.011 | 4.9 |
| Pt/Beta | 21 | 0.30 | 0.021 | 94 |
| Pt/MOR | 8.3 | 0.38 | 0.011 | 35 |
| Pt/Y | 18 | 0.24 | 0.014 | 41 |

[a]Percentage of total aluminum present in pairs, estimated as the atomic ratio, 2Co/Al, measured for cobalt-exchanged zeolite samples (see Table S3.1 for details).

**Reversible Reductive Platinum Cluster Formation and Oxidative Cluster Fragmentation in HZSM-5 demonstrated by X-ray Absorption Spectroscopy (XAS).**

Pt $L_3$-edge X-ray absorption near edge spectra (XANES) were recorded as Pt/ZSM-5 (initially incorporating $[Pt(NH_3)_4]^{2+}$) was heated in flowing 20% $O_2$ in helium at a rate of 10 °C/min. An initial small decrease in white line intensity at temperatures between 300 and 400 °C was followed by an increase in intensity at temperatures > 400 °C (Figure S3.4) demonstrating oxidation of the platinum. $[Pt(NH_3)_4]^{2+}$ complexes decompose in this temperature range,[42] as made evident by the evolution of $N_2$ and $H_2O$ detected by mass spectrometry of the reactor effluent stream at temperatures between 250 and 400 °C (Figure S3.5). Separately, thermogravimetric analysis (TGA) revealed a mass loss at temperatures between 250 and 400 °C under equivalent calcination conditions (Figure S3.6). The XAS sample was held for one hour at the final calcination temperature of 700 °C before cooling back to room temperature for measurement of XANES and extended X-ray absorption fine structure (EXAFS) spectra (Figure 3.1). The white line intensity of Pt/ZSM-5 after calcination (Figure 3.1a) was similar to that of the compound $Pt(acac)_2$ (acac is acetylacetonato), which contains platinum in the +2 formal oxidation state, showing that the platinum in

the zeolite was in nearly the +2 formal oxidation state (spectra of standards shown in Figure S3.7). The Fourier-transformed EXAFS data (Figure 3.1c) are characterized by peaks in the magnitude of the Fourier-transform at 1.6 and 2.6 Å which result from platinum coordination with oxygen and Si or Al, respectively (justification for these assignments in Supporting Information). We emphasize that a meaningful fit of the EXAFS spectrum of calcined Pt/ZSM-5 could not be achieved using a model consisting of a combination of Pt–O and Pt–Pt (metallic) scattering paths (Figure S3.12), which implies the absence of a detectable Pt–Pt scattering path. We conclude that platinum was predominantly atomically dispersed and coordinated to oxygen.

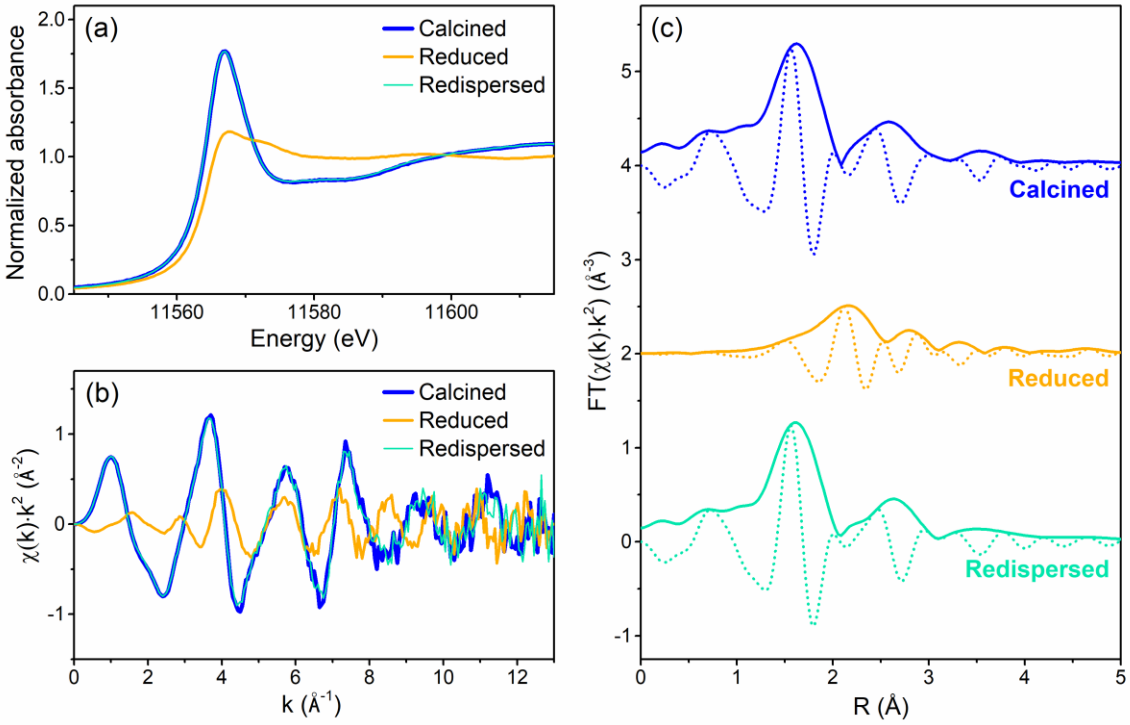


**Figure 3.1.** Redox behavior of platinum in Pt/ZSM-5: characterization by X-ray absorption spectroscopy. **(a)** Normalized XANES spectra at room temperature characterizing Pt/ZSM-5 following exposure to $O_2$ at 700 °C (calcined), $O_2$ at 700 °C then $H_2$ at 500 °C (reduced), or $O_2$ at 700 °C, then $H_2$ at 500 °C, then $O_2$ at 700 °C (redispersed). **(b)** $k^2$-Weighted EXAFS data characterizing Pt/ZSM-5 at room temperature following each of the treatments in (a). **(c)** Magnitude (solid) and imaginary component (dotted) of $k^2$-weighted Fourier-transform of EXAFS data characterizing Pt/ZSM-5 at room temperature following each of the treatments in (a).

Subsequent exposure of the sample to flowing 10% $H_2$ in helium as the temperature was ramped to 500 °C led to an expected decrease in the XANES white line intensity (Figure 3.1a) as the platinum was

reduced. After cooling the sample to room temperature, a shoulder at 11573 eV and the slightly higher edge energy with respect to the reference platinum foil (comparison shown in Figure S3.13) are consistent with the presence of hydrogen adsorbed on platinum clusters.[43,48] Following $H_2$ treatment (Figure 3.1c), the peak in the magnitude of the Fourier-transformed EXAFS between 1 and 2 Å was eliminated, and the spectrum was instead characterized by peaks between 2 and 3 Å, indicating the presence of Pt-Pt bonding and therefore of platinum clusters (fit shown in Figure S3.14).

Recalcination in 20% $O_2$ in helium at 700 °C resulted in a spectrum the same as that characterizing the original calcined sample (Figures 3.1a-3.1c). This result demonstrates cluster fragmentation and the reversibility of the redox process.

After low-pair Pt/ZSM-5 was exposed to $O_2$ at 700 °C, the room-temperature XANES spectrum (Figure S3.15) was characterized by a significantly lower white line intensity than that of Pt/ZSM-5. The XANES spectrum of low-pair Pt/ZSM-5 was well represented by a linear combination of the spectrum of calcined Pt/ZSM-5 and that of platinum foil, with a 45% contribution of the metallic platinum spectrum (Figure S3.15). Furthermore, the Fourier-transformed EXAFS spectrum of calcined low-pair Pt/ZSM-5 indicated a significant Pt–Pt scattering path (Figure S3.16). After calcined low-pair Pt/ZSM-5 was exposed to $H_2$ at 500 °C followed by $O_2$ at 700 °C, the XANES spectrum did not match that following the initial calcination, indicating the lack of reversible switching of platinum between two states when the content of paired aluminum sites was low (Figure S3.15). These results support the hypothesis that cationic platinum is preferentially stabilized at paired aluminum sites under high-temperature, oxidizing conditions. In contrast, when fewer paired aluminum sites were present to host the platinum, platinum clusters formed.

**Structural Characterization of Atomically Dispersed Platinum by Extended X-ray Absorption Fine Structure Spectroscopy.**

EXAFS spectra of Pt/ZSM-5 in flowing helium at room temperature recorded after exposure to 20% $O_2$ in helium at 700 °C were fitted with the theory-guided QuantEXAFS approach[49] using models of platinum anchored at various aluminum sites in the defect-free zeolite (details provided in Supporting Information).

Assuming the presence of divalent platinum coordinated to oxygen only and in analogy to Cu- and Pd-containing zeolites,[16,25,50] two platinum site motifs, each compensating the local negative charge of one or two aluminum sites in the support, were evaluated (denoted as 2Al–Pt and 1Al–PtOH, where Al represents a framework $[AlO_{4/2}]^-$ site and OH represents a hydroxyl coordinated to platinum). The fitting was done to identify individual structures that best represent the EXAFS data; the data represent an average of all platinum species in the zeolite, and mixtures of species are expected.

Structures of 2Al–Pt and 1Al–PtOH for all geometrically unique framework aluminum arrangements were optimized using DFT (301 total structures). From these structures, theoretical EXAFS spectra were generated. These were compared with experiment, and the quality of each fit was quantified by the r-factor (Figure 3.2a; the lower the value, the better the fit). The 118 best EXAFS fits (those giving the lowest 118 values of the r-factor) resulted from 2Al–Pt structures. Relative energies determined by DFT are plotted against the zeolite framework Al–Al distance in Figure 3.2b for all 2Al–Pt structures with relative energies ≤ 2.6 eV. The most stable 2Al–Pt structures displayed Al–Al distances of approximately 5–6 Å.

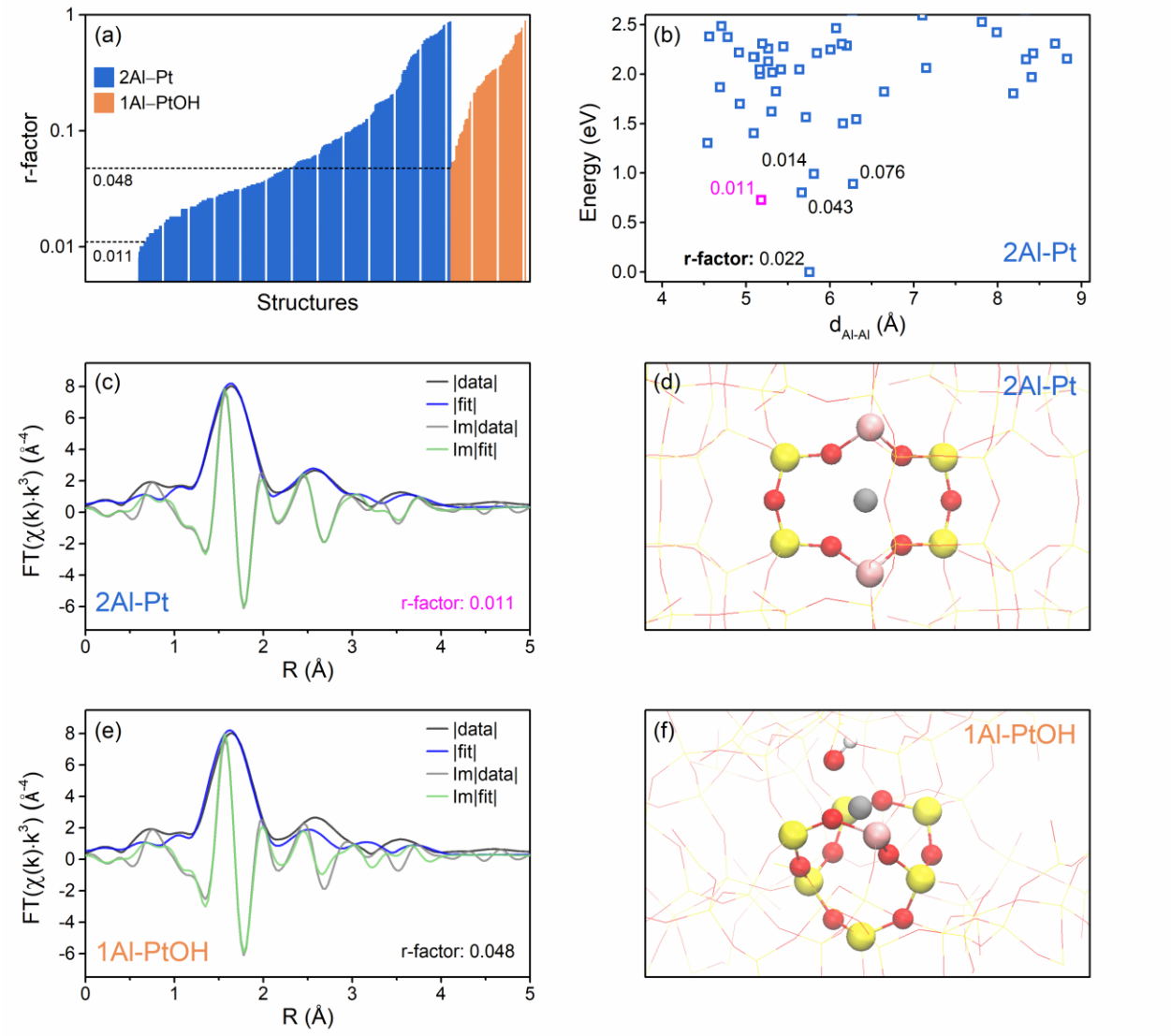


**Figure 3.2.** Local environment of platinum in Pt/ZSM-5: interpretation of EXAFS spectra. **(a)** r-factors representative of EXAFS fits of each of 301 DFT-optimized structures of 2Al–Pt and 1Al–PtOH in ZSM-5. Vertical white gridlines mark increments of 20 structures. **(b)** Dependence of relative energy on zeolite Al–Al distance of 2Al–Pt structures with relative energies ≤ 2.6 eV. Labeled in magenta is the structural model of (c) and (d). **(c)** Magnitudes (fit, blue; experiment, black) and imaginary parts (fit, green; experiment, gray) of Fourier-transformed EXAFS of Pt/ZSM-5 after exposure to $O_2$ at 700 °C with fitting based on a 2Al–Pt structure. **(d)** Visual representation of the 2Al–Pt structure corresponding to fit shown in (c). Red, O; yellow, Si; pink, Al; gray, Pt; white, H. **(e)** Same as (c), except with fitting based on the lowest r-factor 1Al–PtOH structure. **(f)** Visual representation of the 1Al–PtOH structure from (e).

Considering both the relative energies determined with DFT and the quality of the EXAFS fits, we conclude that the preferred structural model consists of platinum coordinated to four oxygen atoms of a six-membered ring (6-MR) that contains two next-next-nearest neighbor aluminum atoms (Figure 3.2d). The theoretical Fourier-transformed EXAFS spectrum of this structure closely matches the experimental

spectrum characterizing calcined Pt/ZSM-5 (Figure 3.2c). Labeled in magenta in Figure 3.2b, this structure had the second lowest energy of all 2Al–Pt structures found. The lowest-energy structure in Figure 3.2b also includes platinum at a 6-MR paired aluminum site, but this structure is rejected as unlikely because access to the site is restricted by 5-MR openings, which platinum is not known to penetrate. Structures and EXAFS fitting of the other four lowest-relative-energy models in Figure 3.2b are shown in Figures S3.17-S3.20. The location of platinum in the preferred model of Figure 3.2d, in contrast, is accessible from the pore intersection of HZSM-5. Preference for this type of 6-MR binding site, in which the divalent cation is coordinated to support oxygen atoms only, has been shown for Co, Fe, Cu, and Pd.[21–24,51–54] Notwithstanding the good fit of the data to this model, we recognize that it is oversimplifying matters to represent the supported platinum as a single species (vide infra).

The EXAFS spectra generated using 1Al–PtOH structural models did not represent the experimental results nearly as well as those of the 2Al–Pt models (Figure 3.2a). The best-fitting 1Al–PtOH structure also contained platinum coordinated to four oxygen atoms, but with one of the oxygen atoms belonging to an extra-framework hydroxyl ligand on platinum (Figure 3.2f). Nevertheless, the region in the Fourier-transformed EXAFS spectrum at approximately 1–2 Å, representative of Pt–O bonding, fits the experimental results quite well (Figure 3.2e). The region at distances > 2 Å, however, which reflects the presence of Si, Al, and O atoms at greater distances from platinum, does not.

**Formation of Platinum *gem*-Dicarbonyls and Bonding of Atomically Dispersed Platinum to Zeolite.** Further evidence of the atomically dispersed platinum in the zeolite was provided by IR spectra collected at 30 °C after exposure of Pt/ZSM-5 which had been calcined at 700 °C to flowing 10% CO in $N_2$ at 30 °C and ambient pressure for 15 min (Figure 3.3a). Two strong $\nu_{co}$ bands characterized the calcined samples, at 2173 and 2207 $cm^{-1}$; these represent CO bonded to cationic platinum in platinum *gem*-dicarbonyls.[27,55,56] This assignment is supported by results of experiments with isotopically labeled CO. Spectra recorded at 30 °C after exposure of calcined Pt/ZSM-5 to flowing 10% $^{13}CO$ in $N_2$ at 30 °C and ambient pressure for 15 min led to the appearance of $\nu_{co}$ bands at 2156 and 2123 $cm^{-1}$, with the differences in frequency of the

samples incorporating $^{13}CO$ and $^{12}CO$ being consistent with the harmonic approximation (Figure 3.3b). The spectrum collected after exposure of calcined Pt/ZSM-5 to an equimolar mixture of $^{12}CO$ and $^{13}CO$ (Figure 3.3d) at 30 °C includes all the $\nu_{co}$ bands observed during adsorption of either $^{12}CO$ or $^{13}CO$ alone (Figures 3.3a and 3.3b, respectively), plus two additional bands, at 2196 and 2134 $cm^{-1}$ (a 1:1 linear combination of the spectra of Figures 3.3a and 3.3b, which would be expected for the existence of only platinum monocarbonyls, is presented in Figure 3.3c as a further comparison). These latter two bands confirm the presence of platinum *gem*-dicarbonyls and are assigned to the antisymmetric and symmetric $\nu_{co}$ bands of mixed, $^{12}CO$–$^{13}CO$ platinum *gem*-dicarbonyls.[38] The frequencies match those estimated by the group of Hadjiivanov,[55] and the relative intensities are consistent with the 1:2:1 ratio of $Pt(^{12}CO)_2$:$Pt(^{12}CO)(^{13}CO)$:$Pt(^{13}CO)_2$ expected for an equimolar mixture of adsorbed $^{12}CO$ and $^{13}CO$.

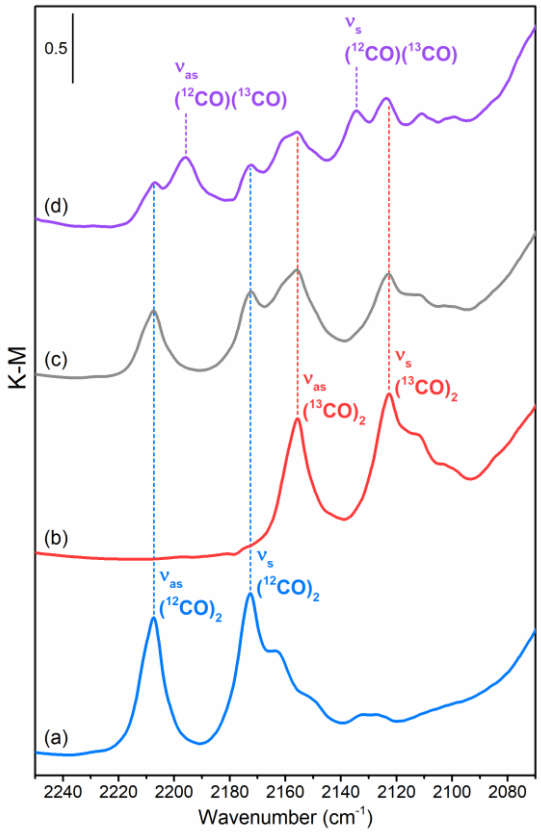


**Figure 3.3.** Identification of zeolite-supported platinum *gem*-dicarbonyls by IR spectroscopy. **(a)** Spectrum of calcined Pt/ZSM-5 after exposure to $^{12}CO$ at room temperature. **(b)** Spectrum of calcined Pt/ZSM-5 after exposure to $^{13}CO$ at room temperature. **(c)** Linear combination (1:1) of spectra in (a) and (b). **(d)** Spectrum of calcined Pt/ZSM-5 after exposure to an equimolar mixture of $^{12}CO$ and $^{13}CO$ at room temperature.

The $\nu_{co}$ bands are narrow (typical full width at half maximum (fwhm) of band at 2207 $cm^{-1}$ = 9.8 $cm^{-1}$) indicating highly uniform supported metal species.[57] This value of the fwhm is comparable to that reported for a $\nu_{co}$ band associated with atomically dispersed platinum on $TiO_2$, whereby the sharpness of the band was taken as an indication of the bonding of platinum at a single surface site on $TiO_2$.[58,59] Considering the crystalline nature of the zeolite, the small fwhm values of the $\nu_{co}$ bands observed for Pt/ZSM-5 likely reflect the location of platinum predominantly at structurally uniform binding sites, such as the one depicted in Figure 3.2d, after calcination. However, examination of the $\nu_{co}$ band at 2207 $cm^{-1}$ reveals that the band is composed of several, overlapping bands at slightly different frequencies (Figure S3.21), indicating the existence of multiple surface binding sites for platinum, consistent with the results of Figures 3.2a and 3.2b.

Shoulders at 2162 and 2150 $cm^{-1}$ (Figure 3.2a) show that minor platinum species were present with the platinum *gem*-dicarbonyls. These bands have not been previously observed in the spectra of similar samples, and they are tentatively assigned to monocarbonyl species formed from atomically dispersed platinum ions (such as 1Al–PtOH) or $PtO_x$ species.[44]

IR spectra of Pt/ZSM-5 with adsorbed CO also provided evidence of reversible reductive cluster formation and oxidative redispersion (Figure S3.22). Exposure of calcined Pt/ZSM-5 to $H_2$ at 500 °C, followed by probing with CO at 30 °C, gave rise to an intense, broad absorbance between 2050 and 2100 $cm^{-1}$, indicative of CO adsorbed linearly on metallic platinum nanoparticles.[56,60] Exposure of calcined Pt/ZSM-5 to $H_2$ at 500 °C and then $O_2$ at 700 °C, followed by probing with CO at 30 °C, resulted in an IR spectrum similar to that of the initially calcined sample. These results demonstrate that cationic platinum species were reformed from platinum nanoparticles, consistent with the XAS results in Figure 3.1 and with an oxidative fragmentation process like those reported for supported noble metals other than platinum.[33–35]

**Conversion of $Pt^{2+}$ to $Pt^{\delta+}$.**

To characterize the reduction of the $Pt^{2+}$ in platinum *gem*-dicarbonyls, IR spectra of the samples in flowing 10% $H_2$ in $N_2$ were recorded as the temperature was ramped from 30 to 120 °C (Figure 3.4a). Bands in the

$\nu_{co}$ region at 2207, 2173, and 2162 $cm^{-1}$ decreased in intensity, accompanied by the growth of a single, strong band at 2124 $cm^{-1}$, which did not change at 120 °C whether or not $H_2$ was present. The intensities of the 2207 and 2173 $cm^{-1}$ bands decreased proportionally to one another (Figure S3.23), as expected, as they represent the same platinum *gem*-dicarbonyl complex. The band at 2124 $cm^{-1}$ increased linearly in intensity with the decrease in intensity of each of the dicarbonyl bands, but not with the decrease in intensity of the band at 2162 $cm^{-1}$. These results suggest that platinum dicarbonyls were converted to a monocarbonyl species characterized by a band at 2124 $cm^{-1}$. The 2124 $cm^{-1}$ band remained after the sample had been cooled to 30 °C in flowing $N_2$, only shifting to 2125 $cm^{-1}$ during cooling. Re-exposure to CO (Figure 3.4b) after cooling did not cause the reappearance of the platinum *gem*-dicarbonyl bands at 2207 and 2173 $cm^{-1}$.

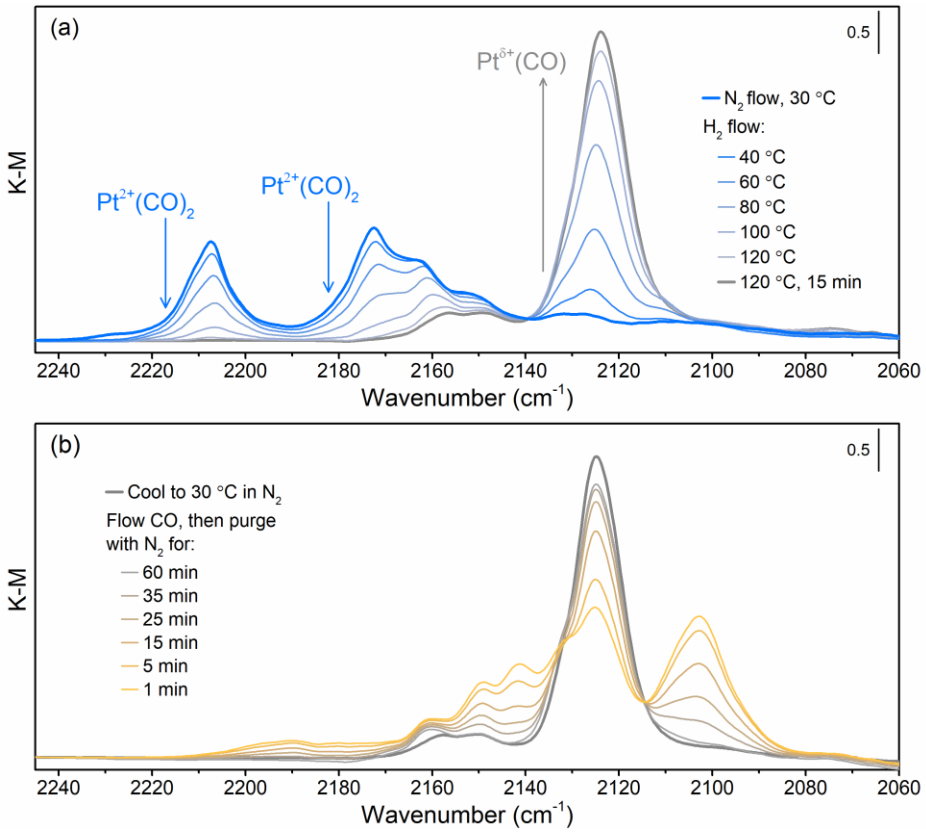


**Figure 3.4. (a)** IR spectra of CO adsorbed on calcined Pt/ZSM-5 in the presence of $N_2$ at 30 °C, during subsequent temperature ramp at 5 °C/min to 120 °C with sample in flowing $H_2$, and after holding for 15 min with sample in flowing $H_2$ at 120 °C. **(b)** IR spectra of Pt/ZSM-5 following the treatments described in (a): Spectra collected after cooling to 30 °C with sample in flowing $N_2$ and after exposure to flowing CO for 10 min and purging with $N_2$ for 1 min, 5 min, 15 min, 25 min, and 60 min.

Upon re-exposure of Pt/ZSM-5 to CO at 30 °C, the intensity of the band at 2125 $cm^{-1}$ decreased sharply as bands appeared at 2103, 2134, 2141, 2149, and 2162 $cm^{-1}$. During subsequent exposure to flowing $N_2$, the bands at 2103, 2141, and 2149 $cm^{-1}$ disappeared and that at 2125 $cm^{-1}$ reappeared. These changes are consistent with the adsorption and desorption of additional CO molecules on the atomically dispersed platinum, the monocarbonyl structure of which is characterized by the 2125 $cm^{-1}$ band. Previous researchers assigned bands near this frequency to CO on nearly charge-neutral $Pt^{\delta+}$.[15,56,61–63] The spectra of Figure 3.4b give evidence of an isosbestic point at 2114 $cm^{-1}$ during desorption of CO, supporting the assignment of the band at 2103 $cm^{-1}$ to a $Pt^{\delta+}$ multi-carbonyl complex that decomposes to a $Pt^{\delta+}$ monocarbonyl (band at 2125 $cm^{-1}$). The position of the 2103 $cm^{-1}$ band was found not to be coverage-dependent, implying that it should not be assigned to CO adsorbed on platinum nanoparticles, for which dipolar coupling between adsorbed CO molecules would cause shifts of the frequency of the $\nu_{co}$ band of linearly adsorbed CO during desorption.[64] Also evident is a shoulder at 2108 $cm^{-1}$, suggesting the presence of multiple types of $Pt^{\delta+}$ carbonyl complexes. The appearance of bands at 2142 and 2149 $cm^{-1}$ which, upon purging of CO, decayed in concert with the bands at 2103 and 2108 $cm^{-1}$, supports this claim. Experiments with mixtures of $^{12}CO$ and $^{13}CO$ did not further resolve these complex matters because of the number and overlap of the carbonyl bands.

**Structural Evidence from Zeolite Framework Vibrations.**

Further structural information emerged from IR data showing changes in the region of framework T–O–T stretching vibrations (T is Si or Al) during the treatments described in the caption of Figure 3.4. The perturbation of T–O–T bonds by incorporation of metal ions in a zeolite causes T–O–T stretching frequencies to decrease from near 1100 $cm^{-1}$ to 850–1000 $cm^{-1}$.[65,66] The band locations have been used to identify the metals and to monitor changes in their coordination and oxidation states.[24,53,72,73,54,65–71] When calcined Pt/ZSM-5 was exposed to CO, a loss in intensity centered at 926 $cm^{-1}$ was observed (Figure S3.24), signifying that bonding of CO to $Pt^{2+}$ caused a relaxation of the zeolite ring distortion—that is, platinum relaxed from the surface during formation of the platinum *gem*-dicarbonyl. During subsequent heating of

this sample in flowing 10% $H_2$ in $N_2$ at 120 °C, a band appeared at 950 $cm^{-1}$, indicating that the conversion of $Pt^{2+}(CO)_2$ to $Pt^{\delta+}(CO)$ was accompanied by a reappearance of a close interaction between platinum and the zeolite framework. The shift in the T–O–T distortion band from 926 to 950 $cm^{-1}$ (i.e., towards the unperturbed band) indicates that $Pt^{\delta+}$ monocarbonyl complexes distorted the framework less than $Pt^{2+}$ present after calcination (in the absence of CO), indicating their weaker interaction with the framework than that of bare $Pt^{2+}$. In addition, a band at 907 $cm^{-1}$ appeared, which might indicate that a fraction of platinum retained strong bonding to the zeolite framework. Alternatively, a band near this frequency has been previously assigned to the $\delta_{OH}$ mode of $Cu^{2+}(OH)$ species in zeolite CHA, and so the band at 907 $cm^{-1}$ might be attributed to such a model.[74]

**Probing the Cationic Platinum Sites with Low-Molecular-Weight Adsorbates.**

Additional experiments were done to probe the properties of $Pt^{\delta+}$ with low-molecular-weight adsorbates. The experiments involved $Pt^{\delta+}$ with adsorbed CO, so that the carbonyl band could be used to track changes in the platinum. First, to evaluate the activity of $Pt^{\delta+}$ for CO oxidation catalysis, a Pt/ZSM-5 sample containing $Pt^{\delta+}$ (synthesized by the procedures described in the caption of Figure 3.4a) was exposed to flowing $O_2$ as the temperature was increased (Figure 3.5a). The intensity of the 2125 $cm^{-1}$ band decreased only after the temperature reached 300 °C, and the band was almost completely eliminated at 350 °C. We infer that CO either desorbed or was converted to $CO_2$ at temperatures above 250 °C, but no evidence of $CO_2$ formation was observed by IR spectroscopy, perhaps because the concentration of $CO_2$ in the gas phase was too low to detect.

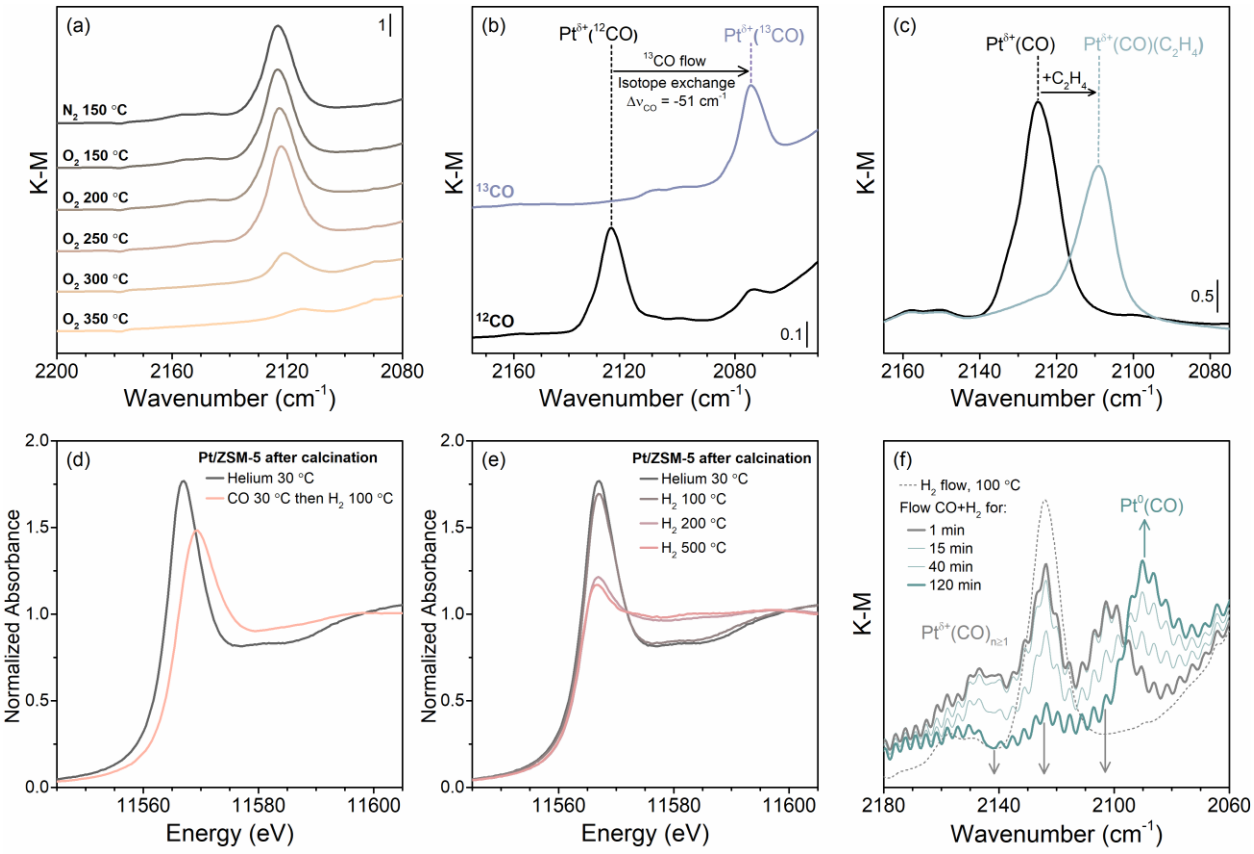


**Figure 3.5.** Characterization of $Pt^{\delta+}$ by IR spectroscopy and XAS. **(a)** IR spectra of Pt/ZSM-5 containing $Pt^{\delta+}$–(CO) in flowing $N_2$ at 150 °C and subsequent exposure to flowing $O_2$ at increasing temperatures. **(b)** IR spectra of $Pt^{\delta+}$–($^{12}$CO) in Pt/ZSM-5 at room temperature (black) and after subsequent exposure to $^{13}$CO flowing at room temperature for 10 min and $N_2$ flowing for 30 min (purple). **(c)** IR spectra of $Pt^{\delta+}$–($^{12}$CO) in Pt/ZSM-5 at room temperature in flowing $N_2$ (black) and after exposure to a subsequent dose of $C_2H_4$ into the IR cell (blue). **(d)** XANES spectra of Pt/ZSM-5 collected with the sample in flowing helium at room temperature after calcination (gray) or, alternatively, after calcination followed by exposure to CO at room temperature and then exposure to $H_2$ at 100 °C (orange). **(e)** XANES spectra of calcined Pt/ZSM-5 collected with the sample in helium at room temperature or during exposure to flowing 10% $H_2$ at 100, 200, or 500 °C. **(f)** IR spectra of Pt/ZSM-5 containing $Pt^{\delta+}$–(CO) during exposure to flowing $H_2$ at 100 °C or during subsequent exposure to flowing 10% $H_2$ and 10% CO for 120 min.

Figure 3.5b displays evidence of rapid ligand exchange of isotopically labeled CO on $Pt^{\delta+}$ at 30 °C, consistent with results of Figure 3.4b showing that $Pt^{\delta+}$ can bind multiple CO ligands. In contrast, platinum *gem*-dicarbonyls did not exchange CO to a similar extent under these conditions (Figure S3.25).

Complementary experiments were performed with another small probe molecule, ethylene. The data of Figure 3.5c, indicating a shift of the 2125 $cm^{-1}$ band in response to $C_2H_4$ exposure, show that $Pt^{\delta+}$ adsorbed $C_2H_4$ and CO simultaneously.[27,75,76] The 2125 $cm^{-1}$ band of $Pt^{\delta+}$ carbonyl was reformed when the

sample was heated to 160 °C in flowing $H_2$ (Figure S3.26), demonstrating the reversibility of the $Pt^{\delta+}$–$C_2H_4$ interaction.

The conversion of platinum *gem*-dicarbonyls to $Pt^{\delta+}$ carbonyls was also interrogated with XAS (Figure 3.5d) under conditions matching those of the IR experiment showing a single platinum carbonyl band, at 2125 $cm^{-1}$ (Figure 3.4). XANES spectra were collected after exposure of Pt/ZSM-5 to $O_2$ at 700 °C and after subsequent exposure to CO at room temperature and flowing $H_2$ at 100 °C. Following CO exposure and heating in $H_2$, the white line intensity was lower than that of the calcined sample but higher than that of platinum foil and of Pt/ZSM-5 exposed to $H_2$ at 500 °C. This comparison implies that platinum, on average, remained mainly cationic under conditions in which $Pt^{\delta+}$ carbonyls were observed by IR spectroscopy, consistent with the high $\nu_{co}$ value (2125 $cm^{-1}$).

In the absence of CO (Figure 3.5e), exposure of calcined Pt/ZSM-5 to $H_2$ at 100 °C had little influence on the XANES spectrum. However, the white line intensity decreased substantially as the temperature was raised to 200 °C, as platinum was reduced to metallic nanoparticles. Only a slight change in the XANES was observed at temperatures between 200 and 500 °C.

The conversion of $Pt^{\delta+}$ carbonyls to platinum nanoparticles was monitored by IR spectroscopy with CO as a probe (Figure 3.5f). After formation of $Pt^{\delta+}$–(CO), the band at 2125 $cm^{-1}$ was stable with the sample in flowing 10% $H_2$ in $N_2$. CO was then added to the feed stream, and IR spectra were collected periodically at 100 °C with the sample in flowing 10% CO and 10% $H_2$ in $N_2$. Within 1 min of adding CO to the feed, the $Pt^{\delta+}$ monocarbonyl band intensity decreased, and $Pt^{\delta+}$ multiple-carbonyl bands, at about 2103 and 2140–2150 $cm^{-1}$, were observed in addition to gas-phase CO bands. Gradually, all the $Pt^{\delta+}$ carbonyl bands decreased in intensity and were replaced by a single absorbance centered at 2086 $cm^{-1}$, assigned to CO adsorbed on metallic platinum nanoparticles.[56,60] The results of this experiment demonstrate the enhanced mobility of $Pt^{\delta+}$ multiple-carbonyls relative to platinum monocarbonyls, resulting in the facile conversion of $Pt^{\delta+}$ to $Pt^0$ nanoparticles. These results are broadly consistent with observations of cluster formation from other noble metals in zeolites.[77]

**Pt(II) *gem*-Dicarbonyls Stabilized in Zeolites Other Than HZSM-5.**

To demonstrate the generality of the above results, experiments were carried out with zeolites other than ZSM-5. Platinum was incorporated into protonic forms of zeolites Y (Zeolyst; Si/Al = 18), mordenite (Zeolyst; Si/Al = 8.3), and Beta (Zeolyst; Si/Al = 21) using the procedures described for Pt/ZSM-5. Figure 3.6 shows IR spectra of these Pt/zeolite samples after exposure to $O_2$ at 700 °C (600 °C for Pt/Beta zeolite) and CO at 30 °C. The dominant carbonyl bands characterizing each sample closely resemble the 2173 and 2207 $cm^{-1}$ bands characteristic of platinum *gem*-dicarbonyls in ZSM-5, implying a generality of the chemistry of zeolite-supported platinum carbonyl complexes. Small differences in the symmetric and antisymmetric stretching frequencies from zeolite to zeolite were observed, as well as variations in the peak widths and the appearance of shoulders. Notably, carbonyl bands were broader for Pt/Beta zeolite (fwhm = 12–16 $cm^{-1}$) and sharper for Pt/Y zeolite (fwhm = 5.2, 5.8 $cm^{-1}$). The fwhm of the platinum *gem*-dicarbonyl bands observed for Pt/Y zeolite are the lowest known to the authors for supported platinum carbonyls, implying an unusually high degree of uniformity comparable to those reported for *gem*-dicarbonyls of rhodium and of iridium supported on Y zeolite.[36–38] This result is an indication of the uniformity of binding sites on the surfaces of zeolites. Also observed for each sample was a loss of intensity between 910 and 935 $cm^{-1}$, evidence of distortion of zeolite six-membered rings by divalent cations.[24,53,72,54,65–71]

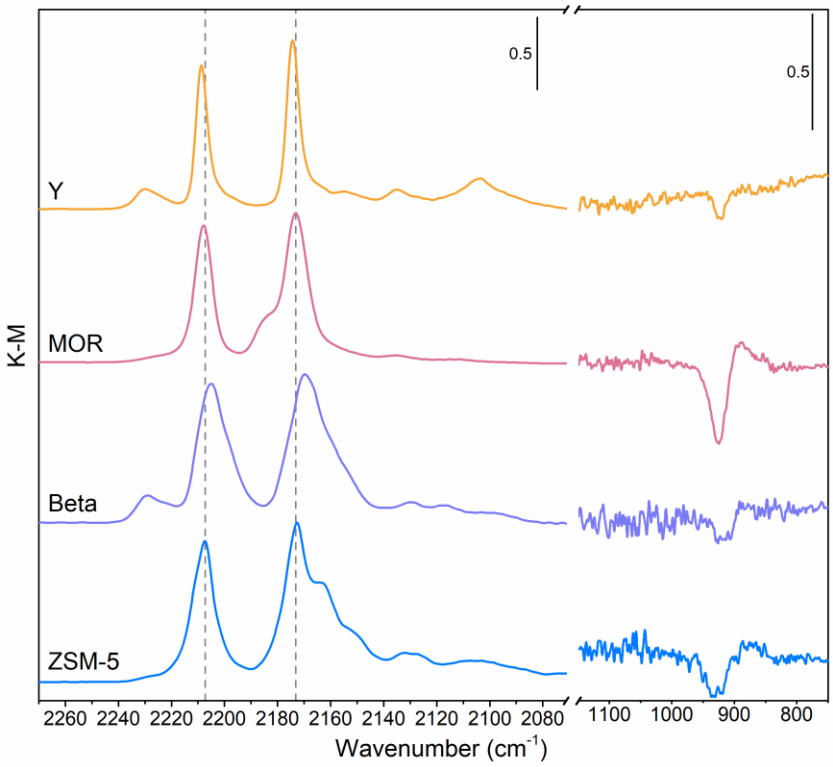


**Figure 3.6.** IR difference spectra recorded before and after CO adsorption at 30 °C on Pt/Y zeolite (Y; Si/Al = 18), Pt/mordenite (MOR; Si/Al = 8.3), Pt/Beta zeolite (Beta; Si/Al = 21), and Pt/ZSM-5 (ZSM-5; Si/Al = 25) after calcination in 20% $O_2$ in $N_2$ at 700 °C (600 °C for Pt/Beta zeolite). For comparison, data to the left of the break are normalized to the intensity of the peak at approximately 2207 $cm^{-1}$. The other data are not normalized.

## 3.4 Discussion

**Reversible Transformation of Platinum Clusters and Cationic Complexes in HZSM-5.**

Our results demonstrate the formation of atomically dispersed platinum ions in HZSM-5 during exposure to $O_2$ at 700 °C, conversion of these cations to metallic platinum clusters during exposure to $H_2$ at 500 °C, and redispersion of platinum clusters to atomically dispersed platinum ions during exposure to $O_2$ at 700 °C. These results are broadly similar to those reported by Moliner, Serna, Corma, and coworkers,[13] who proposed that the interconversion of platinum clusters and atomically dispersed platinum cations in the zeolite CHA requires strong binding sites for stabilization of platinum ions during calcination. They found that CHA had sufficient sites, whereas, in contrast, HZSM-5 did not. These authors did not report results characterizing Pt/ZSM-5 directly following calcination in $O_2$. Thus, our results characterizing Pt/ZSM-5

directly following exposure to $O_2$ at 700 °C are distinct from, although not inconsistent with, the results of these authors.

To understand how HZSM-5 facilitated this reversible redox process, it was essential to determine the sites that stabilize cationic platinum under high-temperature oxidizing conditions.

**Stabilization of $Pt^{2+}$ at Paired Aluminum Sites Under High-Temperature Oxidizing Conditions.**

Cationic platinum carbonyls have been observed in zeolites, but the copresence of multiple forms of platinum has precluded resolution of individual species by the techniques that have been applied, predominantly IR spectroscopy of adsorbed CO.[15,44,82,83,55,56,61,62,78–81] Atomically dispersed platinum in zeolites has been characterized by XAS,[12,13,39,83–86] but not with complementary characterization of the speciation of platinum amongst various surface sites. The combination of techniques presented here has provided structural information, enabling a markedly broader interpretation of the platinum chemistry in the zeolite.

Our sample is unique in that, after exposure to $O_2$ at 700 °C, it contained a high proportion of a single, isolated platinum species, characterized by $\nu_{co}$ bands at 2173 and 2207 $cm^{-1}$ (Figure 3.3a). The clear resolution of these IR bands (bolstered by the results of isotopic labeling experiments) enabled their assignment as symmetric and antisymmetric stretching vibrations, respectively, of platinum *gem*-dicarbonyls. The high degree of structural uniformity of platinum indicated by the small fwhm values characterizing the $\nu_{co}$ bands implies that platinum was stabilized at well-defined binding sites on the surface of HZSM-5. A central result is that, along with evidence from the IR region of framework T–O–T stretching vibrations indicating the presence of platinum at unique 6-MR sites in HZSM-5 (Figure S3.24), the IR data support the postulate of unique, individual structures inferred in the fitting of the EXAFS results.

Structures evaluated by DFT guiding the EXAFS fitting were limited to two structural motifs of divalent platinum, which are differentiated by the compensation by platinum of the local negative charge of either one (1Al–PtOH) or two (2Al–Pt) aluminum sites in the HZSM-5 framework, as described in the Results section. For each structural motif, an ensemble of platinum-containing structures was generated

that included all possible geometrically unique combinations of one or two aluminum sites in the HZSM-5 structure.

The data of Figure 3.2a show that, overall, theoretical EXAFS spectra representing the 2Al–Pt models account for the EXAFS data markedly better than those of 1Al–PtOH models. Comparing Figures 3.2c and 3.2e, we see that most of the difference in the EXAFS spectra of the 2Al–Pt and 1Al–PtOH structures shown is evident in the 2–3 Å region. This point highlights the importance of fitting second-shell contributions in order to distinguish these atomically dispersed species by EXAFS spectroscopy.[87]

Figure 3.2b reflects the variety of 2Al–Pt structures possible in ZSM-5; several of the lowest-energy structures (E < 1.0 eV) result in theoretical EXAFS spectra that fit the data quite well. Strikingly, the most stable structures consistently feature platinum coordinated to four oxygen atoms of a 6-MR that includes two next-next-nearest neighbor (paired) aluminum sites (Figures S3.17-S3.20). This configuration of paired framework aluminum atoms has been implicated in the stabilization of numerous divalent metal ions in zeolites,[16,21,22,24–27,52,88,89] and the EXAFS and DFT results reported here suggest these sites to be the most likely location for stabilization of platinum in HZSM-5 during calcination in $O_2$ at 700 °C. This statement does not rule out the possibility of other forms of cationic platinum; a mixture of platinum species would explain the minority platinum monocarbonyl species observed after calcination (Figure 3.3a).

The observation of similar platinum *gem*-dicarbonyl species in zeolites HZSM-5, Y, Beta, and mordenite suggests that these zeolites share a common binding site capable of accommodating platinum in a similar coordination. Each of the frameworks contains 6-MR paired aluminum sites that are known to stabilize divalent metals,[89,90] and the T–O–T stretching vibrations observed at 910–935 $cm^{-1}$ for each of these platinum-containing zeolites provide evidence of the location of platinum at these sites.[65] Indeed, precedent for this behavior of zeolite-supported platinum is provided by the X-ray diffraction results of Gallezot *et al.*[91] showing that platinum populated 6-MR sites in the sodalite cages of zeolite Y following thermal treatment in $O_2$.

Framework defect sites might be expected to stabilize platinum ions, but the low fwhm values of the $\nu_{co}$ bands (Figure 3.6) imply that these cations were in nearly equivalent sites and thus that framework

defect sites were not involved in stabilizing the platinum *gem*-dicarbonyls. The results thus imply that the oxidative fragmentation of platinum clusters in Pt/ZSM-5 during calcination in $O_2$ is facilitated by paired aluminum 6-MR sites in the zeolite framework and that the location of platinum ions is largely directed by these sites, the concentration and location of which can be tuned synthetically.[45,92] This inference suggests the possibility of designing catalysts with controlled platinum siting following catalyst regeneration in $O_2$, and the similarity of the platinum ions formed in various zeolites during calcination in $O_2$ at 700 °C highlights the generality of this design parameter. The oxidative fragmentation of platinum clusters is a complicated process involving multiple zeolite properties, and the chemistry is not yet fully resolved; our results are a start toward such a resolution.

**Identification of Multiple Cationic Platinum Species ($Pt^{2+}$ and $Pt^{\delta+}$).**

The results presented here characterize two distinct species of cationic platinum that display distinct properties. Each cationic platinum species bonds to multiple CO molecules, but the platinum *gem*-dicarbonyl is stable in the absence of gas-phase CO, whereas the $Pt^{\delta+}$ dicarbonyl has lost one of the original CO ligands. The weak binding of the second CO molecule enables $Pt^{\delta+}$ to carry out rapid exchange of isotopically labeled CO, yet the platinum monocarbonyl is particularly stable: $Pt^{\delta+}$ retains CO at 120 °C in flowing $H_2$ (Figure 3.4b) and at 250 °C in flowing $O_2$ (Figure 3.5a).

The adsorptive-reactive properties of platinum are evidently influenced strongly by its coordination to the zeolite framework. The T–O–T stretching vibration at 926 $cm^{-1}$ associated with $Pt^{2+}$ indicates the interaction of $Pt^{2+}$ with paired aluminum 6-MR sites, and the band at 950 $cm^{-1}$ observed for $Pt^{\delta+}$ (Figure S3.24) is consistent with $Pt^{\delta+}$ interacting with a single aluminum only.[68,93] The weaker interaction with the framework is consistent with the higher degree of lability of $Pt^{\delta+}(CO)$ than of $Pt^{2+}(CO)_2$.

Heterolytic $H_2$ activation by atomically dispersed platinum supported on zeolite Y was reported recently.[39] We might suggest that $Pt^{\delta+}(CO)$ is a product of $H_2$ activation by $Pt^{2+}(CO)_2$, but this suggestion is tentative; a $\nu_{CO}$ band near 2125 $cm^{-1}$ was observed when calcined Pt/ZSM-5 was exposed to CO in the presence of adventitious moisture (Figure S3.27), and so $Pt^{\delta+}(CO)$ might instead be platinum with co-

adsorbed CO and $H_2O$. In either case, platinum would be coordinated to a ligand other than CO. Similar results were reported for $Pd^{2+}$ in CHA, as a $\nu_{co}$ band assigned to $Pd^{2+}(CO)(OH)$ at 2146 $cm^{-1}$ was redshifted 67 and 47 $cm^{-1}$ from those of $Pd^{2+}(CO)_2$ at 2213 and 2193 $cm^{-1}$.[27] In the present case, the $\nu_{co}$ band of $Pt^{\delta+}(CO)$ at 2125 $cm^{-1}$ was redshifted 82 and 48 $cm^{-1}$ from those of $Pt^{2+}(CO)_2$ at 2207 and 2173 $cm^{-1}$.

We could suggest that one aluminum site might be protonated by reaction with $H_2$ or $H_2O$, facilitating a shift of $Pt^{\delta+}$ towards the neighboring aluminum site:

$$(AlO_2)_2Pt^{2+}(CO)_2 + XH \rightarrow (AlO_2)H + (AlO_2)Pt^{\delta+}(X)(CO) + CO$$

(where X = OH or H).

Protonation of an aluminum site is consistent with heterolytic $H_2$ activation and with the changes in platinum siting indicated by the T–O–T stretching vibrations, and it would not require a change in the formal oxidation state of platinum. Correspondingly, the XANES results of Figure 3.5d show that platinum remained cationic during exposure of $Pt^{2+}(CO)_2$ to flowing $H_2$ at 100 °C, notwithstanding significant changes in the spectrum that are consistent with changes in the platinum ligation. The considerable decrease in $\nu_{co}$ when $Pt^{2+}(CO)_2$ was converted to $Pt^{\delta+}(CO)$ indicates a higher degree of electron donation from platinum to CO, but the formal oxidation state of platinum remains ambiguous (but the $\nu_{co}$ value of 2125 $cm^{-1}$ is comparable to those of supported[58,59,94] and molecular[95,96] platinum(II) carbonyl compounds).

The lack of a significant change in the XANES spectrum during exposure of the sample to $H_2$ in the absence of CO at 100 °C (Figure 3.5e) indicates that $H_2$ did not react with $Pt^{2+}$ at 100 °C. At temperatures between 100 and 200 °C, however, $Pt^{2+}$ was reduced and converted to clusters in the presence of $H_2$. Reported DFT and kinetic Monte Carlo calculations indicate that $PtH_2$ units are highly mobile in zeolites and that adsorption of CO enhances platinum mobility, forming Pt(CO) species with weakened bonding to the zeolite framework and thus lowered barriers to diffusion.[14,31] The results showing that $Pt^{\delta+}(CO)$ species are stable in $H_2$ at 100 °C but reduced to form clusters when CO is present with the $H_2$ (Figure 3.5f) demonstrate that $Pt^{\delta+}$ with multiple carbonyl ligands is more mobile in the zeolite than $Pt^{\delta+}(CO)$.

The results further show that adsorption of CO facilitated the conversion of $Pt^{2+}$ to $Pt^{\delta+}$ at 100 °C and that this did not occur when $H_2$ was present without CO (Figures 3.5d and 3.5e). This result might be

described as an activation of $Pt^{2+}$ by CO and $H_2$ under conditions mild enough to avoid the rapid formation of clusters that occurred in the absence of CO. Thus, the CO ligand stabilized the labile, intermediate $Pt^{\delta+}(CO)$ complex, and this stabilization could be a useful property for catalytic applications of platinum ions. Although, in line with the results of Stair and coworkers,[56] $Pt^{\delta+}(CO)$ did not readily oxidize CO in the presence of $O_2$, the stabilized cationic complex may catalyze other reactions, and the use of small adsorbate molecules other than CO may offer the opportunity to tune the properties of $Pt^{\delta+}$ complexes.

The properties of cationic platinum might additionally be tuned through use of the zeolite support. Small variations in the frequencies of $\nu_{co}$ bands characterizing platinum *gem*-dicarbonyls in various zeolites (Figure 3.6) illustrates the subtle, but distinct, influence that the zeolite framework exerts as a ligand on platinum, which could impact such properties as stability, mobility, or reactivity of platinum supported on various zeolites. Such differences may also result from different surface sites within a single zeolite, the presence of which are evidenced by variations in the fwhm values of $\nu_{co}$ bands across zeolite frameworks, as well as by the overlap of multiple, narrow $\nu_{co}$ bands in the IR spectrum of Pt/ZSM-5 (Figures 3.3a and S3.21).

The interaction of $Pt^{\delta+}(CO)$ with $C_2H_4$ (Figure 3.5c) indicates the possibility that $Pt^{\delta+}(CO)$ may catalyze reactions such as olefin hydrogenation. It was recently reported that $Pt^{\delta+}$ in zeolite Y enabled the selective hydrogenation of unsaturated aldehydes to unsaturated alcohols,[39] but we recognize that platinum clusters in zeolite Y were reported to catalyze the same reaction, with the selectivity to unsaturated alcohol attributed to constraints imposed by the zeolite pores,[97] and so questions remain about the catalytically active species. It remains a challenge to distinguish atomically dispersed metals from minor amounts of metal clusters as catalysts, as the latter may often elude characterization.[98–100] The IR data presented here, however, provide clear evidence that $C_2H_4$ interacts with atomically dispersed $Pt^{\delta+}(CO)$ sites, consistent with the hypothesis that $Pt^{\delta+}$ catalyzes hydrogenation reactions.

## 3.5 Conclusions

The results presented here show that $Pt^{2+}$ ions are stabilized at 6-MR containing paired aluminum sites in HZSM-5 during exposure to $O_2$ at 700 °C. When exposed to CO, these $Pt^{2+}$ ions are converted into platinum *gem*-dicarbonyls that have a high degree of uniformity. These in turn are converted in the presence of $H_2$ into $Pt^{\delta+}$ monocarbonyls, and this conversion is accompanied by a weakening of the platinum–zeolite bonding that facilitates migration of the platinum in the zeolite. The results support the hypothesis that following oxidative regeneration of zeolite-supported platinum catalysts in $O_2$, a first step in formation of platinum clusters or atomically dispersed platinum active sites is the release of $Pt^{2+}$ from stable 6-MR binding sites, and the results show how adsorbed CO impacts this process. Similar platinum *gem*-dicarbonyls in several commercially important zeolites other than HZSM-5 (Beta, mordenite, and Y) were identified by IR spectroscopy, highlighting the generality of the chemistry of such zeolite-supported platinum complexes. The identification of multiple, cationic, carbonyl-containing platinum complexes emphasizes the value of an in-depth understanding of the coordination environment of atomically dispersed platinum as determined by X-ray absorption and IR spectroscopies to control catalyst structures and properties.

## 3.6 Acknowledgements

The authors gratefully acknowledge funding from the CeRCaS NSF IUCRC. Stanford Synchrotron Radiation Lightsource (SSRL) of SLAC National Accelerator Laboratory is supported by BES under Contract No. DE-AC02- 76SF00515. Co-ACCESS is supported by the BES Chemical Sciences, Geosciences, and Biosciences Division. This research used resources of the National Energy Research Scientific Computing Center (NERSC), a U.S. Department of Energy Office of Science User Facility located at Lawrence Berkeley National Laboratory, operated under Contract No. DE-AC02-05CH11231.

## 3.7 References

(1) Liu, L.; Corma, A. Metal Catalysts for Heterogeneous Catalysis: From Single Atoms to Nanoclusters and Nanoparticles. *Chem. Rev.* **2018**, *118*, 4981–5079.

(2) Goel, S.; Zones, S. I.; Iglesia, E. Encapsulation of Metal Clusters within MFI via Interzeolite Transformations and Direct Hydrothermal Syntheses and Catalytic Consequences of Their Confinement. *J. Am. Chem. Soc.* **2014**, *136*, 15280–15290.

(3) Goel, S.; Wu, Z.; Zones, S. I.; Iglesia, E. Synthesis and Catalytic Properties of Metal Clusters Encapsulated within Small-Pore (SOD, GIS, ANA) Zeolites. *J. Am. Chem. Soc.* **2012**, *134*, 17688–17695.

(4) Wang, C.; Guan, E.; Wang, L.; Chu, X.; Wu, Z.; Zhang, J.; Yang, Z.; Jiang, Y.; Zhang, L.; Meng, X.; Gates, B. C.; Xiao, F. S. Product Selectivity Controlled by Nanoporous Environments in Zeolite Crystals Enveloping Rhodium Nanoparticle Catalysts for $CO_2$ Hydrogenation. *J. Am. Chem. Soc.* **2019**, *141*, 8482–8488.

(5) Wang, C.; Wang, L.; Zhang, J.; Wang, H.; Lewis, J. P.; Xiao, F. S. Product Selectivity Controlled by Zeolite Crystals in Biomass Hydrogenation over a Palladium Catalyst. *J. Am. Chem. Soc.* **2016**, *138*, 7880–7883.

(6) Aitani, A.; Akhtar, M. N.; Al-Khattaf, S.; Jin, Y.; Koseoglo, O.; Klein, M. T. Catalytic Upgrading of Light Naphtha to Gasoline Blending Components: A Mini Review. *Energy and Fuels* **2019**, *33*, 3828–3843.

(7) Cho, H. J.; Kim, D.; Li, J.; Su, D.; Xu, B. Zeolite-Encapsulated Pt Nanoparticles for Tandem Catalysis. *J. Am. Chem. Soc.* **2018**, *140*, 13514–13520.

(8) Cho, H. J.; Kim, D.; Li, S.; Su, D.; Ma, D.; Xu, B. Molecular-Level Proximity of Metal and Acid Sites in Zeolite-Encapsulated Pt Nanoparticles for Selective Multistep Tandem Catalysis. *ACS Catal.* **2020**, *10*, 3340–3348.

(9) Hong, D. Y.; Miller, S. J.; Agrawal, P. K.; Jones, C. W. Hydrodeoxygenation and Coupling of Aqueous Phenolics over Bifunctional Zeolite-Supported Metal Catalysts. *Chem. Commun.* **2010**, *46*, 1038–1040.

(10) Morgan, K.; Goguet, A.; Hardacre, C. Metal Redispersion Strategies for Recycling of Supported Metal Catalysts: A Perspective. *ACS Catal.* **2015**, *5*, 3430–3445.

(11) Argyle, M. D.; Bartholomew, C. H. Heterogeneous Catalyst Deactivation and Regeneration: A Review. *Catalysts* **2015**, *5*, 145–269.

(12) Moliner, M.; Gabay, J. E.; Kliewer, C. E.; Carr, R. T.; Guzman, J.; Casty, G. L.; Serna, P.; Corma, A. Reversible Transformation of Pt Nanoparticles into Single Atoms inside High-Silica Chabazite Zeolite. *J. Am. Chem. Soc.* **2016**, *138*, 15743–15750.

(13) Moliner, M.; Gabay, J.; Kliewer, C.; Serna, P.; Corma, A. Trapping of Metal Atoms and Metal Clusters by Chabazite under Severe Redox Stress. *ACS Catal.* **2018**, *8*, 9520–9528.

(14) Hou, D.; Grajciar, L.; Nachtigall, P.; Heard, C. J. Origin of the Unusual Stability of Zeolite-Encapsulated Sub-Nanometer Platinum. *ACS Catal.* **2020**, *10*, 11057–11068.

(15) Yakovlev, A. L.; Neyman, K. M.; Zhidomirov, G. M.; Rösch, N. Interaction of CO Molecules with Electron-Deficient Pt Atoms in Zeolites: A Density Functional Model Cluster Study. *J. Phys. Chem.* **1996**, *100*, 3482–3487.

(16) Paolucci, C.; Parekh, A. A.; Khurana, I.; Di Iorio, J. R.; Li, H.; Albarracin Caballero, J. D.; Shih, A. J.; Anggara, T.; Delgass, W. N.; Miller, J. T.; Ribeiro, F. H.; Gounder, R.; Schneider, W. F.

Catalysis in a Cage: Condition-Dependent Speciation and Dynamics of Exchanged Cu Cations in SSZ-13 Zeolites. *J. Am. Chem. Soc.* **2016**, *138*, 6028–6048.

(17) Paolucci, C.; Khurana, I.; Parekh, A. A.; Li, S.; Shih, A. J.; Li, H.; Iorio, J. R. Di; Albarracin-Caballero, J. D.; Yezerets, A.; Miller, J. T.; Delgass, W. N.; Ribeiro, F. H.; Schneider, W. F.; Gounder, R. Dynamic Multinuclear Sites Formed by Mobilized Copper Ions in NOx Selective Catalytic Reduction. *Science* **2017**, *357*, 898–903.

(18) Dinh, K. T.; Sullivan, M. M.; Narsimhan, K.; Serna, P.; Meyer, R. J.; Dincă, M.; Román-Leshkov, Y. Continuous Partial Oxidation of Methane to Methanol Catalyzed by Diffusion-Paired Copper Dimers in Copper-Exchanged Zeolites. *J. Am. Chem. Soc.* **2019**, *141*, 11641–11650.

(19) Snyder, B. E. R.; Vanelderen, P.; Schoonheydt, R. A.; Sels, B. F.; Solomon, E. I. Second-Sphere Effects on Methane Hydroxylation in Cu-Zeolites. *J. Am. Chem. Soc.* **2018**, *140*, 9236–9243.

(20) Pappas, D. K.; Martini, A.; Dyballa, M.; Kvande, K.; Teketel, S.; Lomachenko, K. A.; Baran, R.; Glatzel, P.; Arstad, B.; Berlier, G.; Lamberti, C.; Bordiga, S.; Olsbye, U.; Svelle, S.; Beato, P.; Borfecchia, E. The Nuclearity of the Active Site for Methane to Methanol Conversion in Cu-Mordenite: A Quantitative Assessment. *J. Am. Chem. Soc.* **2018**, *140*, 15270–15278.

(21) Snyder, B. E. R.; Vanelderen, P.; Bols, M. L.; Hallaert, S. D.; Böttger, L. H.; Ungur, L.; Pierloot, K.; Schoonheydt, R. A.; Sels, B. F.; Solomon, E. I. The Active Site of Low-Temperature Methane Hydroxylation in Iron-Containing Zeolites. *Nature* **2016**, *536*, 317–321.

(22) Bols, M. L.; Hallaert, S. D.; Snyder, B. E. R.; Devos, J.; Plessers, D.; Rhoda, H. M.; Dusselier, M.; Schoonheydt, R. A.; Pierloot, K.; Solomon, E. I.; Sels, B. F. Spectroscopic Identification of the α-Fe/α-O Active Site in Fe-CHA Zeolite for the Low-Temperature Activation of the Methane C-H Bond. *J. Am. Chem. Soc.* **2018**, *140*, 12021–12032.

(23) Bols, M. L.; Devos, J.; Rhoda, H. M.; Plessers, D.; Solomon, E. I.; Schoonheydt, R. A.; Sels, B. F.; Dusselier, M. Selective Formation of α-Fe(II) Sites on Fe-Zeolites through One-Pot Synthesis. *J. Am. Chem. Soc.* **2021**, *143*, 16243–16255.

(24) Tabor, E.; Lemishka, M.; Sobalik, Z.; Mlekodaj, K.; Andrikopoulos, P. C.; Dedecek, J.; Sklenak, S. Low-Temperature Selective Oxidation of Methane over Distant Binuclear Cationic Centers in Zeolites. *Commun. Chem.* **2019**, *2*, 1–9.

(25) Mandal, K.; Gu, Y.; Westendorff, K. S.; Li, S.; Pihl, J. A.; Grabow, L. C.; Epling, W. S.; Paolucci, C. Condition-Dependent Pd Speciation and NO Adsorption in Pd/Zeolites. *ACS Catal.* **2020**, *10*, 12801–12818.

(26) Lardinois, T. M.; Bates, J. S.; Lippie, H. H.; Russell, C. K.; Miller, J. T.; Meyer, H. M.; Unocic, K. A.; Prikhodko, V.; Wei, X.; Lambert, C. K.; Getsoian, A. B.; Gounder, R. Structural Interconversion between Agglomerated Palladium Domains and Mononuclear Pd(II) Cations in Chabazite Zeolites. *Chem. Mater.* **2021**, *33*, 1698–1713.

(27) Khivantsev, K.; Jaegers, N. R.; Koleva, I. Z.; Aleksandrov, H. A.; Kovarik, L.; Engelhard, M.; Gao, F.; Wang, Y.; Vayssilov, G. N.; Szanyi, J. Stabilization of Super Electrophilic $Pd^{+2}$ Cations in Small-Pore SSZ-13 Zeolite. *J. Phys. Chem. C* **2020**, *124*, 309–321.

(28) Xie, P.; Pu, T.; Aranovich, G.; Guo, J.; Donohue, M.; Kulkarni, A.; Wang, C. Bridging Adsorption Analytics and Catalytic Kinetics for Metal-Exchanged Zeolites. *Nat. Catal.* **2021**, *4*, 144–156.

(29) Knott, B. C.; Nimlos, C. T.; Robichaud, D. J.; Nimlos, M. R.; Kim, S.; Gounder, R. Consideration of the Aluminum Distribution in Zeolites in Theoretical and Experimental Catalysis Research. *ACS Catal.* **2018**, *8*, 770–784.

(30) Perea, D. E.; Arslan, I.; Liu, J.; Ristanović, Z.; Kovarik, L.; Arey, B. W.; Lercher, J. A.; Bare, S. R.; Weckhuysen, B. M. Determining the Location and Nearest Neighbours of Aluminium in Zeolites with Atom Probe Tomography. *Nat. Commun.* **2015**, *6*, 1–8.

(31) Hou, D.; Heard, C. J. Migration of Zeolite-Encapsulated Pt and Au under Reducing Environments. *Catal. Sci. Technol.* **2022**, *12*, 1598–1609.

(32) Liu, L.; Zakharov, D. N.; Arenal, R.; Concepcion, P.; Stach, E. A.; Corma, A. Evolution and Stabilization of Subnanometric Metal Species in Confined Space by in Situ TEM. *Nat. Commun.* **2018**, *9*, 1–10.

(33) Fang, C. Y.; Zhang, S.; Hu, Y.; Vasiliu, M.; Perez-Aguilar, J. E.; Conley, E. T.; Dixon, D. A.; Chen, C. Y.; Gates, B. C. Reversible Metal Aggregation and Redispersion Driven by the Catalytic Water Gas Shift Half-Reactions: Interconversion of Single-Site Rhodium Complexes and Tetrarhodium Clusters in Zeolite HY. *ACS Catal.* **2019**, *9*, 3311–3321.

(34) Uzun, A.; Gates, B. C. Real-Time Characterization of Formation and Breakup of Iridium Clusters in Highly Dealuminated Zeolite Y. *Angew. Chem. Int. Ed.* **2008**, *47*, 9245–9248.

(35) Liang, A. J.; Gates, B. C. Time-Resolved Structural Characterization of Formation and Break-up of Rhodium Clusters Supported in Highly Dealuminated Y Zeolite. *J. Phys. Chem. C* **2008**, *112*, 18039–18049.

(36) Uzun, A.; Bhirud, V. A.; Kletnieks, P. W.; Haw, J. F.; Gates, B. C. A Site-Isolated Iridium Diethylene Complex Supported on Highly Dealuminated Y Zeolite: Synthesis and Characterization. *J. Phys. Chem. C* **2007**, *111*, 15064–15073.

(37) Liang, A. J.; Bhirud, V. A.; Ehresmann, J. O.; Kletnieks, P. W.; Haw, J. F.; Gates, B. C. A Site-Isolated Rhodium-Diethylene Complex Supported on Highly Dealuminated Y Zeolite: Synthesis and Characterization. *J. Phys. Chem. B* **2005**, *109*, 24236–24243.

(38) Miessner, H.; Burkhardt, I.; Gutschick, D.; Zecchina, A.; Morterra, C.; Spoto, G. The Formation of Well Defined Rhodium Dicarbonyl and Dinitrosyl with Rhodium Supported on Highly Dealuminated Zeolite Y. *Stud. Surf. Sci. Catal.* **1989**, *48*, 677–684.

(39) Deng, X.; Qin, B.; Liu, R.; Qin, X.; Dai, W.; Wu, G.; Guan, N.; Ma, D.; Li, L. Zeolite-Encaged Isolated Platinum Ions Enable Heterolytic Dihydrogen Activation and Selective Hydrogenations. *J. Am. Chem. Soc.* **2021**, *143*, 20898–20906.

(40) Liu, L.; Lopez-Haro, M.; Lopes, C. W.; Li, C.; Concepcion, P.; Simonelli, L.; Calvino, J. J.; Corma, A. Regioselective Generation and Reactivity Control of Subnanometric Platinum Clusters in Zeolites for High-Temperature Catalysis. *Nat. Mater.* **2019**, *18*, 866–873.

(41) Serna, P.; Rodríguez-Fernández, A.; Yacob, S.; Kliewer, C.; Moliner, M.; Corma, A. Single-Site vs. Cluster Catalysis in High Temperature Oxidations. *Angew. Chem.* **2021**, 15954–15962.

(42) Gallezot, P. The State and Catalytic Properties of Platinum and Palladium in Faujasite-Type Zeolites. *Catal. Rev.* **1979**, *20*, 121–154.

(43) Samant, M. G.; Boudart, M. Support Effects on Electronic Structure of Platinum Clusters in Y Zeolite. *J. Phys. Chem.* **1991**, *95*, 4070–4074.

(44) Chakarova, K.; Mihaylov, M.; Hadjiivanov, K. FTIR Spectroscopic Study of CO Adsorption on Pt-H-ZSM-5. *Microporous Mesoporous Mater.* **2005**, *81*, 305–312.

(45) Dedecek, J.; Balgová, V.; Pashkova, V.; Klein, P.; Wichterlová, B. Synthesis of ZSM-5 Zeolites with Defined Distribution of Al Atoms in the Framework and Multinuclear MAS NMR Analysis of the Control of Al Distribution. *Chem. Mater.* **2012**, *24*, 3231–3239.

(46) Babucci, M.; Guntida, A.; Gates, B. C. Atomically Dispersed Metals on Well-Defined Supports Including Zeolites and Metal-Organic Frameworks: Structure, Bonding, Reactivity, and Catalysis. *Chem. Rev.* **2020**, *120*, 11956–11985.

(47) Xiang, Y.; Wang, H.; Cheng, J.; Matsubu, J. Progress and Prospects in Catalytic Ethane Aromatization. *Catal. Sci. Technol.* **2018**, *8*, 1500–1516.

(48) Ankudinov, A. L.; Rehr, J. J.; Low, J.; Bare, S. R. Effect of Hydrogen Adsorption on the X-Ray Absorption Spectra of Small Pt Clusters. *Phys. Rev. Lett.* **2001**, *86*, 1642–1645.

(49) Chen, Y.; Rana, R.; Sours, T.; Vila, F. D.; Cao, S.; Blum, T.; Hong, J.; Hoffman, A. S.; Fang, C. Y.; Huang, Z.; Shang, C.; Wang, C.; Zeng, J.; Chi, M.; Kronawitter, C. X.; Bare, S. R.; Gates, B. C.; Kulkarni, A. R. A Theory-Guided X-Ray Absorption Spectroscopy Approach for Identifying Active Sites in Atomically Dispersed Transition-Metal Catalysts. *J. Am. Chem. Soc.* **2021**, *143*, 20144–20156.

(50) Giordanino, F.; Vennestrøm, P. N. R.; Lundegaard, L. F.; Stappen, F. N.; Mossin, S.; Beato, P.; Bordiga, S.; Lamberti, C. Characterization of Cu-Exchanged SSZ-13: A Comparative FTIR, UV-Vis, and EPR Study with Cu-ZSM-5 and Cu-β with Similar Si/Al and Cu/Al Ratios. *Dalton Trans.* **2013**, *42*, 12741–12761.

(51) Smeets, P. J.; Woertink, J. S.; Sels, B. F.; Solomon, E. I.; Schoonheydt, R. A. Transition-Metal Ions in Zeolites: Coordination and Activation of Oxygen. *Inorg. Chem.* **2010**, *49*, 3573–3583.

(52) Groothaert, M. H.; Pierloot, K.; Delabie, A.; Schoonheydt, R. A. Identification of Cu(II) Coordination Structures in Cu-ZSM-5, Based on a DFT/Ab Initio Assignment of the EPR Spectra. *Phys. Chem. Chem. Phys.* **2003**, *5*, 2135–2144.

(53) Tabor, E.; Dedecek, J.; Mlekodaj, K.; Sobalik, Z.; Andrikopoulos, P. C.; Sklenak, S. Dioxygen Dissociation over Man-Made System at Room Temperature to Form the Active α-Oxygen for Methane Oxidation. *Sci. Adv.* **2020**, *6*, 1–9.

(54) Mlekodaj, K.; Lemishka, M.; Sklenak, S.; Dedecek, J.; Tabor, E. Dioxygen Splitting at Room Temperature over Distant Binuclear Transition Metal Centers in Zeolites for Direct Oxidation of Methane to Methanol. *Chem. Commun.* **2021**, *57*, 3472–3475.

(55) Chakarova, K.; Mihaylov, M.; Hadjiivanov, K. Polycarbonyl Species in Pt/H-ZSM-5: FTIR Spectroscopic Study of $^{12}CO$-$^{13}CO$ Co-Adsorption. *Catal. Commun.* **2005**, *6*, 466–471.

(56) Ding, K.; Gulec, A.; Johnson, A. M.; Schweitzer, N. M.; Stucky, G. D.; Marks, L. D.; Stair, P. C. Identification of Active Sites in CO Oxidation and Water-Gas Shift over Supported Pt Catalysts. *Science* **2015**, *350*, 189–192.

(57) Hoffman, A. S.; Fang, C.-Y.; Gates, B. C. Homogeneity of Surface Sites in Supported Single-Site Metal Catalysts: Assessment with Band Widths of Metal Carbonyl Infrared Spectra. *J. Phys. Chem. Lett.* **2016**, *7*, 3854–3860.

(58) DeRita, L.; Resasco, J.; Dai, S.; Boubnov, A.; Thang, H. V.; Hoffman, A. S.; Ro, I.; Graham, G. W.; Bare, S. R.; Pacchioni, G.; Pan, X.; Christopher, P. Structural Evolution of Atomically Dispersed Pt Catalysts Dictates Reactivity. *Nat. Mater.* **2019**, *18*, 746–751.

(59) DeRita, L.; Dai, S.; Lopez-Zepeda, K.; Pham, N.; Graham, G. W.; Pan, X.; Christopher, P. Catalyst Architecture for Stable Single Atom Dispersion Enables Site-Specific Spectroscopic and Reactivity Measurements of CO Adsorbed to Pt Atoms, Oxidized Pt Clusters, and Metallic Pt Clusters on $TiO_2$. *J. Am. Chem. Soc.* **2017**, *139*, 14150–14165.

(60) Kubanek, P.; Schmidt, H. W.; Spliethoff, B.; Schüth, F. Parallel IR Spectroscopic Characterization of CO Chemisorption on Pt Loaded Zeolites. *Microporous Mesoporous Mater.* **2005**, *77*, 89–96.

(61) Zholobenko, V. L.; Lei, G. D.; Carvill, B. T.; Lerner, B. A.; Sachtler, W. M. H. Identification of Isolated Pt Atoms in H-Mordenite. *J. Chem. Soc., Faraday Trans.* **1994**, *90*, 233–238.

(62) Stakheev, A. Y.; Shpiro, E. S.; Tkachenko, O. P.; Jaeger, N. I.; Schulz-Ekloff, G. Evidence for Monatomic Platinum Species in H-ZSM-5 from FTIR Spectroscopy of Chemisorbed CO. *J. Catal.* **1997**, *169*, 382–388.

(63) Treesukol, P.; Srisuk, K.; Limtrakul, J.; Truong, T. N. Nature of the Metal-Support Interaction in Bifunctional Catalytic Pt/H-ZSM-5 Zeolite. *J. Phys. Chem. B* **2005**, *109*, 11940–11945.

(64) Hadjiivanov, K. I.; Vayssilov, G. N. Characterization of Oxide Surfaces and Zeolites by Carbon Monoxide as an IR Probe Molecule. *Adv. Catal.* **2002**, *47*, 307–511.

(65) Sobalík, Z.; Tvarůžková, Z.; Wichterlová, B. Skeletal T-O-T Vibrations as a Tool for Characterization of Divalent Cation Complexation in Ferrierite. *J. Phys. Chem. B* **1998**, *102*, 1077–1085.

(66) Jacobs, W. P. J. H.; van Wolput, J. H. M. C.; van Santen, R. A. An in Situ Fourier Transform Infrared Studyof Zeolitic Vibrations: Dehydration, Deammoniation, and Reammoniation of Ion-Exchanged Y Zeolites. *Zeolites* **1993**, *13*, 170–182.

(67) Sárkány, J. Effects of Water and Ion-Exchanged Counterion on the FT-IR Spectra of ZSM-5 - Part III. $Cu^+(CO)_2$-ZSM-5: Interaction of $Cu^+(CO)_2$ Complex with $H_2O$ and Changes in Skeletal T-O-T Vibrations. *Appl. Catal. A Gen.* **2002**, *229*, 291–312.

(68) Luo, J.; Wang, D.; Kumar, A.; Li, J.; Kamasamudram, K.; Currier, N.; Yezerets, A. Identification of Two Types of Cu Sites in Cu/SSZ-13 and Their Unique Responses to Hydrothermal Aging and Sulfur Poisoning. *Catal. Today* **2016**, *267*, 3–9.

(69) Lei, G. D.; Adelman, B. J.; Sárkány, J.; Sachtler, W. M. H. Identification of Copper(II) and Copper(I) and Their Interconversion in Cu/ZSM-5 De-NOx Catalysts. *Appl. Catal. B, Environ.* **1995**, *5*, 245–256.

(70) Sobalík, Z.; Tvarůžková, Z.; Wichterlová, B. Monitoring of Skeletal T-O-T Vibrations of Metal Ion Exchanged Zeolites an Attempt at Quantitative Evaluation. *Microporous Mesoporous Mater.* **1998**, *25*, 225–228.

(71) Calligaris, M.; Nardin, G.; Randaccio, L. Crystal Structures of Hydrated and Dehydrated Forms of a Co(II)-Exchanged Chabazite. *Zeolites* **1984**, *4*, 251–254.

(72) Calligaris, M.; Mezzetti, A.; Nardin, G.; Randaccio, L. Crystal Structures of Hydrated and Dehydrated Forms of a Mn(II)-Exchanged Chabazite. *Zeolites* **1985**, *5*, 317–319.

(73) Song, I.; Khivantsev, K.; Wang, Y.; Szanyi, J. Elucidating the Role of CO in the NO Storage Mechanism on Pd/SSZ-13 with in Situ DRIFTS. *J. Phys. Chem. C* **2022**, *126*, 1439–1449.

(74) Borfecchia, E.; Lomachenko, K. A.; Giordanino, F.; Falsig, H.; Beato, P.; Soldatov, A. V.; Bordiga, S.; Lamberti, C. Revisiting the Nature of Cu Sites in the Activated Cu-SSZ-13 Catalyst for SCR Reaction. *Chem. Sci.* **2015**, *6*, 548–563.

(75) Khivantsev, K.; Vityuk, A.; Aleksandrov, H. A.; Vayssilov, G. N.; Alexeev, O. S.; Amiridis, M. D. Effect of Si/Al Ratio and Rh Precursor Used on the Synthesis of HY Zeolite-Supported Rhodium Carbonyl Hydride Complexes. *J. Phys. Chem. C* **2015**, *119*, 17166–17181.

(76) Martinez-Macias, C.; Chen, M.; Dixon, D. A.; Gates, B. C. Single-Site Zeolite-Anchored Organoiridium Carbonyl Complexes: Characterization of Structure and Reactivity by Spectroscopy and Computational Chemistry. *Chem. Eur. J.* **2015**, *21*, 11825–11835.

(77) Lu, J.; Aydin, C.; Browning, N. D.; Gates, B. C. Hydrogen Activation and Metal Hydride Formation Trigger Cluster Formation from Supported Iridium Complexes. *J. Am. Chem. Soc.* **2012**, *134*, 5022–5025.

(78) Yamasaki, Y.; Matsuoka, M.; Anpo, M. Characterization of the Active Sites on Pt-Loaded ZSM-5 (Pt/ZSM-5) Prepared by an Ion-Exchange Method for the Oxidation of CO at Low Temperatures. *Catal. Lett.* **2003**, *91*, 111–113.

(79) Bischoff, H.; Jaeger, N. I.; Schulz-Ekloff, G.; Kubelkova, L. Interaction of CO with Platinum Species in Zeolites. Evidence for Platinum Carbonyls in Partially Reduced Zeolite PtNaX. *J. Mol. Catal.* **1993**, *80*, 95–103.

(80) Bisio, C.; Fajerwerg, K.; Krafft, J. M.; Massiani, P.; Martra, G. Dispersion and States of Platinum Ions in BEA-Zeolite Pores: Effect of the Framework Basicity. *Res. Chem. Intermed.* **2008**, *34*, 565–576.

(81) Chakarova, K.; Hadjiivanov, K.; Atanasova, G.; Tenchev, K. Effect of Preparation Technique on the Properties of Platinum in NaY Zeolite: A Study by FTIR Spectroscopy of Adsorbed CO. *J. Mol. Catal. A: Chem.* **2007**, *264*, 270–279.

(82) Mihaylov, M.; Chakarova, K.; Hadjiivanov, K.; Marie, O.; Daturi, M. FTIR Spectroscopy Study of CO Adsorption on Pt-Na-Mordenite. *Langmuir* **2005**, *21*, 11821–11828.

(83) Perez-Aguilar, J. E.; Hughes, J. T.; Chen, C. Y.; Gates, B. C. Transformation of Atomically Dispersed Platinum in SAPO-37 into Platinum Clusters: Catalyst for Ethylene Hydrogenation. *Catal. Sci. Technol.* **2021**, *11*, 6666–6681.

(84) Kistler, J. D.; Chotigkrai, N.; Xu, P.; Enderle, B.; Praserthdam, P.; Chen, C. Y.; Browning, N. D.; Gates, B. C. A Single-Site Platinum CO Oxidation Catalyst in Zeolite KLTL: Microscopic and Spectroscopic Determination of the Locations of the Platinum Atoms. *Angew. Chem. Int. Ed.* **2014**, *53*, 8904–8907.

(85) Tzou, M. S.; Teo, B. K.; Sachtler, W. M. . Formation of Pt Particles in Y-Type Zeolites. *J. Catal.* **1988**, *113*, 220–235.

(86) Liu, Y.; Li, Z.; Yu, Q.; Chen, Y.; Chai, Z.; Zhao, G.; Liu, S.; Cheong, W. C.; Pan, Y.; Zhang, Q.; Gu, L.; Zheng, L.; Wang, Y.; Lu, Y.; Wang, D.; Chen, C.; Peng, Q.; Liu, Y.; Liu, L.; Chen, J.; Li, Y. A General Strategy for Fabricating Isolated Single Metal Atomic Site Catalysts in Y Zeolite. *J. Am. Chem. Soc.* **2019**, *141*, 9305–9311.

(87) Guan, E.; Ciston, J.; Bare, S. R.; Runnebaum, R. C.; Katz, A.; Kulkarni, A.; Kronawitter, C. X.; Gates, B. C. Supported Metal Pair-Site Catalysts. *ACS Catal.* **2020**, *10*, 9065–9085.

(88) Dědeček, J.; Kaucký, D.; Wichterlová, B.; Gonsiorová, O. $Co^{2+}$ Ions as Probes of Al Distribution in the Framework of Zeolites. ZSM-5 Study. *Phys. Chem. Chem. Phys.* **2002**, *4*, 5406–5413.

(89) Godiksen, A.; Vennestrøm, P. N. R.; Rasmussen, S. B.; Mossin, S. Identification and Quantification of Copper Sites in Zeolites by Electron Paramagnetic Resonance Spectroscopy. *Top. Catal.* **2017**, *60*, 13–29.

(90) Dedecek, J.; Sobalík, Z.; Wichterlová, B. Siting and Distribution of Framework Aluminium Atoms in Silicon-Rich Zeolites and Impact on Catalysis. *Catal. Rev. Sci. Eng.* **2012**, *54*, 135–223.

(91) Gallezot, P.; Alarcon-Diaz, A.; Dalmon, J. A.; Renouprez, A. J.; Imelik, B. Location and Dispersion of Platinum in PtY Zeolites. *J. Catal.* **1975**, *39*, 334–349.

(92) Biligetu, T.; Wang, Y.; Nishitoba, T.; Otomo, R.; Park, S.; Mochizuki, H.; Kondo, J. N.; Tatsumi, T.; Yokoi, T. Al Distribution and Catalytic Performance of ZSM-5 Zeolites Synthesized with Various Alcohols. *J. Catal.* **2017**, *353*, 1–10.

(93) Sárkány, J. Effects of Water and Ion-Exchanged Counterion on the FTIR Spectra of ZSM-5. II. ($Cu^+$-CO)-ZSM-5: Coordination of $Cu^+$-CO Complex by $H_2O$ and Changes in Skeletal T-O-T Vibrations. *Top. Catal.* **2002**, *18*, 271–277.

(94) Thang, H. V.; Pacchioni, G.; DeRita, L.; Christopher, P. Nature of Stable Single Atom Pt Catalysts Dispersed on Anatase $TiO_2$. *J. Catal.* **2018**, *367*, 104–114.

(95) Zhong, H. A.; Labinger, J. A.; Bercaw, J. E. C-H Bond Activation by Cationic Platinum(II) Complexes: Ligand Electronic and Steric Effects. *J. Am. Chem. Soc.* **2002**, *124*, 1378–1399.

(96) Cherwinski, W. J.; Clark, H. C. Chemistry of Metal Hydrides. X. The Effect of Trans Ligands on Cationic Platinum(II) Carbonyls. *Inorg. Chem.* **1971**, *10*, 2263–2267.

(97) Gallezot, P.; Giroir-Fendler, A.; Richard, D. Chemioselectivity in Cinnamaldehyde Hydrogenation Induced by Shape Selectivity Effects in Pt-Y Zeolite Catalysts. *Catal. Lett.* **1990**, *5*, 169–174.

(98) Resasco, J.; Yang, F.; Mou, T.; Wang, B.; Christopher, P.; Resasco, D. E. Relationship between Atomic Scale Structure and Reactivity of Pt Catalysts: Hydrodeoxygenation of *m*-Cresol over Isolated Pt Cations and Clusters. *ACS Catal.* **2020**, *10*, 595–603.

(99) Resasco, J.; Dai, S.; Graham, G.; Pan, X.; Christopher, P. Combining In-Situ Transmission Electron Microscopy and Infrared Spectroscopy for Understanding Dynamic and Atomic-Scale Features of Supported Metal Catalysts. *J. Phys. Chem. C* **2018**, *122*, 25143–25157.

(100) Resasco, J.; DeRita, L.; Dai, S.; Chada, J. P.; Xu, M.; Yan, X.; Finzel, J.; Hanukovich, S.; Hoffman, A. S.; Graham, G. W.; Bare, S. R.; Pan, X.; Christopher, P. Uniformity Is Key in Defining

Structure-Function Relationships for Atomically Dispersed Metal Catalysts: The Case of $Pt/CeO_2$. *J. Am. Chem. Soc.* **2020**, *142*, 169–184.

## 3.8 Supporting Information

### Supporting Information Table of Contents

**References**

## Experimental Methods

### Sample Preparation

**Zeolite pretreatment.** $NH_4$-form ZSM-5 was supplied by Zeolyst International (SAR 50; CBV 5524G). Before incorporation of platinum, $NH_4$-ZSM-5 was converted to HZSM-5 by calcination in air as follows. Zeolite was placed in a horizontal quartz tube (19 mm OD), which itself was placed into a tubular furnace (Applied Test Systems). With 50 mL/min of air (Praxair, Zero Grade) flow through the quartz tube, the furnace was heated to 120 °C at 5 °C/min and held at 120 °C for 1 h. Then the temperature was increased at a rate of 2 °C/min to 550 °C and held constant for 6 h. All zeolites used in this study were treated in this way before incorporation of platinum. Zeolites Y (SAR 30; CBV 720), MOR (SAR 13; CBV 10A), and beta (SAR 38; CP814C) were supplied by Zeolyst International. Low pair ZSM-5 was synthesized as described below.

**Platinum ion exchange.** Platinum was incorporated into all zeolites using the following aqueous ion exchange procedure. H-form zeolite was added to a magnetically-stirred aqueous solution of approximately 50 mM ammonium nitrate ($NH_4NO_3$; Acros Organics, 99+%) in a ratio of approximately 199 mL solution per g zeolite. To this mixture was added a small volume (approximately 1 mL) of a stock solution of aqueous tetraammineplatinum(II) nitrate ($Pt(NH_3)_4(NO_3)_2$; Sigma Aldrich, 99.995%). The concentration of stock solution was typically 20.4 mM. After addition of $Pt(NH_3)_4(NO_3)_2$ solution, the resulting mixture had a ratio of 200 mL solution per g zeolite, a $Pt(NH_3)_4(NO_3)_2$ concentration of 0.10 mM, and an $NH_4NO_3$ concentration of 50 mM. This mixture was covered and stirred under ambient conditions for 20 h before separation by centrifugation. Separated solids were washed with deionized water and centrifuged again. The solids were washed and centrifuged a total of three times before drying in an oven at 80 °C overnight. Dried Pt/zeolite samples were stored at room temperature in ambient conditions until use.

**Synthesis of low pair ZSM-5.** Synthesis of low pair ZSM-5 was based on published procedures.[1] 0.25 g aluminum nitrate nonahydrate ($Al(NO_3)_3{\cdot}9H_2O$) was added to 1.6 g deionized water and stirred until dissolved. Separately, 0.77 mL ethanol was added to 3.46 g tetraethyl orthosilicate (TEOS) and stirred until

mixed, about 10 min. The ethanol-TEOS mixture was added to the $Al(NO_3)_3$ solution and stirred covered for 45 minutes. The cover was then removed, and the mixture was stirred to allow evaporation of all ethanol (approximately 3.7 g total ethanol). A mixture of 3.18 g tetrapropylammonium hydroxide (TPAOH, 40% in water) and 9.2 g deionized water was added to the $Al(NO_3)_3$-TEOS mixture. This was stirred, uncovered, for 90 min, before transferring to a 23 mL, PTFE lined autoclave. The gel molar composition was 1 Si : 0.04 Al : 0.38 TPAOH : 42 $H_2O$. The autoclave was sealed and placed into an oven, rotating at 20 rpm, at 170 °C for 6 days. The autoclave was cooled and its contents filtered and washed with deionized water. The rinsed solids were dried in an oven at 80 °C under ambient conditions. Dried solids were calcined to remove organics and obtain the H-form zeolite, using calcination conditions described above.

**Cobalt ion exchange.** Aluminum pairs in HZSM-5 and low pair ZSM-5 were quantified by ion exchange with cobalt.[1] First, proton form zeolites were ion exchanged with sodium nitrate ($NaNO_3$). HZSM-5 was mixed with an aqueous solution of 1 M $NaNO_3$ (100 mL solution per g zeolite) and stirred for 12 h. The mixture was filtered and solids were rinsed with deionized water. This process was repeated twice more to obtain Na-ZSM-5. Na-ZSM-5 samples were ion exchanged with cobalt (II) nitrate hexahydrate ($Co(NO_3)_2 \cdot 6H_2O$). Na-ZSM-5 was added to an aqueous solution of 50 mM $Co(NO_3)_2$ and stirred for 24 h. The mixture was filtered and solids were rinsed with deionized water. This process was repeated twice more, and the solids were then dried under ambient conditions in an oven at 80 °C to obtain Co-Na-ZSM-5 samples.

**Characterization Methods**

**Physicochemical characterization.** Nitrogen physisorption measurements were performed using a Micromeritics 3Flex Physisorption/Chemisorption Instrument. Nitrogen adsorption isotherms were measured at -196 °C. Surface areas were determined by the BET method, and micropore volumes were determined by the t-plot method. Elemental compositions of samples were determined by inductively coupled plasma mass spectrometry (ICP-MS) using an Agilent 7500 quadrupole ICP-MS instrument at UC Davis or by inductively coupled plasma optical emission spectroscopy (ICP-OES) at Galbraith Laboratories. Samples were prepared for ICP-MS by microwave acid digestion. X-ray diffraction was

performed using a Rigaku Miniflex 6G Benchtop Powder XRD instrument with Cu-Kα radiation or a Bruker D8 Advance Eco instrument with Cu-Kα radiation.

**Thermogravimetric analysis (TGA).** The TGA experiment was performed on a Netzsch STA 449 F3 Jupiter thermogravimetric analysis unit with QMS 403 D Aeolos mass spectrometer. As prepared Pt/ZSM-5 (20-30 mg) was loaded into the instrument in a small ceramic cup under ambient conditions. Under flow of 50 mL/min air (Praxair, Zero grade) and 10 mL/min $N_2$ (Praxair, 4.8), temperature was increased at 5 °C/min to 120 °C. After holding for 1 h at 120 °C, temperature was increased 5 °C/min to 700 °C. The effluent gas stream was analyzed by online mass spectrometry.

**IR spectroscopy.** Diffuse reflectance infrared Fourier transform spectra (DRIFTS) were collected using a Bruker Tensor II instrument (2 $cm^{-1}$ resolution and 128 scans per spectrum) and a Pike Technologies DiffusIR accessory with high temperature environmental chamber. A spectrum of powdered $CaF_2$ was used as a background, and sample absorbance spectra were calculated using the Kulbelka-Munk equation. As-prepared Pt/zeolite samples (5-10 mg) were loaded into the environmental chamber in a ceramic cup, and the chamber was purged with flowing $N_2$ (Airgas, Research Purity). Then $N_2$ flow was replaced with 50 mL/min air (Praxair, Zero grade) flow, and the temperature was increased at 5 °C/min to 120 °C, where it was held for 1 h to remove adsorbed waster. Next, samples were heated at 2 °C/min to 700 °C and held at this temperature for 2 h before cooling at 25 °C/min to 500 °C. With sample at 500 °C, flow was switched to $N_2$ and held under this condition for 1 h. Samples were then cooled to 30 °C before subsequent exposure to probe molecules.

For IR spectra of adsorbed CO, calcined samples were exposed to flowing 10% CO in $N_2$ at 30 °C for 15 minutes before flow was switched to $N_2$ to remove gas phase CO. Spectra were collected after 2 min of $N_2$ flow. Subsequent treatments were performed as described in figure captions.

**X-ray Absorption Spectroscopy.** X-ray absorption spectroscopy (XAS) measurements were performed at the Stanford Synchrotron Radiation Lightsource (SSRL) at SLAC National Accelerator Laboratory at beam line 4—1 using a Si(220) monochromator. X-ray absorption near edge structure (XANES) and extended X-ray absorption fine structure (EXAFS) spectra were recorded at the Pt $L_3$-edge

(11564 eV) in fluorescence mode using a 32 element, liquid nitrogen-cooled Ge detector (Canberra). The catalysts (approximately 30 mg) were loaded into 3 mm OD quartz tubes, which were heated with resistive coils and fitted with o-rings to a gas flow manifold. A platinum foil was scanned simultaneously for energy calibration. Raw XAS data was energy-calibrated, merged and normalized using the Athena interface of the Demeter software package.[2] For conventional EXAFS analysis, the EXAFS data was extracted in k-space and the Fourier-transform was conducted on the $k^2$-weighted EXAFS function. Phase shifts and amplitudes for relevant backscattering paths were calculated using FEFF6. The Artemis interface of the Demeter package was used for EXAFS modeling, taking into account $k^1$-, $k^2$-, and $k^3$-weighting. The maximum number of parameters extracted from the data was determined using the Nyquist criterion. Automated, DFT-based EXAFS modeling was also performed as described below in the Computational Methods section.

**In-situ XAS Experiments.** The conditions of the in-situ XAS experiments for Pt/ZSM-5 and low-pair Pt/ZSM-5 were as follows. Samples (directly following ion exchange and drying, as described in the Sample Preparation section) were loaded into 3 mm OD quartz tubes, and helium was flowed to purge air out of the reactor. With sample under helium at room temperature, EXAFS spectra were collected (4 scans). Next, 20% $O_2$ in helium was flowed (20 mL/min) and temperature was increased at 10 °C/min to 120 °C. Temperature was held constant at 120 °C for 20 min to allow desorption of water from the sample. Then temperature was increased at 10 °C/min to 700 °C. Temperature was held constant at 700 °C for 1 h before sample was cooled to room temperature. XANES spectra were collected continuously during the entire thermal treatment. With the sample at room temperature, flow was switched to helium (20 mL/min) and EXAFS spectra were collected (4 scans). Next, 10% $H_2$ in helium was flowed (20 mL/min) and the sample was heated at 10 °C/min to 100 °C and held constant at that temperature for 1.5 h while EXAFS spectra were collected. Then the sample was heated at 10 °C/min to 200 °C and held constant at that temperature for 2.5 h while EXAFS spectra were collected. Then the sample was heated at 10 °C/min to 500 °C and held constant at that temperature for 30 min before cooling the sample to room temperature. XANES spectra were collected continuously during temperature ramps. With the sample at room temperature, flow was

switched to helium and EXAFS spectra were collected (4 scans). Finally, with sample under flowing 20% $O_2$ in helium (20 mL/min), temperature was increased at 3 °C/min to 700 °C and held at that temperature for 15 min before the sample was cooled to room temperature. With sample at room temperature, flow was switched to helium (20 mL/min) and EXAFS spectra were collected (4 scans). Effluent gas flow was continuously monitored by mass spectrometer (Hiden).

For the experiment in Figure 5d, Pt/ZSM-5 was calcined in $O_2$ at 700 °C as described above. After cooling the sample to room temperature, 10% CO in helium was flowed (20 mL/min) for 15 min before purging with helium (20 mL/min) for 20 min. Then, 10% $H_2$ in helium was flowed (20mL/min) and sample was heated to 100 °C and held at this temperature for 30 min before cooling to room temperature. XAS spectra were collected with sample at room temperature under flowing helium.

**Computational Methods**

**Initial structure generation and DFT calculations.** The complete ensemble of all geometrically unique structures of isolated platinum sitting in between paired framework aluminum (denoted as 2Al-Pt) was generated systematically using the Multiscale Atomic Zeolite Simulation Environment (MAZE) package.[3] All periodic DFT calculations were performed using the Vienna Ab-initio Simulation Package (VASP) with a plane-wave cut-off of 400 eV and the revised-Perdew-Burke-Ernzerhof (RPBE) functional.[4–6] Dispersion interactions were included using the Grimme D3 method with Becke-Jonson damping, and a 0.03 eV/A force cut-off on each atom was used for geometry optimization. The initial pure-silica ZSM-5 topology was obtained from the International Zeolite Association (IZA) database and was unit-cell optimized at a higher plane-wave cut-off of 700 eV with lattice constants 20.09, 19.74, and 13.14 Å. The entire unit cell was fully relaxed (no constraint on atom positions) during the optimization. The formation energy (E) for the 2Al-Pt structures was calculated as:

$$\Delta E = E(Z'\text{-Pt-}Z'') - E(Z'\text{-Pt}) - E(Z''\text{-Pt})$$

where Z' and Z'' represent single Al substitution within the framework. By including the E(Z-Pt) terms in the energy equation, we minimized the energy bias caused by stabilizing Pt with Al atoms substituted in different T-site identities (12 crystallographically unique T-sites in MFI topology). The relative formation

energy (ΔE), as shown in Figure 3.2b, was the formation energy normalized by the lowest energy for clearer comparisons.

**Theoretical EXAFS fitting.** The recently developed QuantEXAFS package was used for the EXAFS fitting and data analysis, utilizing the open-source Larch library. Unlike conventional EXAFS fitting tools, which only allow analysis on a few averaged scattering paths, QuantEXAFS automatically extracted all the relevant scattering paths related to each DFT optimized structure. Taking one of the best-fit 2Al-Pt EXAFS as an example with an r-factor of 0.011, the algorithm rendered 92 scattering paths important and further classified them into different categories, explained in the next paragraph. By taking the DFT optimized structures "as-is" to feed into the EXAFS fitting algorithms, we can capture each of the unique local environments of the Pt species with fixed coordination numbers. Moreover, owing to the rapid advances in high-performance computing resources, we can now perform EXAFS analysis for over >300 DFT optimized structures in under 2 hours.

In order to fit the theoretical EXAFS equation with the experimentally obtained data, we used nine fitting parameters in the current analysis, which is within the upper bound of fifteen based on the Nyquist criterion. The nine fitting parameters include (1) A single energy correction term for all relevant scattering paths; (2) Three distance correction terms, categorizing scattering paths by effective scattering distances (reff), using different values for each of the three shells in ranges <2.1, 2.1~3, and >3A in the r-space; and (3) Five disorder (sigma squared) terms classifying paths based on both reff and bond types, including $1^{st}$-shell Pt-O single scattering (sig2_0), $2^{nd}$-shell Pt-Al single scattering (sig2_1), $2^{nd}$-shell Pt-Si single scattering (sig2_2), $3^{rd}$-shell single scattering (sig2_3), and rest of the multiple scattering paths (sig2_4). The $So^2$ term was 0.8, obtained by fitting EXAFS spectrum of Pt foil (Table S3.3). All fittings are done in the r-space of $k^3$ weighted EXAFS, with R-range 1.2 – 4.2 A, and K-range 3-10.8 $A^{-1}$.

As an illustrative example, EXAFS fitting results from the structure of Figures 3.2c and 3.2d are shown below. The overall fit is shown in Figure S3.i (equivalent to Figure 3.2c). The algorithm renders 92 scattering paths important and classifies them into five categories with different disorder terms, which are each depicted in Figure S3.ii. Table S3.i shows the optimized parameters of fitting the simulated spectra to

the experimentally obtained spectra, with the CNs taken directly from DFT optimized structures. Fit parameters are shown in Table S3.i. Since the scatter types are not specifically defined in category 3 and 4 (with sig2_3 & sig2_4), CN (coordination number) and R (bond distance) are not shown in Table S3.i.

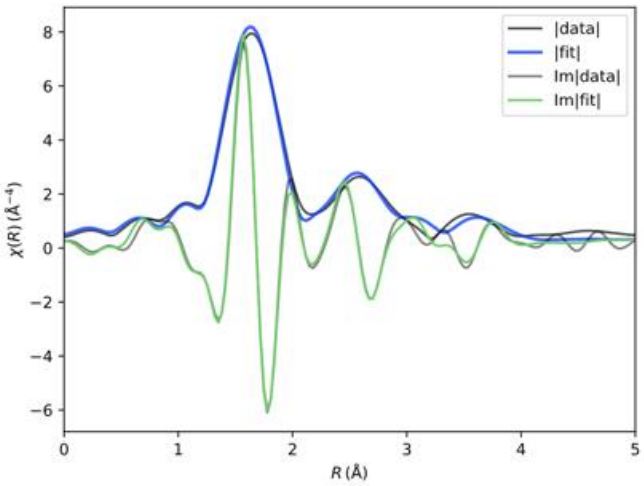


**Figure S3.i.** Theoretical EXAFS fitting — DFT model A (structural model of Figure 3.2c-d). Magnitudes (fit, blue; experiment, black) and imaginary parts (fit, green; experiment, gray) of Fourier-transformed EXAFS of Pt/ZSM-5 at room temperature after exposure to $O_2$ at 700 °C.

**Table S3.i.** Theoretical EXAFS fit parameters from model A (model of Figures 3.2c-d and S3.i).

| Category | N | R (Å) | $\Delta\sigma^2$ (Å$^2$) | $\Delta E_0$ (eV) | R-factor | Reduced $\chi^2$ |
|---|---|---|---|---|---|---|
| 0 (Pt—O) | 4 | 2.02 ± 0.02 | 0.004 | 12.3 | 0.011 | 4.69 |
| 1 (Pt—Al) | 2 | 2.77 ± 0.01 | 0.007 | | | |
| 2 (Pt—Si) | 3 | 3.28 ± 0.02 | 0.019 | | | |
| 3 | | | 0.011 | | | |
| 4 | | | 0.090 | | | |

Notation: N, coordination number; R, scattering path length; $\Delta\sigma^2$, disorder term; $\Delta E_0$, inner potential correction.

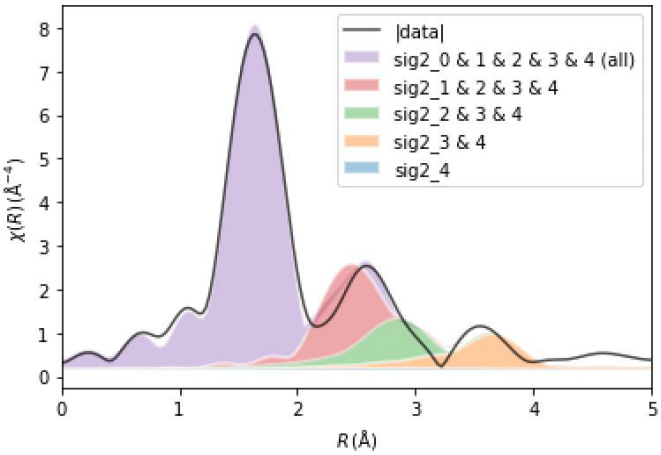


**Figure S3.ii.** Partial contributions of each category of scattering paths (based on the disorder term) to the overall EXAFS fitting shown in Figure S3.i. Here, we choose not to display the imaginary part of the fitting for clearer visualization. The black line shows the magnitude of the Fourier-transformed EXAFS from experiment, while the colored portions are additional contributions given by adding one more category of scattering paths into the overall EXAFS fitting. The figure shows that the multiple scattering paths (sig2_4, blue) have negligible contributions, while all the Pt-X single scattering contributes to the 3$^{rd}$ shell. The Pt-Al and Pt-Si single scattering correspond to the 2$^{nd}$ shell, and Pt-O single scattering contributes to the 1$^{st}$ shell, consistent with expectation.

**Supporting Tables and Figures**

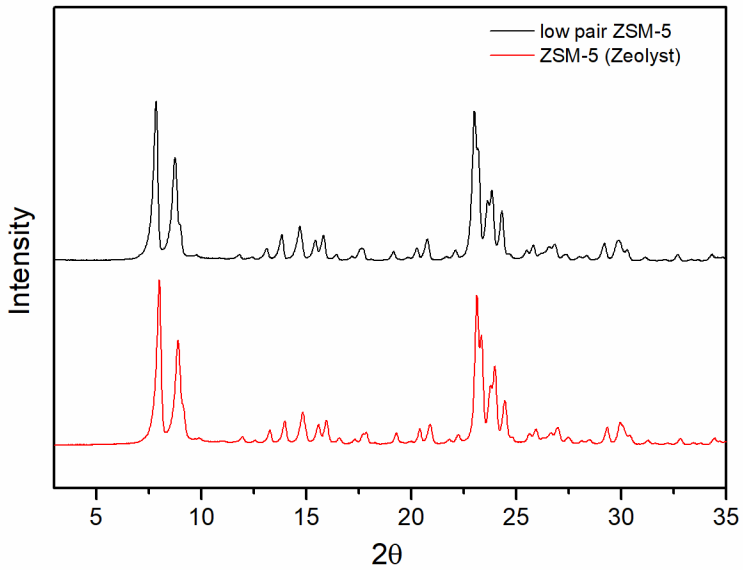


**Figure S3.1.** XRD of ZSM-5 samples. X-ray diffraction patterns of low pair ZSM-5 (black) and Zeolyst ZSM-5 (red).

**Table S3.1**. Elemental compositions of samples.

| Sample | Si/Al[a] | wt% Pt | Pt/Al[a] | Co/Al[a] | 2Co/Al[a,b] | (2Co+Na)/Al[a] |
|---|---|---|---|---|---|---|
| Pt/ZSM-5 | 31 | 0.37 | 0.036 | - | - | - |
| Low-pair Pt/ZSM-5 | 25 | 0.14 | 0.011 | - | - | - |
| Pt/Y | 18 | 0.24 | 0.014 | - | - | - |
| Pt/MOR | 8.3 | 0.38 | 0.011 | - | - | - |
| Pt/Beta | 21 | 0.30 | 0.021 | - | - | - |
| Co-Na-ZSM-5 | 29 | - | - | 0.11 | 0.23 | 0.76 |
| Low pair Co-Na-ZSM-5 | 25 | - | - | 0.024 | 0.049 | 0.59 |
| Co-Na-Y | 18 | - | - | 0.20 | 0.41 | 0.79 |
| Co-Na-MOR | 8.3 | - | - | 0.32 | 0.64 | 1.00 |
| Co-Na-Beta | 21 | - | - | 0.47 | 0.94 | 0.94 |

[a]Atomic ratio. [b]This value is taken as the fraction of total aluminum that is present as pairs.

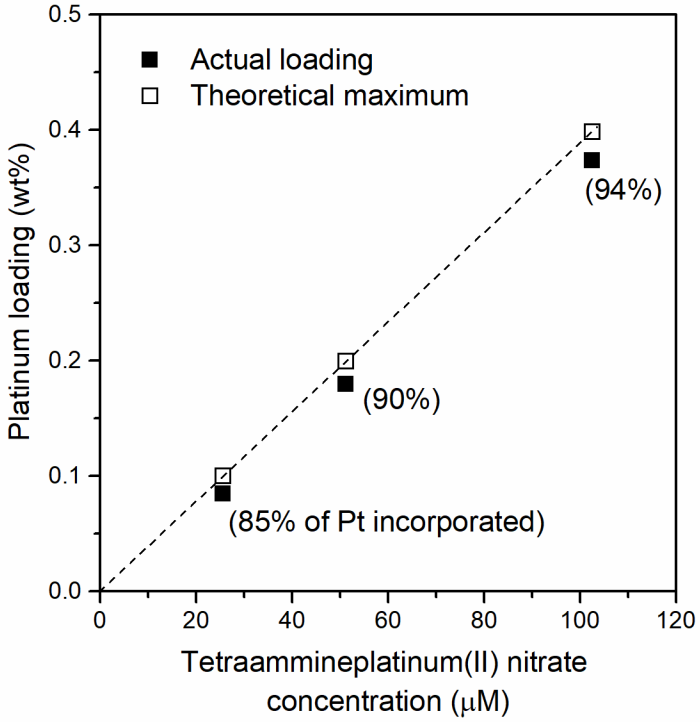


**Figure S3.2.** Platinum incorporation into HZSM-5 by ion exchange. Platinum loading (in wt%, measured by ICP-MS) of Pt/ZSM-5 samples prepared by ion exchange of HZSM-5 with $Pt(NH_3)_4(NO_3)_2$ (full squares) and the theoretical maximum platinum loading in Pt/ZSM-5 assuming all platinum in solution is incorporated into the solid (open squares) as a function of $Pt(NH_3)_4(NO_3)_2$ concentration in solution. Values in parentheses represent the percentages of platinum in solution that were incorporated into the resulting Pt/ZSM-5 samples.

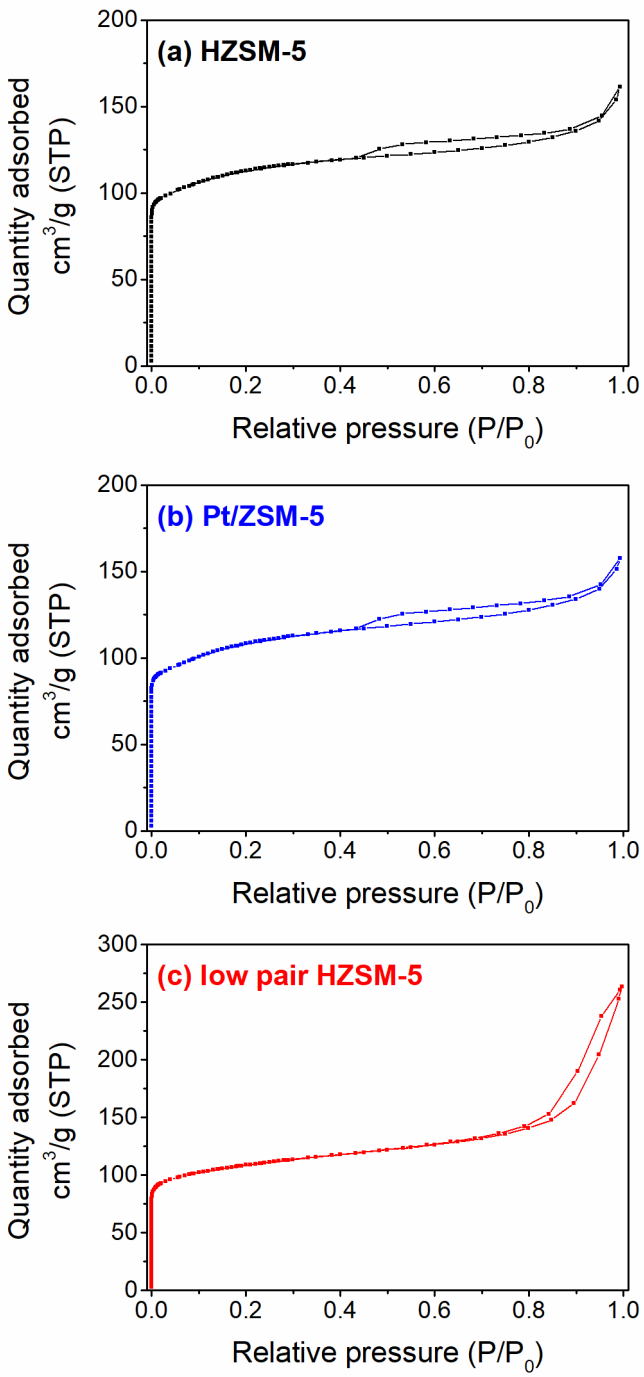


**Figure S3.3.** $N_2$ physisorption isotherms. $N_2$ physisorption isotherms collected at 77 K.

**Table S3.2.** $N_2$ physisorption results

| Sample | BET surface area ($m^2/g$) | External surface area ($m^2/g$)[a] | Micropore surface area ($m^2/g$)[a] | Micropore volume ($cm^3/g$)[a] |
|---|---|---|---|---|
| HZSM-5 (Zeolyst) | 418.1 | 129.0 | 289.2 | 0.118 |
| 0.37 wt% Pt/ZSM-5[b] | 394.3 | 145.9 | 248.4 | 0.103 |
| Low pair HZSM-5 | 399.3 | 145.1 | 245.2 | 0.105 |

[a]Determined by t-plot method. [b]Sample was calcined in 20% $O_2$ in $N_2$ at 700 °C before $N_2$ physisorption was performed.

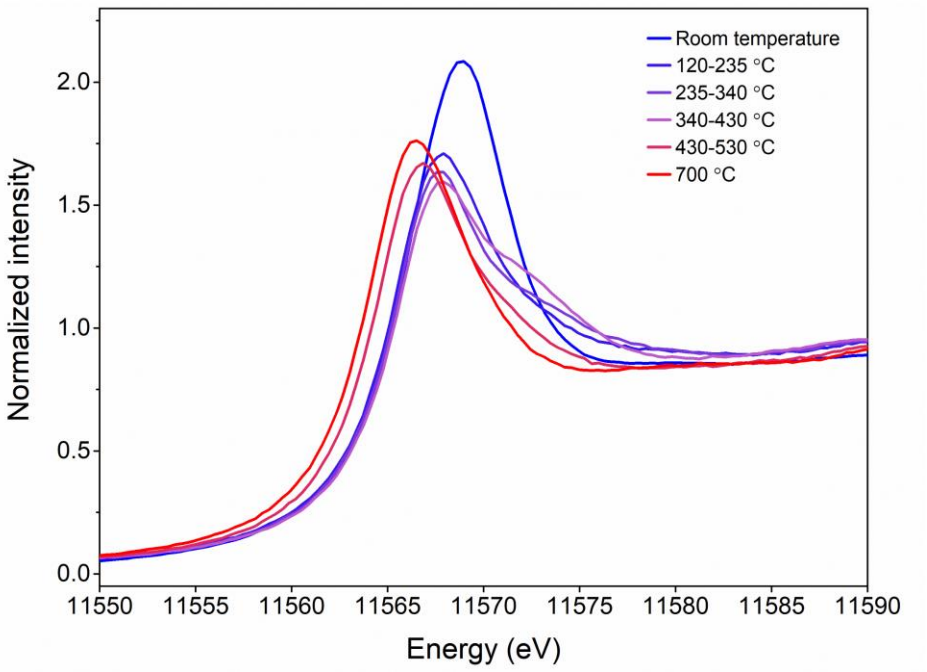


**Figure S3.4.** XANES characterizing Pt/ZSM-5 during calcination. XANES spectra collected as Pt/ZSM-5 (as prepared) was heated under flowing 20% $O_2$ in helium. Temperature was increased at 10 °C/min. Acquisition of each spectra required approximately 10 min. Temperatures noted in figure legend refer to the sample temperature at the beginning and end of collection of each XANES spectrum.

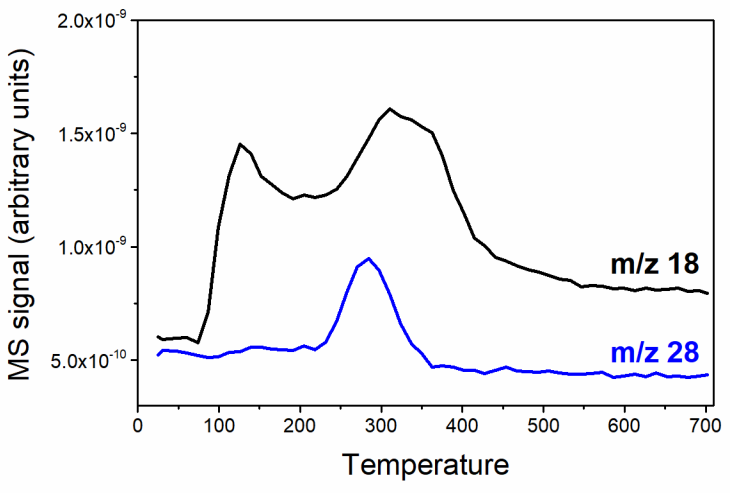


**Figure S3.5.** Mass spectrometry of effluent gas during calcination, XAS experiment.

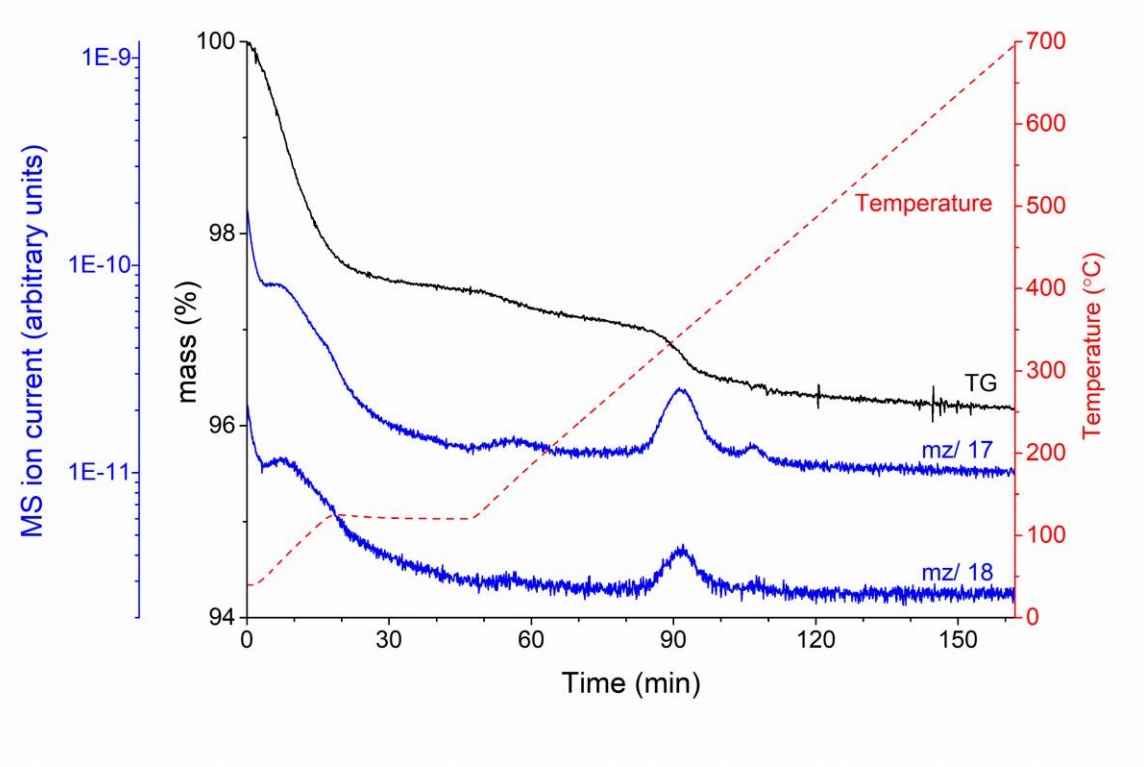


**Figure S3.6.** TGA during calcination of Pt/ZSM-5. Thermogravimetric analysis with online mass spectrometry during heating of as-prepared Pt/ZSM-5 in 20% $O_2$ in $N_2$.

(a)

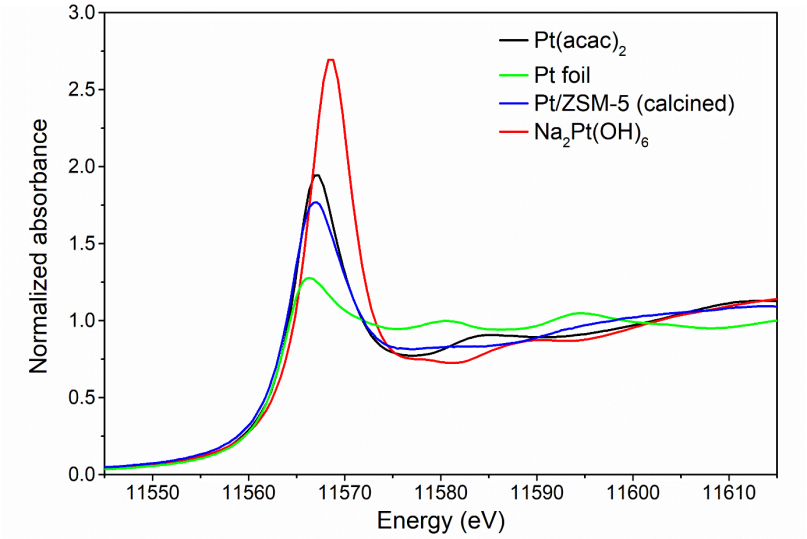


(b)

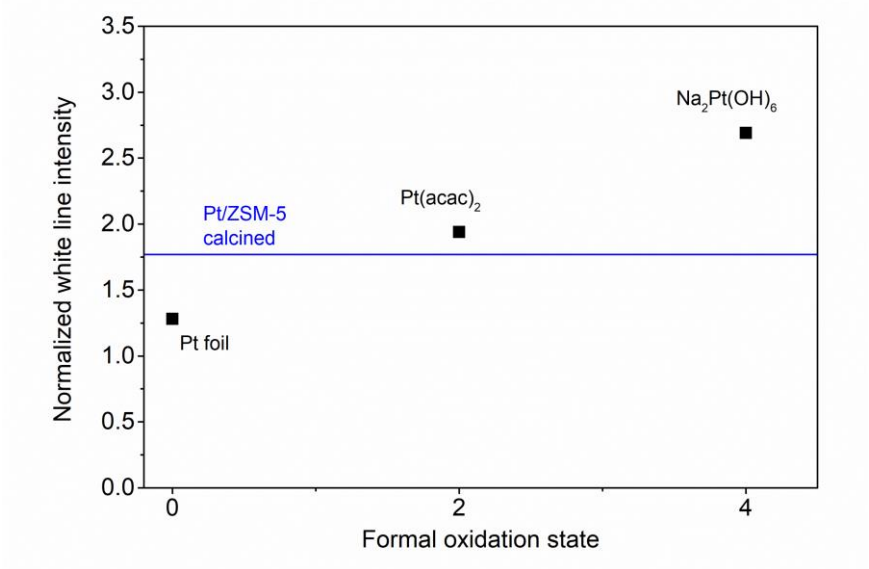


**Figure S3.7.** (a) XANES characterizing calcined Pt/ZSM-5 and platinum reference compounds with formal oxidation state +4, $Na_2Pt(OH)_6$; +2, $Pt(acac)_2$; or 0, Pt foil; acac = acetylacetonato. XANES spectrum of Pt/ZSM-5 was collected at room temperature under helium flow after exposure to 20% $O_2$ in helium at 700 °C. (b) Plot of white line intensity against formal oxidation state of the compounds in (a). White line intensity of calcined Pt/ZSM-5 is labeled in blue.

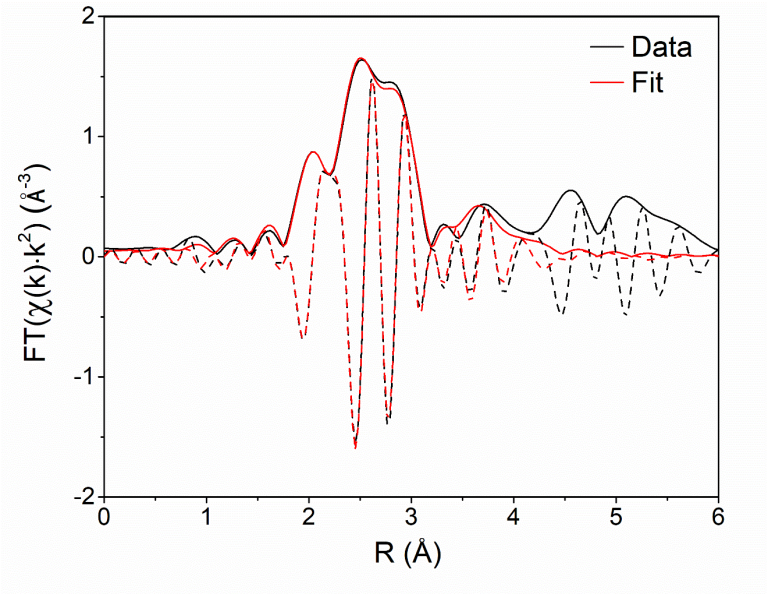


**Figure S3.8.** EXAFS fitting of spectrum characterizing Pt foil. Magnitude (solid) and imaginary component (dash) of the $k^2$-weighted Fourier-transform of EXAFS characterizing a Pt foil (black) compared to the best-fit model (red).

**Table S3.3.** Best-fit EXAFS model characterizing a Pt foil

| **Scattering path [$R_{eff}$ (Å)]** | **N** | **$S_0^2$** | **$\Delta E_0$ [eV]** | **R [Å]** | **$10^3 \cdot \sigma^2$ [Å$^2$]** | **R-factor** |
|---|---|---|---|---|---|---|
| Pt-Pt [2.81] | 12 | 0.81 ± 0.05 | 7.5 ± 0.5 | 2.76 ± 0.00 | 4.7 ± 0.4 | 0.008 |
| Pt-Pt [3.98] | 6 | | | 3.92 ± 0.01 | 5.5 ± 1.0 | |

Notation: N, coordination number; $S_0^2$, amplitude correction term; $\Delta E_0$, energy correction factor; R, scattering path length; $\sigma^2$, disorder term.

k-range: 3.1—12.5 Å$^{-1}$

R-range: 1.0—4.1 Å

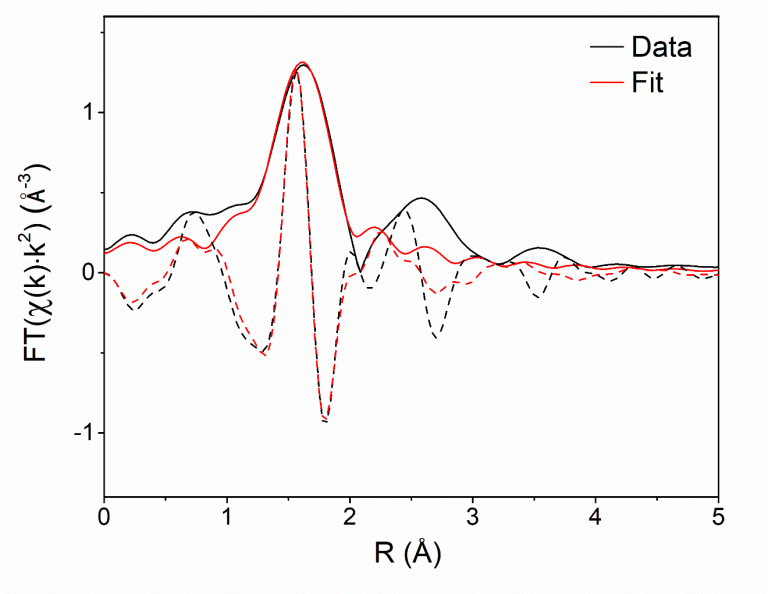


**Figure S3.9.** EXAFS fitting of spectrum characterizing calcined Pt/ZSM-5 – Model 1 (Pt-O). Magnitude (solid) and imaginary component (dash) of the $k^2$-weighted Fourier-transform of EXAFS characterizing Pt/ZSM-5 at room temperature in helium after exposure to $O_2$ at 700 °C (black) compared to the best-fit model 1 (red).

**Table S3.4.** Best-fit EXAFS model 1 (Pt-O) characterizing calcined Pt/ZSM-5

| **Scattering path [$R_{eff}$ (Å)]** | **N** | **$S_0^2$** | **$\Delta E_0$ [eV]** | **R [Å]** | **$10^3 \cdot \sigma^2$ [Å$^2$]** | **R-factor** |
|---|---|---|---|---|---|---|
| Pt-O [2.00] | 4.08 ± 0.80 | 0.81 | 13.3 ± 2.2 | 2.01 ± 0.02 | 3.0 ± 2.8 | 0.015 |

Notation: N, coordination number; $S_0^2$, amplitude correction term; $\Delta E_0$, energy correction factor; R, scattering path length; $\sigma^2$, disorder term.

Values without error bounds were held constant.

k-range: 3.0—10.8 Å$^{-1}$

R-range: 1.0—2.1 Å

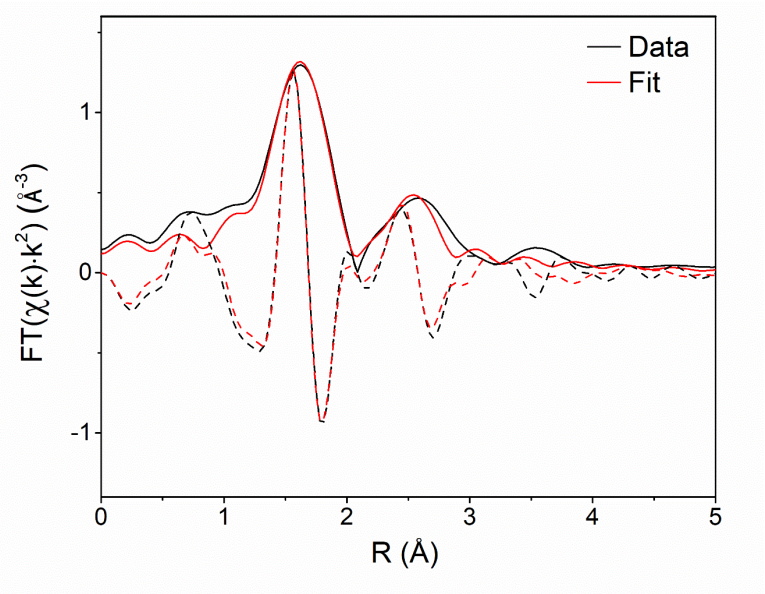


**Figure S3.10.** EXAFS fitting of spectrum characterizing calcined Pt/ZSM-5 – Model 2 (Pt-O, Pt-Si). Magnitude (solid) and imaginary component (dash) of the $k^2$-weighted Fourier-transform of EXAFS characterizing Pt/ZSM-5 at room temperature in helium after exposure to $O_2$ at 700 °C (black) compared to the best-fit model 2 (red).

**Table S3.5.** Best-fit EXAFS model 2 (Pt-O, Pt-Si) characterizing calcined Pt/ZSM-5

| **Scattering path [$R_{eff}$ (Å)]** | **N** | **$S_0^2$** | **$\Delta E_0$ [eV]** | **R [Å]** | **$10^3 \cdot \sigma^2$ [Å$^2$]** | **R-factor** |
|---|---|---|---|---|---|---|
| Pt-O [2.00] | 3.91 ± 0.83 | 0.81 | 14.9 ± 2.5 | 2.02 ± 0.02 | 2.5 ± 2.8 | 0.020 |
| Pt-Si [2.70] | 1.86 ± 1.42 | | 15.0 ± 7.0 | 2.78 ± 0.07 | 5.7 ± 9.7 | |

Notation: N, coordination number; $S_0^2$, amplitude correction term; $\Delta E_0$, energy correction factor; R, scattering path length; $\sigma^2$, disorder term.

Values without error bounds were held constant.

k-range: 3.0—10.8 Å$^{-1}$

R-range: 1.0—3.1 Å

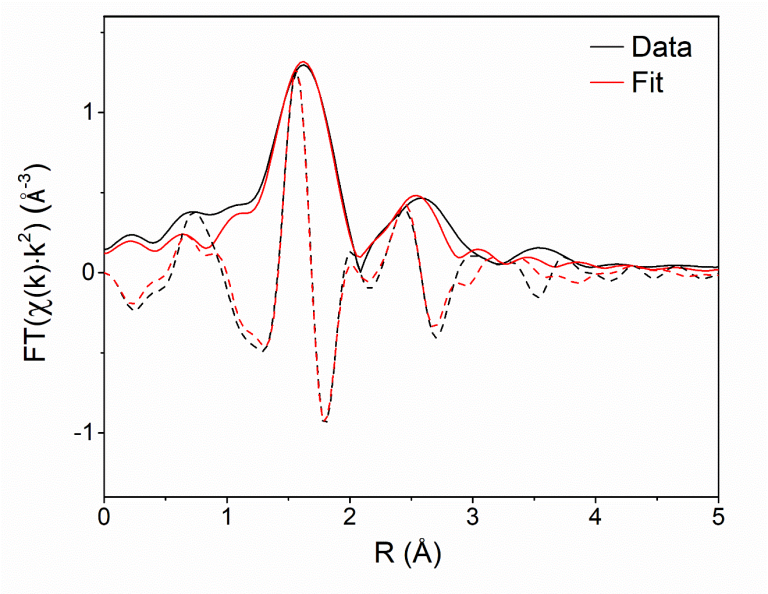


**Figure S3.11.** EXAFS fitting of spectrum characterizing calcined Pt/ZSM-5 – Model 3 (Pt-O, Pt-Al). Magnitude (solid) and imaginary component (dash) of the $k^2$-weighted Fourier-transform of EXAFS characterizing Pt/ZSM-5 at room temperature in helium after exposure to $O_2$ at 700 °C (black) compared to the best-fit model 3 (red).

**Table S3.6.** Best-fit EXAFS model 3 (Pt-O, Pt-Al) characterizing calcined Pt/ZSM-5

| **Scattering path [$R_{eff}$ (Å)]** | **N** | **$S_0^2$** | **$\Delta E_0$ [eV]** | **R [Å]** | **$10^3 \cdot \sigma^2$ [Å$^2$]** | **R-factor** |
|---|---|---|---|---|---|---|
| Pt-O [2.00] | 3.95 ± 0.86 | 0.81 | 15.1 ± 0.9 | 2.02 ± 0.02 | 2.6 ± 2.8 | 0.020 |
| Pt-Al [2.80] | 2.00 ± 1.55 | | 10.8 ± 7.1 | 2.79 ± 0.07 | 5.4 ± 9.8 | |

Notation: N, coordination number; $S_0^2$, amplitude correction term; $\Delta E_0$, energy correction factor; R, scattering path length; $\sigma^2$, disorder term.

Values without error bounds were held constant.

k-range: 3.0—10.8 Å$^{-1}$

R-range: 1.0—3.1 Å

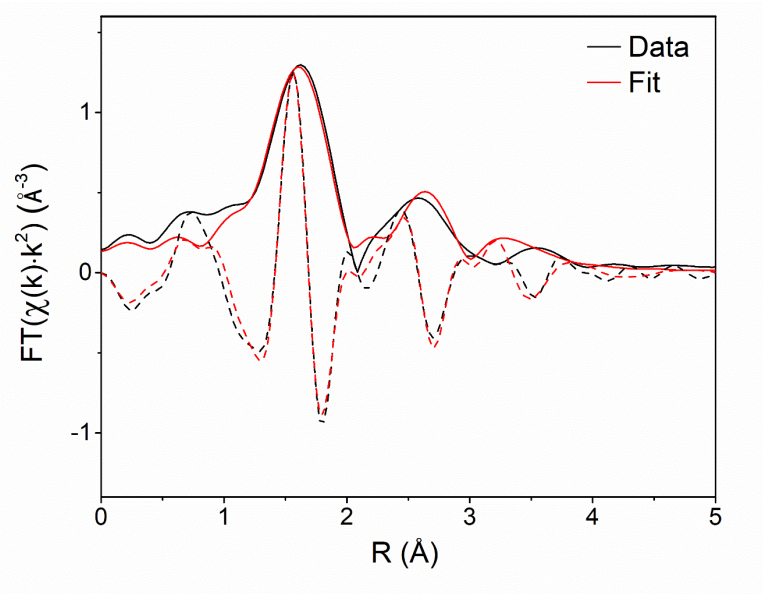


**Figure S3.12.** EXAFS fitting of spectrum characterizing calcined Pt/ZSM-5 – Model 4 (Pt-O, Pt-Pt). Magnitude (solid) and imaginary component (dash) of the $k^2$-weighted Fourier-transform of EXAFS characterizing Pt/ZSM-5 at room temperature in helium after exposure to $O_2$ at 700 °C (black) compared to the best-fit model 4 (red).

**Table S3.7.** Best-fit EXAFS model 4 (Pt-O, Pt-Pt) characterizing calcined Pt/ZSM-5

| **Scattering path [$R_{eff}$ (Å)]** | **N** | **$S_0^2$** | **$\Delta E_0$ [eV]** | **R [Å]** | **$10^3 \cdot \sigma^2$ [Å$^2$]** | **R-factor** |
|---|---|---|---|---|---|---|
| Pt-O [2.00] | 4.48 ± 0.84 | 0.81 | 13.2 ± 2.0 | 2.01 ± 0.02 | 4.1 ± 2.8 | 0.025 |
| Pt-Pt [2.80] | -9.53 ± 6.64 | | 23.0 ± 3.9 | 2.95 ± 0.06 | 16.7 ± 9.6 | |

Notation: N, coordination number; $S_0^2$, amplitude correction term; $\Delta E_0$, energy correction factor; R, scattering path length; $\sigma^2$, disorder term.

Values without error bounds were held constant.

k-range: 3.0—10.8 Å$^{-1}$

R-range: 1.0—3.1 Å

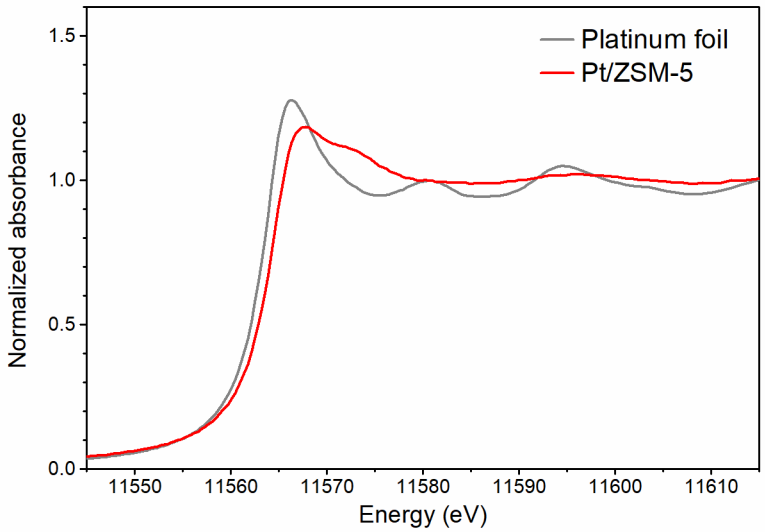


**Figure S3.13.** XANES characterizing Pt/ZSM-5 after exposure to $H_2$ at 500 °C. XANES spectrum of Pt/ZSM-5 was collected at room temperature under helium flow after sample was heated to 500 °C in 10% $H_2$ in helium.

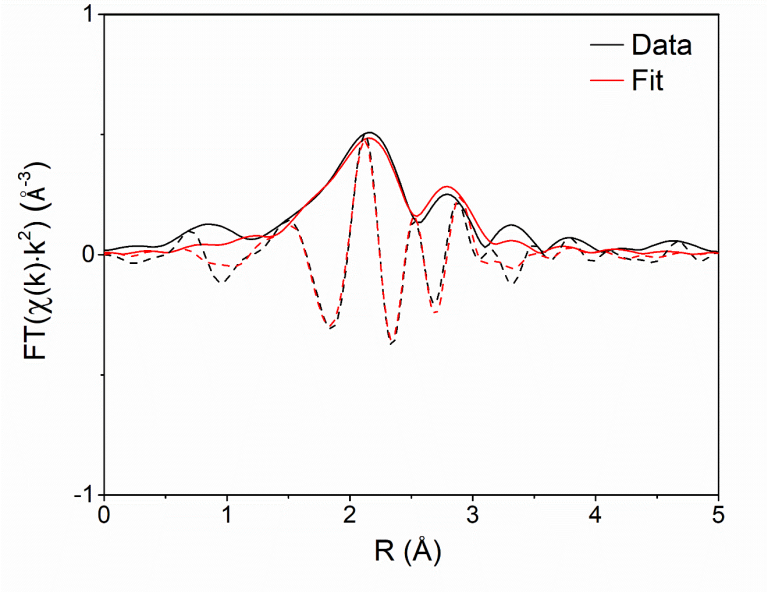


**Figure S3.14.** EXAFS fitting of spectrum characterizing Pt/ZSM-5 after exposure to $H_2$ at 500 °C – Model 5 (Pt-Pt). Magnitude (solid) and imaginary component (dash) of the $k^2$-weighted Fourier-transform of EXAFS characterizing Pt/ZSM-5 at room temperature in helium after exposure to $H_2$ at 500 °C (black) compared to the best-fit model 5 (red).

**Table S3.8.** Best-fit EXAFS model 5 (Pt-Pt) characterizing reduced ($H_2$ 500 °C) Pt/ZSM-5

| **Scattering path [$R_{eff}$ (Å)]** | **N** | **$S_0^2$** | **$\Delta E_0$ [eV]** | **R [Å]** | **$10^3 \cdot \sigma^2$ [Å$^2$]** | **R-factor** |
|---|---|---|---|---|---|---|
| Pt-Pt [2.70] | 8.24 ± 0.98 | 0.81 | 1.68 ± 1.0 | 2.65 ± 0.01 | 12.4 ± 1.3 | 0.023 |

Notation: N, coordination number; $S_0^2$, amplitude correction term; $\Delta E_0$, energy correction factor; R, scattering path length; $\sigma^2$, disorder term.

Values without error bounds were held constant.

k-range: 3.0—10.6 Å$^{-1}$

R-range: 1.0—3.1 Å

(a)

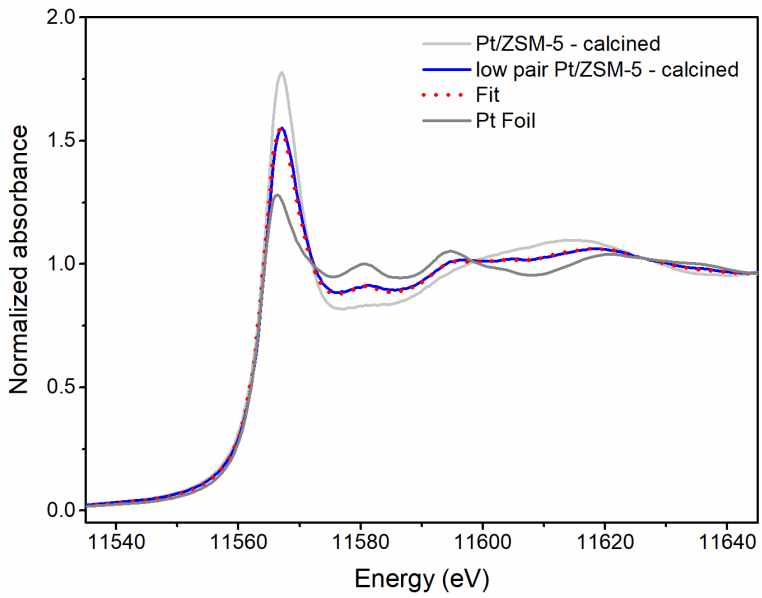


(b)

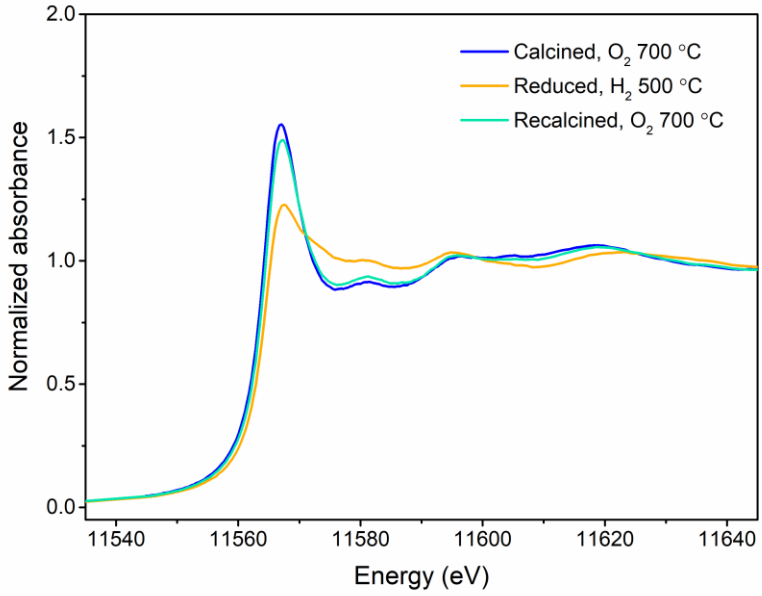


**Figure S3.15.** XANES spectra of low pair Pt/ZSM-5. **(a)** XANES spectra of calcined Pt/ZSM-5 (light gray), calcined low pair Pt/ZSM-5 (blue), and platinum foil (dark gray) and fit (red dot) of low pair Pt/ZSM-5 spectrum as linear combination of Pt/ZSM-5 (55% contribution) and platinum foil (45% contribution) spectra. **(b)** XANES spectra of low-pair Pt/ZSM-5 after calcination ($O_2$ at 700 °C), subsequent reduction ($H_2$ at 500 °C), and subsequent recalcination ($O_2$ at 700 °C).

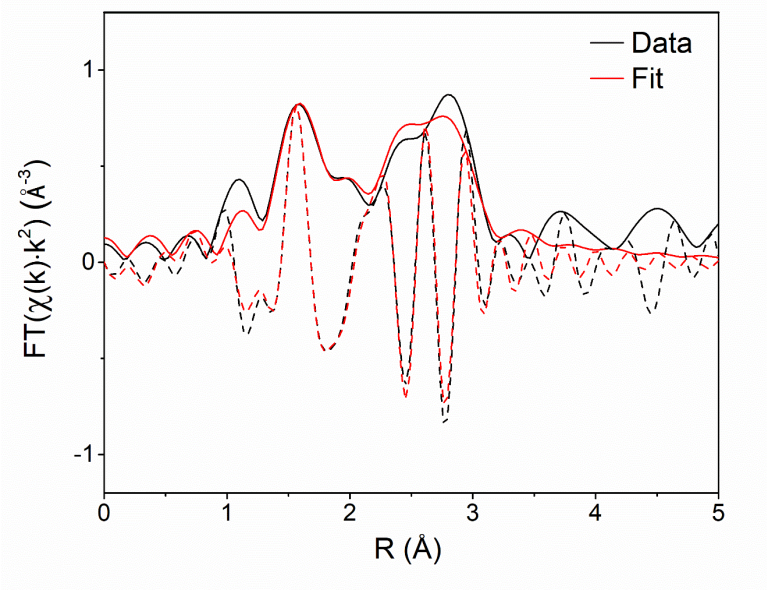


**Figure S3.16.** EXAFS fitting of spectrum characterizing calcined low pair Pt/ZSM-5 – Model 6 (Pt-O, Pt-Pt). Magnitude (solid) and imaginary component (dash) of the $k^2$-weighted Fourier-transform of EXAFS characterizing low pair Pt/ZSM-5 at room temperature in helium after exposure to $O_2$ at 700 °C (black) compared to the best-fit model 6 (red).

**Table S3.9.** Best-fit EXAFS model 6 (Pt-O, Pt-Pt) characterizing calcined Pt/ZSM-5

| **Scattering path [$R_{eff}$ (Å)]** | **N** | **$S_0^2$** | **$\Delta E_0$ [eV]** | **R [Å]** | **$10^3 \cdot \sigma^2$ [Å$^2$]** | **R-factor** |
|---|---|---|---|---|---|---|
| Pt-O [2.00] | 1.84 ± 0.57 | 0.81 | 12.8 ± 3.5 | 2.01 ± 0.03 | 0.6 ± 3.3 | 0.023 |
| Pt-Pt [2.77] | 3.95 ± 1.50 | | 6.6 ± 3.6 | 2.76 ± 0.02 | 1.9 ± 2.2 | |

Notation: N, coordination number; $S_0^2$, amplitude correction term; $\Delta E_0$, energy correction factor; R, scattering path length; $\sigma^2$, disorder term.

Values without error bounds were held constant.

k-range: 3.0—12.0 Å$^{-1}$

R-range: 1.2—3.1 Å

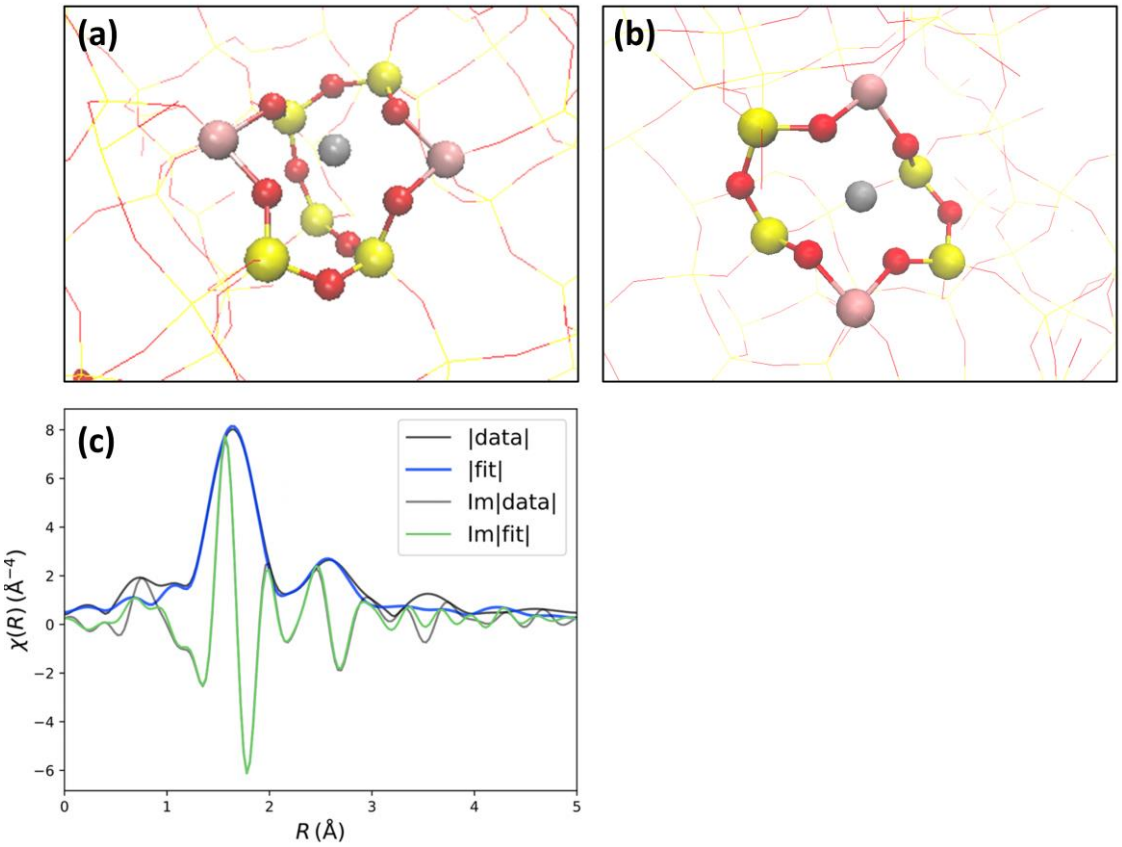


**Figure S3.17.** Structure and EXAFS fitting of DFT model B (labeled in Figure 3.2b with r-factor of 0.014). (a) Visual representation of 2Al—Pt model B. Red, O; yellow, Si; pink, Al; gray, Pt; white, H. (b) Same as (a), except showing only the 6-MR surrounding platinum. (c) Magnitudes (fit, blue; experiment, black) and imaginary parts (fit, green; experiment, gray) of Fourier-transformed EXAFS of Pt/ZSM-5 after exposure to $O_2$ at 700 °C with fitting based on 2Al–Pt structure B.

In model B, platinum is coordinated to four oxygen atoms of a 6-MR that is composed of two 5-MR's. This site is accessible from the straight channel of MFI. This is a likely structure, as the r-factor and relative energy of model B are comparable to those of the preferred model A (Figure 3.2b and 3.2c).

**Table S3.10.** Theoretical EXAFS fit parameters – Model B

| Category | N | R (Å) | $10^3 \cdot \sigma^2$ (Å$^2$) | $\Delta E_0$ (eV) | R-factor | Reduced $\chi^2$ |
|---|---|---|---|---|---|---|
| 0 (Pt—O) | 4 | 2.06 ± 0.02 | 4.0 | 12.3 | 0.014 | 5.71 |
| 1 (Pt—Al) | 2 | 2.91 ± 0.004 | 7.3 | | | |
| 2 (Pt—Si) | 4 | 2.96 ± 0.16 | 16 | | | |
| 3 | | | 3.5 | | | |
| 4 | | | 16 | | | |

Notation: N, coordination number; R, scattering path length; $\sigma^2$, disorder term; $\Delta E_0$, inner potential correction.

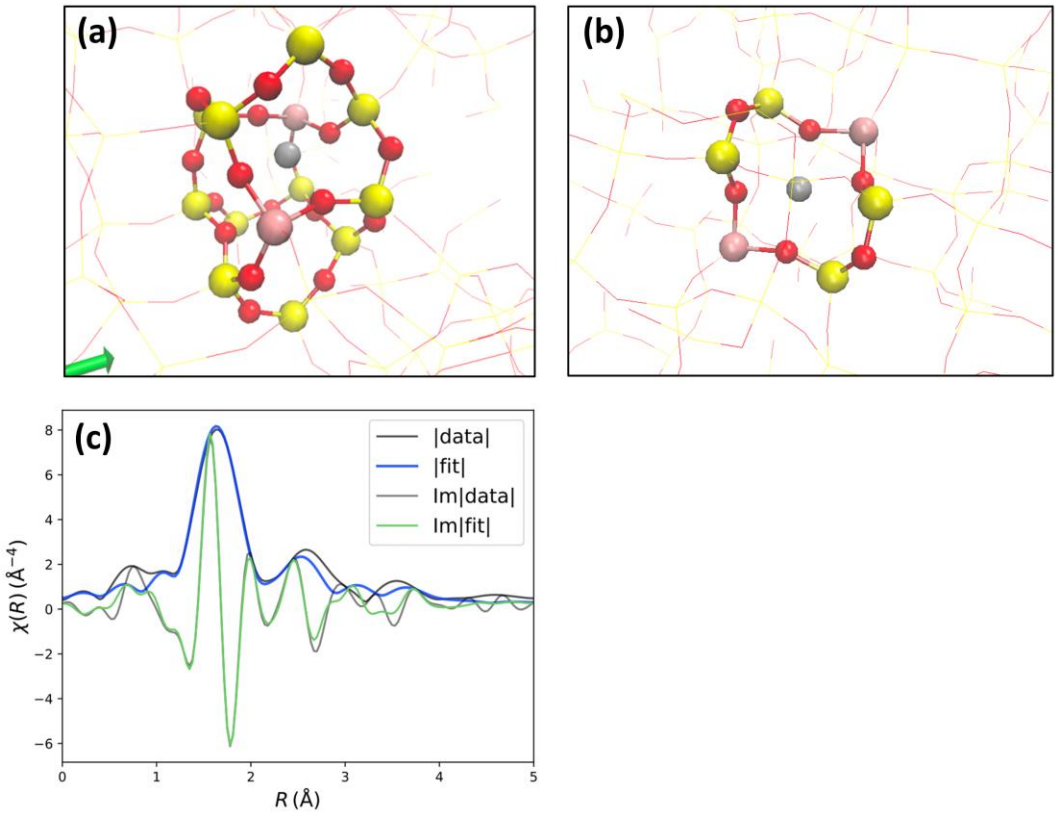


**Figure S3.18.** Structure and EXAFS fitting of DFT model C (labeled in Figure 3.2b with r-factor of 0.022). (a) Visual representation of 2Al—Pt model C. Red, O; yellow, Si; pink, Al; gray, Pt; white, H. (b) Same as (a), except showing only the 6-MR surrounding platinum. (c) Magnitudes (fit, blue; experiment, black) and imaginary parts (fit, green; experiment, gray) of Fourier-transformed EXAFS of Pt/ZSM-5 after exposure to $O_2$ at 700 °C with fitting based on 2Al–Pt structure C.

Model C had the lowest relative energy of all structures found. In model C, platinum is coordinated to four oxygen atoms of a 6-MR that is part of a $5^8$ cage (cage formed by eight 5-MR's). This site is only accessible to platinum through 5-MR openings, and for this reason, it is considered unlikely. It should be noted that the theoretical EXAFS spectrum from this model fit the experimental data relatively well.

**Table S3.11.** Theoretical EXAFS fit parameters – Model C

| Category | N | R (Å) | $10^3 \cdot \sigma^2$ (Å$^2$) | $\Delta E_0$ (eV) | R-factor | Reduced $\chi^2$ |
|---|---|---|---|---|---|---|
| 0 (Pt—O) | 4 | 2.06 ± 0.01 | 4.1 | 12.8 | 0.022 | 8.97 |
| 1 (Pt—Al) | 2 | 2.87 ± 0.001 | 6.4 | | | |
| 2 (Pt—Si) | 4 | 2.95 ± 0.11 | 53 | | | |
| 3 | | | 12 | | | |
| 4 | | | 90 | | | |

Notation: N, coordination number; R, scattering path length; $\sigma^2$, disorder term; $\Delta E_0$, inner potential correction.

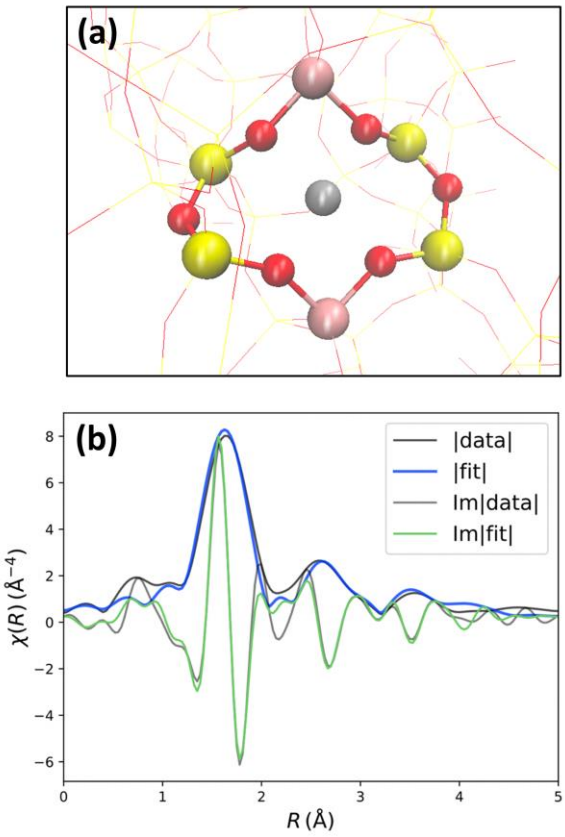


**Figure S3.19.** Structure and EXAFS fitting of DFT model D (labeled in Figure 3.2b with r-factor of 0.043). (a) Visual representation of 2Al—Pt model D. Red, O; yellow, Si; pink, Al; gray, Pt; white, H. (b) Magnitudes (fit, blue; experiment, black) and imaginary parts (fit, green; experiment, gray) of Fourier-transformed EXAFS of Pt/ZSM-5 after exposure to $O_2$ at 700 °C with fitting based on 2Al–Pt structure D.

In model D, platinum is coordinated to four oxygen atoms of a 6-MR. This model had the third lowest relative energy of all 2Al—Pt structures found, but the theoretical EXAFS spectrum from this model did not fit the experimental data as well as those from other models.

**Table S3.12.** Theoretical EXAFS fit parameters – Model D

| Category | N | R (Å) | $10^3 \cdot \sigma^2$ (Å$^2$) | $\Delta E_0$ (eV) | R-factor | Reduced $\chi^2$ |
|---|---|---|---|---|---|---|
| 0 (Pt—O) | 4 | 2.04 ± 0.01 | 4.1 | 10.2 | 0.043 | 17.64 |
| 1 (Pt—Al) | 2 | 2.85 ± 0.02 | 11 | | | |
| 2 (Pt—Si) | 4 | 3.11 ± 0.10 | 0.8 | | | |
| 3 | | | 18 | | | |
| 4 | | | 2 | | | |

Notation: N, coordination number; R, scattering path length; $\sigma^2$, disorder term; $\Delta E_0$, inner potential correction.

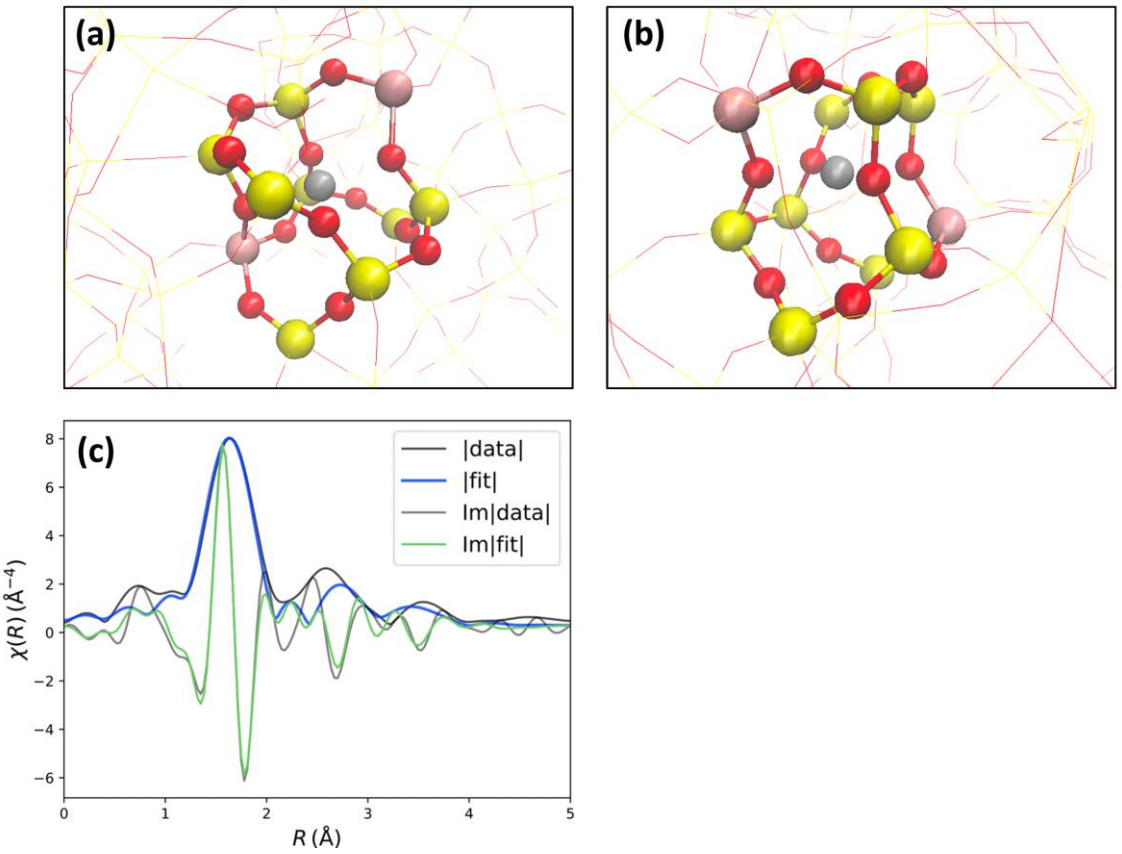


**Figure S3.20.** Structure and EXAFS fitting of DFT model E (labeled in Figure 3.2b with r-factor of 0.076). (a) Visual representation of 2Al—Pt model E. Red, O; yellow, Si; pink, Al; gray, Pt; white, H. (b) Same as (a), except viewing at a different angle that highlights the plane of four oxygen atoms surrounding platinum. (c) Magnitudes (fit, blue; experiment, black) and imaginary parts (fit, green; experiment, gray) of Fourier-transformed EXAFS of Pt/ZSM-5 after exposure to $O_2$ at 700 °C with fitting based on 2Al–Pt structure E.

In model E, platinum is coordinated to four oxygen atoms at similar distances to those in models A, B, C, and D, but in model E, the oxygen atoms are not part of a single 6-MR. This had the highest Al—Al distance of the five lowest relative energy structures, and the theoretical EXAFS spectrum from this model did not fit the experimental data as well as those from other models.

**Table S3.13.** Theoretical EXAFS fit parameters – Model E

| Category | N | R (Å) | $10^3 \cdot \sigma^2$ (Å$^2$) | $\Delta E_0$ (eV) | R-factor | Reduced $\chi^2$ |
|---|---|---|---|---|---|---|
| 0 (Pt—O) | 4 | 2.04 ± 0.01 | 4.2 | 10.0 | 0.076 | 31.25 |
| 1 (Pt—Al) | 2 | 3.22 ± 0.005 | 7.0 | | | |
| 2 (Pt—Si) | 5 | 2.95 ± 0.15 | 15 | | | |
| 3 | | | 12 | | | |
| 4 | | | 76 | | | |

Notation: N, coordination number; R, scattering path length; $\sigma^2$, disorder term; $\Delta E_0$, inner potential correction.

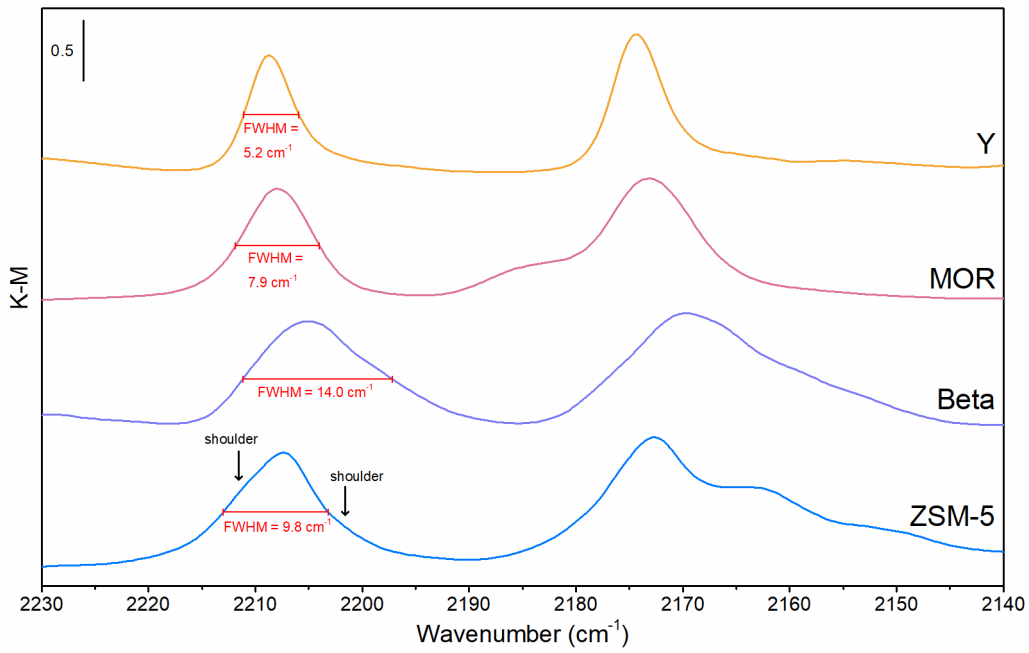


**Figure S3.21.** IR spectra of platinum *gem*-dicarbonyls. IR difference spectra before and after CO adsorption at 30 °C on Pt/Y (Y; Si/Al 15), Pt/mordenite (MOR; Si/Al 6.5), Pt/Beta (Beta; Si/Al 19), and Pt/ZSM-5 (ZSM-5; Si/Al 31) after calcination in 20% $O_2$ in $N_2$ at 700 °C (600 °C for Pt/Beta). For comparison, data are normalized to the intensity of the peak at approximately 2207 $cm^{-1}$.

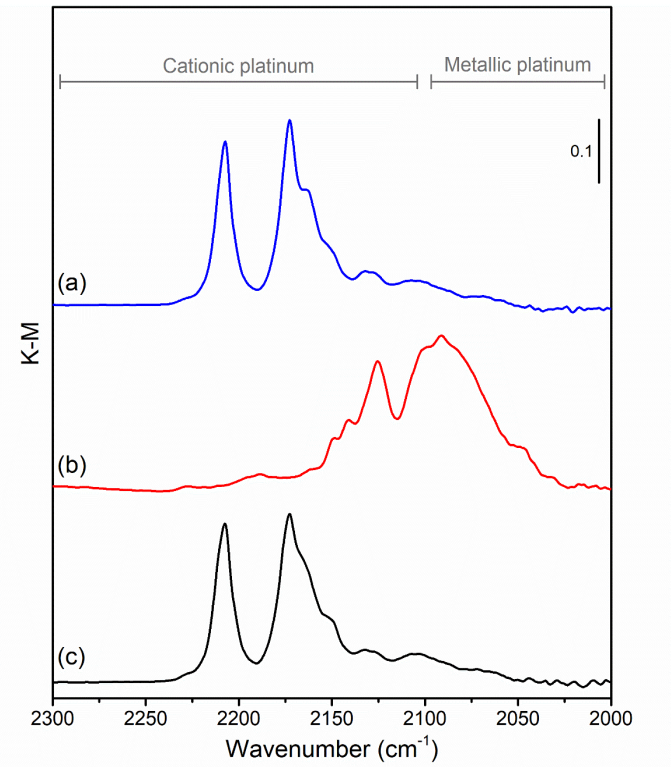


**Figure S3.22.** IR spectra of CO adsorbed at 30 °C on Pt/ZSM-5 under $N_2$ following exposure to (a) $O_2$ at 700 °C, (b) $O_2$ at 700 °C then $H_2$ at 500 °C, or (c) $O_2$ at 700 °C, then $H_2$ at 500 °C, then $O_2$ at 700 °C. In (b), sample was cooled from 700 °C to 500 °C before introducing flowing 10% $H_2$ in $N_2$ for 30 min. In (c), sample was treated as in (b), except following $H_2$ treatment, flow was switched to 20% $O_2$ in $N_2$ and sample was heated to 700 °C. Temperature was held at 700 °C for 30 min before cooling to 30 °C.

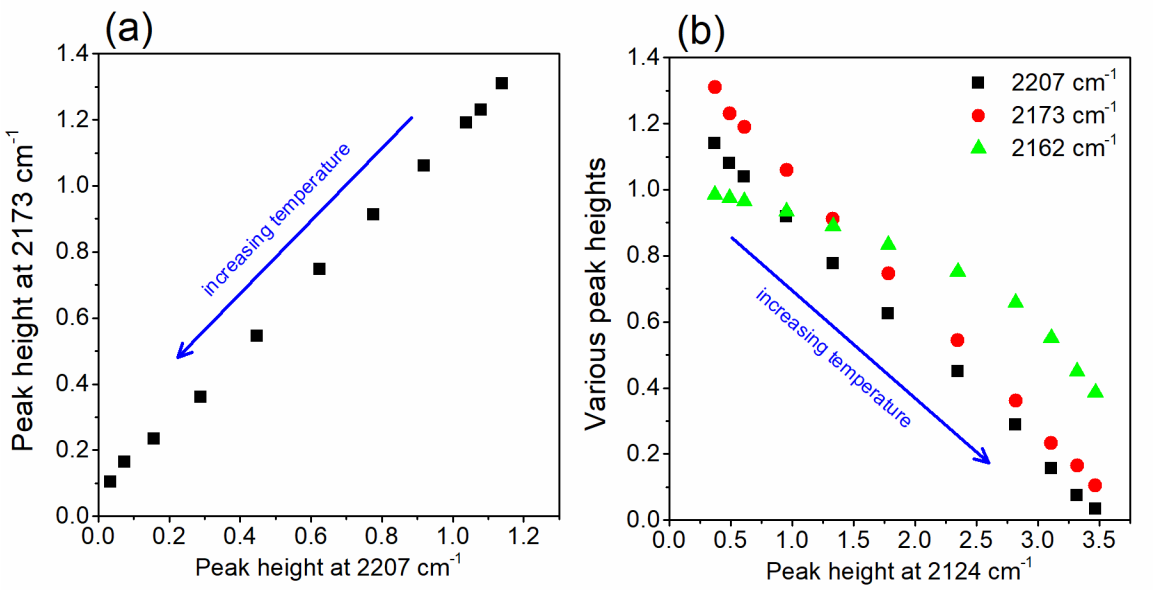


**Figure S3.23.** IR carbonyl band intensities during heating platinum *gem*-dicarbonyls in $H_2$. (a) Maximum IR peak heights of $Pt^{2+}$ *gem*-dicarbonyl bands at 2173 and 2207 $cm^{-1}$ plotted against one another while sample was heated from 30 to 120 °C under flow of 10% $H_2$ in $N_2$. (b) Peak heights of carbonyl bands at 2207, 2173, and 2162 $cm^{-1}$ plotted against the $Pt^{\delta+}$ carbonyl peak height at 2124 $cm^{-1}$ under the same conditions as (a). In both (a) and (b), the first data point represents a spectrum collected under $N_2$ flow at 30 °C, and each subsequent point was collected under $H_2$ at 10 °C increments from 30 to 120 °C.

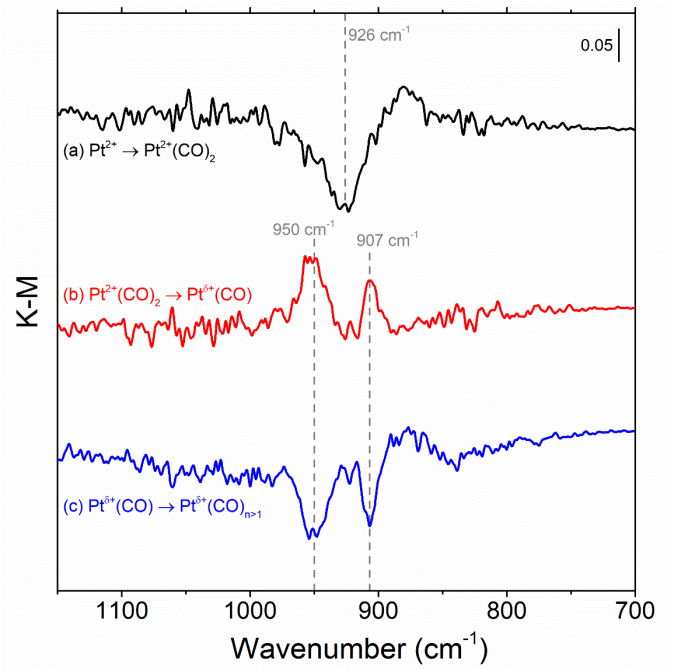


**Figure S3.24.** IR spectra characterizing framework T–O–T region of Pt/ZSM-5. (a) Difference IR spectrum before and after exposure of Pt/ZSM-5, which had been calcined in $O_2$ at 700 °C, to 10% CO flow at 30 °C for 15 min. (b) Difference IR spectrum before and after converting $Pt^{2+}(CO)_2$ in sample from (a) to $Pt^{\delta+}(CO)$ using procedure described in Figure 4a. Both before and after spectra were collected at 30 °C under $N_2$ flow. (c) Difference IR spectrum before and after exposure of sample from (b) to 10% CO flow at 30 °C for 15 min.

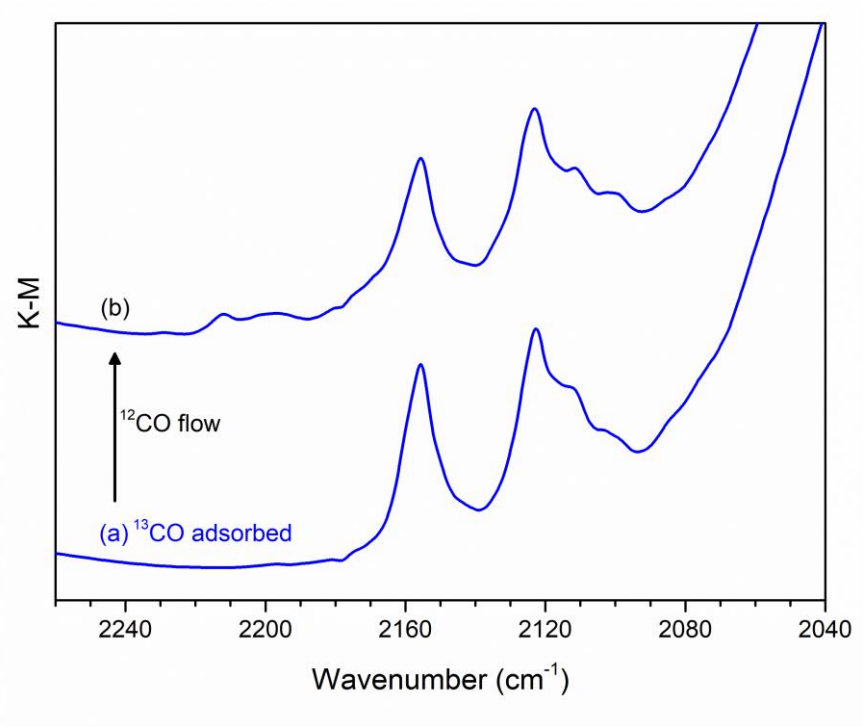


**Figure S3.25.** IR spectra characterizing CO isotope exchange by $Pt^{2+}(CO)_2$. (a) IR spectrum of Pt/ZSM-5 at 30 °C under $N_2$ flow after calcination at 700 °C in 20% $O_2$ in $N_2$ and exposure to flowing 10% $^{13}$CO in $N_2$ at 30 °C for 5 minutes. (b) IR spectrum collected after sample from (a) was exposed to flowing 10% $^{12}$CO in $N_2$ at 30 C for 10 minutes.

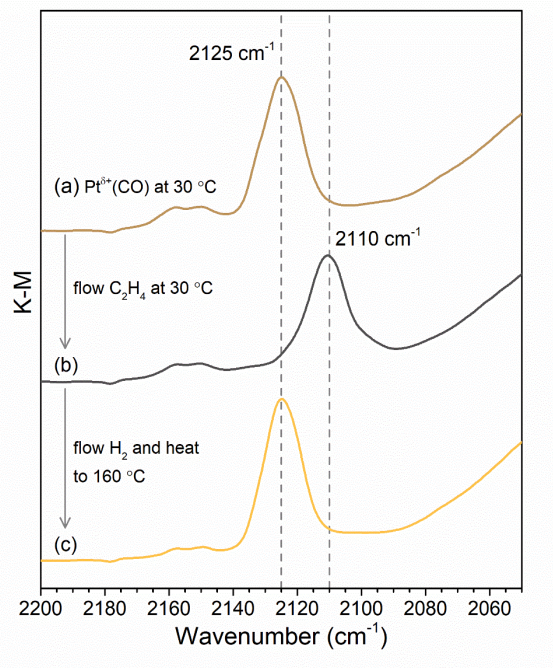


**Figure S3.26.** IR spectra characterizing $C_2H_4$ interaction with $Pt^{\delta+}$(CO). IR spectrum of (a) Pt/ZSM-5 that contained $Pt^{\delta+}$(CO), following treatments described in Figure 4a, under $N_2$ flow at 30 °C. (b) Sample from (a) under $N_2$ flow at 30 °C after exposure to $C_2H_4$ for 15 min. (c) Sample from (b) under $N_2$ flow at 30 °C after exposure to flowing 10% $H_2$ in $N_2$ while heating to 160 °C.

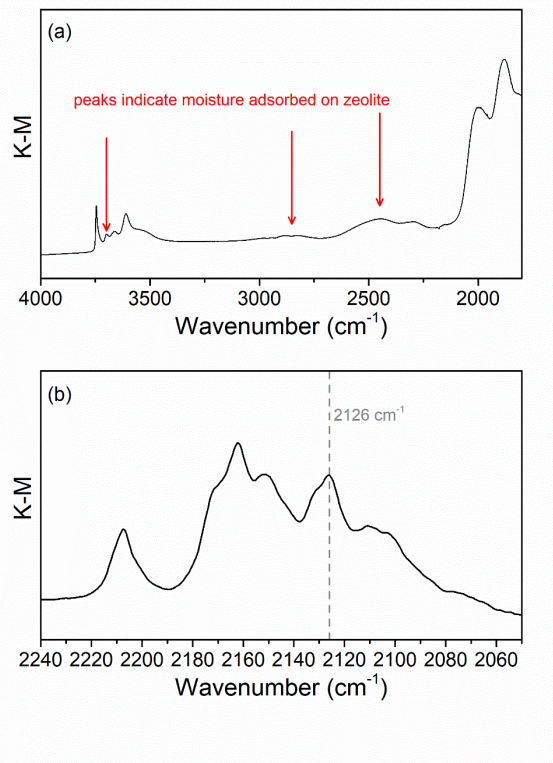


**Figure S3.27.** IR spectra characterizing CO adsorption onto Pt/ZSM-5 in the presence of moisture. (a) IR spectrum of Pt/ZSM-5 in $N_2$ flow at 30 °C after calcination in $O_2$ at 700 °C. The presence of adventitious moisture is indicated by peaks at approximately 3700, 2850, and 2450 $cm^{-1}$.[7] (b) IR spectrum of Pt/ZSM-5 from (a) after exposure to flow of 10% CO in $N_2$ for 15 min and subsequent purging of CO with $N_2$ flow for 2 min.

## References


(1) Dedecek, J.; Balgová, V.; Pashkova, V.; Klein, P.; Wichterlová, B. Synthesis of ZSM-5 Zeolites with Defined Distribution of Al Atoms in the Framework and Multinuclear MAS NMR Analysis of the Control of Al Distribution. *Chem. Mater.* **2012**, *24*, 3231–3239.

(2) Ravel, B.; Newville, M. ATHENA, ARTEMIS, HEPHAESTUS: Data Analysis for X-Ray Absorption Spectroscopy Using IFEFFIT. *J. Synchrotron Radiat.* **2005**, *12*, 537–541.

(3) Antonio, D. D.; Guo, J.; Holton, S. J.; Kulkarni, A. R. Simplifying Computational Workflows with the Multiscale Atomic Zeolite Simulation Environment (MAZE). *SoftwareX* **2021**, *16*, 100797.

(4) Kresse, G.; Furthmüller, J. Efficiency of Ab-Initio Total Energy Calculations for Metals and Semiconductors Using a Plane-Wave Basis Set. *Comput. Mater. Sci.* **1996**, *6*, 15–50.

(5) Kresse, G.; Hafner, J. Ab Initio Molecular-Dynamics Simulation of the Liquid-Metalamorphous-Semiconductor Transition in Germanium. *Phys. Rev. B* **1994**, *49*, 14251–14269.

(6) Kresse, G.; Furthmüller, J. Efficient Iterative Schemes for Ab Initio Total-Energy Calculations Using a Plane-Wave Basis Set. *Phys. Rev. B* **1996**, *54*, 11169–11186.

(7) Jentys, A.; Warecka, G.; Derewinski, M.; Lercher, J. A. Adsorption of Water on ZSM5 Zeolites. *J. Phys. Chem.* **1989**, *93*, 4837–4843.

# **Chapter 4.** Evaluating Chromium–Zeolite Catalysts for Ethane Dehydrogenation with $CO_2$

Results of exploratory experiments

## 4.1 Abstract

Supported chromium catalysts are used widely in industry, but their applicability for ethane dehydrogenation to ethylene is limited by low yields and short catalyst lifetimes. The use of $CO_2$ as a co-reactant has been reported to improve dehydrogenation activity and catalyst stability, but the mechanistic role of $CO_2$ in facilitating ethane dehydrogenation has not been elucidated. In this study, a series of Cr/MFI zeolite catalysts with various support compositions were characterized by IR or X-ray absorption spectroscopies and evaluated for ethane dehydrogenation with or without $CO_2$ in order to identify supported chromium structures whose catalytic activity is impacted by the presence of $CO_2$. Borosilicate and siliceous MFI zeolite supports resulted in similar distributions of supported chromium species including a mixture of $Cr^{2+}$ and $Cr^{3+}$. The copresence of $Cr^{2+}$ and $Cr^{3+}$ correlated with significant enhancements in the rates ethane dehydrogenation when $CO_2$ was added to the reaction mixture. The aluminosilicate MFI zeolite, in contrast, stabilized chromium in the +2 oxidation state during reaction, resulting in a catalyst that exhibited low rates of $CO_2$ reduction to CO by $H_2$ and no enhancement of ethane dehydrogenation by $CO_2$. The mechanistic role of $CO_2$ is discussed in the context of ethane dehydrogenation with Cr/MFI catalysts.

## 4.1 Introduction

Catalytic dehydrogenation of light alkanes shows strong potential to more efficiently utilize natural gas compared to traditional technologies based on energy-intensive hydrocarbon cracking and therefore represents a promising avenue for increased production of value-added chemicals from abundant $C_2$–$C_4$ feedstocks. The need for this technology is especially clear in the context of the recent dramatic increase in supply of light alkanes in the U.S. and the ever-growing demand for olefins in the chemical manufacturing industry. Current alkane dehydrogenation process economics are limited by low single-pass olefin yields, which result from the prevalence of side reactions, and catalyst deactivation by coke deposition.[1] It has been observed that the use of $CO_2$ as a co-reactant enhances catalyst activity, facilitates high olefin selectivities at high alkane conversions, and extends catalyst lifetimes by reducing coking.[2–21]

The use of $CO_2$ as a functional co-reactant for alkane dehydrogenation also contributes to critical ongoing efforts to develop processes that utilize $CO_2$ as a carbon feedstock.[22,23] The use of $CO_2$ for this application has been described as the concurrent of tandem reduction of $CO_2$ to CO and alkane dehydrogenation to its corresponding alkene.[24] Therefore, $CO_2$-assisted alkane dehydrogenation produces two critical chemical feedstocks simultaneously – olefins and syngas.

While the limitations of current approaches to alkane dehydrogenation are well-documented,[1,25] there is a clear lack of comprehensive understanding regarding the influences of catalyst structure and the presence of $CO_2$ on reaction kinetics and catalyst deactivation. In this context, there exists an urgent need to better understand $CO_2$-assisted ethane dehydrogenation in order to design new catalysts capable of overcoming limitations such as low olefin yields and high deactivation rates.

After conducting a broad review of the light alkane dehydrogenation literature, we selected supported chromium (Cr) catalysts as a starting point for investigation. Supported Cr is known to catalyze alkane conversion with high selectivity to olefins.[1,26–28] In fact, alumina-supported Cr ($Cr/Al_2O_3$) is a catalyst applied industrially for dehydrogenation of propane.[1,26] Under certain circumstances, supported Cr catalysts used for alkane dehydrogenation have displayed enhanced ethylene yields in the presence of co-fed $CO_2$.[2–8,11–13,15,21,29,30] Our review of this literature prompted a clear need for compilation of $CO_2$-assisted ethane dehydrogenation selectivity-conversion data for all catalysts analyzed. Results of our literature review are presented in Figure 4.1. Consistent with the observations above regarding the functionality of Cr for dehydrogenation reactions, analysis of the $CO_2$-assisted ethane dehydrogenation literature reveals that the highest ethylene yields are often achieved using catalysts containing Cr (Figure 4.1, open squares).

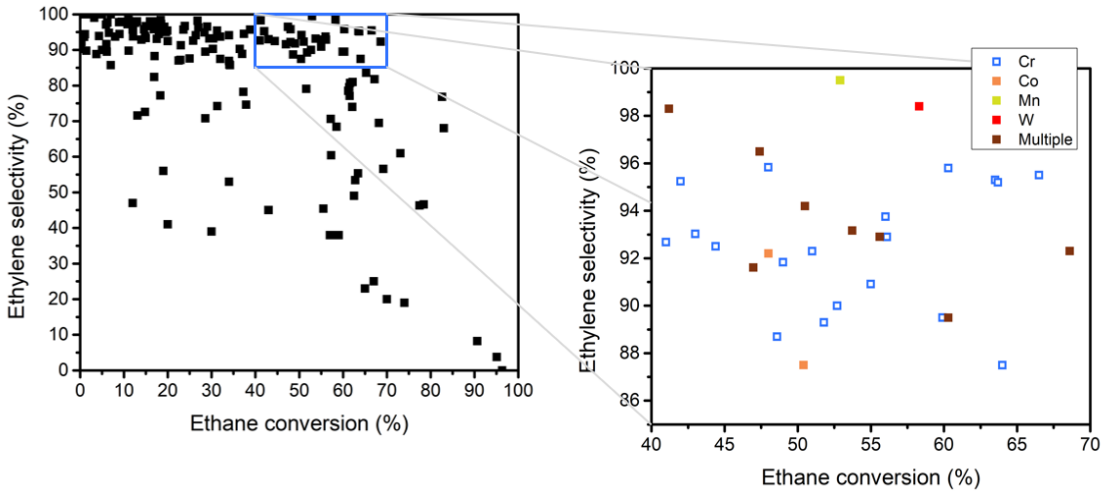


**Figure 4.1.** Compilation of selectivity-conversion data from our analysis of the known $CO_2$-assisted ethane dehydrogenation literature[3–8,10–13,15,21,30–35] (left), with catalysts facilitating high ethylene selectivity at high ethane conversion indicated (right). Highest ethylene yields are often achieved using catalysts containing Cr.

Several investigations report significantly higher rates of ethane dehydrogenation in the presence of $CO_2$ for Cr-based catalysts, and the composition of the catalyst support was found to be a critical parameter determining the impact of $CO_2$ on ethane dehydrogenation kinetics.[15,36] Although the mechanistic role of $CO_2$ has been the subject of several studies, the interplay between catalytic pathways of ethane dehydrogenation and $CO_2$ reduction has not been clearly resolved. In this set of exploratory experiments, Cr was dispersed onto zeolites with varying composition, and the catalytic performance for ethane dehydrogenation with or without $CO_2$ was evaluated in order to identify exemplary catalysts for the investigation of the mechanistic role of $CO_2$. Ongoing work builds from the results in this Chapter towards the goal of understanding the reaction network for Cr-based catalysts.

## 4.3 Experimental Methods

**Sample preparation.** ZSM-5 (referred to as Al-MFI) was supplied by Zeolyst International (Si/Al = 15; CBV 3024E). Beta zeolite was supplied by Zeolyst International (Si/Al = 19; CP814C). Borosilicate

MFI zeolite (referred to as B-MFI) was synthesized using a procedure adapted from Forni et al,[37] as described below.

B-MFI was prepared using a method adapted from Forni et al.[37] A solution of 1.78 g of NaOH in 18.4 g $H_2O$ was added to a solution of 3.62 g of tetrapropylammonium bromide (TPABr) in 18.4 g $H_2O$. The resulting solution was stirred for one hour before adding to it 25.0 g of colloidal silica solution (40 % $SiO_2$ in $H_2O$) dropwise under vigorous stirring. Next, a mixture of 0.823 g $H_3BO_3$ in 8.23 g $H_2O$ was added to the NaOH-TPABr-$SiO_2$-$H_2O$ mixture. The resulting mixture, having a molar composition of Si : $B_2$ : $Na_2$ : TPA : $H_2O$ = 1 : 0.04 : 0.13 : 0.08 : 20, was covered and stirred overnight. The aged gel was transferred to a 120 mL PTFE beaker in a stainless steel Parr reactor and heated in an oven, without mixing, at 170 °C for 48 h. After cooling the reactor, the solid products were separated by centrifugation and washed with $H_2O$ before drying at 120 °C. The dried zeolite was calcined in flowing $O_2$ at 550 °C to remove organics. Next, it was ammonium exchanged in aqueous 1 M $NH_4NO_3$ and calcined again in $O_2$ at 550 °C to convert to its protonic form before use.

Si-MFI was prepared by treating B-MFI in acid as follows. 1 g of B-MFI was added to 50 mL of a 1 M HCl solution in a sealed, pressure-rated glass vessel. The zeolite-HCl mixture was stirred while the glass vessel was heated in an oil bath at 90 °C for 20 h. The solids were separated by filtration and washed thoroughly with deionized water to obtain Si-MFI, which was dehydrated under flowing $N_2$ at 300 °C before use.

Si-Beta was prepared by treating aluminum-containing Beta zeolite in acid as follows. 1 g of aluminosilicate Beta zeolite (Zeolyst CP814C) was added to 40 mL $HNO_3$ (70% in $H_2O$) in a sealed, pressure-rated glass vessel. The zeolite-$HNO_3$ mixture was stirred while the glass vessel was heated in an oil bath at 95 °C for 20 h. The solids were separated by filtration and washed thoroughly with deionized water to obtain Si-Beta, which was dehydrated under flowing $N_2$ at 300 °C before use.

Chromium was dispersed onto proton forms of Al-MFI and B-MFI by incipient wetness impregnation as follows. An aqueous solution of $Cr(NO_3)_3$ was mixed with zeolite in a ratio of 0.5 mL solution per g zeolite, and the mixture was dried under ambient conditions. The dried samples were calcined

in a quartz tube reactor placed in a tube furnace. With 50 mL/min flow of air (Zero grade, Praxair) the furnace temperature was raised at a rate of 2 °C/min to 500 °C and held at this temperature for 6 h. Calcined, chromium-containing samples prepared in this method were referred to as Cr/Al-MFI(IWI) and Cr/B-MFI(IWI).

Chromium was dispersed onto zeolites Al-MFI, B-MFI, Si-MFI, and Si-Beta by vapor deposition of chromium(III) acetylacetonate ($Cr(acac)_3$), as described in Chapter 2. All steps of the preparation were performed without exposing the samples to ambient air. In a glovebox, zeolite (up to 0.5 g) was added with an appropriate amount of $Cr(acac)_3$ to a 2 mL glass ampoule. The ampoule was transferred to a Schlenk line, where it was evacuated and flame-sealed at approximately 80 mtorr pressure. The sealed ampoule, containing the light purple mixture, was heated in the calcination furnace at 5 °C $min^{-1}$ to 200 °C and held for 2 h. Then temperature was ramped at 5 °C $min^{-1}$ to 300 °C and held for 2 h. Sample color changed to either green or brown/gray during vacuum heat treatment. After vacuum heat treatment, the sample was transferred to the glovebox, where it was removed from the ampoule and placed into the quartz tube calcination reactor. The sample in the calcination tube was transferred to the furnace, where it was heated under 50 mL/min flow of air at 5 °C/min to 300 °C and 2 °C/min from 300 °C to 500 °C, at which temperature the furnace was held for 3 h. After cooling, the calcination tube was transferred back to the glovebox, where samples were stored prior to use.

**Catalyst performance testing.** Ethane dehydrogenation was carried out in a quartz down- flow, packed-bed reactor with 4 mm ID. Sample powders were sieved between mesh sizes 60–40 before use. Reactor effluent was measured online by an Agilent 7890a gas chromatography (GC) unit equipped with FID and TCD detectors. In a typical reaction experiment, the reactor was heated in a tubular furnace at 5 °C/min to 650 °C under 48 mL/min $N_2$ flow. Holding at 650 °C, flow was switched to bypass the reactor in order to initialize gas flow rates and composition for ethane dehydrogenation. Unless otherwise specified, the flow rates used were 44 mL/min $N_2$ and 4 mL/min $C_2H_6$ or 40 mL/min $N_2$, 4 mL/min $CO_2$, and 4 mL/min $C_2H_6$. Space velocity was adjusted by changing the mass of catalyst in the bed. After initial flow rates

stabilized, flow was reintroduced to the reactor and the reaction began. The reactor spent about 20 min under static $N_2$ at 650 °C before flow of $C_2H_6$ or $CO_2$ began. Catalyst bed pressure was 3 psig.

**IR spectroscopy.** Powder samples were prepared for diffuse reflectance infrared Fourier-transform spectroscopy (DRIFTS) by dropping/sprinkling pure sample (1–3 mg) onto the top of a pile of $CaF_2$ in a ceramic sample cup. The loaded sample cup was placed into a Pike Technologies DiffusIR Heated Chamber inside a glovebox, allowing air-free transfer to the spectrometer. DRIFTS measurements were performed using a Bruker Tensor II FTIR Spectrometer equipped with a Pike Technologies DiffusIR MidIR Accessory. Spectra were collected using 256 scans and 2 $cm^{-1}$ resolution. For spectra of samples under nitrogen atmosphere, a background spectrum of dried $CaF_2$ under $N_2$ was used, and data are reported as Kubelka–Munk spectra. For spectra of samples with adsorbed probe molecules, a background spectrum of the sample was collected just prior to introduction of the probe gas, and data are reported as log of inverse reflectance. More detail is given in Chapter 2, section 2.9, Supporting Information.

Sample treatments were performed in the DRIFTS heated chamber. The chamber was ramped at 10 °C $min^{-1}$ to 650 °C under 30 mL $min^{-1}$ $N_2$ flow and held for 30 min at this temperature before cooling the chamber under $N_2$ flow. Probe molecules were dosed at 30 °C.

**X-ray absorption spectroscopy (XAS).** XAS measurements were performed at the Stanford Synchrotron Radiation Lightsource (SSRL) at SLAC National Laboratory at beam line 2–2. X-ray absorption near edge structure spectra were recorded at the Cr K edge (5989 eV) in fluorescence mode. Samples were loaded into quartz tubes that were heated with resistive coils and fitted to a gas flow manifold. Reported XANES spectra were energy-calibrated and normalized. A chromium foil was scanned simultaneously for energy calibration. Raw XAS data was energy-calibrated, merged and normalized using the Athena interface of the Demeter software package.[38]

## 4.4 Results and Discussion

Chromium was dispersed on MFI zeolites with different support compositions to yield Cr/MFI samples containing 0.5 wt% Cr, as described in Experimental Methods. An initial series of experiments

focused on samples prepared by incipient wetness impregnation (IWI) of protonic forms of aluminosilicate and borosilicate MFI zeolites. At Cr loadings below 1 wt%, Cr/Al-MFI catalysts contained stable active sites during ethane dehydrogenation without $CO_2$ (Chapter 2). In prior studies, when Cr was dispersed on Al-containing supports (e.g. $Al_2O_3$), it was reported that $CO_2$ had a negative impact on ethane dehydrogenation.[7,39] The beneficial effects of $CO_2$ on ethane dehydrogenation were most pronounced for $Cr/SiO_2$ catalysts.[7,39]

The catalytic performance in ethane dehydrogenation in the absence of $CO_2$ at 650 °C for Cr/B-MFI(IWI) and Cr/Al-MFI(IWI) is compared in Figure 4.2. The initial ethane conversion was similar for both samples. Cr/B-MFI(IWI) displayed minor deactivation at early times on stream, whereas Cr/Al-MFI(IWI) showed no deactivation, consistent with the results for Cr/ZSM-5 catalysts in Chapter 2.

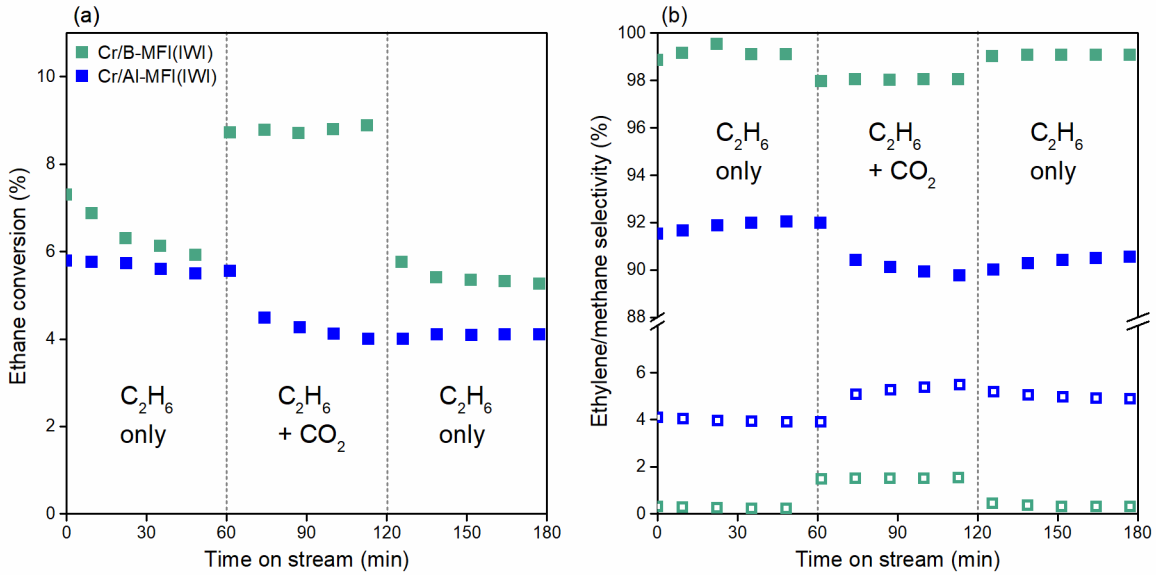


**Figure 4.2.** Conversion (a) of ethane and selectivity (b) to ethylene (filled squares) or methane (open squares) with time on stream at 650 °C for Cr/B-MFI(IWI) (green) or Cr/Al-MFI(IWI) (blue). At 60 min, $CO_2$ was added to the reactor feed in a ratio of $CO_2$:$C_2H_6$ = 1:1. At 120 min, the reactor was returned to the initial feed composition. Reactor conditions: 90 mg catalyst, 4 mL/min $C_2H_6$, 4 mL/min $CO_2$ (or 0 mL/min $CO_2$), balance $N_2$ for total flow rate of 48 mL/min.

The two samples responded differently to the presence of $CO_2$. When $CO_2$ was added to the feed in a 1:1 ratio with ethane, the ethane conversion for Cr/B-MFI(IWI) immediately increased by 50% and was stable over time. Ethane conversion for Cr/Al-MFI(IWI) gradually decreased over 60 min in the

presence of $CO_2$. Subsequently removing $CO_2$ from the feed did not restore the initial ethane conversion for Cr/Al-MFI(IWI), indicating that $CO_2$ caused an irreversible change to Cr/Al-MFI(IWI). For Cr/B-MFI(IWI), removing $CO_2$ from the feed caused the ethane conversion to return to the same level as before addition of $CO_2$, thus demonstrating reversibility of the changes to Cr/B-MFI(IWI) due to the presence of $CO_2$. Changes in product selectivities when $CO_2$ was added or removed (Figure 4.2b) were consistent with these inferences regarding reversibility.

Notably, both catalysts displayed higher selectivity to methane in the presence of $CO_2$, but only for Cr/Al-MFI(IWI) were significant amounts of propylene formed as well (Figure S4.1). For Cr/Al-MFI(IWI), propylene formed in similar amounts to methane, suggesting that methane and propylene formed together through cracking of products generated by acid-catalyzed ethylene oligomerization. Thus, ethylene selectivity was higher for Cr/B-MFI(IWI), which lacked strong Brønsted acid sites, compared with Cr/Al-MFI(IWI). Additionally, a significant increase in methane selectivity in the presence of $CO_2$ was observed for Cr/B-MFI(IWI) which was not accompanied by a proportional increase in the selectivity to propylene, indicating that methane was not formed through a pathway involving oligomerization. Instead, methane may form through steam cracking of ethane with $H_2O$ or from $CO_2$ hydrogenation.

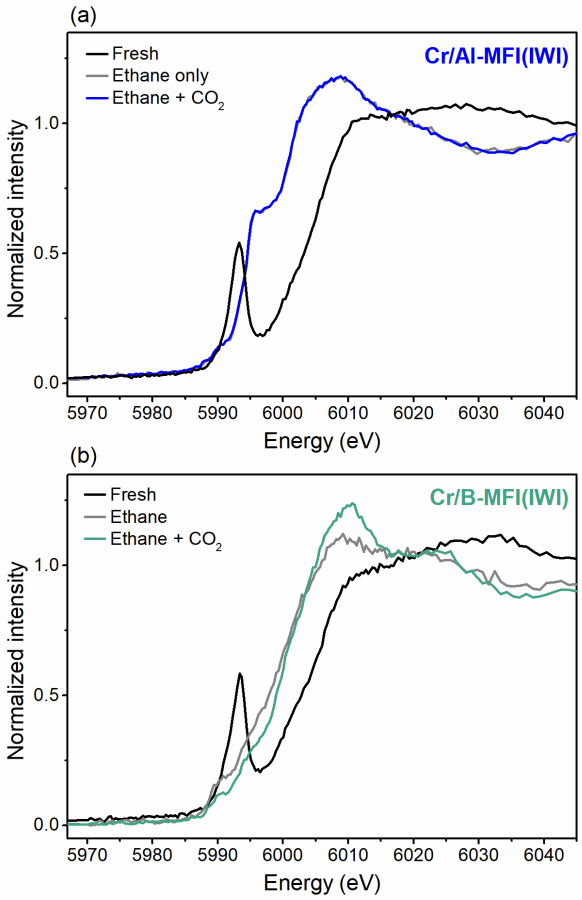


**Figure 4.3.** XANES spectra characterizing (a) Cr/Al-MFI(IWI) and (b) Cr/B-MFI(IWI). Black: freshly calcined samples; gray: samples during exposure to $C_2H_6$ at 650 °C; green/blue: samples during exposure to $C_2H_6$ and $CO_2$ at 650 °C.

The state of chromium in Cr/Al-MFI(IWI) and Cr/B-MFI(IWI) was monitored by XANES (Figure 4.3) during exposure to the same conditions as in Figure 4.2. The spectra characterizing each of the fresh samples contain a pre-edge peak at approximately 5993 eV, indicating that chromium exists in approximately an oxidation state of +6 in both samples following calcination. The near edge spectra characterizing the samples during exposure to ethane at 650 °C contain no pre-edge peak, and the edge energies in both spectra are red-shifted. These changes indicate that chromium was reduced to the +2 or +3 oxidation state during ethane dehydrogenation, consistent with prior reports of supported-chromium catalysts.[30] A shoulder in the absorption edge at approximately 5996 eV, indicative of $Cr^{2+}$,[40] is present in both spectra, but the intensity of the shoulder is different in each spectrum. The spectrum characterizing Cr/Al-MFI(IWI) displays an intense edge shoulder at 5996 eV, suggesting the presence of mainly $Cr^{2+}$

during ethane dehydrogenation, consistent with the findings of Chapter 2. The edge shoulder in the spectrum characterizing Cr/B-MFI(IWI) is less intense, indicating the average oxidation state of chromium was closer to +3. After $CO_2$ was added to the feed, no change to the near edge spectrum characterizing Cr/Al-MFI(IWI) was observed. The spectrum characterizing Cr/B-MFI during exposure to ethane and $CO_2$, however, displayed a decrease in the edge shoulder intensity compared with that in the absence of $CO_2$, indicating that some of the $Cr^{2+}$ in Cr/B-MFI(IWI) was oxidized to $Cr^{3+}$ in the presence of $CO_2$. Taken together with the results of Figure 4.2, increased ethane conversion when $CO_2$ was added to the feed is correlated with the ability of $Cr^{2+}$ to convert to $Cr^{3+}$. Since the bonding of chromium with the support surface strongly influences the oxidation state and chemistry of dispersed chromium,[28,40,41] the speciation of chromium in chromium-containing aluminosilicate and borosilicate MFI zeolites was investigated by IR spectroscopy.

Chromium was dispersed onto aluminosilicate (Al-MFI) and borosilicate (B-MFI) MFI zeolites by vapor deposition of $Cr(acac)_3$, as described in section 4.3 Experimental Methods. Additionally, chromium was dispersed by vapor deposition of $Cr(acac)_3$ onto a zeolite (Si-MFI) obtained through acid treatment of B-MFI. The acid treatment was intended to remove boron,[37] creating zeolite framework defects for binding of chromium cations.[42] IR spectra characterizing Cr/Al-MFI, Cr/B-MFI, and Cr/Si-MFI with adsorbed probe molecule nitric oxide (NO) are displayed in Figure 4.4.

Before room temperature exposure to NO, each of the samples was exposed to flowing $N_2$ at 650 °C for 30 min, as described in section 4.3 Experimental Methods. This sample treatment condition is identical to the conditions experienced by the catalysts prior to ethane dehydrogenation catalysis. The IR spectra characterizing samples probed with NO at room temperature provide insight into the speciation of chromium in the samples before catalysis.

The spectrum characterizing Cr/Al-MFI (Figure 4.4a) indicates the presence of mainly $Cr^{2+}(NO)_2$ species with chromium located at zeolite Al sites; the detailed assignments of these bands are discussed in in Chapter 2 and not repeated here.

The IR spectra of Cr/B-MFI and Cr/Si-MFI in contact with NO contained $\nu_{NO}$ bands characteristic of cationic chromium bonded to siliceous supports via Cr-O-Si linkages.[40,43] Bands at approximately 1745 and 1870 $cm^{-1}$ are typical of the antisymmetric and symmetric $\nu_{NO}$ stretches of dinitrosyl $Cr^{2+}(NO)_2$ species, and the band at approximately 1794 $cm^{-1}$ is typical of mononitrosyl $Cr^{2+}(NO)$ or $Cr^{3+}(NO)$.[40,42,44] Mononitrosyl chromium species are thought to be bonded to more occluded sites on the surface of $SiO_2$, which prevents additional NO molecules from bonding to chromium. Similar $\nu_{NO}$ bands have been reported for a samples containing chromium dispersed on a purely siliceous Beta zeolite.[45] This band can be assigned to chromium, most likely in the +3 oxidation state, located at zeolite framework defect sites, which are functionally similar to the occluded surface sites invoked for $Cr/SiO_2$ samples.[42] The sharpness of the 1794 $cm^{-1}$ band is consistent with this interpretation, as the structural uniformity implied could reasonably result from the presence of chromium at uniform defect sites in the crystalline zeolite framework. The $\nu_{NO}$ bands at 1745 and 1870 $cm^{-1}$ are much broader, implying that these bands characterize a relatively heterogeneous family of chromium species, possibly including oligomeric chromium oxides.

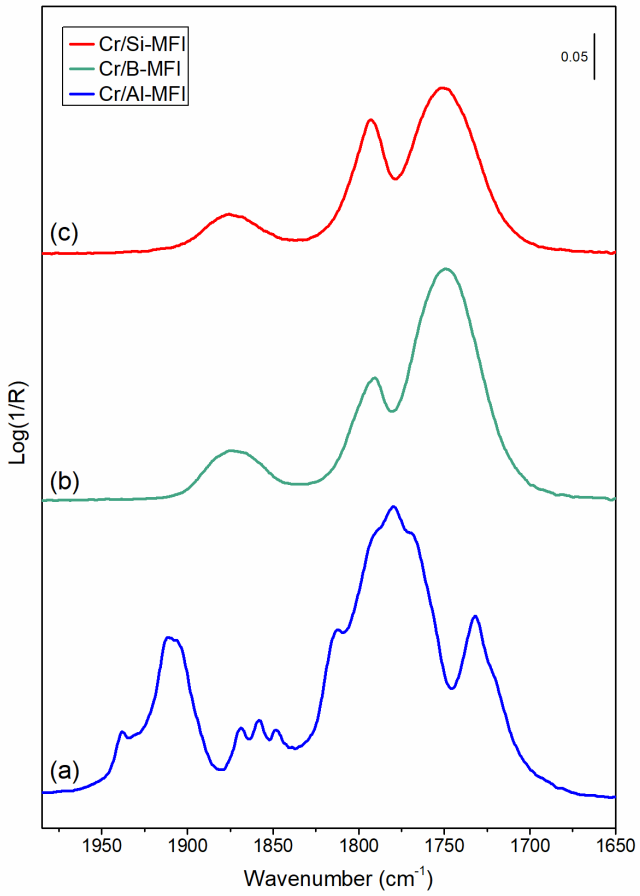


**Figure 4.4.** IR spectra characterizing (a) Cr/Al-MFI, (b) Cr/B-MFI, and (c) Cr/Si-MFI after exposure to NO at 30 °C following exposure to $N_2$ at 650 C.

The spectrum of Cr/Si-MFI displays higher intensity of the $\nu_{NO}$ band at 1794 $cm^{-1}$ relative to those at 1745 and 1870 $cm^{-1}$, indicating a higher relative abundance of $Cr^{3+}$(NO) species in this sample. Boron removal from B-MFI during preparation of Si-MFI generated framework defects in Si-MFI. In view of this and the proposed assignment of the 1794 $cm^{-1}$ band, the IR results of Figure 4.4 suggest that Cr/Si-MFI contained a higher fraction of chromium located at structurally uniform framework defect sites compared with Cr/B-MFI. No $\nu_{NO}$ bands were present in the spectrum of Cr/B-MFI that were not present in the spectrum of Cr/Si-MFI, so no facile identification of chromium in close contact with boron sites can be made from the data.

The ethane dehydrogenation performance of Cr/Si-MFI was evaluated in the presence and absence of $CO_2$ (Figure 4.5). When $CO_2$ was added to the reactor feed in a ratio of $CO_2$:$C_2H_6$ = 1:1, the initial rate

of ethane dehydrogenation increased by 61% compared with the initial rate in the absence of $CO_2$ (Figure 4.5a). No deactivation occurred in the presence of $CO_2$, in contrast to a significant loss of activity observed in the absence of $CO_2$. After 3 h on stream, the rate of ethane conversion in the presence of $CO_2$ was nearly triple that in the presence of ethane only.

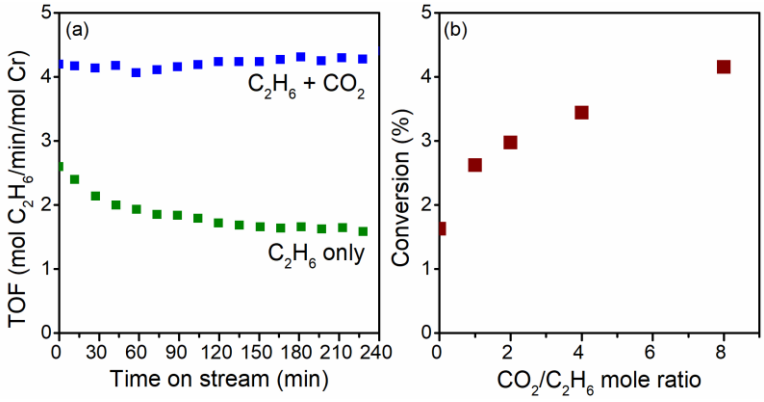


**Figure 4.5.** (a) Rate of ethane conversion with time on stream for Cr/Si-MFI in the presence (blue) or absence (green) of $CO_2$. Reactor conditions: 650 °C; 14–21 mg catalyst, 4 mL/min $C_2H_6$, 4 mL/min $CO_2$ (or 0 mL/min $CO_2$), balance $N_2$ for total flow rate of 48 mL/min. (b) Ethane conversion for Cr/Si-MFI as a function of $CO_2$:$C_2H_6$ molar feed ratio. Reactor conditions: 650 °C; 21 mg catalyst, 4 mL/min $C_2H_6$, 0–32 mL/min $CO_2$, balance $N_2$ for total flow rate of 48 mL/min.

The amount of $CO_2$ in the reactor feed was varied, keeping space velocity with respect to ethane constant (Figure 4.5b). Ethane conversion increased sharply with the $CO_2$:$C_2H_6$ feed ratio at values of $CO_2$:$C_2H_6$ < 2, but the impact of additional $CO_2$ on ethane conversion was less pronounced at higher $CO_2$:$C_2H_6$ values.

A comparison of initial ethane dehydrogenation rates in the presence of $CO_2$ for all chromium-containing samples studies is shown in Figure 4.6. Cr/B-MFI displayed the highest initial activity, and Cr/Al-MFI displayed by far the lowest initial activity. Interestingly, the two zeolites that had been acid treated in order to create framework defects displayed nearly identical initial rates of ethane conversion.

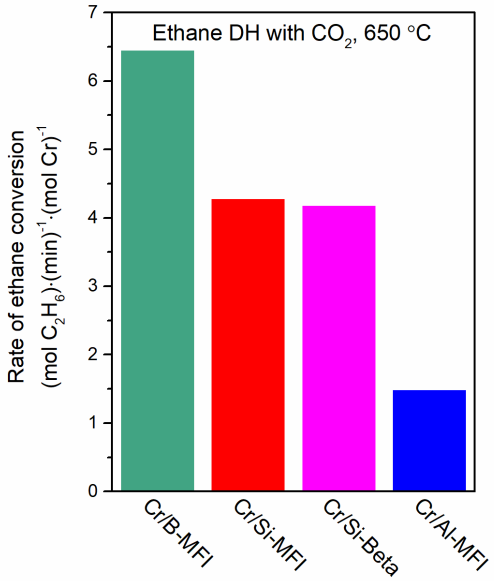


**Figure 4.6.** Initial rates of ethane conversion for Cr/B-MFI, Cr/Si-MFI, Cr/Si-Beta, and Cr/Al-MFI. Reactor conditions: 650 °C; 4 mL/min $C_2H_6$, 4 mL/min $CO_2$, balance $N_2$ for total flow rate of 48 mL/min.

Some agreement on the mechanism of light alkane dehydrogenation over supported chromium catalysts has been established, as outlined in Scheme 4.1, adapted from Lillehaug et al.[46] The rate-limiting step is thought to be the heterolytic activation of a C-H bond in the alkane across a Cr-O bond, forming an alkyl species and a hydroxyl (step 1). β-hydride transfer from the alkyl to Cr followed by ethylene desorption leave a hydroxyl and Cr-hydride pair (step 2). Recombinative desorption of $H_2$ and re-forming of the Cr-O bond can complete the catalytic cycle (step 3). However, if step 3 does not occur readily, alkane activation may occur over the Cr-H bond, enabling a cycle consisting of steps 2 and 4.

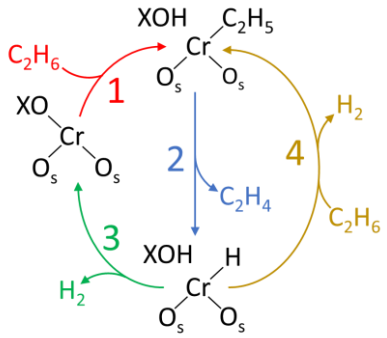


**Scheme 4.1.** Proposed catalytic cycle for ethane dehydrogenation (adapted from Lillehaug et al.[46]). $O_s$ represents a support surface oxygen, and X represents either a proton or a support surface metal (e.g. Si, Al).

The Cr-ethyl intermediate is thought to be short-lived for supported chromium catalysts.[47] Thus, when $CO_2$ is added to the ethane dehydrogenation reaction atmosphere, it most likely reacts with the bare Cr site or the Cr-H intermediate. If $CO_2$ reacts with the bare Cr site, forming CO and Cr=O, enhancement of ethane conversion by $CO_2$ may be explained by ethane activation at the Cr=O site. If $CO_2$ reacts with the Cr-H site, forming CO, $H_2O$, and a bare Cr site, the enhancement may be explained by $CO_2$-facilitated regeneration of bare Cr sites for ethane activation.

Insight into the different responses to the presence of $CO_2$ observed for Cr/Al-MFI and Cr/Si-MFI was provided by rates of reverse water-gas shift reaction ($CO_2 + H_2 \rightarrow CO + H_2O$), evaluated at 650 °C. Studying this reaction allows to observe $CO_2$ reduction by $H_2$ without the confounding influence of ethane dehydrogenation reaction pathways. The rate of $CO_2$ conversion to CO by $H_2$ was nearly ten times higher for Cr/Si-MFI than for Cr/Al-MFI. Taken together with the results of Figures 4.2 and 4.5, the results of Figure 4.7 indicate that activity for $CO_2$ reduction by $H_2$ may be related to the enhancement of ethane dehydrogenation by $CO_2$. Further research should investigate the pathway of $CO_2$ reduction in order to understand the impact of $CO_2$ on ethane dehydrogenation catalytic cycles.

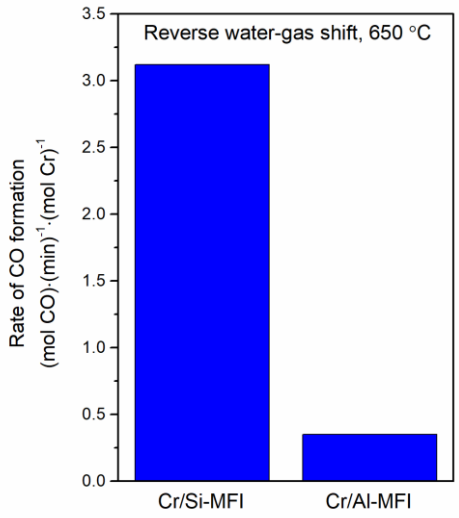


**Figure 4.7.** Initial rates of $CO_2$ reduction during reverse water-gas shift using Cr/Si-MFI and Cr/Al-MFI. Reactor conditions: 650 °C, 4 mL/min $H_2$, 4 mL/min $CO_2$, balance $N_2$ for total flow rate of 48 mL/min.

## 4.5 Conclusions

The results presented here demonstrate that the bonding of chromium to MFI zeolite surfaces strongly impacts the catalytic performance of Cr/MFI catalysts for ethane dehydrogenation in the presence of $CO_2$. A series of Cr/MFI catalysts were prepared using MFI supports varying in support composition, and these were evaluated as catalysts for ethane dehydrogenation with or without $CO_2$. When supported on the aluminosilicate MFI, chromium was present in the +2 oxidation state during ethane dehydrogenation regardless of the presence of $CO_2$, and $CO_2$ did not strongly impact ethane dehydrogenation kinetics. When supported on borosilicate or siliceous MFI, chromium was present in either the +2 or +3 oxidation state, and the average oxidation state of chromium in Cr/B-MFI was influenced by the presence of $CO_2$. This correlated with significant enhancements in ethane dehydrogenation when $CO_2$ was added to the reaction feed for Cr/B-MFI and Cr/Si-MFI. Further mechanistic study of ethane dehydrogenation and CO2 reduction by $H_2$ will provide insight into the origins of $CO_2$-enhanced ethane dehydrogenation.

## 4.6 References


(1) Sattler, J. J. H. B.; Ruiz-Martinez, J.; Santillan-Jimenez, E.; Weckhuysen, B. M. Catalytic Dehydrogenation of Light Alkanes on Metals and Metal Oxides. *Chem. Rev.* **2014**, *114*, 10613–10653.

(2) Ansari, M. B.; Park, S.-E. Carbon Dioxide Utilization as a Soft Oxidant and Promoter in Catalysis. *Energy Environ. Sci.* **2012**, *5*, 9419–9437.

(3) Mimura, N.; Takahara, I.; Inaba, M.; Okamoto, M.; Murata, K. High-Performance Cr/H-ZSM-5 Catalysts for Oxidative Dehydrogenation of Ethane to Ethylene with $CO_2$ as an Oxidant. *Catal. Commun.* **2002**, *3*, 257–262.

(4) Zhu, J.; Qin, S.; Ren, S.; Peng, X.; Tong, D.; Hu, C. $Na_2WO_4/Mn/SiO_2$ Catalyst for Oxidative Dehydrogenation of Ethane Using $CO_2$ as Oxidant. *Catal. Today* **2009**, *148*, 310–315.

(5) Michorczyk, P.; Ogonowski, J.; Zeńczak, K. Activity of Chromium Oxide Deposited on Different Silica Supports in the Dehydrogenation of Propane with $CO_2$ - A Comparative Study. *J. Mol. Catal. A: Chem.* **2011**, *349*, 1–12.

(6) Xu, L.; Liu, J.; Yang, H.; Xu, Y.; Wang, Q.; Lin, L. Regeneration Behaviors of Fe/Si-2 and Fe–Mn/Si-2 Catalysts for $C_2H_6$ Dehydrogenation with $CO_2$ to $C_2H_4$. *Catal. Lett.* **1999**, *62*, 185–189.

(7) Shishido, T.; Shimamura, K.; Teramura, K.; Tanaka, T. Role of $CO_2$ in Dehydrogenation of Propane over Cr-Based Catalysts. *Catal. Today* **2012**, *185*, 151–156.

(8) Baek, J.; Yun, H. J.; Yun, D.; Choi, Y.; Yi, J. Preparation of Highly Dispersed Chromium Oxide

Catalysts Supported on Mesoporous Silica for the Oxidative Dehydrogenation of Propane Using $CO_2$: Insight into the Nature of Catalytically Active Chromium Sites. *ACS Catal.* **2012**, *2*, 1893–1903.

(9) Cheng, Y.; Miao, C.; Hua, W.; Yue, Y.; Gao, Z. Cr/ZSM-5 for Ethane Dehydrogenation: Enhanced Catalytic Activity through Surface Silanol. *Appl. Catal. A Gen.* **2017**, *532*, 111–119.

(10) Cheng, Y.; Lei, T.; Miao, C.; Hua, W.; Yue, Y.; Gao, Z. Single-Site $CrO_x$ Moieties on Silicalite: Highly Active and Stable for Ethane Dehydrogenation with $CO_2$. *Catal. Lett.* **2018**, *148*, 1375–1382.

(11) Koirala, R.; Buechel, R.; Krumeich, F.; Pratsinis, S. E.; Baiker, A. Oxidative Dehydrogenation of Ethane with $CO_2$ over Flame-Made Ga-Loaded $TiO_2$. *ACS Catal.* **2015**, *5*, 690–702.

(12) Asghari, E.; Haghighi, M.; Rahmani, F. $CO_2$-Oxidative Dehydrogenation of Ethane to Ethylene over Cr/MCM-41 Nanocatalyst Synthesized via Hydrothermal/Impregnation Methods: Influence of Chromium Content on Catalytic Properties and Performance. *J. Mol. Catal. A: Chem.* **2016**, *418–419*, 115–124.

(13) Talati, A.; Haghighi, M.; Rahmani, F. Oxidative Dehydrogenation of Ethane to Ethylene by Carbon Dioxide over $Cr/TiO_2$-$ZrO_2$ Nanocatalyst: Effect of Active Phase and Support Composition on Catalytic Properties and Performance. *Adv. Powder Technol.* **2016**, *27*, 1195–1206.

(14) Mimura, N.; Okamoto, M.; Yamashita, H.; Ted Oyama, S.; Murata, K. Oxidative Dehydrogenation of Ethane over Cr/ZSM-5 Catalysts Using $CO_2$ as an Oxidant. *J. Phys. Chem. B* **2006**, *110*, 21764–21770.

(15) Wang, S.; Murata, K.; Hayakawa, T.; Hamakawa, S.; Suzuki, K. Dehydrogenation of Ethane with Carbon Dioxide over Supported Chromium Oxide Catalysts. *Appl. Catal. A Gen.* **2000**, *196*, 1–8.

(16) Valenzuela, R. X.; Bueno, G.; Cortés Corberán, V.; Xu, Y.; Chen, C. Selective Oxidehydrogenation of Ethane with $CO_2$ over $CeO_2$-Based Catalysts. *Catal. Today* **2000**, *61*, 43–48.

(17) Wang, S.; Murata, K.; Hayakawa, T.; Hamakawa, S.; Suzuki, K. Effect of Promoters on Catalytic Performance of $Cr/SiO_2$ Catalysts in Oxidative Dehydrogenation of Ethane with Carbon Dioxide. *Catal. Lett.* **2001**, *73*, 2–6.

(18) Zhao, X.; Wang, X. Oxidative Dehydrogenation of Ethane to Ethylene by Carbon Dioxide over Cr/TS-1 Catalysts. *Catal. Commun.* **2006**, *7*, 633–638.

(19) Zhang, X.; Ye, Q.; Xu, B.; He, D. Oxidative Dehydrogenation of Ethane over Co-$BaCO_3$ Catalysts Using $CO_2$ as Oxidant: Effects of Co Promoter. *Catal. Lett.* **2007**, *117*, 140–145.

(20) Deng, S.; Li, H.; Li, S.; Zhang, Y. Activity and Characterization of Modified $Cr_2O_3/ZrO_2$ Nano-Composite Catalysts for Oxidative Dehydrogenation of Ethane to Ethylene with $CO_2$. *J. Mol. Catal. A: Chem.* **2007**, *268*, 169–175.

(21) Shi, X.; Ji, S.; Wang, K.; Li, C. Oxidative Dehydrogenation of Ethane with $CO_2$ over Novel $Cr/SBA\text{-}15/Al_2O_3$/FeCrAl Monolithic Catalysts. *Energy Fuels* **2008**, No. 10, 3631–3638.

(22) Aresta, M.; Dibenedetto, A.; Angelini, A. Catalysis for the Valorization of Exhaust Carbon: From $CO_2$ to Chemicals, Materials, and Fuels. Technological Use of $CO_2$. *Chem. Rev.* **2014**, *114*, 1709–1742.

(23) Artz, J.; Müller, T. E.; Thenert, K.; Kleinekorte, J.; Meys, R.; Sternberg, A.; Bardow, A.; Leitner,

W. Sustainable Conversion of Carbon Dioxide: An Integrated Review of Catalysis and Life Cycle Assessment. *Chem. Rev.* **2018**, *118*, 434–504.

(24) Gomez, E.; Yan, B.; Kattel, S.; Chen, J. G. Carbon Dioxide Reduction in Tandem with Light-Alkane Dehydrogenation. *Nat. Rev. Chem.* **2019**, *3*, 638–649.

(25) Gärtner, C. A.; vanVeen, A. C.; Lercher, J. A. Oxidative Dehydrogenation of Ethane: Common Principles and Mechanistic Aspects. *ChemCatChem* **2013**, *5*, 3196–3217.

(26) Ertl, G.; Knozinger, H.; Schuth, F.; Weitkamp, J. *Handbook of Heterogeneous Catalysis*; Wiley-VCH Verlag, 2008.

(27) Lugo, H. J.; Lunsford, J. H. The Dehydrogenation of Ethane over Chromium Catalysts. *J. Catal.* **1985**, *91*, 155–166.

(28) Delley, M. F.; Silaghi, M. C.; Nuñez-Zarur, F.; Kovtunov, K. V.; Salnikov, O. G.; Estes, D. P.; Koptyug, I. V.; Comas-Vives, A.; Coperet, C. X-H Bond Activation on Cr(III),O Sites (X = R, H): Key Steps in Dehydrogenation and Hydrogenation Processes. *Organometallics* **2017**, *36*, 234–244.

(29) Valenzuela, R. X.; Bueno, G.; Solbes, a; Sapina, F.; Martinez, E.; Corberan, V. C. Nanostructured Ceria-Based Catalysts for Oxydehydrogenation of Ethane with $CO_2$. *Top. Catal.* **2001**, *15*, 181–188.

(30) Botavina, M.; Barzan, C.; Piovano, A.; Braglia, L.; Agostini, G.; Martra, G.; Groppo, E. Insights into $Cr/SiO_2$ Catalysts during Dehydrogenation of Propane: An Operando XAS Investigation. *Catal. Sci. Technol* **2017**, *7*, 1690–1700.

(31) Rahmani, F.; Haghighi, M.; Mohammadkhani, B. Microporous and Mesoporous Materials Enhanced Dispersion of Cr Nanoparticles over Nanostructured $ZrO_2$-Doped ZSM-5 Used in $CO_2$-Oxydehydrogenation of Ethane. *Microporous Mesoporous Mater.* **2017**, *242*, 34–49.

(32) Wang, S.; Zhu, Z. H. Catalytic Conversion of Alkanes to Olefins by Carbon Dioxide Oxidative Dehydrogenation - A Review. *Energy and Fuels* **2004**, *18*, 1126–1139.

(33) Krylov, O. V.; Mamedov, A. K.; Mirzabekova, S. R. The Regularities in the Interaction of Alkanes with CO2 on Oxide Catalysts. *Catal. Today* **1995**, *24*, 371–375.

(34) Krylov, O. V.; Mamedov, A. K.; Mirzabekova, S. R. Catalytic Oxidation of Hydrocarbons and Alcohols by Carbon Dioxide on Oxide Catalysts. *Ind. Eng. Chem. Prod. Res. Dev.* **1995**, *34*, 474–482.

(35) Cheng, Y.; Zhang, F.; Zhang, Y.; Miao, C.; Hua, W.; Yue, Y.; Gao, Z. Oxidative Dehydrogenation of Ethane with $CO_2$ over Cr Supported on Submicron ZSM-5 Zeolite. *Chinese J. Catal.* **2015**, *36*, 1242–1248.

(36) Wang, S.; Murata, K.; Hayakawa, T.; Hamakawa, S.; Suzuki, K. Oxidative Dehydrogenation of Ethane by Carbon Dioxide over Sulfate-Modified $Cr_2O_3/SiO_2$ Catalysts. *Catal. Lett.* **1999**, *63*, 59–64.

(37) Forni, L.; Fornasari, G.; Trifirò, F.; Aloise, A.; Katovic, A.; Giordano, G.; Nagy, J. B. Calcination and Deboronation of B-MFI Applied to the Vapour Phase Beckmann Rearrangement. *Microporous Mesoporous Mater.* **2007**, *101*, 161–168.

(38) Ravel, B.; Newville, M. Athena, Artemis, Hephaestus: Data Analysis for X-Ray Absorption Spectroscopy Using IFEFFIT. *J. Synchrotron Radiat.* **2005**, *12*, 537–541.

(39) Michorczyk, P.; Ogonowski, J. Effect of Supports on Catalytic Activity of Chromium Oxide-Based Catalysts in the Dehydrogenation of Propane with $CO_2$. *Catal. Lett.* **2005**, *101*, 53–57.

(40) Groppo, E.; Lamberti, C.; Bordiga, S.; Spoto, G.; Zecchina, A. The Structure of Active Centers and the Ethylene Polymerization Mechanism on the $Cr/SiO_2$ Catalyst: A Frontier for the Characterization Methods. *Chem. Rev.* **2005**, *105*, 115–183.

(41) Conley, M. P.; Delley, M. F.; Núnez-Zarur, F.; Comas-Vives, A.; Copéret, C. Heterolytic Activation of C-H Bonds on $Cr^{III}$-O Surface Sites Is a Key Step in Catalytic Polymerization of Ethylene and Dehydrogenation of Propane. *Inorg. Chem.* **2015**, *54*, 5065–5078.

(42) Zecchina, A.; Spoto, G.; Ghiotti, G.; Garrone, E. $Cr^{2+}$ ions Grafted to Silica and Silicalite Surfaces: FTIR Characterization and Ethylene Polymerization Activity. *J. Mol. Catal.* **1994**, *86*, 423–446.

(43) Garrone, E.; Ghiotti, G.; Coluccia, S.; Zecchina, A. On the Chemistry Of Silica Supported Chromium Ions. IV. Three-Ligand Complexes. Interaction of Pyridine, Ammonia, Carbon Monoxide and Water with Preadsorbed Nitric Oxide. *J. Phys. Chem.* **1975**, *79*, 984–988.

(44) Spoto, G.; Bordiga, S.; Garrone, E.; Ghiotti, G.; Zecchina, A.; Petrini, G.; Leofanti, G. Cr(II) and Cr(III) Ions Grafted at Internal Nests of a Pentasilic Zeolite (Silicalite): Characterization and Formation of Polycarbonylic, Polynitrosylic, and Mixed Species by Interaction with CO and NO. *J. Mol. Catal.* **1992**, *74*, 175–184.

(45) Hadjiivanov, K.; Penkova, A.; Kefirov, R.; Dzwigaj, S.; Che, M. Influence of Dealumination and Treatments on the Chromium Speciation in Zeolite CrBEA. *Microporous Mesoporous Mater.* **2009**, *124*, 59–69.

(46) Lillehaug, S.; Børve, K. J.; Sierka, M.; Sauer, J. Catalytic Dehydrogenation of Ethane over Mononuclear Cr (III) Surface Sites on Silica. Part I. C–H Activation by σ-Bond Metathesis Y. *J. Phys. Org. Chem.* **2004**, *17*, 990–1006.

(47) Olsbye, U.; Virnovskaia, A.; Prytz, Ø.; Tinnemans, S. J.; Weckhuysen, B. M. Mechanistic Insight in the Ethane Dehydrogenation Reaction over $Cr/Al_2O_3$ Catalysts. *Catal. Lett.* **2005**, *103*, 143–148.

## 4.7 Supporting Information

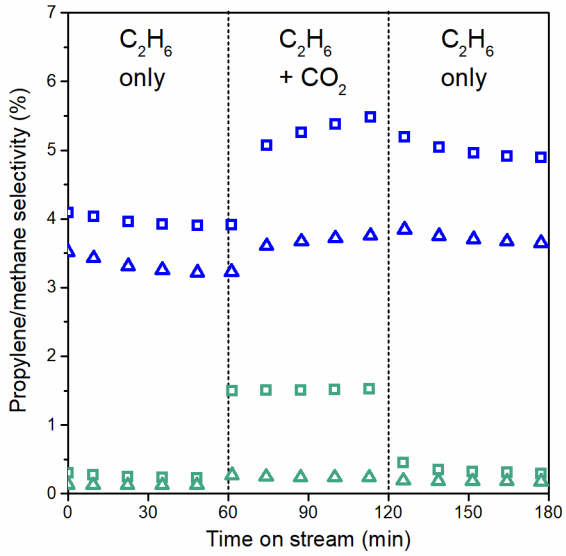


**Figure S4.1.** Selectivity to methane (squares) and propylene (triangles) with time on stream at 650 °C for Cr/B-MFI(IWI) (green) or Cr/Al-MFI(IWI) (blue). At 60 min, $CO_2$ was added to the reactor feed in a ratio of $CO_2$:$C_2H_6$ = 1:1. At 120 min, the reactor was returned to the initial feed composition. Reactor conditions: 90 mg catalyst, 4 mL/min $C_2H_6$, 4 mL/min $CO_2$ (or 0 mL/min $CO_2$), balance $N_2$ for total flow rate of 48 mL/min.

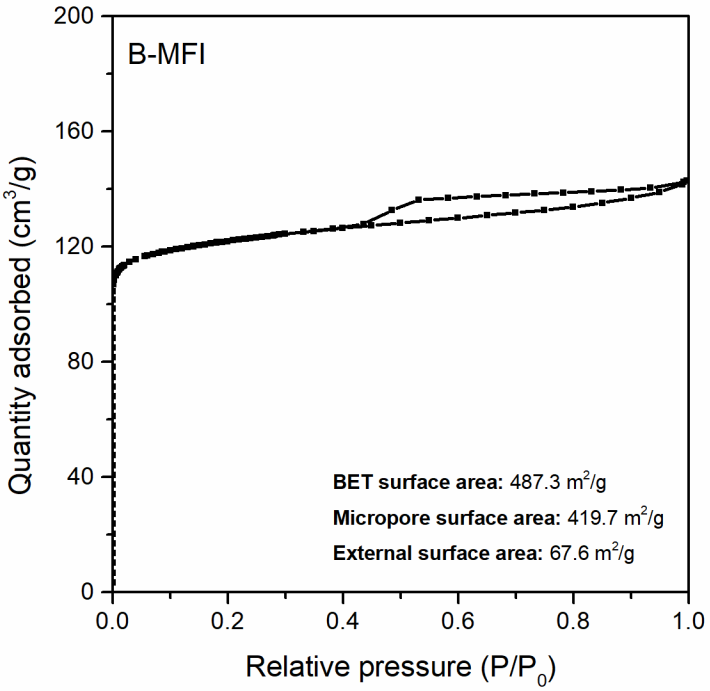


**Figure S4.2.** $N_2$ adsorption isotherm for B-MFI collected at 77 K.

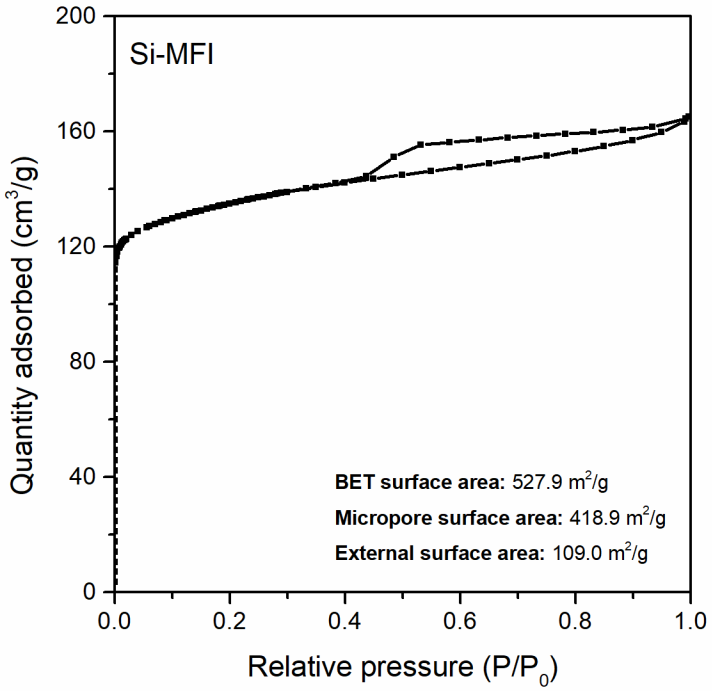


**Figure S4.3.** $N_2$ adsorption isotherm for Si-MFI collected at 77 K.

# **Appendix A.** Characterization of Chromium–Zeolite Catalysts Using Infrared and X-ray Absorption Spectroscopies

## 5.1 Abstract

The crystalline surfaces of zeolite supports present an opportunity to prepare supported-chromium catalysts having structurally uniform populations of dispersed chromium, but additional characterization is needed to identify zeolite-supported chromium species and control the distribution of chromium among various locations on the zeolite surface. In this Chapter, a series of Cr/zeolite samples was synthesized using multiple techniques, and the resulting distributions of supported-chromium species was characterized by IR or X-ray absorption spectroscopies.

## 5.2 Introduction

Supported-chromium catalysts are industrially relevant catalysts for ethylene polymerization and alkane dehydrogenation and have thus been studied extensively for decades.[1,2] The polydispersity of polymers produced by $Cr/SiO_2$ (Phillips catalyst), and the small fraction of total chromium that is active for polymerization, demonstrate the extent to which the local bonding environment of chromium on the surface of an oxide support influences its catalytic properties.[3] The alkane dehydrogenation literature also reflects this quality of supported chromium. As discussed in Chapter 4, the local environment of chromium greatly influences its dehydrogenation activity and response to the addition of $CO_2$ to the reaction environment.[4] The heterogeneity of supported chromium is thought to result in part from the heterogeneity in the structures of binding sites present on support surfaces.[1,3] It has been suggested that crystalline supports could result in more structurally uniform populations of supported chromium, which would facilitate characterization of, or control over, the properties of chromium catalysts.[3,5]

The aims of Chapters 2 and 4 were to relate results characterizing the speciation of chromium in ZSM-5 to catalytic performance. In this Chapter, additional results from IR and X-ray absorbance spectroscopies are presented, which represent attempts to characterize or control chromium speciation by changing framework Al distribution, zeolite heteroatom elemental identity, or chromium deposition technique.

## 5.3 Experimental Methods

**Preparation of zeolites.** The following aluminosilicate zeolites were supplied by Zeolyst: Beta (CP814C, Si/Al = 19), ZSM-5 (CBV 3024E, Si/Al =15), ZSM-5 (CBV 5524G, Si/Al = 25). Before use, zeolites were calcined in flowing 20% $O_2$ at 550 °C for 5 h with temperature ramp rates of 2 °C/min. Na-ZSM-5 was prepared by ion exchange of ZSM-5 (Si/Al = 15) with $NaNO_3$. H-ZSM-5 was added to an aqueous solution of 1 M $NaNO_3$ (1 g zeolite / 100 mL solution) and stirred for 48 h. The solution was periodically adjusted to pH 7.0 using 0.1 M NaOH. Na-ZSM-5 was recovered by centrifugation and washed several times with deionized water before drying at 80 °C.

**Synthesis of Ga-MFI.** Gallosilicate MFI zeolite was synthesized using a procedure adapted from Lanh et al.[6] A mixture of 0.4 g NaOH and 9.9 g $H_2O$ was added to a mixture of 1.18 g tetrapropylammonium bromide (TPABr) and 9.9 g $H_2O$ and stirred for 15 min. To this mixture was added 5 g colloidal silica solution (40% $SiO_2$ in $H_2O$). After stirring the resulting mixture for 15 min, a mixture of 0.37 $Ga(NO_3)_3{\cdot}H_2O$ and 3.64 g $H_2O$ was added. The final gel was stirred, covered, for 20 h and then transferred to a 23 mL, PTFE lined autoclave. The autoclave was sealed and placed into an oven at 170 °C for 48 h. The autoclave was cooled and its contents filtered and washed with deionized water. The rinsed solids were dried in an oven at 80 °C under ambient conditions. Dried solids were calcined to remove organics and obtain the H-form zeolite, using calcination conditions described above.

**Synthesis of low-pair-Al ZSM-5.** ZSM-5 with low content of paired Al sites was prepared using a procedure adapted from Dedecek et al.[7] 0.25 g aluminum nitrate nonahydrate ($Al(NO_3)_3{\cdot}9H_2O$) was added to 1.6 g deionized water and stirred until dissolved. Separately, 0.77 mL ethanol was added to 3.46 g tetraethyl orthosilicate (TEOS) and stirred until mixed, about 10 min. The ethanol-TEOS mixture was added to the $Al(NO_3)_3$ solution and stirred covered for 45 minutes. The cover was then removed, and the mixture was stirred to allow evaporation of all ethanol (approximately 3.7 g total ethanol). A mixture of 3.18 g tetrapropylammonium hydroxide (TPAOH, 40% in water) and 9.2 g deionized water was added to the $Al(NO_3)_3$-TEOS mixture. This was stirred, uncovered, for 90 min, before transferring to a 23 mL, PTFE

lined autoclave. The gel molar composition was 1 Si : 0.04 Al : 0.38 TPAOH : 42 $H_2O$. The autoclave was sealed and placed into an oven, rotating at 20 rpm, at 170 °C for 6 days. The autoclave was cooled and its contents filtered and washed with deionized water. The rinsed solids were dried in an oven at 80 °C under ambient conditions. Dried solids were calcined to remove organics and obtain the H-form zeolite, using calcination conditions described above.

**Incorporation of chromium into zeolites by vapor deposition.** Unless otherwise stated in the figure caption, chromium was incorporated into zeolites by vapor deposition of chromium(III) acetylacetonate ($Cr(acac)_3$), using the published technique described in Section 2.3, Experimental Methods. The target chromium loading for all samples was 0.5 wt% Cr.

**Incorporation of chromium into zeolites by aqueous ion exchange.** The samples described in Figures 5.3 and 5.4 were prepared by aqueous ion exchange of H-Beta zeolite with chromium (II) chloride ($CrCl_2$). $CrCl_2$ contains divalent chromium, which reacts spontaneously with $O_2$, and ion exchange was performed under anhydrous conditions using conventional Schlenk techniques. Into a flask containing $CrCl_2$ and H-Beta under argon was added deionized water that had been deoxygenated by bubbling argon through it for 30 min. Zeolite, $CrCl_2$, and water were mixed in proportions to produce a solution of 50 mM $CrCl_2$ with 1 g H-Beta per 100 mL solution. The blue-colored solution was stirred under argon for 24 h before solids were recovered by centrifugation and washing several times with deionized water. Centrifugation and washing were performed under aerobic conditions. Cr/Beta was dried in an oven under ambient conditions at 80 °C. The dried sample was loaded into a quartz tube reactor and heated under flowing $N_2$ to 500 °C at 2 °C/min. At this temperature, the sample was then exposed to flowing 10% $H_2$ for 1 h before cooling to room temperature under flowing $N_2$. The reactor was transferred to an argon-filled glove box, where Cr/Beta was stored before use.

**IR spectroscopy.** Powder samples were prepared for diffuse reflectance infrared Fourier-transform spectroscopy (DRIFTS) by dropping/sprinkling pure sample (1–3 mg) onto the top of a pile of $CaF_2$ in a ceramic sample cup. The loaded sample cup was placed into a Pike Technologies DiffusIR Heated Chamber inside a glovebox, allowing air-free transfer to the spectrometer. DRIFTS measurements were performed

using a Bruker Tensor II FTIR Spectrometer equipped with a Pike Technologies DiffusIR MidIR Accessory. Spectra were collected using 256 scans and 2 $cm^{-1}$ resolution. For spectra of samples under nitrogen atmosphere, a background spectrum of dried $CaF_2$ under $N_2$ was used, and data are reported as Kubelka–Munk spectra. For spectra of samples with adsorbed probe molecules, a background spectrum of the sample was collected just prior to introduction of the probe gas, and data are reported as log of inverse reflectance unless otherwise stated. More detail is given in Chapter 2, section 2.9, Supporting Information.

Sample treatments were performed in the DRIFTS heated chamber as described in figure captions. The chamber was ramped at 10 °C $min^{-1}$. Probe molecules were dosed at 30 °C.

**X-ray absorption spectroscopy.** XAS measurements were performed at the Stanford Synchrotron Radiation Lightsource (SSRL) at SLAC National Laboratory at beam line 4–3. X-ray absorption near edge structure spectra were recorded at the Cr K edge (5989 eV) in fluorescence mode. Samples were loaded into stainless-steel or quartz cells with Kapton windows that were fitted to a gas flow manifold. Reported XANES spectra were energy-calibrated and normalized. A chromium foil was scanned simultaneously for energy calibration. Raw XAS data was energy-calibrated, merged and normalized using the Athena interface of the Demeter software package

## 5.4 Results and Discussion

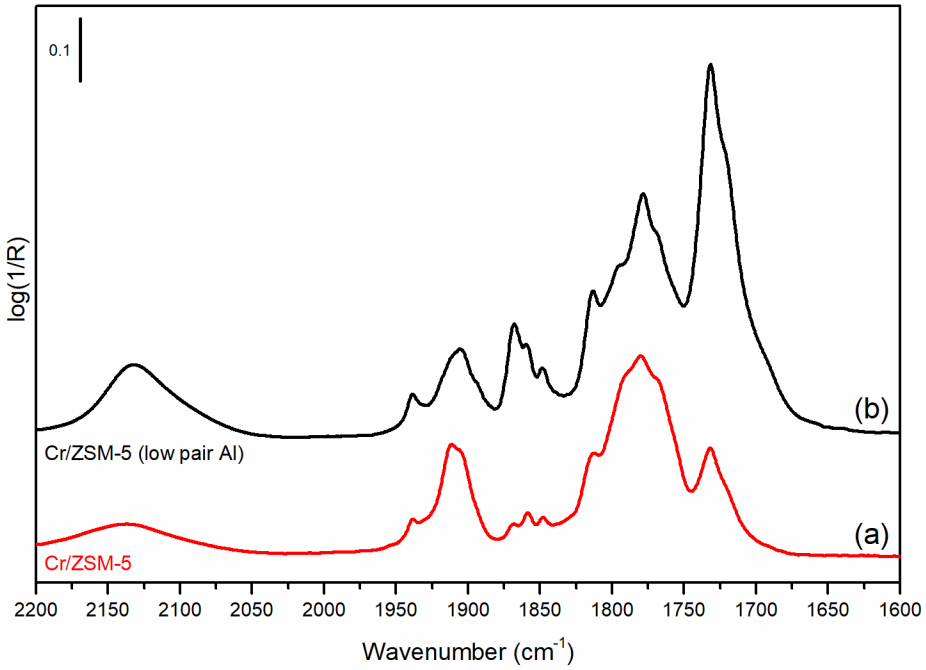


**Figure 5.1.** IR spectra characterizing (a) Cr/ZSM-5 (Si/Al = 15) and (b) Cr/ZSM-5 (low pair Al) at room temperature during exposure to NO following exposure to $N_2$ at 650 °C.

Following the assignments from Chapter 2, the IR spectrum characterizing Cr/ZSM-5 during exposure to NO at room temperature (Figure 5.1a; reproduced from Chapter 2) reflects the presence of mainly $Cr^{2+}$ dinitrosyl species located at Al sites in ZSM-5. In an attempt to differentiate chromium species located at paired or isolated Al sites in ZSM-5, chromium was incorporated into a ZSM-5 sample that was synthesized following procedures that were previously reported to result in ZSM-5 having a low concentration of paired Al.[7] The MFI crystal structure of this sample was confirmed using X-ray diffraction (results not shown), but the content of Al pairs was not determined for this sample. The IR spectrum characterizing Cr/ZSM-5 (low pair Al) during exposure to NO (Figure 5.1b) showed clear differences from that of Cr/ZSM-5. Specifically, the intensity of the $\nu_{NO}$ band at approximately 1730 $cm^{-1}$ was considerably higher in the spectrum of Cr/ZSM-5 (low pair Al), suggesting a higher fraction of the related chromium nitrosyl species was present in the sample. Bands at approximately 1815, 1870, 1938, and 2140 $cm^{-1}$ were also more intense in the spectrum characterizing Cr/ZSM-5 (low pair Al), suggesting that these bands may

be related to one another. Although detailed assignments of these bands cannot be made at this time, the fact that none of the bands were observed for Cr/Na-ZSM-5 or Cr/Si-MFI samples (Chapters 2 and 4), which lack Al sites available for binding chromium, implies that they result from chromium nitrosyl complexes located at Al sites. Thus, the differences in the spectra of Figures 5.1a and 5.1b likely result from differences in the Al distribution of the two ZSM-5 samples, reflected by the population of chromium present in the samples.

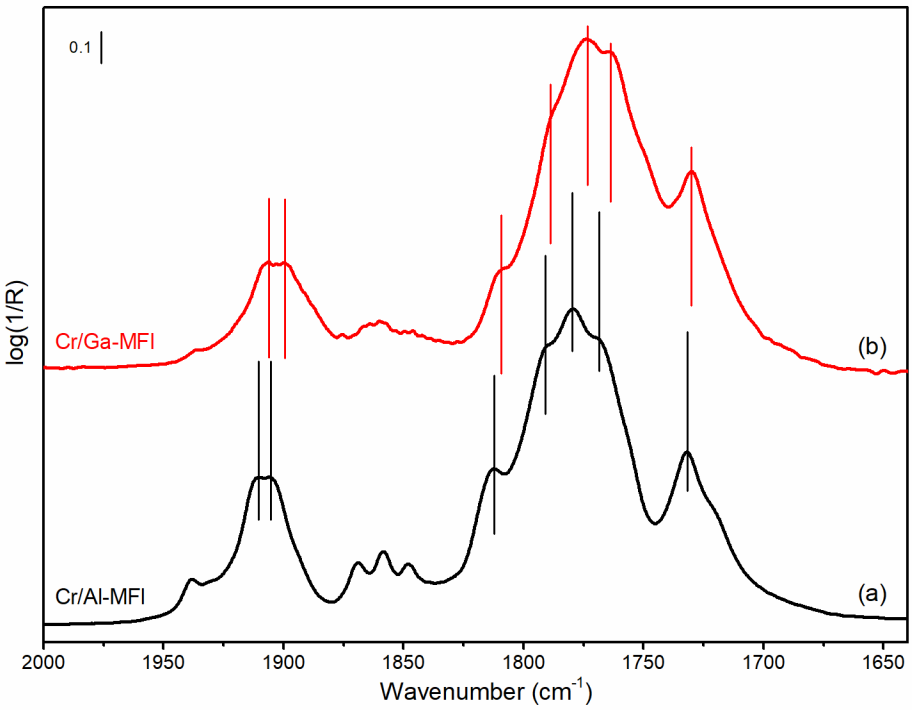


**Figure 5.2.** IR spectra characterizing (a) Cr/ZSM-5 (Cr/Al-MFI, Si/Al = 15) and (b) Cr/Ga-MFI at room temperature during exposure to NO following exposure to $N_2$ at 650 °C.

The spectrum of Figure 5.1a is reproduced in Figure 5.2 for comparison with that of Cr/Ga-MFI, a gallosilicate MFI zeolite with dispersed chromium. The spectrum of Cr/Ga-MFI, which contains no Al sites – only framework Ga sites – during exposure to NO displays a nearly identical combination of $\nu_{NO}$ bands to that of Cr/ZSM-5. The similarity in the relative positions, line-shapes, and intensities of $\nu_{NO}$ bands in the two spectra imply that the local environments of chromium is similar in each of the samples. A key difference between the spectra is that each of the $\nu_{NO}$ bands in the spectrum of Cr/Ga-MFI is red-shifted by 2–5 $cm^{-1}$ from the respective bands in the spectrum of Cr/ZSM-5. These shifts reflect subtle differences in electron sharing between chromium and NO as a result of the replacement of Al in the zeolite framework by Ga. Notwithstanding these subtle differences, the overall similarities in the spectra of 5.2 highlight the similarity in the geometry of bonding between chromium and the zeolite surface, as expected from the fact that ZSM-5 and Ga-MFI share the same crystal structure.

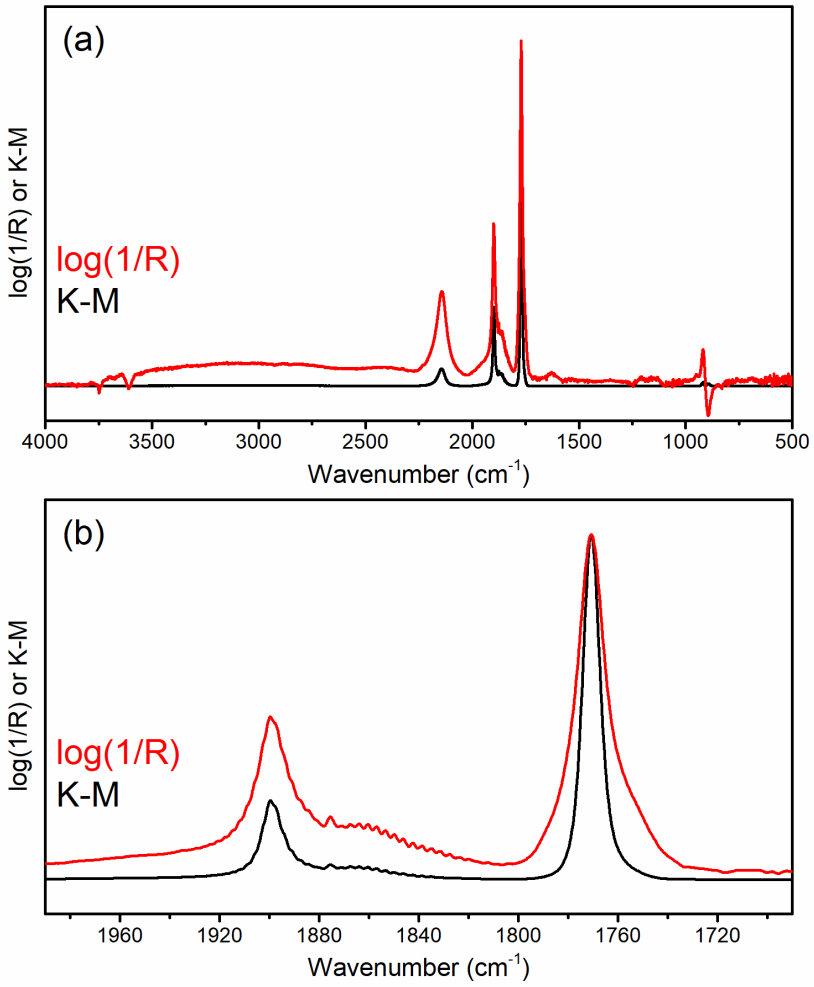


**Figure 5.3.** Log–inverse reflectance or Kubelka-Munk IR spectra in the region (a) full range or (b) $\nu_{NO}$ region characterizing Cr/Beta(aqueous ion exchange) at room temperature during exposure to NO.

Figure 5.3 compares two methods of calculating pseudo-absorbance in diffuse-reflectance IR spectra. The log–inverse reflectance and Kubelka-Munk spectra result from the same reflectance spectrum characterizing Cr/Beta(aqueous ion exchange) during exposure to NO at room temperature. The log–inverse reflectance spectrum is more sensitive to small changes in absorbance, whereas the Kubelka-Munk spectrum appears to flatten areas of low absorbance (Figure 5.3a). This can be interpreted in terms of the relative intensities of background and sample spectra.[8]

Critical differences between log–inverse reflectance and Kubelka-Munk spectra are observed in Figure 5.3b, which focuses only on the $\nu_{NO}$ region. The spectra are normalized to the intensity of the 1765 $cm^{-1}$ band. This allows a clear comparison of the full width at half maximum (fwhm) of the 1765 $cm^{-1}$ band.

The fwhm of the 1765 $cm^{-1}$ in the Kubelka-Munk spectrum is considerably smaller than that of the log–inverse reflectance spectrum. Additionally, small shoulders on either side of the 1765 $cm^{-1}$ band observed in the log–inverse reflectance spectrum are not clearly visible in the Kubelka-Munk spectrum. Considering that fwhm and number of bands are commonly used to assess the structural uniformity and speciation of dispersed metals on catalyst surfaces, the impact of pseudo-absorbance calculation (which is rarely discussed in the catalysis literature) should be an important consideration.

With respect to Cr/Beta(aqueous ion exchange), the presence of mainly a single set of particularly sharp $\nu_{NO}$ bands (regardless of our choice of pseudo-absorbance) indicates the existence of structurally uniform $Cr^{2+}(NO)_2$ complexes in the sample. The spectrum of Figure 5.3 is reproduced in Figure 5.4 in order to compare the speciation of chromium in the sample following different pre-treatments. Heating Cr/Beta(aqueous ion exchange) to 350 °C (Figure 5.4a) resulted in clear differences from heating to 200 °C (Figure 5.3 and 5.4b). After exposure to the higher temperature, exposure of the sample to NO at room temperature revealed additional $\nu_{NO}$ bands that did not appear after heating at the lower temperature. A likely hypothesis is that the sample was exposed to adventitious moisture during transfer to, and storage in, the glove box, and that differences in the spectra of Figure 5.4 due to pre-treatment temperature reflect different strengths of $H_2O$ binding to the various $Cr^{2+}$ species present in the sample. Desorption of $H_2O$ during heating created coordinatively unsaturated $Cr^{2+}$ which were able to adsorb NO.

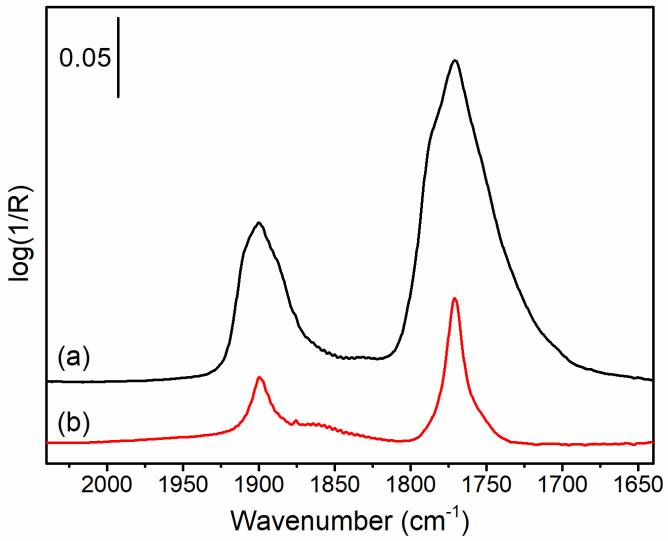


**Figure 5.4.** IR spectra characterizing Cr/Beta(aqueous ion exchange) at room temperature during exposure to NO following exposure to $N_2$ at (a) 350 °C or (b) 200 °C.

See discussion of Figure 5.4 above.

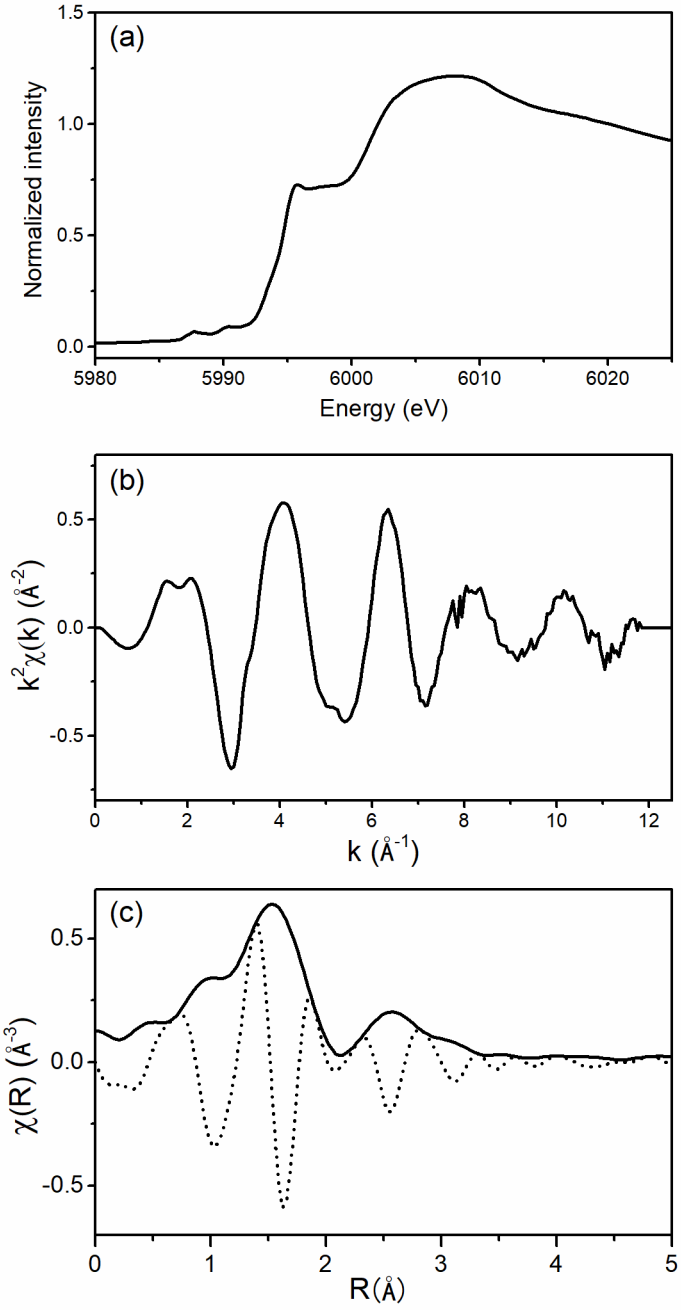


**Figure 5.5.** (a) Normalized XANES, (b) $k^2$-weighted EXAFS, and (c) $k^2$-weighted, Fourier-transformed EXAFS characterizing Cr/ZSM-5 (Si/Al = 15) during exposure to 10% $H_2$ at 500 °C.

Figures 5.5–5.11 contain X-ray absorption spectra (XANES and EXAFS) characterizing chromium-containing zeolite samples during exposure to $H_2$ at 500 °C. Each XANES spectrum contains a shoulder in the absorption edge at approximately 5995 eV, which is considered a fingerprint of divalent chromium coordinated in approximately fourfold coordination with support oxygen atoms in reduced

$Cr/SiO_2$ samples.[1] This indicates that chromium was in nearly the +2 oxidation state in every sample evaluated. When chromium was dispersed on proton-form zeolites, the 5995 eV shoulder displayed an unusually sharp feature that was nearly resolved as a peak. This feature is most clearly visible in the spectrum characterizing Cr/Beta (Figure 5.7). When chromium was dispersed on Na-ZSM-5, no sharp feature in the edge shoulder was observed (Figure 5.9). The appearance of this unusually well-resolved feature in the near-edge spectra may be related to an unusual coordinative state or degree of structural uniformity characteristic of chromium bonded to the crystalline surface of zeolites with respect to chromium bonded to the surface of amorphous $SiO_2$, which is more commonly studied.[1,9]

The corresponding EXAFS data characterizing each Cr/zeolite sample during exposure to $H_2$ at 500 °C is included in Figures 5.5–5.11. The EXAFS data are consistent with the existence of chromium coordinated mainly with oxygen,[1] but fitting of the EXAFS was not performed and so a more detailed interpretation is not possible at this time.

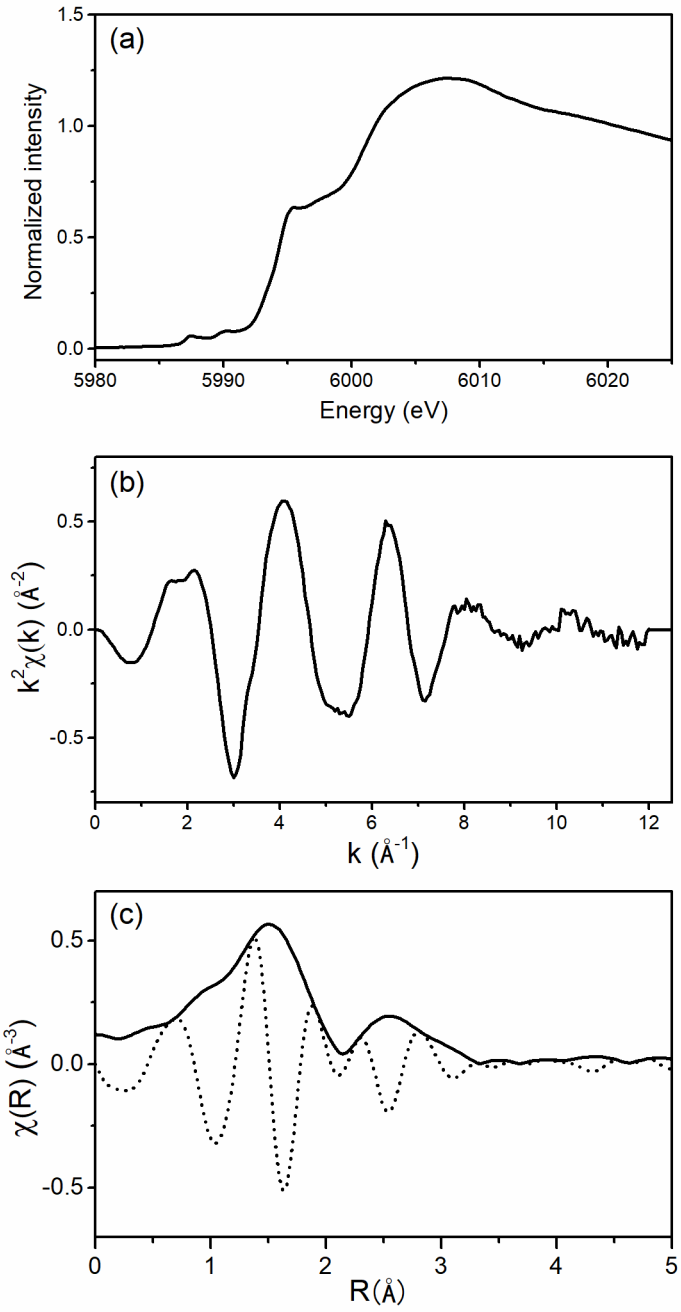


**Figure 5.6.** (a) Normalized XANES, (b) $k^2$-weighted EXAFS, and (c) $k^2$-weighted, Fourier-transformed EXAFS characterizing Cr/ZSM-5 (Si/Al = 25) during exposure to 10% $H_2$ at 500 °C.

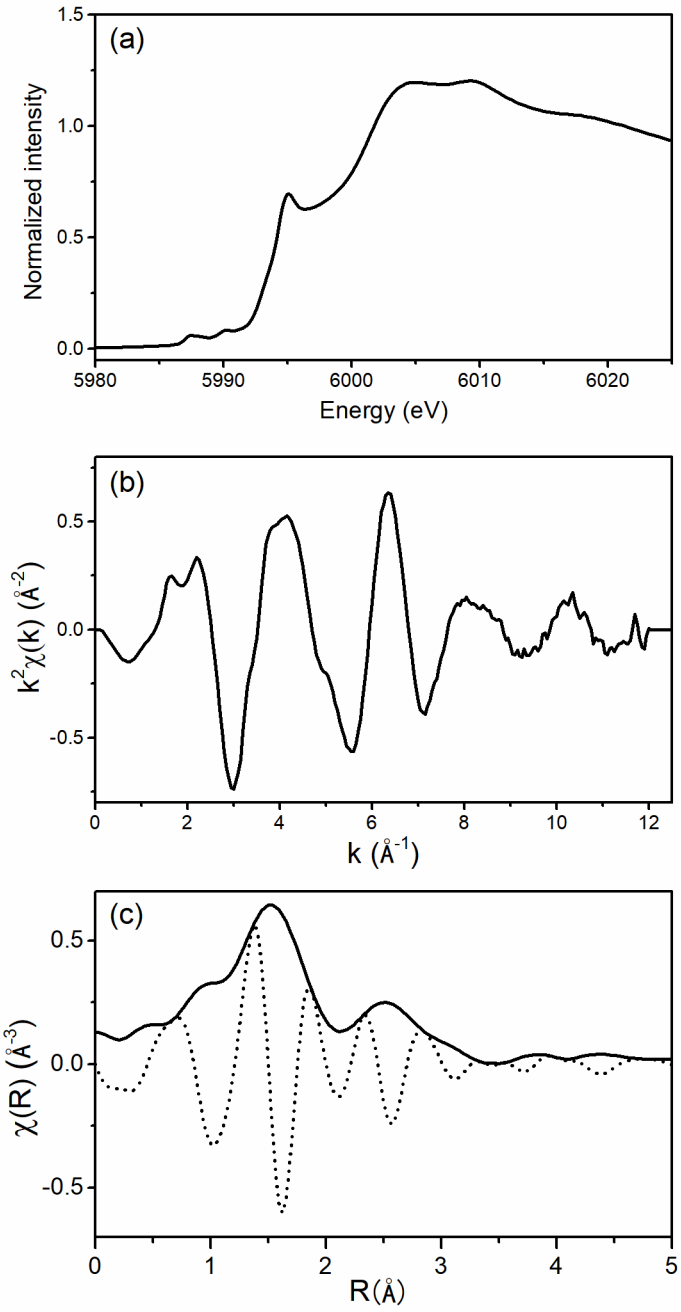


**Figure 5.7.** (a) Normalized XANES, (b) $k^2$-weighted EXAFS, and (c) $k^2$-weighted, Fourier-transformed EXAFS characterizing Cr/Beta (Si/Al = 19) during exposure to 10% $H_2$ at 500 °C.

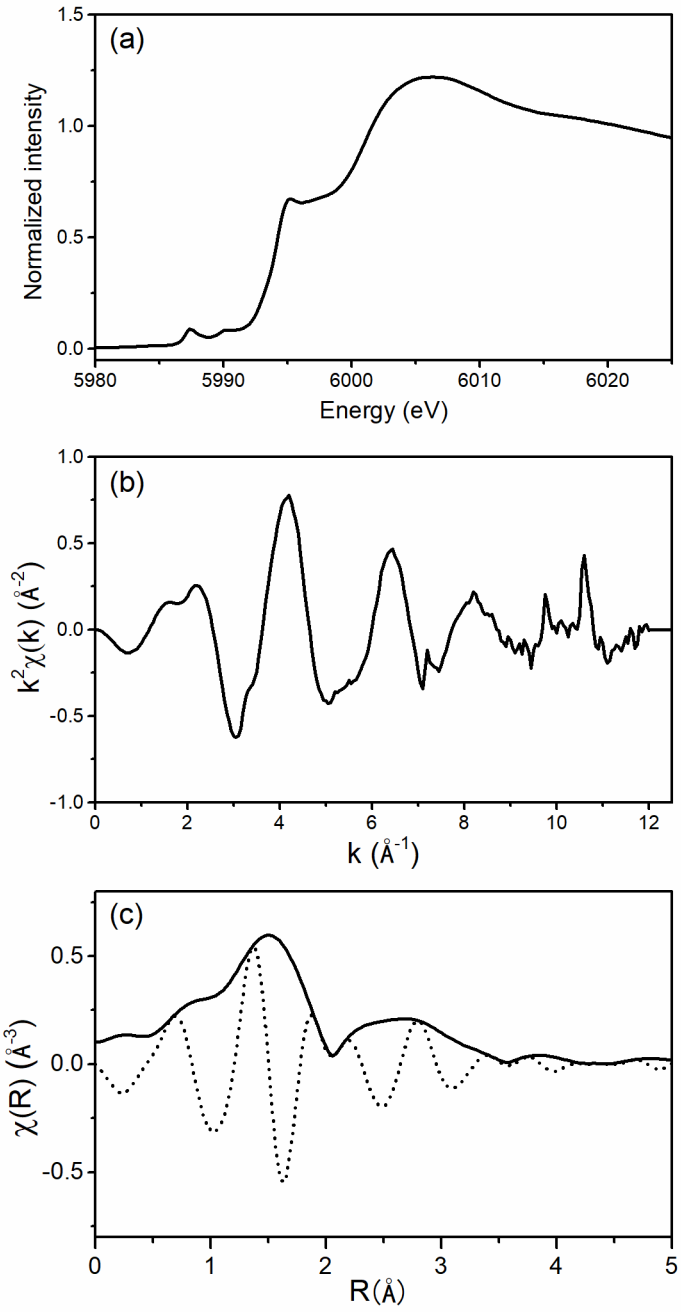


**Figure 5.8.** (a) Normalized XANES, (b) $k^2$-weighted EXAFS, and (c) $k^2$-weighted, Fourier-transformed EXAFS characterizing Cr/Ga-MFI during exposure to 10% $H_2$ at 500 °C.

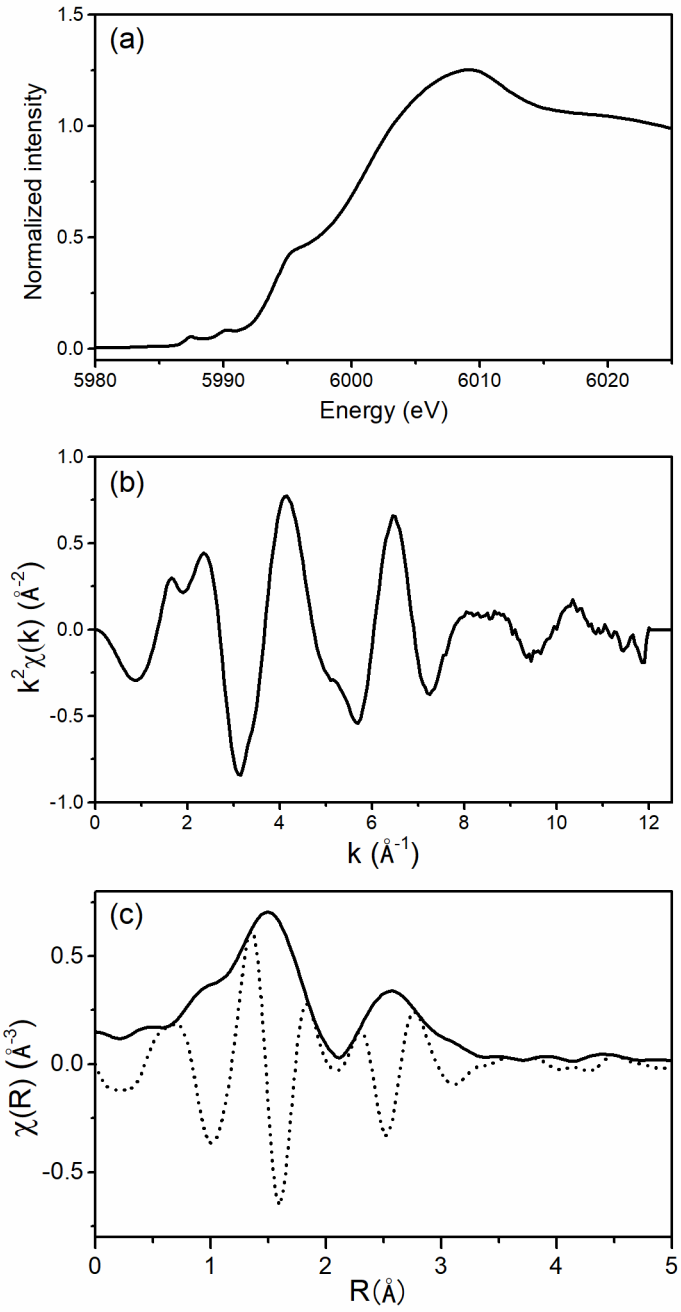


**Figure 5.9.** (a) Normalized XANES, (b) $k^2$-weighted EXAFS, and (c) $k^2$-weighted, Fourier-transformed EXAFS characterizing Cr/Na-ZSM-5 (Si/Al = 15) during exposure to 10% $H_2$ at 500 °C.

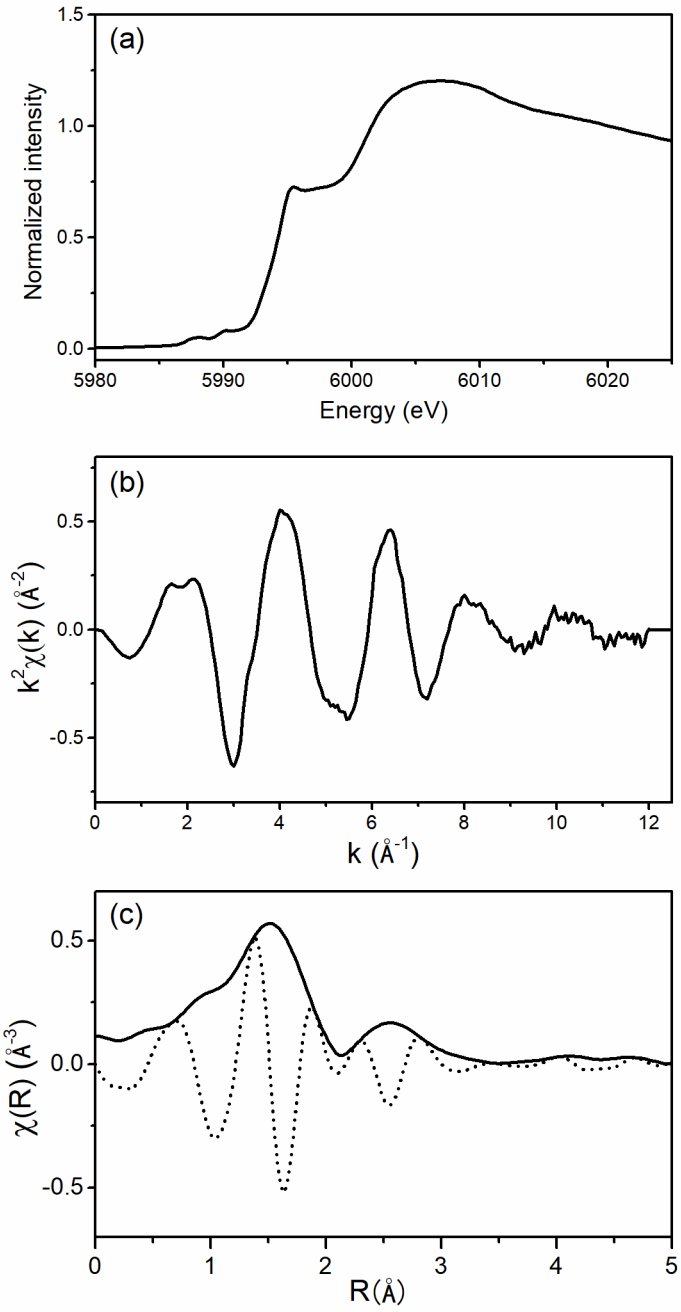


**Figure 5.10.** (a) Normalized XANES, (b) $k^2$-weighted EXAFS, and (c) $k^2$-weighted, Fourier-transformed EXAFS characterizing Cr/ZSM-5 (Si/Al = 15, Cr/Al = 0.30) during exposure to 10% $H_2$ at 500 °C.

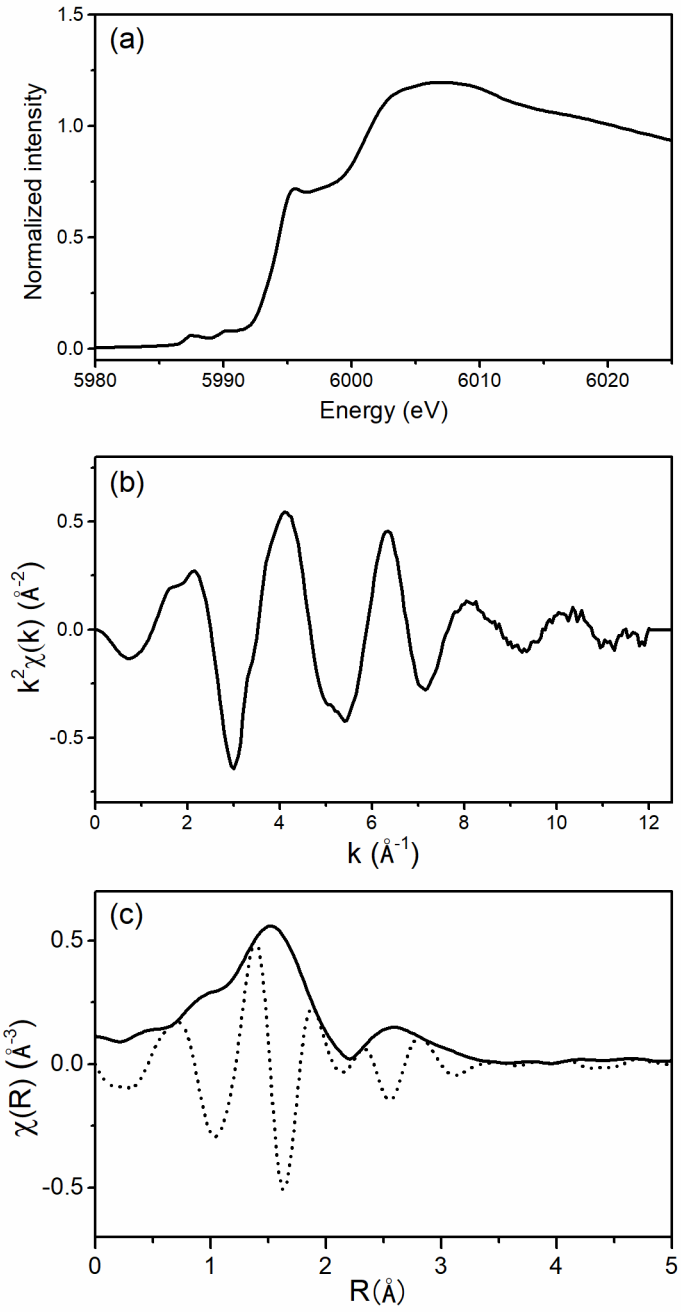


**Figure 5.11.** (a) Normalized XANES, (b) $k^2$-weighted EXAFS, and (c) $k^2$-weighted, Fourier-transformed EXAFS characterizing Cr/ZSM-5 (low pair Al) during exposure to 10% $H_2$ at 500 °C.

## 5.5 References


(1) Groppo, E.; Lamberti, C.; Bordiga, S.; Spoto, G.; Zecchina, A. The Structure of Active Centers and the Ethylene Polymerization Mechanism on the $Cr/SiO_2$ Catalyst: A Frontier for the Characterization Methods. *Chem. Rev.* **2005**, *105*, 115–183.

(2) Sattler, J. J. H. B.; Ruiz-Martinez, J.; Santillan-Jimenez, E.; Weckhuysen, B. M. Catalytic Dehydrogenation of Light Alkanes on Metals and Metal Oxides. *Chem. Rev.* **2014**, *114*, 10613–10653.

(3) Grosso-Giordano, N. A.; Zones, S. I.; Katz, A. *Opportunities for Controlling Catalysis by Designing Molecular Environments around Active Sites: Cations Supported on Amorphous: Versus Crystalline Zeolitic Silicate Supports*; 2019; Vol. 31.

(4) Shishido, T.; Shimamura, K.; Teramura, K.; Tanaka, T. Role of $CO_2$ in Dehydrogenation of Propane over Cr-Based Catalysts. *Catal. Today* **2012**, *185*, 151–156.

(5) Spoto, G.; Bordiga, S.; Garrone, E.; Ghiotti, G.; Zecchina, A.; Petrini, G.; Leofanti, G. Cr(II) and Cr(III) Ions Grafted at Internal Nests of a Pentasilic Zeolite (Silicalite): Characterization and Formation of Polycarbonylic, Polynitrosylic, and Mixed Species by Interaction with CO and NO. *J. Mol. Catal.* **1992**, *74*, 175–184.

(6) Lanh, H. D.; Tuan, V. A.; Kosslick, H.; Parlitz, B.; Fricke, R.; Völter, J. N-Hexane Aromatization on Synthetic Gallosilicates with MFI Structure. *Appl. Catal. A, Gen.* **1993**, *103*, 205–222.

(7) Dedecek, J.; Balgová, V.; Pashkova, V.; Klein, P.; Wichterlová, B. Synthesis of ZSM-5 Zeolites with Defined Distribution of Al Atoms in the Framework and Multinuclear MAS NMR Analysis of the Control of Al Distribution. *Chem. Mater.* **2012**, *24*, 3231–3239.

(8) Sirita, J.; Phanichphant, S.; Meunier, F. C. Quantitative Analysis of Adsorbate Concentrations by Diffuse Reflectance FT-IR. *Anal. Chem.* **2007**, *79*, 3912–3918.

(9) Botavina, M.; Barzan, C.; Piovano, A.; Braglia, L.; Agostini, G.; Martra, G.; Groppo, E. Insights into $Cr/SiO_2$ Catalysts during Dehydrogenation of Propane: An Operando XAS Investigation. *Catal. Sci. Technol* **2017**, *7*, 1690–1700.

## 5.6 Supporting Information

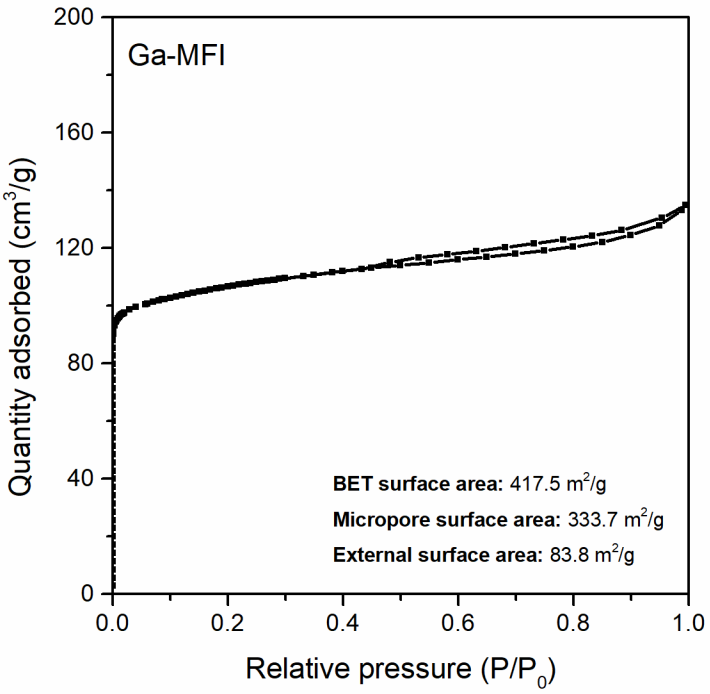


**Figure S5.1.** $N_2$ adsorption isotherm for Ga-MFI collected at 77 K.

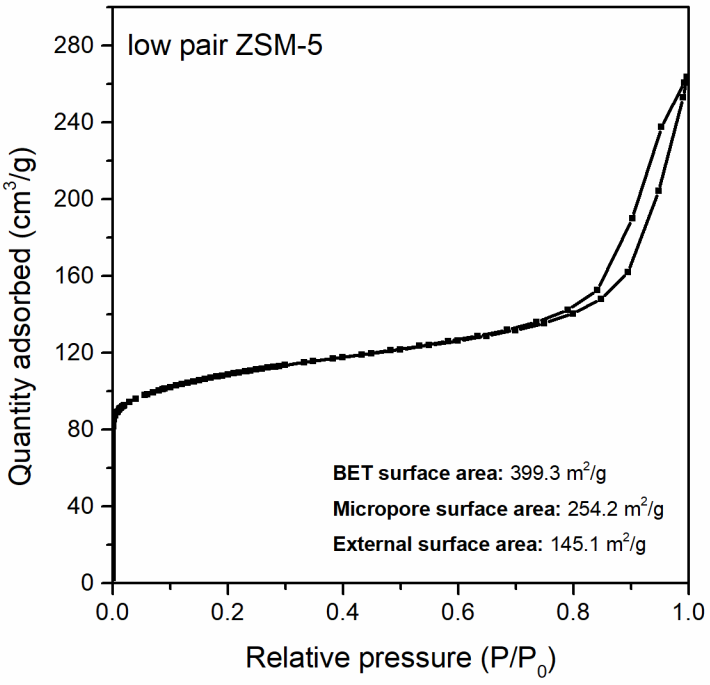


**Figure S5.2.** $N_2$ adsorption isotherm for ZSM-5 (low pair aluminum) collected at 77 K.

# **Appendix B.** Characterization of Platinum–Zeolite Catalysts Using Infrared and X-ray Absorption Spectroscopies

## 6.1 Abstract

A more detailed understanding of the local environment of platinum cations would aid efforts to understand and control the chemistry involved in the stabilization of platinum or the interconversion of platinum cations and clusters, either of which would be of great industrial value. IR and X-ray absorption spectroscopies were demonstrated in Chapter 3 to be effective tools for characterizing platinum cations in zeolites. This Chapter presents related results using the same techniques. XAS was used to monitor the formation of platinum *gem*-dicarbonyls in zeolites under equivalent conditions to those examined in the IR experiments characterizing Pt/ZSM-5 (in Chapter 3) and Pt/Y (in this Chapter). Another set of experiments used IR spectroscopy to demonstrate the formation of platinum *gem*-dicarbonyls in zeolites CHA and heteroatom-substituted Beta.

## 6.2 Introduction

Chapter 3 emphasized the impact that the bonding of platinum with the zeolite surface has on the state of platinum during harsh redox cycling. The experiments also began to explore the chemistry involved in the transformation of platinum from cations to clusters, a process that, depending on environmental conditions, can include multiple steps. It was proposed that the binding of CO pulls platinum away from zeolite oxygen atoms during formation of *gem*-dicarbonyls. Structural characterization of the *gem*-dicarbonyls would help to understand the chemistry involved, opening the possibility of tuning the process to achieve desired outcomes, including location or size of platinum clusters. This Chapter presents results from initial sets of IR and X-ray absorbance spectroscopy experiments designed to understand the chemistry or tune the properties of platinum cations in zeolites.

## 6.3 Experimental Methods

**Preparation of zeolites.** Aluminosilicate zeolites ZSM-5 (5524G, SiAl = 25) and Y (CBV 720, Si/Al = 15) were supplied by Zeolyst. Chabazite zeolite was supplied by Chevron. Zeolites were calcined in flowing 20% $O_2$ at 550 °C for 5 h with temperature ramp rates of 2 °C/min before use. Gallosilicate Ga-Beta and

ferrosilicate Fe-Beta zeolites were supplied by Michael J. Meloni, who documented the preparation and characterization of the samples in a recent publication.[1]

**Incorporation of platinum into zeolites.** Platinum was incorporated into protonic forms of zeolites using the following aqueous ion exchange procedure. Zeolite was added to a magnetically-stirred aqueous solution of approximately 50 mM ammonium nitrate ($NH_4NO_3$; Acros Organics, 99+%) in a ratio of approximately 199 mL solution per g zeolite. To this mixture was added a small volume (approximately 1 mL) of a stock solution of aqueous tetraammineplatinum(II) nitrate ($Pt(NH_3)_4(NO_3)_2$; Sigma Aldrich, 99.995%). The concentration of stock solution was typically 20.4 mM. After addition of $Pt(NH_3)_4(NO_3)_2$ solution, the resulting mixture had a ratio of 200 mL solution per g zeolite, a $Pt(NH_3)_4(NO_3)_2$ concentration of 0.10 mM, and an $NH_4NO_3$ concentration of 50 mM. This mixture was covered and stirred under ambient conditions for 20 h before separation by centrifugation. Separated solids were washed with deionized water and centrifuged again. The solids were washed and centrifuged a total of three times before drying in an oven at 80 °C overnight. Dried Pt/zeolite samples were stored at room temperature in ambient conditions until use. For the Pt/Y sample described in Figures 6.6–6.10, the amount of stock $Pt(NH_3)_4(NO_3)_2$ solution used was increased to yield a concentration of 0.25 mM during exchange. The platinum loading of this Pt/Y sample was determined by inductively-coupled plasma optical emission spectroscopy to be 0.47 wt% Pt. The platinum loading of the Pt/ZSM-5 sample described below was 0.37 wt%. The elemental compositions of the remainder of the samples were not determined.

**IR spectroscopy.** Diffuse reflectance infrared Fourier transform spectra (DRIFTS) were collected using a Bruker Tensor II instrument (2 $cm^{-1}$ resolution and 128 scans per spectrum) and a Pike Technologies DiffusIR accessory with high temperature environmental chamber. A spectrum of powdered $CaF_2$ was used as a background, and sample absorbance spectra were calculated using the Kulbelka-Munk equation. As-prepared Pt/zeolite samples (5-10 mg) were loaded into the environmental chamber in a ceramic cup, and the chamber was purged with flowing $N_2$ (Airgas, Research Purity). Then $N_2$ flow was replaced with 50 mL/min air (Praxair, Zero grade) flow, and the temperature was increased at 5 °C/min to 120 °C, where it was held for 1 h to remove adsorbed waster. Next, samples were heated at 2 °C/min to 700 °C (unless

otherwise stated) and held at this temperature for 2 h before cooling at 25 °C/min to 500 °C. With sample at 500 °C, flow was switched to $N_2$ and held under this condition for 1 h. Samples were then cooled to 30 °C before subsequent exposure to probe molecules.

For IR spectra of adsorbed CO, calcined samples were exposed to flowing 10% CO in $N_2$ at 30 °C for 15 minutes before flow was switched to $N_2$ to remove gas phase CO. Spectra were collected during $N_2$ flow.

**X-ray absorption spectroscopy.** X-ray absorption spectroscopy (XAS) measurements were performed at the Stanford Synchrotron Radiation Lightsource (SSRL) at SLAC National Accelerator Laboratory at beam line 4–1 using a Si(220) monochromator. X-ray absorption near edge structure (XANES) and extended X-ray absorption fine structure (EXAFS) spectra were recorded at the Pt $L_3$-edge (11564 eV) in fluorescence mode. The catalysts (approximately 30 mg) were loaded into 3 mm OD quartz tubes, which were heated with resistive coils and fitted with o-rings to a gas flow manifold. A platinum foil was scanned simultaneously for energy calibration. Raw XAS data was energy-calibrated, merged and normalized using the Athena interface of the Demeter software package.

The conditions of the in-situ XAS experiments for Pt/ZSM-5 and Pt/Y were as follows. Samples (directly following ion exchange and drying, as described above) were loaded into 3 mm OD quartz tubes, and helium was flowed to purge air out of the reactor. With sample under helium at room temperature, EXAFS spectra were collected. Next, 20% $O_2$ in helium was flowed (20 mL/min) and temperature was increased at 10 °C/min to 120 °C. Temperature was held constant at 120 °C for 20 min to allow desorption of water from the sample. Then temperature was increased at 10 °C/min to 700 °C. Temperature was held constant at 700 °C for 0.5 h before sample was cooled to room temperature. XANES spectra were collected continuously during the entire thermal treatment. With the sample at room temperature, flow was switched to helium (20 mL/min) and EXAFS spectra were collected. Next, 10% CO in helium was flowed (20 mL/min) for 15 min before purging with helium (20 mL/min) and collecting XAS spectra. Then, 10% $H_2$ in helium was flowed (20 mL/min) and the sample was heated to 100 °C and held at this temperature for

30 min before cooling to room temperature. XAS spectra were collected with sample at room temperature under flowing helium.

The Pt/ZSM-5 sample described in Figure 6.12 was calcined in $O_2$ at 700 °C and stored at room temperature under argon before use. The sample was exposed to ambient air and pressed into a wafer before XAS measurements were performed under ambient conditions.

## 6.4 Results and Discussion

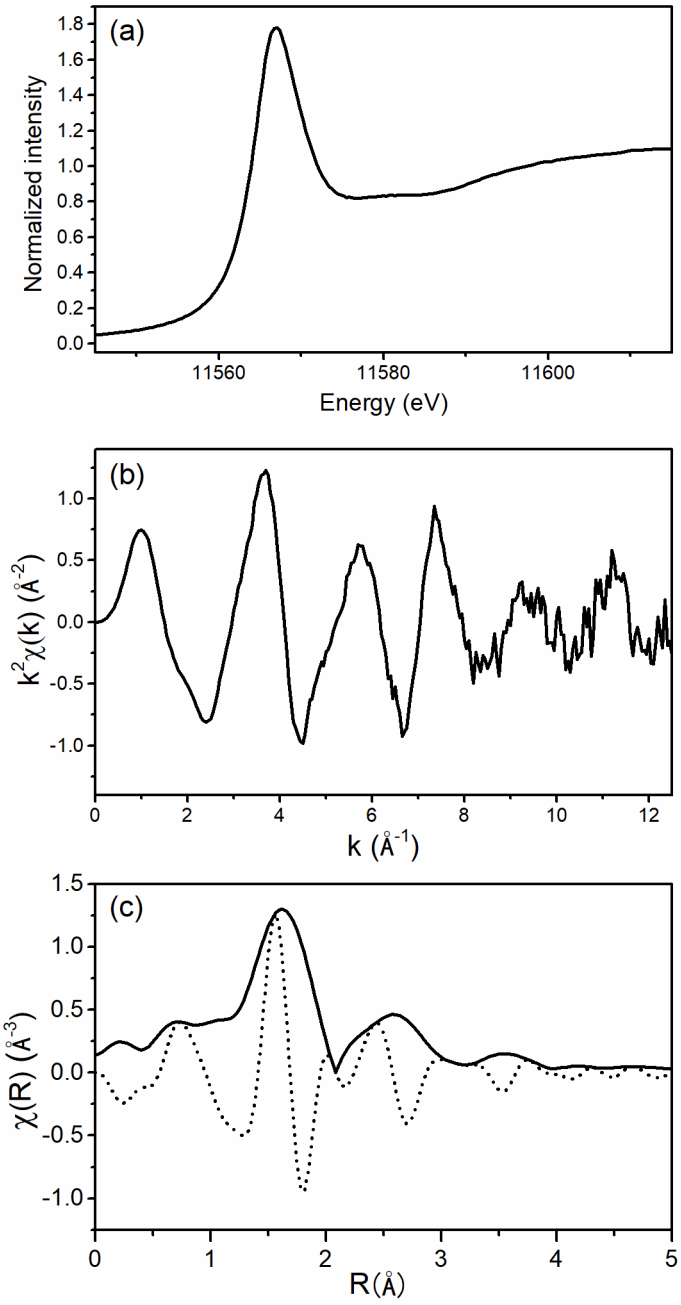


**Figure 6.1.** (a) Normalized XANES spectrum, (b) $k^2$-weighted EXAFS data, and (c) Magnitude (solid) and imaginary component (dotted) of $k^2$-weighted Fourier-transformed EXAFS data characterizing Pt/ZSM-5 at room temperature under flowing helium following exposure to $O_2$ at 700 °C. This data, collected in July 2021, is reproduced from Chapter 3 for comparison here.

The XAS results from Chapter 3 characterizing Pt/ZSM-5 that had been calcined in $O_2$ at 700 °C are reproduced in Figure 6.1 for comparison to other data in this Chapter. The data of Figure 6.1 was

collected in July 2021. The data shown consist of multiple spectra, collected over time, merged into a single spectrum in order to reduce the level of signal noise. In the experiment of Figure 6.1, the spectra collected did not change over time, confirming that the sample was stable over the timescale of the measurements. The data of Figure 6.2 represent an attempt, in January 2022, to repeat the experiment of Figure 6.1. This time, however, the sample did not appear to be stable in flowing helium at room temperature following calcination, as indicated by the changes in successive spectra collected approximately 20 min apart. The XANES white line intensity decreased steadily (Figure 6.2a), and the intensities of peaks in the magnitude of the Fourier-transformed EXAFS decreased (Figure 6.2c). According to interpretations from Chapter 3, the decrease in intensity of the 1.6 Å peak in the magnitude of the Fourier-transformed EXAFS suggests the number of Pt–O bonds decreased as platinum became less closely coordinated with the zeolite surface. This interpretation is also consistent with the shifting of the peak at 1.6 Å towards larger radial distances, which may be expected if platinum is withdrawn from the zeolite surface. Decrease in intensity of the peak at 2.6 Å, which represents Pt–Al (or Pt–Si) bonding, also indicates a change in the local environment of platinum with respect to the zeolite surface. However, since potential contributions to the Fourier-transformed EXAFS resulting from Pt–Pt bonding are expected in a similar R range, and since the spectra are fairly noisy, interpretation of the EXAFS data is difficult.

The changes in Pt/ZSM-5 reflected in the XAS spectra may be explained by impurities, most likely $H_2O$, in the helium gas feed. Platinum would be expected to adsorb $H_2O$ strongly at room temperature, displacing platinum from its original bonding with the zeolite surface, as discussed in Chapter 3. This alone may explain the changes in XAS, but the influence of the X-ray beam may also play a role in facilitating changes to the state of platinum.[2]

Subtle changes in the XANES and EXAFS data were observed when Pt/ZSM-5 was exposed to CO at room temperature and then $H_2$ at 100 °C (Figure 6.3). Interpretation of this data is difficult because of the changes that had already occurred under helium flow, as discussed above. XAS data characterizing Pt/ZSM-5 following exposure to each of CO at room temperature and $H_2$ at 100 °C are displayed in Figures 6.4 and 6.5, respectively.

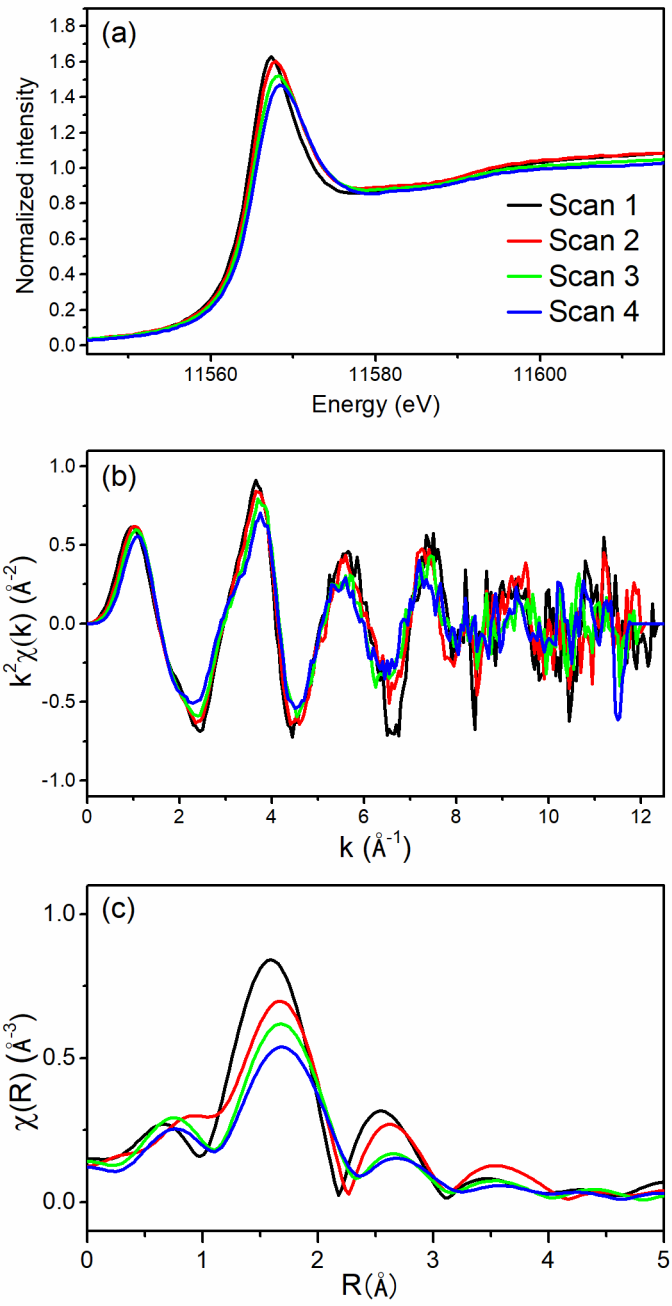


**Figure 6.2.** (a) Normalized XANES spectra, (b) $k^2$-weighted EXAFS data, and (c) Magnitude of $k^2$-weighted Fourier-transformed EXAFS data characterizing Pt/ZSM-5 at room temperature in flowing helium following exposure to $O_2$ at 700 °C. Spectra were collected 20 min apart under flowing helium. This data was collected in January 2022.

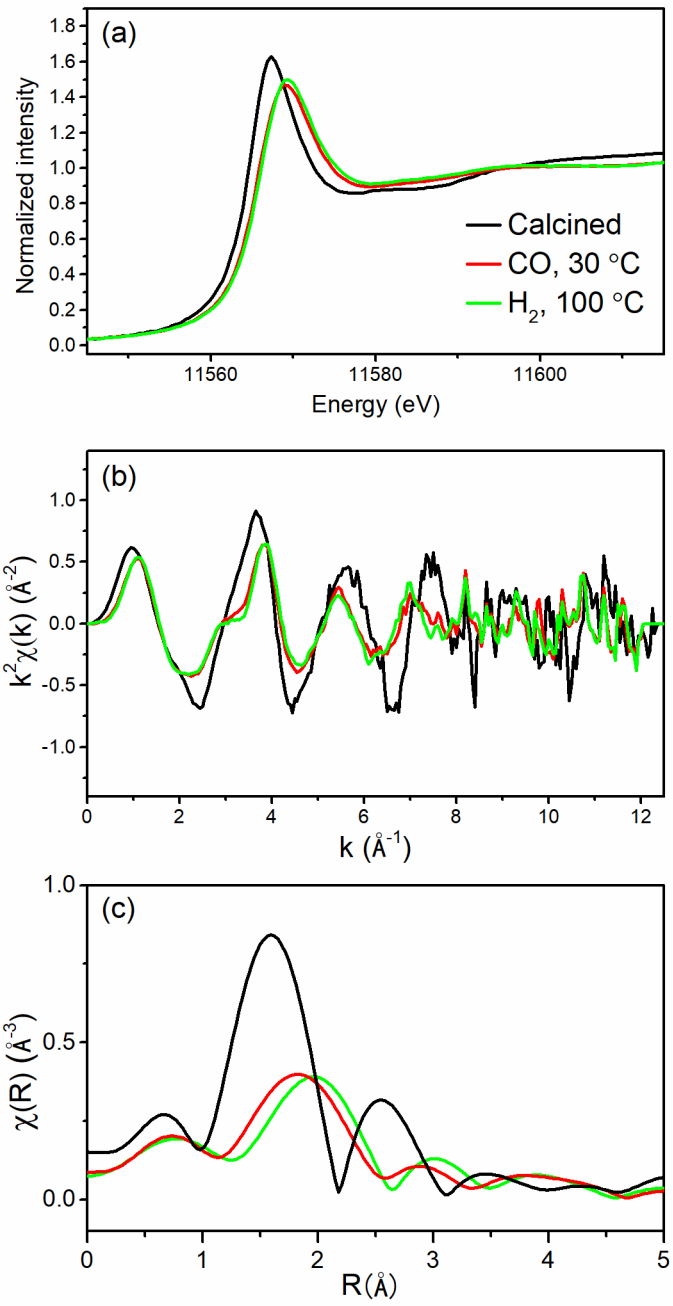


**Figure 6.3.** (a) Normalized XANES spectra, (b) $k^2$-weighted EXAFS data, and (c) Magnitude of $k^2$-weighted Fourier-transformed EXAFS data characterizing Pt/ZSM-5 at room temperature in flowing helium following each step in a sequence of treatment conditions: exposure to $O_2$ at 700 °C (black), subsequent exposure to CO at room temperature (red), and subsequent exposure to $H_2$ at 100 °C (green). This data was collected in January 2022 and is a continuation of the experiment of Figure 6.2.

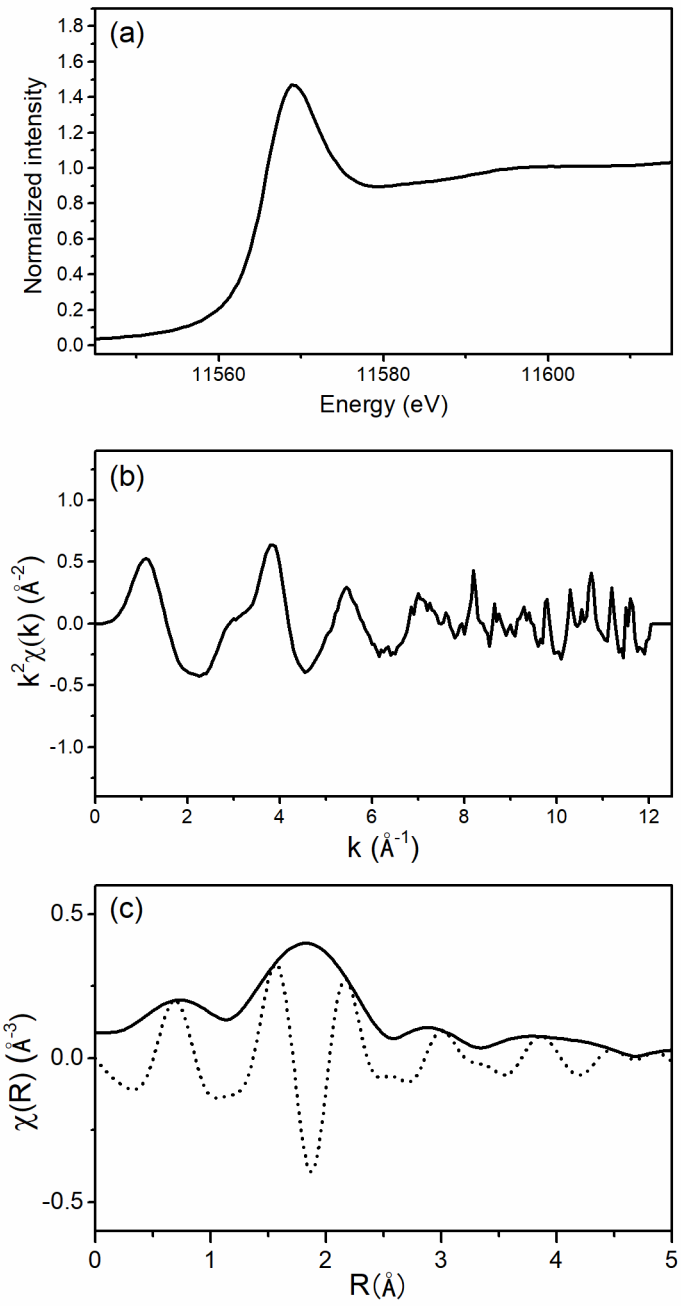


**Figure 6.4.** (a) Normalized XANES spectrum, (b) $k^2$-weighted EXAFS data, and (c) Magnitude (solid) and imaginary component (dotted) of $k^2$-weighted Fourier-transformed EXAFS data characterizing Pt/ZSM-5 at room temperature under flowing helium following exposure to $O_2$ at 700 °C and CO at room temperature.

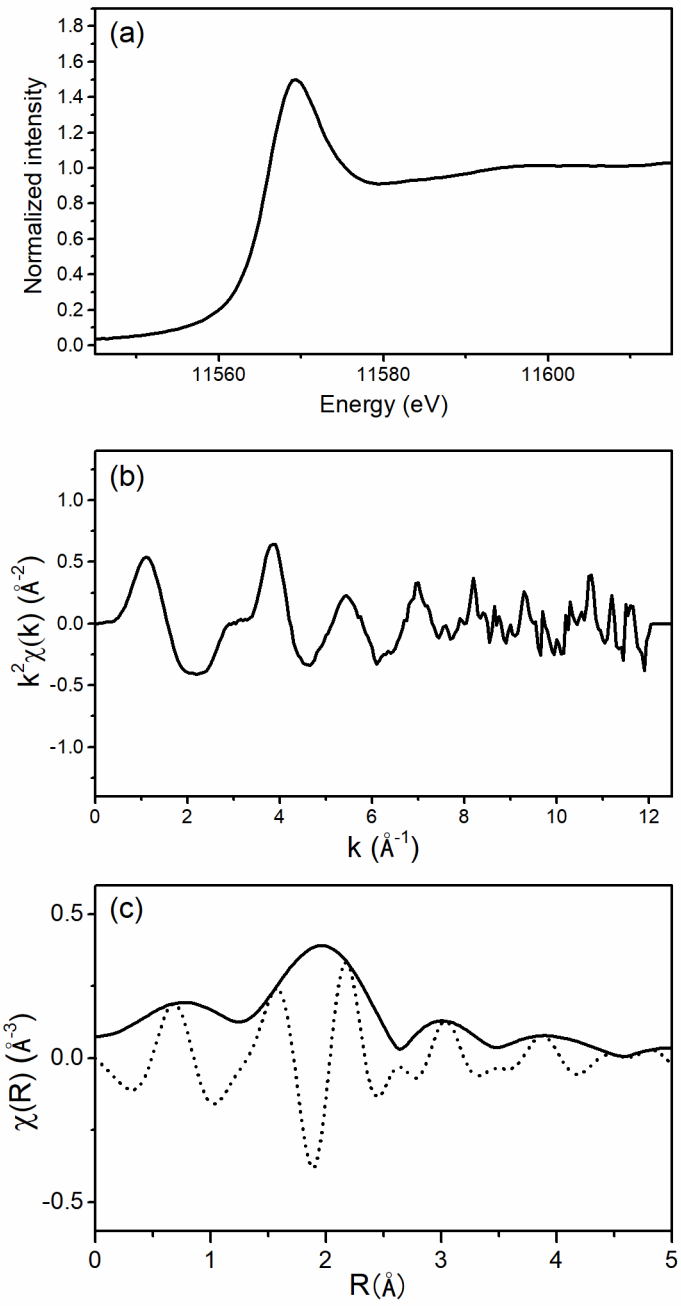


**Figure 6.5.** (a) Normalized XANES spectrum, (b) $k^2$-weighted EXAFS data, and (c) Magnitude (solid) and imaginary component (dotted) of $k^2$-weighted Fourier-transformed EXAFS data characterizing Pt/ZSM-5 at room temperature under flowing helium following exposure to $O_2$ at 700 °C, CO at room temperature, and then $H_2$ at 100 °C.

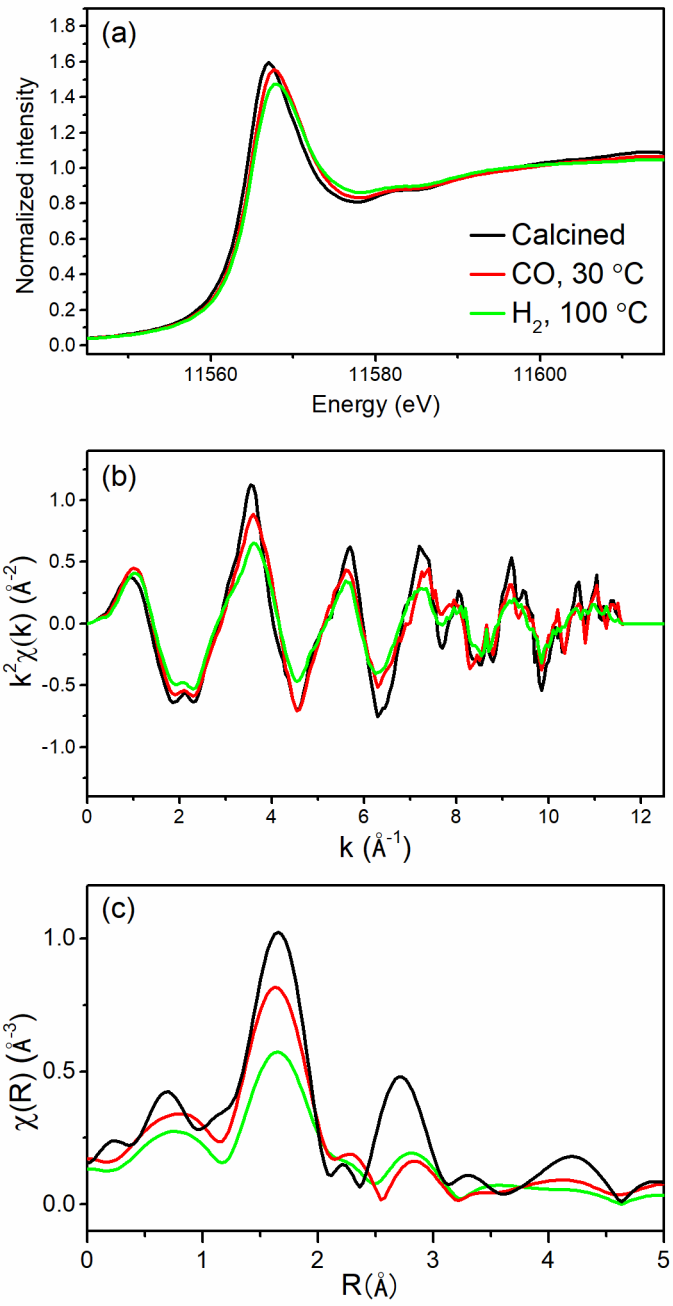


**Figure 6.6.** (a) Normalized XANES spectra, (b) $k^2$-weighted EXAFS data, and (c) Magnitude of $k^2$-weighted Fourier-transformed EXAFS data characterizing Pt/Y at room temperature in flowing helium following each step in a sequence of treatment conditions: exposure to $O_2$ at 700 °C (black), subsequent exposure to CO at room temperature (red), and subsequent exposure to $H_2$ at 100 °C (green).

The sequence of treatments described in Figure 6.3 were performed on a Pt/Y sample containing 0.47 wt% Pt. After calcination in $O_2$ at 700 °C, the X-ray absorption spectra collected with the sample in helium at room temperature were unchanging over time (data not shown). The XANES spectrum of the

calcined Pt/Y (Figure 6.6) was consistent with the result for Pt/ZSM-5 that platinum was present in approximately the +2 oxidation state. Fitting of the EXAFS data was not performed, but the EXAFS data characterizing calcined Pt/Y is qualitatively similar to that characterizing calcined Pt/ZSM-5 (Chapter 3 and Figure 6.1). Thus, we can tentatively conclude that platinum in Pt/Y was present as cations bonded to zeolite surface oxygen atoms.

Exposure of calcined Pt/Y to CO at room temperature caused a nearly complete disappearance of the peak at 2.7 Å in the Fourier-transformed EXAFS data (Figure 6.6c). Following the interpretation of the EXAFS of Pt/ZSM-5 in Chapter 3, the disappearance of the peak at 2.7 Å suggests that platinum no longer had a close coordination with zeolite Al or Si atoms after exposure to CO. IR spectra characterizing Pt/Y samples that had been calcined in $O_2$ at 700 °C and then exposed to CO at room temperature (Figure 6.7) display $\nu_{CO}$ bands assigned to platinum *gem*-dicarbonyl complexes, in accordance with Chapter 3. In the Pt/ZSM-5 samples described in Chapter 3, the bonding of CO to platinum caused a weakening of the interaction between platinum and the zeolite. The disappearance of the peak at 2.7 Å in the Fourier-transformed EXAFS characterizing Pt/Y (Figure 6.6c) could represent additional evidence of this weakening.

Also consistent with a CO-induced withdrawal of platinum from the zeolite surface is the decrease in intensity of the peak at 1.7 Å of the Fourier-transformed EXAFS after exposure of Pt/Y to CO. This most likely represents a decrease in the number of zeolite framework oxygen atoms to which platinum was bonded. After exposure of the CO-exposed sample to $H_2$ at 100 °C, the peak at 1.7 Å decreased further, indicating platinum was further removed from the zeolite surface. IR spectra of Pt/Y treated under equivalent conditions, a $\nu_{CO}$ band at 2129 $cm^{-1}$ was observed which is assigned, following the interpretations in Chapter 3, to $Pt^{\delta+}$ carbonyls. A $\nu_{CO}$ band at approximately 2080 $cm^{-1}$, characteristic of platinum clusters, was also observed.[3]

Fitting of the EXAFS data should be performed in order to interpret the data further. For clarity, the XAS results from each step of the experiment of Figure 6.6 are presented individually in Figures 6.8–6.10.

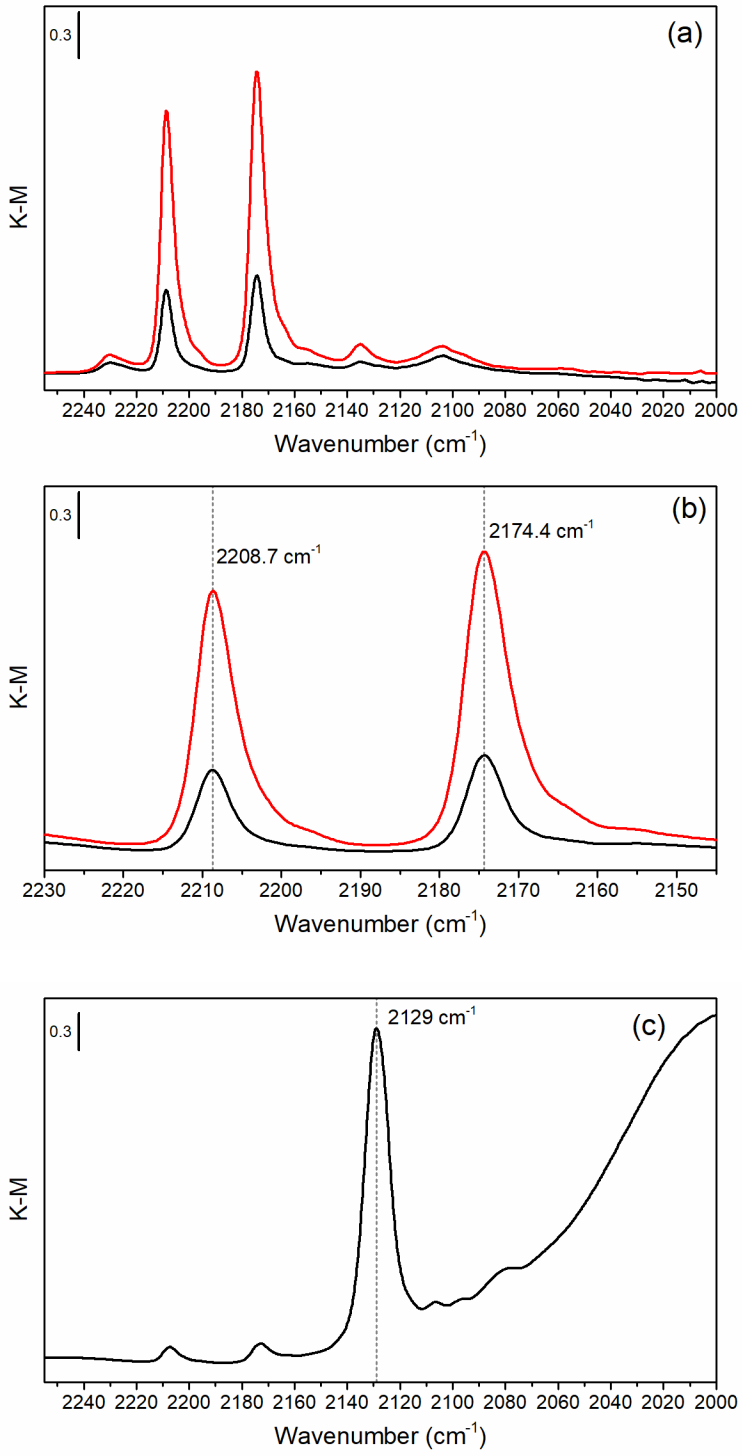


**Figure 6.7.** (a) Wide wavenumber region and (b) narrow wavenumber region of IR spectra characterizing 0.24 wt% Pt/Y (black) and 0.47 wt% Pt/Y that had been calcined in $O_2$ at 700 °C after exposure to CO at room temperature. (c) IR spectra of 0.47 wt% Pt/Y sample from (a) and (b) during subsequent exposure to $H_2$ at 100 °C. In spectra of (a) and (b), sample background absorbance was subtracted, but this was not done for spectrum of (c) due to variation of sample absorptivity with temperature.

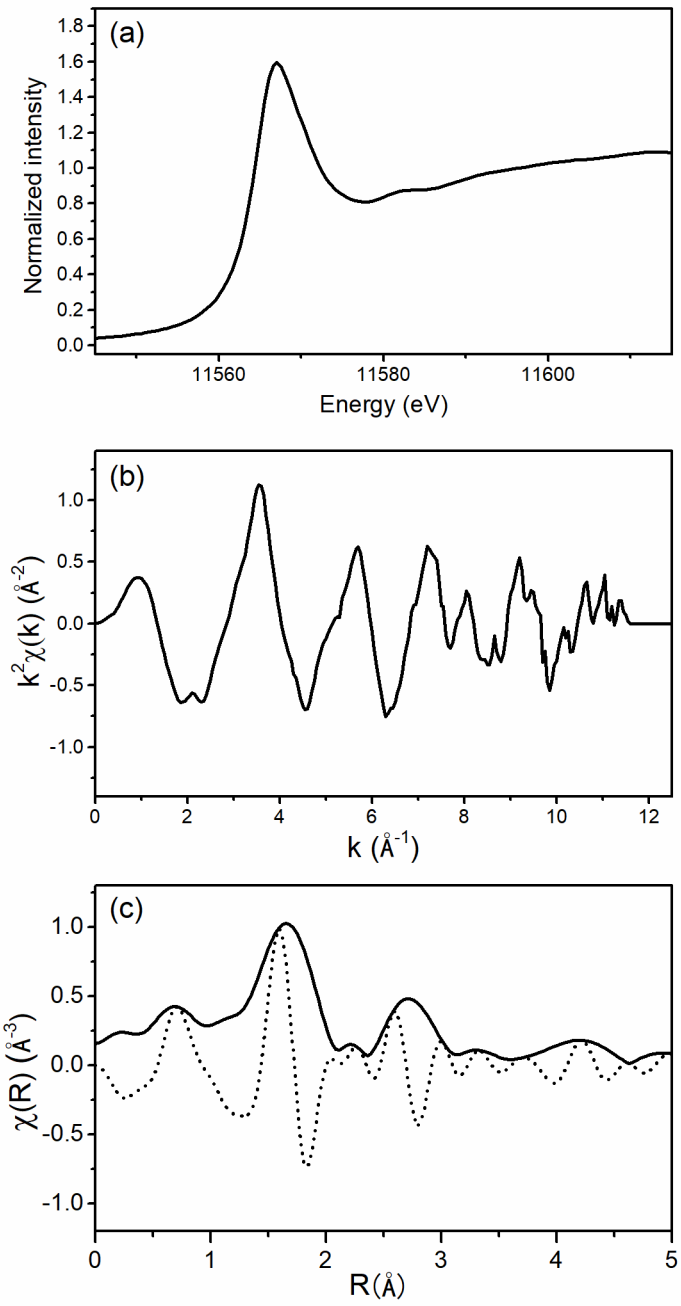


**Figure 6.8.** (a) Normalized XANES spectrum, (b) $k^2$-weighted EXAFS data, and (c) Magnitude (solid) and imaginary component (dotted) of $k^2$-weighted Fourier-transformed EXAFS data characterizing Pt/Y at room temperature under flowing helium following exposure to $O_2$ at 700 °C.

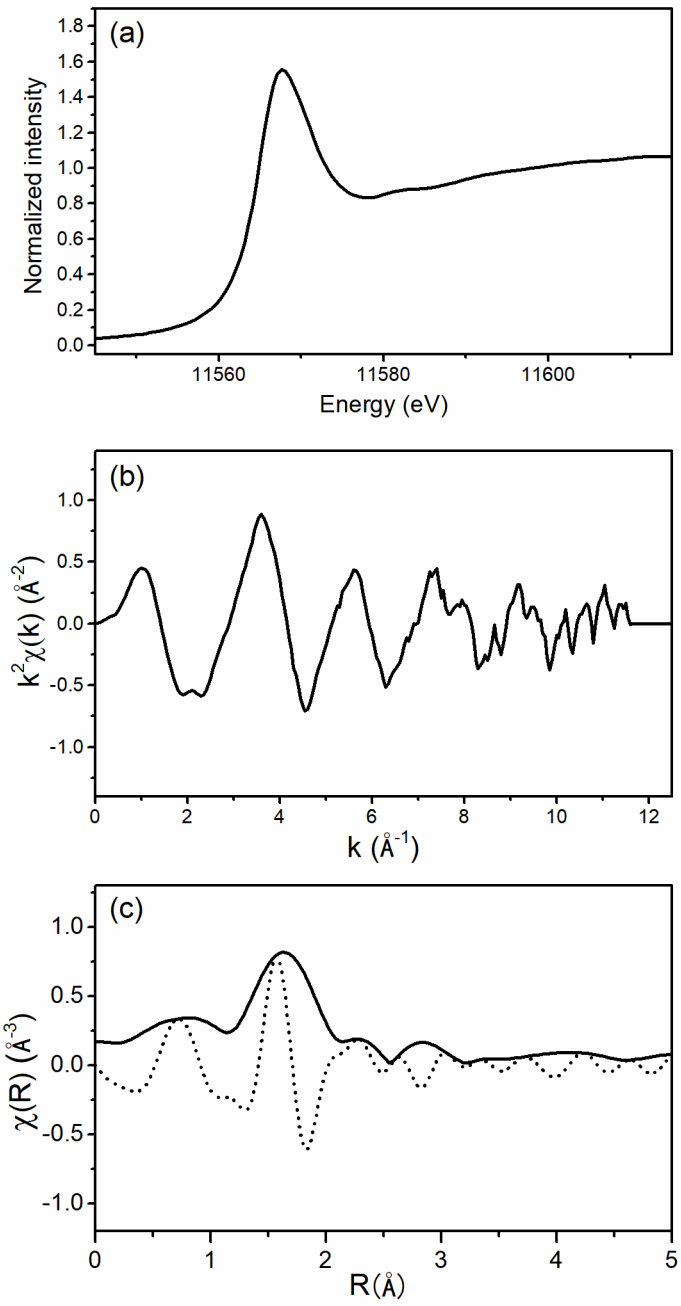


**Figure 6.9.** (a) Normalized XANES spectrum, (b) $k^2$-weighted EXAFS data, and (c) Magnitude (solid) and imaginary component (dotted) of $k^2$-weighted Fourier-transformed EXAFS data characterizing Pt/Y at room temperature under flowing helium following exposure to $O_2$ at 700 °C and CO at room temperature.

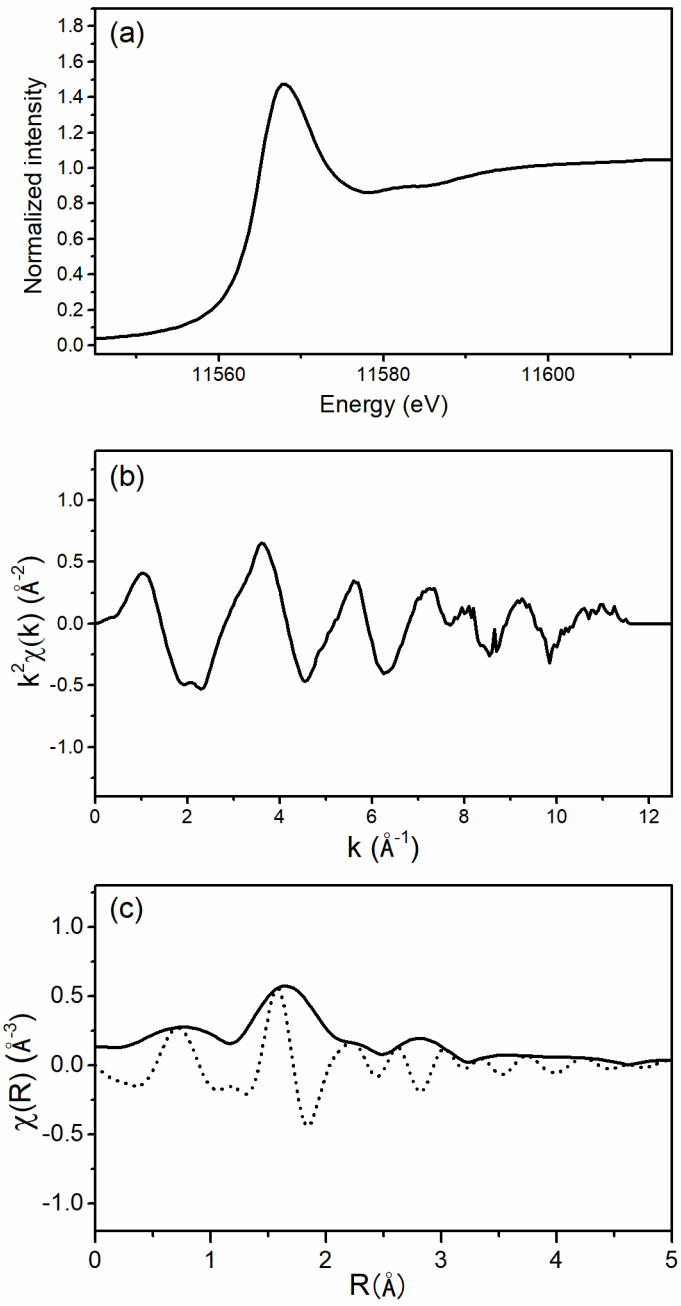


**Figure 6.10.** (a) Normalized XANES spectrum, (b) $k^2$-weighted EXAFS data, and (c) Magnitude (solid) and imaginary component (dotted) of $k^2$-weighted Fourier-transformed EXAFS data characterizing Pt/Y at room temperature under flowing helium following exposure to $O_2$ at 700 °C, CO at room temperature, and then $H_2$ at 100 °C.

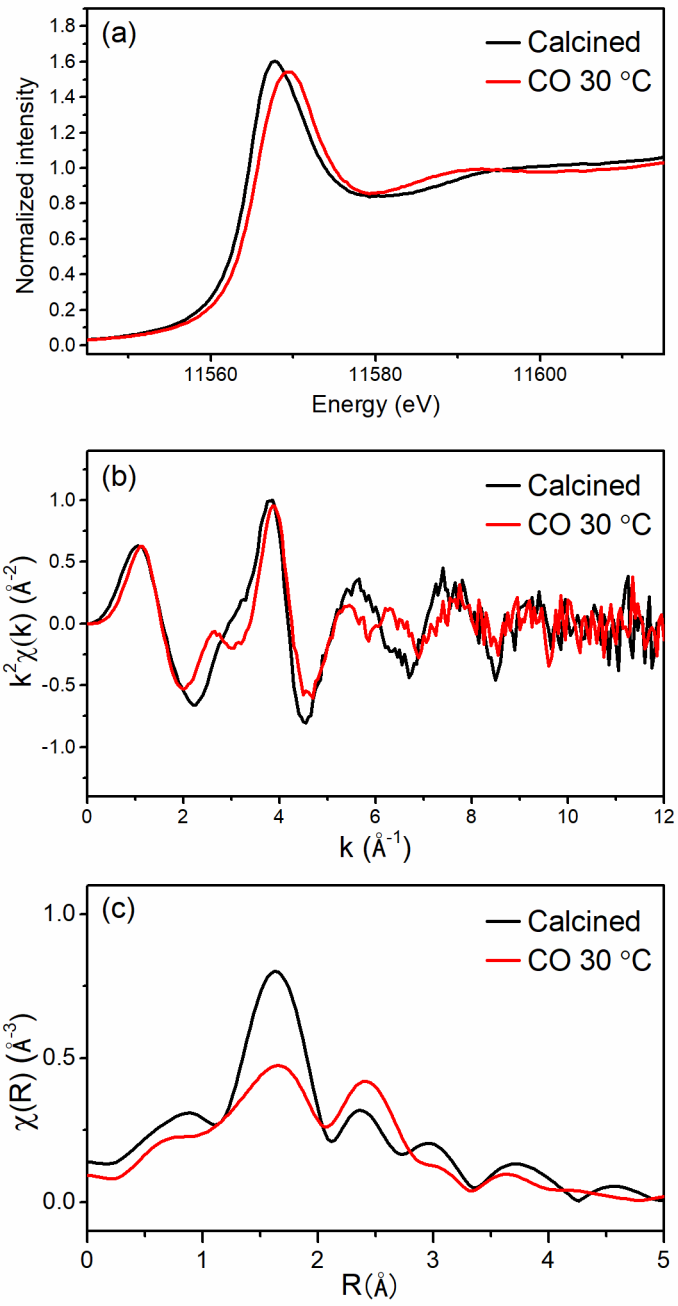


**Figure 6.11.** (a) Normalized XANES spectra, (b) $k^2$-weighted EXAFS data, and (c) Magnitude of $k^2$-weighted Fourier-transformed EXAFS data characterizing Pt/ZSM-5 at room temperature in flowing helium following exposure to $O_2$ at 700 °C (black) and subsequent exposure to CO at room temperature (red). Data was collected in May 2022.

Another attempt to collect EXAFS characterizing Pt/ZSM-5 under conditions under which platinum *gem*-dicarbonyls were present is represented in Figure 6.11. Two consecutive spectra (not shown) characterizing Pt/ZSM-5 under helium at room temperature following exposure to $O_2$ at 700 °C did not

show much change to the sample over time. The data obtained by merging these first two spectra is shown in black Figure 6.11. The EXAFS data of Figure 6.11 displays a bit more noise (Figure 6.11b), and the XANES white line intensity is slightly lower (Figure 6.11a), compared with those of Figure 6.1. Overall, however, the data of Figure 6.11 are qualitatively similar to the corresponding data in Figure 6.1. The XANES white line intensity suggests platinum is present in approximately the +2 oxidation state, and the Fourier-transformed EXAFS is consistent with platinum predominantly bonded to oxygen atoms of the zeolite support.

A number changes were observed when the sample was exposed to CO at room temperature. First, the position of the XANES white line shifted towards higher energy. The white line intensity decreased only very slightly, suggesting only a small decrease in the average oxidation state of platinum occurred as a result of CO exposure. In the Fourier-transformed EXAFS, the peak at 1.6 Å decreased, indicating a decrease in the number of bonds between platinum and the zeolite support as a result of CO adsorption. This is similar to what was observed in Figure 6.6 for Pt/Y. In contrast to the results for Pt/Y, however, the intensity of the peak at 2–3 Å in the Fourier-transformed EXAFS characterizing Pt/ZSM-5 increased. The EXAFS data should be fit using structural models in order to interpret further.

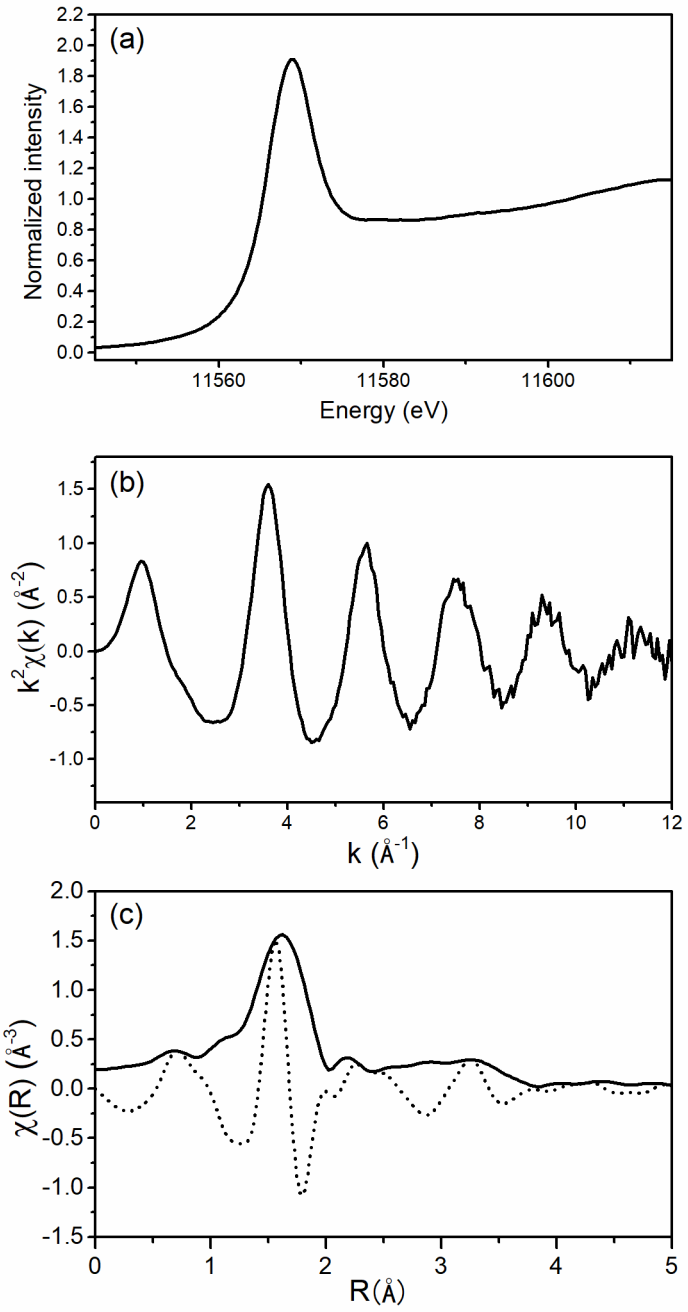


**Figure 6.12.** (a) Normalized XANES spectrum, (b) $k^2$-weighted EXAFS data, and (c) Magnitude (solid) and imaginary component (dotted) of $k^2$-weighted Fourier-transformed EXAFS data characterizing Pt/ZSM-5 under ambient conditions (*ex situ*) following exposure to $O_2$ at 700 °C.

XAS data characterizing Pt/ZSM-5 that was calcined in $O_2$ at 700 °C and then exposed to ambient conditions at room temperature is shown in Figure 6.12. The XANES white line intensity of the air-exposed sample was higher than that of calcined Pt/ZSM-5 under helium and the white line position was shifted to

slightly higher energy. The air exposure also caused a significant loss of intensity in the 2–3 Å region of the Fourier-transformed EXAFS, which is consistent with the findings of Figures 6.2 and 6.6 that adsorbed molecules withdraw platinum from the zeolite surface. Further interpretation of the data in Figure 6.12 would benefit from fitting the EXAFS data or from experiments aimed at understanding the shifting of the XANES white line.

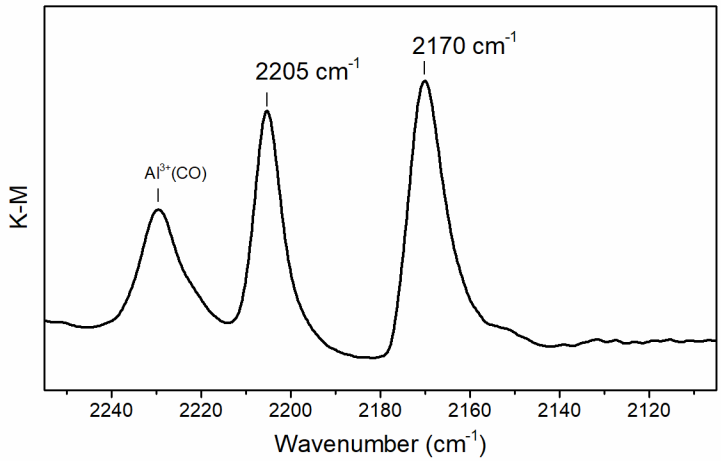


**Figure 6.13.** IR spectrum characterizing Pt/CHA in $N_2$ at room temperature following exposure to $O_2$ at 700 °C and CO at room temperature.

A platinum containing chabazite (CHA) zeolite sample was prepared by ion exchange with $Pt(NH_3)_4(NO_3)_2$ using the same conditions as those of samples in Chapter 3. After calcination in $O_2$ at 700 °C, Pt/CHA was probed with CO at room temperature. The IR spectrum in Figure 6.13 displays $\nu_{CO}$ bands at 2170 and 2205 $cm^{-1}$ that are similar to bands representative of platinum *gem*-dicarbonyl complexes in zeolites Y, ZSM-5, Beta, and MOR (Chapter 3). The corresponding $\nu_{CO}$ bands observed for Pt/CHA are particularly narrow (full width at half maximum < 10 $cm^{-1}$), implying a high degree of structural uniformity of the platinum *gem*-dicarbonyl complexes.

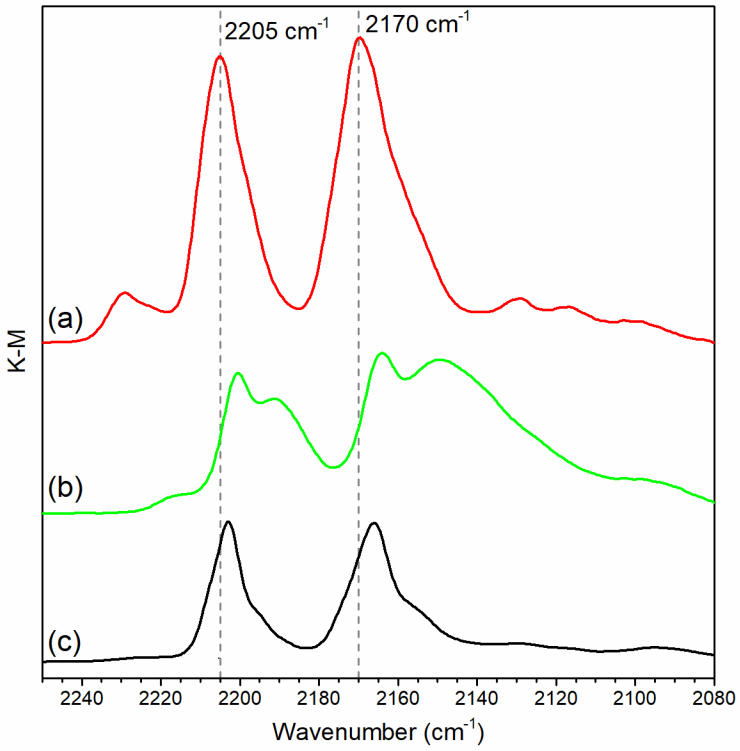


**Figure 6.14.** IR spectra characterizing (a) Pt/Al-BEA, (b) Pt/Fe-BEA, and (c) Pt/Ga-BEA in $N_2$ at room temperature following exposure to $O_2$ at 600 °C and CO at room temperature.

Platinum was incorporated into aluminosilicate (Al-BEA), ferrosilicate (Fe-BEA), and Gallosilicate (Ga-BEA) Beta zeolites by ion exchange of $Pt(NH_3)_4(NO_3)_2$. After calcination in $O_2$ at 700 °C, each sample was probed with CO at room temperature. IR spectra of each sample after exposure to CO at room temperature are shown in Figure 6.14. In each spectrum, $\nu_{CO}$ bands at approximately 2170 and 2205 $cm^{-1}$, characteristic of platinum *gem*-dicarbonyl complexes, are present, following the interpretations of Chapter 3. The positions of the $\nu_{CO}$ bands characterizing platinum *gem*-dicarbonyls in each sample vary by 3–5 $cm^{-1}$, likely as a result of subtle differences in electron sharing with supports having different framework heteroatom elemental composition. This subtle influence is also represented in the results of Figure 5.2 for Cr/Al-MFI and Cr/Ga-MFI samples. Future work should explore catalytically-relevant outcomes that are influenced by this tuning of the platinum–zeolite interaction (e.g. platinum reducibility, mobility, or adsorbate binding).

## 6.5 References


(1) Meloni, M.; Runnebaum, R. C. Tuning Supported Ni Catalysts by Varying Zeolite Beta Heteroatom Composition: Effects on Ethylene Adsorption and Dimerization Catalysis. *Catal. Sci. Technol.* **2021**, *11*, 3393–3401.

(2) Albrahim, M.; Thompson, C.; Leshchev, D.; Shrotri, A.; Unocic, R. R.; Hong, J.; Hoffman, A. S.; Meloni, M. J.; Runnebaum, R. C.; Bare, S. R.; Stavitski, E.; Karim, A. M. Reduction and Agglomeration of Supported Metal Clusters Induced by High-Flux X-Ray Absorption Spectroscopy Measurements. *J. Phys. Chem. C* **2021**, *125*, 11048–11057.

(3) Ding, K.; Gulec, A.; Johnson, A. M.; Schweitzer, N. M.; Stucky, G. D.; Marks, L. D.; Stair, P. C. Identification of Active Sites in CO Oxidation and Water-Gas Shift over Supported Pt Catalysts. *Science* **2015**, *350*, 189–192.

# Chapter 7. Perspective

Supported-chromium catalysts are notoriously difficult to characterize. The structure of chromium active sites in Phillips catalysts ($Cr/SiO_2$) is still a matter of intense interest, despite the fact that these catalysts represent a highly developed technology that has been in use for decades. Structural heterogeneity of supported chromium species presents a significant challenge. Individual cations, dimeric or oligomeric oxide clusters, or ordered oxide nanoparticles can exist simultaneously on a support surface. Cations and small clusters can be indistinguishable by spectroscopic methods. $Cr/SiO_2$ catalysts with mainly mononuclear chromium cations can be prepared, but this does not solve the heterogeneity issue, as the variability in bonding of chromium cations with the oxygen atoms of the amorphous support will result in a population of chromium cations having a wide distribution of local environments and thus catalytic function. If the goal were to rationalize catalyst performance by characterizing the structures of the active sites, then one would want to prepare a nearly monodisperse population of supported chromium. This might require a structurally well-defined surface such as that of a crystalline material. If one then wanted to modify the monodisperse population, one would want the support material to be tunable.

When we first sought to study ethane dehydrogenation with $CO_2$ using chromium-zeolite catalysts, we wondered whether the use of zeolite supports would enable the preparation of uniform and tunable supported chromium structures. To a certain extent, this was the case, but we ran into challenges that changed the path of our work.

The work in my first publication, which appears as Chapter 2 in this dissertation, investigated the ethane dehydrogenation performance (without $CO_2$) of Cr/ZSM-5 catalysts with different populations of supported chromium structures. We learned the extent to which we could control and characterize the speciation of chromium in ZSM-5 and related structural differences to catalytic performance. The significant result was the finding that structurally well-defined chromium cations were stabilized at aluminum sites in ZSM-5 under high-temperature reducing or oxidizing conditions. We postulated that these chromium cations were located at paired aluminum sites in the zeolite framework. The catalysts that

contained mostly this type of chromium, however, displayed relatively low activity for ethane dehydrogenation and, moreover, did not exhibit a strong influence of $CO_2$ on the kinetics of ethane dehydrogenation. In order to continue working towards our broader objective of studying the kinetics of ethane dehydrogenation in the presence of $CO_2$, we decided to target different zeolite supports for chromium. This led to the work described in Chapters 4 and 5, and the work is ongoing.

Meanwhile, our findings from Chapter 2 led to a hypothesis that influenced the work described in Chapter 3. During preparation of Cr/ZSM-5 samples in Chapter 2, high-temperature conditions facilitated the mobility of chromium cations, driving them to the most stable surface binding sites, which we proposed were paired aluminum sites. We hypothesized that platinum cations might be stabilized at the same sites, although the conditions may be different from those necessary for chromium. In the platinum-zeolite literature, most research focused on samples containing platinum nanoparticles or clusters, and there seemed to be synthetic challenges to preparing well-defined platinum complexes in zeolites. In a small number of publications, however, atomically dispersed platinum cations were reported to form during exposure of platinum-zeolite samples to $O_2$ at temperatures higher than 500 °C. The structures of these cations and the surface sites at which they were located had not been determined in detail. We hypothesized that platinum cations may be stabilized by paired aluminum sites at high temperatures, similarly to what was observed for chromium.

We found evidence for this hypothesis in the experiments of Chapter 3, which were bolstered by a theory-driven interpretation of the EXAFS data. The theoretical methods were essential to the findings of the study because they enabled the evaluation of specific platinum structures. This led to an improved understanding of the structure and chemistry of platinum cations in zeolites and the specific features of zeolites needed to stabilize them. The results concern technologically important catalysts under relevant process conditions and thus will be impactful to the development of future catalysts. This work is ongoing, and future experiments will aim to determine the processes controlling platinum nanoparticle formation in zeolites.